Thermal Effects on Particle Production during Cosmic Reheating

Doctoral dissertation presented by

Mubarak Abdallah Suliman Mohammed

in fulfilment of the requirements for the degree of Doctor in Sciences.

Thesis Jury

Prof. Andrea Giammanco	President	Université Catholique de Louvain
Prof. Christophe Ringeval	Secretary	Université Catholique de Louvain
Prof. Marco Drewes	Supervisor	Université Catholique de Louvain
Prof. Björn Garbrecht		Technische Universität München
Prof. Marcello Musso		Universidad de Salamanca

June 19, 2026

Acknowledgments

A PhD thesis may ultimately be written by a single person, but its completion depends on the support, guidance, and encouragement of many others. The years leading to this dissertation have been shaped by numerous mentors, collaborators, friends, and institutions whose contributions, both academic and personal, have been invaluable. Beyond the scientific challenges, this journey also coincided with difficult circumstances that made the kindness, generosity, and support of those around me all the more meaningful. I would therefore like to take this opportunity to express my heartfelt gratitude to all those who accompanied and supported me throughout these years.

I would first and foremost like to express my deepest gratitude to my supervisor, Marco Drewes. Without your guidance, support, and trust, this PhD would not have been possible. Thank you for your continuous encouragement throughout these years and for giving me the opportunity to join such a stimulating and welcoming research environment. I am especially grateful for your unwavering support during difficult times in my home country, which meant far more than academic supervision alone.

A special thank you goes to Yannis Georis, whose friendship, generosity, and support made my life considerably easier in Belgium. I am deeply grateful for our collaboration, for the advice, discussions, and support along the way, and for all the good moments we shared over the years.

I would also like to thank Yuanzhen Li for his support and collaboration, particularly during the final stages of this project. My sincere thanks also go to Sebastian Zell for his assistance, collaboration, and valuable contributions to our work.

I am grateful to all members of my thesis jury for agreeing to review this dissertation. I greatly benefited from their thoughtful feedback and valuable suggestions during the private defense, which helped refine and improve this thesis.

I would like to extend my sincere thanks to Björn Garbrecht for hosting me at the Technical University of Munich during my Erasmus+ stay. The year I spent at TUM was both scientifically enriching and personally rewarding.

A particularly heartfelt thank you goes to Marcello Musso, who has supported me continuously since my Master's studies at ICTP-EAIFR and throughout my PhD journey. Thank you for the opportunities to visit ICTP, for hosting me at the University of Salamanca during the final stages of writing this thesis,

and, most importantly, for encouraging me to join CP3. That recommendation ultimately led me to this wonderful institute and played a decisive role in shaping my academic path.

Beyond the scientific aspects of this journey, I would like to thank my office mates, Yannis, Valentin, and Oğuz for the many enjoyable moments, discussions, and shared experiences. Their company made the day-to-day life of research much more pleasant.

I would also like to express my gratitude to Carinne Martens for her invaluable help with administrative matters and for guiding me through the complexities of Belgian bureaucracy, particularly during my first years in Belgium.

Finally, I would like to acknowledge all friends, colleagues, and members of the CP3 community who contributed, directly or indirectly, to making these years both productive and memorable.

Funding Acknowledgments

I would like to acknowledge the support of the Conseil de l'Action Internationale (CAI) of UCLouvain through the *Coopération au Développement* doctoral grant. I also gratefully acknowledge support from the Erasmus+ Programme of the European Union through the Agence francophone pour l'éducation et la formation tout au long de la vie (AEF-Europe) at UCLouvain. I further acknowledge the Fonds de la Recherche Scientifique (FNRS) and the IISN-TH network for their financial support during my PhD. I am furthermore grateful to the Physics Department of the Technical University of Munich (TUM) for its hospitality during my Erasmus+ stay. I also gratefully acknowledge the hospitality of the University of Salamanca during my research visit. This stay was supported by the grant CNS2024-154286 (*HaloNRG*), funded by the Spanish Ministry of Science, Innovation and Universities.

I would also like to acknowledge the Abdus Salam International Centre for Theoretical Physics (ICTP) for its continuous support throughout my PhD and for its generous hospitality during my research visits. In particular, I thank Paolo Creminelli for facilitating these visits and for his hospitality.

Declaration on the use of generative Artificial Intelligence (AI)

During the preparation of this thesis, generative artificial intelligence tools (ChatGPT) were used as auxiliary tools for grammar correction, language revision, and limited technical assistance. These tools were not used to generate original scientific results, perform research, or draw conclusions. All results, derivations, numerical calculations, interpretations, and scientific judgments are the author's own or obtained together with his collaborators. The author critically reviewed all AI-assisted outputs and accepts full responsibility for the final manuscript.

Abstract

The dynamics of cosmic reheating connect inflation to the hot Big Bang and play a crucial role in determining the thermal history of the Universe and the production of relic particles such as Dark Matter (DM). A consistent description of this epoch requires the computation of particle production and interaction rates in a thermal environment, where excitations are described by quasiparticles with medium-dependent properties.

In this thesis, we study particle production during reheating using real-time non-equilibrium quantum field theory, with a focus on the Closed Time Path formalism. We show that in-medium interaction rates are governed by the spectral structure of self-energies, which encode both dispersive and dissipative effects. Using scalar field theories as a laboratory, we investigate the impact of thermal masses, quantum statistics, finite-width effects, and higher-order processes, and assess the validity of commonly used approximations. In particular, we demonstrate that higher-order scattering processes can significantly modify the dynamics and remain relevant even when decay channels are kinematically suppressed.

In a separate part of this work, we investigate Dark Matter production during reheating in freeze-in scenarios. We find that finite-temperature corrections generally have a limited impact on the predicted relic abundance in regimes where perturbative calculations are reliable, while more complex scenarios can lead to sizeable deviations. We further show that future Cosmic Microwave Background observations can provide constraints on the reheating history that are complementary to collider searches.

Overall, this work provides a systematic framework for particle production in thermal environments and clarifies the role of medium effects in cosmic reheating and Dark Matter generation.

Contents

Introduction

The origin and composition of the Universe are governed by a sequence of dynamical processes that connect fundamental particle physics to cosmological observations. Among these, the period of *cosmic reheating*—the transition between the accelerated expansion during inflation and the onset of radiation domination—plays a central role [1–4]. During reheating, the energy stored in the inflaton field is transferred to the degrees of freedom that eventually form the hot primordial plasma. This process sets the initial conditions for the standard hot Big Bang and can leave observable imprints in both the Cosmic Microwave Background (CMB) and the abundance of relic particles.

A central challenge in describing reheating, as well as a wide class of early-Universe phenomena, lies in the computation of particle production and interaction rates in a hot and dynamical environment. In such settings, the notion of particles as asymptotic states is no longer strictly applicable. Instead, excitations are more appropriately described as quasiparticles with medium-dependent properties, including temperature-dependent dispersion relations, finite lifetimes, and modified interactions. As a result, particle production cannot, in general, be described in terms of vacuum decay rates alone, but must be understood in terms of in-medium processes that include both decays and scatterings.

A commonly used approximation is to relate in-medium interaction rates to vacuum scattering amplitudes supplemented with thermal phase-space distributions [5]. While this prescription provides a useful starting point, it is incomplete beyond leading order. In particular, the presence of a thermal background allows for qualitatively new processes that have no direct vacuum analogue, such as medium-induced decays and collective excitations [6, 7]. Moreover, processes that are distinct in vacuum, such as $n \to m$ decays and $n + \ell \to m + \ell$ scatterings, become intertwined in a thermal environment and can interfere with each other [8].

As a consequence, particle production rates are determined by the full in-medium spectral structure rather than by a simple sum of vacuum-like contributions. This includes multi-particle interactions such as $2 \to 2$ and $2 \to 3$ processes, which can compete with or even dominate over lower-order channels despite being higher order in perturbation theory, due to kinematic enhancements and the large occupation numbers in the plasma [9, 10]. Capturing these effects requires going beyond leading-order approximations and computing higher-order contributions to the self-energy.

A consistent and systematic framework to address these questions is provided by real-time non-equilibrium quantum field theory. In this approach, particle production rates are derived from in-medium self-energies and spectral functions, which encode both the dispersion relations and interaction rates of excitations in a unified way. As discussed in Chapter 1, this formulation naturally emerges within the Closed Time Path (CTP) formalism, which allows for a causal and first-principles description of real-time dynamics in a thermal background.

The first part of this thesis is devoted to the conceptual and technical aspects of particle production in a thermal medium. Using simple scalar field theories as a laboratory, we investigate the structure of in-medium self-energies and assess the validity and limitations of commonly used approximations. Particular emphasis is placed on the role of thermal masses, modified dispersion relations, finite-width effects, and higher-order contributions to interaction rates. The results obtained in this part are of a general nature and can be applied to a wide range of problems involving particle production and dissipation in thermal environments.

In a separate line of investigation, the second part of this thesis addresses the production of Dark Matter (DM) in the early Universe. Observations indicate that DM constitutes more than 80% of the matter density in the observable Universe, yet its microscopic nature remains unknown [11]. While the simplest production mechanism, thermal freeze-out, is increasingly constrained [12, 13], alternative scenarios such as freeze-in [14, 15] provide a viable framework in which DM is produced out of equilibrium through feeble interactions.

In these scenarios, the DM relic abundance is sensitive to the thermal history of the Universe, and in particular to the dynamics of reheating. It has long been recognised that reheating can leave imprints both in the DM abundance [16, 17] and in the CMB [18], opening the possibility to combine cosmological observations with particle physics experiments to constrain or predict properties of new physics [19–24].

The sensitivity of the CMB to reheating arises primarily from its dependence on the expansion history during this epoch [25–30]. While this allows one to constrain global quantities such as the reheating temperature $T_{\rm re}$, it does not uniquely determine the full thermal history that governs DM production. In this context, we investigate how thermal effects—including quantum statistical factors, medium-induced modifications of kinematics, and higher-order interaction processes—can influence the predicted DM relic abundance.

Outline of the thesis:

The overall structure of this thesis is organized as follows:

- **Chapter 1:** We introduce the theoretical framework of real-time non-equilibrium quantum field theory, with a particular focus on the Closed Time Path (CTP) formalism. We discuss its conceptual foundations, including the treatment of finite-time expectation values, causal response functions, and the role of self-energies and spectral functions in describing particle production and dissipation in a thermal medium.

- **Chapter 2:** We analyse particle production in a thermal environment using scalar field theories as a laboratory. The focus is on the spectral properties of excitations, including thermal masses, modified dispersion relations, and finite-width effects. We further investigate the computation of in-medium interaction rates beyond leading order, highlighting the limitations of commonly used approximations and the importance of higher-order processes in determining particle production.

- **Chapter 3:** We investigate Dark Matter production during and after reheating. In this context, we study how the thermal history of the Universe and medium effects influence the production rate and the resulting relic abundance. We assess the extent to which thermal corrections can modify the connection between cosmological observables and particle physics parameters.

This PhD thesis is based on the following scientific articles:

- M. Drewes, Y. Georis, M. A. S. Mohammed, S. Zell, *Thermal Effects on Dark Matter Production During Cosmic Reheating*, arXiv:2604.16085 [31].
- M. Drewes, Y. Li, and M. A. S. Mohammed, *Kinematics of Cosmic Reheating at Next-to-Leading Order*, [in preparation].

Chapter 1

Real-Time Non-Equilibrium Quantum Field Theory and the Closed Time Path Formalism

The processes studied in this thesis, in particular particle production during reheating, take place far from equilibrium and require a real-time description. In this chapter, we introduce the Closed Time Path formalism as the appropriate framework to describe these dynamics.

1.1 Nature of the Problem: Particle Production in the Early Universe

The production of particles in the early Universe, and in particular the generation of Dark Matter (DM) during and after reheating, exemplifies a broad class of physical problems that lie outside the scope of conventional perturbative quantum field theory formulated in terms of asymptotic scattering states. Rather than describing transitions between well-defined in and out vacua, these phenomena involve the real-time evolution of quantum fields in an expanding spacetime, continuously interacting with a thermal environment and evolving far from global equilibrium [32–34].

In this context, the quantities of primary interest are finite-time expectation values, such as number densities, energy transfer rates, and correlation functions evaluated along a cosmological background. The central theoretical question is therefore not the computation of S-matrix elements, but rather

> *given an initial density matrix at a finite time,*
>
> *how does the system evolve causally under interactions?*

This places particle production during reheating firmly in the domain of *real-time, non-equilibrium quantum field theory*, for which standard in-out or Euclidean approaches are intrinsically inadequate [35, 36].

Dark Matter Production as a Quantum Kinetic Problem

Dark Matter production mechanisms such as freeze-in, production from decays, and scattering processes occur over extended cosmological timescales and typically involve species that are never in full thermal equilibrium with the primordial plasma [15, 37]. The evolution of the DM abundance is governed by irreversible processes and depends sensitively on microscopic interaction rates embedded in a time-dependent thermal background.

From a field-theoretic perspective, this corresponds to the evolution of phase-space distributions and number densities derived from non-equilibrium correlation functions. In particular, particle production rates are encoded in *lesser Green's functions* and finite-temperature self-energies, rather than in vacuum decay widths or on-shell scattering amplitudes [38–40]. This reflects the fact that the relevant degrees of freedom are not asymptotic particles, but excitations of a medium whose properties are continuously modified by interactions.

As a result, particle production must be understood in terms of the full in-medium spectral structure, which captures both kinematic effects and interaction rates in a unified manner. This already signals the breakdown of equilibrium methods and highlights the necessity of a real-time formulation capable of consistently describing causal evolution and memory effects.

Dissipation and Particle Production During Reheating

During reheating, the inflaton field transfers its energy to other degrees of freedom that form the primordial plasma. This process is inherently dynamical and involves continuous particle production in a time-dependent background [3, 4, 41]. The relevant observables include not only particle number densities, but also energy transfer rates and effective dissipation terms that govern the evolution of the background field [42–44].

From a microscopic point of view, these effects arise from the same underlying quantum processes encoded in real-time correlation functions and self-energies [34, 45–47]. Dissipation, particle production, and backreaction are therefore not independent phenomena, but different manifestations of the interaction between quantum fields in a medium [48–50].

A consistent theoretical description must therefore:

- treat particle production and dissipation within a unified framework,
- ensure causal time evolution,
- properly account for the non-equilibrium nature of the system.

These considerations strongly motivate the use of real-time, non-equilibrium quantum field theory methods, and in particular the Closed Time Path formalism [34, 45, 46], which provides a first-principles framework to describe the dynamical and statistical aspects of particle production during reheating in a self-consistent way.

1.2 Limitations of Standard Quantum Field Theory Frameworks

To appreciate the necessity of a different formalism, it is instructive to examine why commonly used QFT frameworks are not fully adequate for the problems considered in this work. We emphasize that these approaches remain extremely powerful and can often be applied within suitable limits. However, their domain of applicability is restricted when dealing with genuinely time-dependent and out-of-equilibrium phenomena such as reheating.

In-Out (S-Matrix) Formalism

The in-out formalism of quantum field theory is constructed to compute scattering amplitudes between asymptotic free states. Its central object is the S-matrix,

$$S = \lim_{\substack{t_i \to -\infty \\ t_f \to +\infty}} U(t_f, t_i), \tag{1.1}$$

where the time-evolution operator is defined as

$$U(t_f, t_i) = \mathcal{T} \exp\left[-i \int_{t_i}^{t_f} dt\, H_I(t)\right], \tag{1.2}$$

with $H_I(t)$ the interaction Hamiltonian in the interaction picture. This formulation assumes the existence of well-defined asymptotic “in” and “out” states and underlies the LSZ reduction formalism and standard perturbative Feynman rules [51, 52].

Observable quantities in this framework are transition amplitudes of the form

$$\langle \text{out}|\mathcal{O}|\text{in}\rangle = \langle \text{in}|S^\dagger \mathcal{O} S|\text{in}\rangle, \tag{1.3}$$

which are well-defined when interactions effectively switch off at early and late times. In contrast, during reheating the system evolves in a time-dependent background, and the relevant quantities are expectation values evaluated at finite time,

$$\langle \mathcal{O}(t)\rangle = \langle \text{in}|U^\dagger(t,t_i)\,\mathcal{O}\,U(t,t_i)|\text{in}\rangle, \tag{1.4}$$

which cannot be computed consistently within the in-out framework [34, 53].

The inadequacy of the in-out formalism becomes explicit when attempting to derive effective equations of motion. Integrating out interacting degrees of freedom leads to an in-out effective action $\Gamma_{\text{in-out}}[\phi]$, whose functional variation yields

$$\frac{\delta \Gamma_{\text{in-out}}[\phi]}{\delta \phi(x)} = 0. \tag{1.5}$$

However, the nonlocal terms appearing in $\Gamma_{\text{in-out}}$ are governed by time-ordered (Feynman) correlation functions,

$$G_F(x,y) = \langle \mathcal{T}\phi(x)\phi(y)\rangle, \tag{1.6}$$

which possess support both inside and outside the light cone. As a result, the effective equations of motion take the schematic form

$$\Box\phi(x) + \int d^4y\,\Sigma_F(x,y)\,\phi(y) = 0, \tag{1.7}$$

where the kernel $\Sigma_F(x,y)$ is not manifestly retarded. The integral therefore receives contributions from spacetime points with $y^0 > x^0$, leading to acausal influence of future events on the present dynamics [34, 53].

It is important to stress that this acausality does not contradict relativistic microcausality, which is a statement about operator commutators,

$$[\phi(x),\phi(y)] = 0 \qquad \text{for } (x-y)^2 < 0, \tag{1.8}$$

and remains satisfied in the underlying quantum field theory [51]. Rather, the problem lies in the use of Feynman-ordered correlators as response functions, which are not causal objects and do not describe physical propagation of disturbances [52, 54].

A related point concerns dissipative effects. In non-equilibrium settings, dissipation is associated with the imaginary part of retarded self-energies. Within the in–out formalism, such imaginary parts are directly connected to scattering amplitudes, but their interpretation in terms of real-time evolution requires additional steps. As a result, extracting effective friction terms or energy transfer rates from in–out quantities can be subtle [34, 55]. Similarly, stochastic fluctuations are not directly captured in this framework, as it is formulated in terms of amplitudes rather than expectation values of operators at finite time. A consistent description of both dissipation and fluctuations typically requires a formulation in which these effects appear on equal footing.

In summary, the in–out formalism provides a powerful and well-established framework for scattering processes in stationary settings, and it can often be used to estimate local interaction rates during reheating, provided that the microscopic interaction timescale is much shorter than the timescale of the background evolution [34, 47, 56, 57]. However, a systematic description of real-time evolution, including causal response, dissipation, and fluctuations, motivates the use of a real-time formulation of quantum field theory, which we introduce in the following.

Euclidean Finite-Temperature Field Theory

Finite-temperature quantum field theory is commonly formulated in Euclidean spacetime using the imaginary-time (Matsubara) formalism. In this approach, thermal expectation values are obtained from the partition function

$$Z = \mathrm{Tr}\, e^{-\beta H} = \int_{\mathrm{P/AP}} \mathcal{D}\phi \ \exp\left[- \int_0^\beta d\tau \int d^3x \, \mathcal{L}_E(\phi) \right], \tag{1.9}$$

where $\beta = 1/T$, and fields satisfy periodic (bosons) or antiperiodic (fermions) boundary conditions in imaginary time τ. Thermal correlation functions are then defined as Euclidean time-ordered correlators,

$$G_E(\tau, \mathbf{x}) = \langle \mathcal{T}_\tau \phi(\tau, \mathbf{x}) \phi(0, \mathbf{0}) \rangle, \tag{1.10}$$

with $\tau \in [0, \beta)$ [58, 59].

A central feature of this formulation is the Kubo-Martin-Schwinger (KMS) condition,

$$G^{>}(t) = G^{<}(t - i\beta), \qquad G^{>}(\omega) = e^{\beta\omega} G^{<}(\omega), \tag{1.11}$$

which encodes thermal equilibrium and relies on time-translation invariance [58, 59]. As a result, the Euclidean formalism provides a powerful framework for computing equilibrium quantities such as thermodynamic potentials and thermal masses. However, since the formalism is not formulated in real time, it does not directly provide access to dynamical observables such as causal response functions or time-dependent expectation values [34, 54].

This becomes particularly relevant when considering dissipative effects. In real-time formulations, dissipation is governed by the imaginary part of retarded self-energies,

$$\Upsilon(\omega) \ \propto \ -\frac{1}{\omega} \Im \Pi^{R}(\omega), \tag{1.12}$$

where Π^R denotes the retarded self-energy. In the Euclidean framework, self-energies are computed at discrete Matsubara frequencies,

$$\omega_n = 2\pi n T, \tag{1.13}$$

and extracting real-time information requires an analytic continuation $\omega_n \to -i(\omega + i0^+)$. While this procedure is well-defined in equilibrium, it becomes more subtle in time-dependent or out-of-equilibrium situations [54, 59].

More generally, Euclidean correlation functions encode equilibrium spectral information, but do not describe the real-time evolution of the system. In particular, processes such as particle production, decay, and energy transfer during reheating involve finite-time dynamics that go beyond the scope of the imaginary-time formulation [34].

In summary, Euclidean finite-temperature field theory provides a powerful and widely used framework for equilibrium thermodynamics and for estimating thermal properties of the plasma. However, a direct and systematic description of real-time dynamics during reheating — including causal response, dissipation, and time-dependent particle production — motivates the use of a real-time formulation of quantum field theory, which we introduce in the following section.

Gell-Mann–Low Theorem and the Limits of Adiabatic Mapping

The standard formulation of zero-temperature quantum field theory is based on vacuum expectation values evaluated in the interacting ground state. A central result underlying this construction is the Gell-Mann–Low (GML) theorem, which relates correlation functions in the interacting vacuum $|\Omega\rangle$ to correlators computed in the free vacuum $|0\rangle$. For a time-ordered product of Heisenberg-picture fields, it reads [51, 52]

$$\langle\Omega|\mathcal{T}\,\phi(x_1)\cdots\phi(x_n)|\Omega\rangle = \frac{\langle 0|\mathcal{T}\,\phi_I(x_1)\cdots\phi_I(x_n)\exp\bigl[i\int d^4x\,\mathcal{L}_I(x)\bigr]\,|0\rangle}{\langle 0|\mathcal{T}\,\exp\bigl[i\int d^4x\,\mathcal{L}_I(x)\bigr]\,|0\rangle}, \tag{1.14}$$

where ϕ_I are interaction-picture fields and $\mathcal{L}_I$ denotes the interaction Lagrangian. The denominator removes disconnected vacuum diagrams and ensures proper normalization of vacuum correlators.

A key ingredient in the derivation of Eq. (1.14) is the assumption of an *adiabatic mapping* between the free and interacting vacua. This is implemented by modifying the interaction Hamiltonian as

$$H_I(t) \;\longrightarrow\; e^{-\epsilon|t|}\,H_I(t), \qquad \epsilon\to 0^+, \tag{1.15}$$

such that the interaction is turned on infinitely slowly in the remote past. Under this assumption, the interacting vacuum can be constructed as

$$|\Omega\rangle = \lim_{\epsilon\to 0^+}\frac{U_\epsilon(0,-\infty)\,|0\rangle}{\langle 0|U_\epsilon(0,-\infty)|0\rangle}, \tag{1.16}$$

where U_ϵ denotes the time-evolution operator with adiabatic switching. This procedure presupposes the existence of a stable ground state continuously connected to the free vacuum.

In time-dependent and non-equilibrium settings, such as those encountered during reheating, these assumptions are generally not satisfied in a strict sense. The Hamiltonian H(t) is explicitly time dependent, and energy is not conserved. As a consequence, the notion of a stationary interacting vacuum $|\Omega\rangle$ is ill defined [34, 54]. The system does not relax toward a time-independent ground state, and the adiabatic limit in Eq. (1.15) does not converge.

A related issue arises in the vacuum persistence amplitude appearing in the denominator of Eq. (1.14),

$$\mathcal{Z}_0 = \langle 0|U(+\infty, -\infty)|0\rangle. \tag{1.17}$$

ceases to be finite in non-equilibrium settings. Continuous particle production or energy transfer to the background generically leads to

$$|\mathcal{Z}_0|^2 = |\langle 0|U(+\infty, -\infty)|0\rangle|^2 \ \longrightarrow\ 0, \tag{1.18}$$

rendering the normalization procedure inherent in the GML theorem ill defined. This breakdown is not a perturbative artifact but reflects the physical instability of the vacuum under time-dependent evolution [34].

Furthermore, perturbative expansions based on Eq. (1.14) can develop secular contributions in time-dependent backgrounds. Loop corrections may generate terms that grow with time, schematically of the form

$$\Sigma(t, t') \sim g^2(t - t') + \cdots , \tag{1.19}$$

indicating that perturbation theory organized around a stationary vacuum may become unreliable at late times. This behavior reflects the persistence of memory effects and the sensitivity to initial conditions in non-equilibrium systems [34, 60].

More generally, the GML theorem is formulated in terms of vacuum-to-vacuum amplitudes and a single time-ordered contour. While this is appropriate for equilibrium and scattering problems, it does not directly provide access to real-time expectation values in evolving systems. In particular, it does not naturally encode causal response functions, dissipative effects, or the dependence on an initial density matrix. Attempts to extract such information from in-out correlators can therefore lead to ambiguities or incomplete descriptions of the dynamics [53, 61]. These considerations suggest that, for genuinely time-dependent problems, it is more appropriate to formulate the theory in terms of the real-time evolution of a density matrix specified at a finite initial time, rather than relying solely on vacuum correlators defined via the Gell-Mann–Low construction.

This perspective is naturally realized in the Closed Time Path formalism. By extending the time contour and treating forward and backward evolution on equal footing, it provides a framework in which expectation values, causal response, and non-equilibrium effects can be described in a unified and consistent manner. This makes it a suitable starting point for the analysis of particle production and dissipation during reheating.

Remarks on Kinetic Descriptions

In addition to the quantum field-theoretic frameworks discussed above, particle production and abundance evolution in the early Universe are often described using kinetic or Boltzmann equations. Unlike the in-out or Euclidean formulations, which are intrinsically quantum field-theoretic, kinetic descriptions operate at the level of phase-space distribution functions and provide an effective, semi-classical account of non-equilibrium dynamics [56, 62].

Boltzmann equations are widely used in studies of Dark Matter production and reheating, where they offer an intuitive and computationally efficient description of particle number evolution [15, 56, 63, 64]. In this sense, they can be viewed as an effective approach to the description of non-equilibrium phenomena. At the same time, their scope and domain of applicability differ from those of a fully quantum field-theoretic framework. In particular, kinetic equations are not derived within the Boltzmann approach itself, but rely on interaction rates that must be supplied externally. Their validity typically rests on assumptions such as the existence of well-defined quasi-particles, a separation of microscopic and macroscopic time scales, and approximate locality in time [34, 47]. When these conditions are satisfied, Boltzmann equations provide an accurate and efficient description of the dynamics, while outside this regime their applicability requires additional justification.

From a conceptual standpoint, kinetic equations do not directly encode the full quantum dynamics of the underlying fields. For instance, they do not explicitly track the causal structure of real-time correlation functions, nor do they systematically incorporate stochastic fluctuations or backreaction effects [34, 54]. As a result, while Boltzmann equations provide a powerful phenomenological tool, they are not intended as a fundamental description of non-equilibrium quantum dynamics. Importantly, it is well understood that kinetic equations can be obtained as a limiting description of real-time quantum field theory under controlled approximations. In particular, Markovian Boltzmann-type equations emerge from non-equilibrium quantum field theory in the quasi-particle and gradient expansion limits [47, 49, 65]. A systematic analysis of this reduction for scalar fields in slowly evolving backgrounds has been presented in Ref. [66], where the assumptions underlying the Markovian kinetic description are made explicit.

In the present work, Boltzmann equations are therefore employed as an effective tool where appropriate, while the underlying microscopic dynamics is addressed using a real-time quantum field-theoretic formalism. This perspective naturally motivates the adoption of the Closed Time Path formalism, which provides a unified framework from which kinetic descriptions, linear response theory, and stochastic dynamics can be consistently recovered as limiting cases [34, 54].

Summary

In this chapter, we have examined the limitations of commonly used quantum field-theoretic frameworks when applied to particle production and dissipative dynamics in cosmological settings. We have seen that the in-out (S-matrix) formalism, while ideally suited for scattering processes in stationary backgrounds, does not directly provide access to finite-time expectation values, causal equations of motion, or a systematic treatment of dissipation and fluctuations. These limitations are closely related to its reliance on asymptotic states and vacuum-to-vacuum amplitudes.

We have further discussed that Euclidean finite-temperature field theory, despite its success in describing equilibrium thermodynamics, is not formulated to address real-time dynamics. Its use of imaginary time obscures causal structure and does not directly yield dynamical observables such as response functions or time-dependent expectation values, particularly away from equilibrium.

At a more general level, we have considered the role of the Gell-Mann–Low theorem and the assumptions underlying its application. In time-dependent and non-equilibrium settings, the construction based on adiabatic vacuum mapping becomes less well-defined, and perturbative expansions around a stationary vacuum may exhibit secular behavior. This indicates that vacuum-based formulations are not naturally suited for describing real-time evolution in such systems.

Finally, we have clarified the status of kinetic and Boltzmann descriptions. While these provide efficient and intuitive effective descriptions under suitable assumptions, they are not intended as a fundamental framework for non-equilibrium quantum dynamics. Instead, they can be understood as limiting cases of real-time quantum field theory under controlled approximations.

Taken together, these considerations motivate the use of a framework that is intrinsically real-time, causal, and formulated in terms of finite-time expectation values. In the following, we introduce the Closed Time Path formalism, which provides such a description and serves as the basis for our analysis of particle production during reheating.

Motivation for a Real-Time Formulation

The considerations discussed above highlight a common requirement: a formulation of quantum field theory that allows one to describe real-time evolution and statistical information in a unified way. In particular, such a framework should be formulated at finite times, allow for the specification of an initial density matrix, and provide direct access to causal response functions, dissipation, and fluctuations in time-dependent backgrounds.

While standard approaches can often be applied within suitable approximations, a more general and systematic description of non-equilibrium dynamics is provided by real-time formulations of quantum field theory, in particular the Closed Time Path (CTP) formalism. The key idea of the CTP approach is to extend the time contour so as to treat forward and backward time evolution on equal footing. This construction naturally accommodates expectation values rather than transition amplitudes, and leads to a consistent definition of correlation functions with well-defined causal and statistical properties. Within this framework, quantities such as response functions, dissipation rates, and fluctuation correlators emerge in a transparent and unified manner, and effective kinetic descriptions can be derived as controlled limits.

In the following sections, we introduce the Closed Time Path formalism and develop the tools required to analyse particle production during reheating within this framework. Particular emphasis will be placed on the emergence of causal dynamics, the origin of dissipative and stochastic effects, and the connection between microscopic quantum processes and effective kinetic descriptions.

1.3 Closed Time Path Contour and Doubling of Fields

The physical problems addressed in this thesis, in particular particle production during reheating and the generation of Dark Matter, are naturally formulated as *initial-value problems*. The quantities of interest are expectation values of operators evaluated at finite times in the presence of a time-dependent background and, in general, a non-trivial initial state describing a thermal or out-of-equilibrium medium. In this context, the relevant observables are not transition amplitudes between asymptotic states, but expectation values evaluated at finite times [32–34].

Expectation values and initial density matrix

Consider a quantum field theory specified at some initial time t_0 by a density matrix $\rho(t_0)$. The fundamental observable is the expectation value of a Heisenberg-picture operator $\mathcal{O}_H(t)$ at a later time t,

$$\langle \mathcal{O}(t) \rangle = \mathrm{Tr}[\rho(t_0)\, \mathcal{O}_H(t)]\,. \tag{1.20}$$

This quantity differs conceptually from the in-out matrix elements familiar from scattering theory, as no reference is made to asymptotic final states. Instead, the system is evolved forward in time from a specified initial state, and the observable is evaluated at finite time.

To make the time evolution explicit, one may rewrite Eq. (1.20) in terms of real-time evolution operators,

$$\begin{aligned} \langle \mathcal{O}(t) \rangle &= \mathrm{Tr}\Big[\rho(t_0)\, U^\dagger(t,t_0)\, \mathcal{O}_I(t)\, U(t,t_0)\Big]\,, \\ U(t,t_0) &= \mathcal{T} \exp\left[-i \int_{t_0}^{t} dt'\, H_I(t')\right], \end{aligned} \tag{1.21}$$

where $\mathcal{O}_I$ is the interaction-picture operator, H_I the interaction Hamiltonian, and $\mathcal{T}$ denotes time-ordering. Using the unitarity of the time-evolution operator, Eq. (1.21) may be equivalently written in the "in-in" form,

$$\langle \mathcal{O}(t) \rangle = \mathrm{Tr}[\rho(t_0)\, U(t_0,t)\, \mathcal{O}_I(t)\, U(t,t_0)]\,, \tag{1.22}$$

which makes explicit that the computation involves both *forward* and *backward* real-time evolution [32, 34, 54].

Closed time path contour and contour ordering

We introduce the contour $\mathcal{C}$, referred to as the *Closed Time Path* (CTP), or Schwinger-Keldysh, contour (see Fig. 1.1). It provides a geometric representation of the forward and backward real-time evolution appearing in the in-in expectation value (1.22), with $\mathcal{C}_+$ encoding the evolution operator $U(t,t_0)$

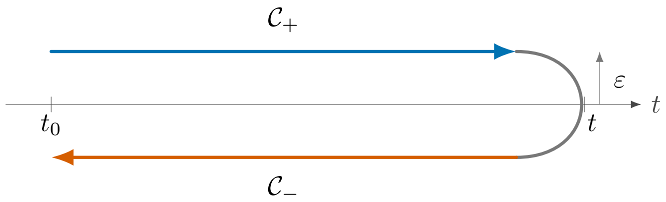

Figure 1.1: Closed Time Path contour for in-in expectation values. The forward branch $\mathcal{C}_+$ runs from t_0 to t, while the backward branch $\mathcal{C}_-$ returns from t to t_0. The small vertical displacement ε ensures a well-defined contour ordering at coincident times.

and $\mathcal{C}_-$ encoding its adjoint $U^\dagger(t, t_0)$. Contour ordering along $\mathcal{C}$ reproduces the operator ordering inherent in real-time expectation values and allows both evolutions to be treated within a single, unified framework [32–34].

$$\mathcal{C} = \mathcal{C}_+ \cup \mathcal{C}_-, \qquad \mathcal{C}_+ : t_0 \to +\infty, \qquad \mathcal{C}_- : +\infty \to t_0. \tag{1.23}$$

Fields and sources are defined on $\mathcal{C}$ and ordered by a contour-ordering operator $T_\mathcal{C}$. The central object is the contour-ordered correlator

$$\begin{aligned} G_\mathcal{C}(x,y) &\equiv \langle T_\mathcal{C}\, \phi(x)\phi(y)\rangle \\ &= \mathrm{Tr}\Big[\rho(t_0)\, T_\mathcal{C}\Big\{\phi(x)\phi(y)\exp\Big[-i\int_\mathcal{C} d^4z\, \mathcal{H}_I(z)\Big]\Big\}\Big], \end{aligned} \tag{1.24}$$

where $\mathcal{H}_I$ is the interaction Hamiltonian density [32, 33].

Doubling of fields and the (2×2) structure

Because the contour has two branches, each field is duplicated,

$$\phi(x) \;\longrightarrow\; \big(\phi_+(x),\, \phi_-(x)\big), \tag{1.25}$$

with ϕ_+ living on $\mathcal{C}_+$ and ϕ_- on $\mathcal{C}_-$. Consequently, the contour-ordered two-point function can be represented as a 2×2 matrix,

$$G^{ab}(x,y) \equiv -i\, \langle T_\mathcal{C}\, \phi_a(x)\phi_b(y)\rangle, \qquad a, b \in \{+, -\}, \tag{1.26}$$

whose components correspond to time-ordered, anti-time-ordered, and Wightman correlators [39, 54, 67].

Unitarity constraint and normalization

A key consistency requirement of the CTP formalism is the preservation of unitarity. When the sources on the two branches are set equal, the forward evolution along $\mathcal{C}_+$ is exactly undone by the backward evolution along $\mathcal{C}_-$, implying the normalization condition

$$Z[J_+ = J_-] = 1, \tag{1.27}$$

provided $\mathrm{Tr}\,\rho(t_0) = 1$. This identity is the functional counterpart of $U(t_0, +\infty)\,U(+\infty, t_0) = \mathbf{1}$ and ensures that the doubling of fields does not introduce spurious physical degrees of freedom [34, 54].

Causality: retarded response from the closed contour

One of the principal advantages of the CTP construction is that *causal* (retarded) response functions arise naturally. Coupling the theory to an external classical source $J(x)$ via

$$\Delta S = \int d^4x\; J(x)\,\phi(x), \tag{1.28}$$

and introducing independent sources (J_+, J_-) on the two branches, the expectation value of the field is obtained as

$$\langle \phi(x) \rangle_J = \frac{1}{i}\,\frac{\delta \ln Z[J_+, J_-]}{\delta J_+(x)}\bigg|_{J_+=J_-=J}. \tag{1.29}$$

The linear response to a small perturbation δJ is then

$$\delta\langle \phi(x) \rangle = \int d^4y\; G_R(x,y)\,\delta J(y), \tag{1.30}$$

where the retarded Green's function is given by

$$G_R(x,y) = \theta(x^0 - y^0)\,\langle [\phi(x), \phi(y)] \rangle = G^{++}(x,y) - G^{+-}(x,y). \tag{1.31}$$

Equation (1.31) immediately implies

$$G_R(x,y) = 0 \qquad \text{for} \quad x^0 < y^0, \tag{1.32}$$

so that the response at x depends only on sources applied at earlier times [34, 53, 54].

The dependence on a thermal or more general medium is encoded in the initial density matrix $\rho(t_0)$. For an equilibrium state at temperature T,

$$\rho(t_0) = \frac{e^{-\beta H}}{\mathrm{Tr}\, e^{-\beta H}}, \qquad \beta \equiv 1/T, \tag{1.33}$$

so that contour-ordered correlators inherit the statistical information of the medium [34, 58, 59].

Summary. The CTP formalism reformulates real-time quantum field theory as an initial-value problem on a closed time contour. The doubling of fields and sources follows directly from the trace structure of expectation values and preserves unitarity via Eq. (1.27). Most importantly, causal response functions arise directly from the contour structure, as illustrated by Eqs. (1.31)–(1.32). In the next subsection, we introduce the CTP generating functional and define the various real-time Green's functions used throughout the analysis of particle production during reheating and the resulting dark matter abundance.

1.4 From the Breakdown of the Gell-Mann-Low Theorem to the CTP Formulation

The discussion in the previous chapter highlighted that the Gell-Mann-Low (GML) theorem is not well suited as a starting point for quantum field theory in genuinely non-equilibrium and time-dependent settings. This limitation is not merely technical, but is tied to its formulation in terms of vacuum correlators and asymptotic time evolution. In this subsection, we outline how the Closed Time Path (CTP) formulation addresses these issues by reformulating quantum field theory directly in terms of finite-time expectation values.

A first issue concerns the absence of an interacting vacuum, the GML theorem assumes the existence of a unique interacting vacuum state $|\Omega\rangle$ adiabatically connected to the free vacuum. In cosmological and non-equilibrium systems, where the Hamiltonian is explicitly time dependent and energy is not conserved, such a state does not exist. As a result, vacuum correlators are ill defined and the adiabatic limit underlying the GML construction fails [34, 54].

The CTP formalism abandons the notion of an interacting vacuum altogether. Instead, the theory is specified by a density matrix $\rho(t_0)$ at a finite initial time, and all observables are defined as expectation values of the form

$$\langle \mathcal{O}(t) \rangle = \mathrm{Tr}\Big[\rho(t_0)\, U^\dagger(t, t_0)\, \mathcal{O}_I(t)\, U(t, t_0)\Big]\,, \tag{1.34}$$

which remain well defined even in the absence of any stationary ground state.

The second related aspect is the role of the vacuum persistence amplitude, the central ingredient of the GML theorem is the vacuum persistence amplitude

$$\mathcal{Z}_0 = \langle 0|U(+\infty, -\infty)|0\rangle, \tag{1.35}$$

which appears in the normalization of vacuum correlators. In non-equilibrium systems, continuous particle production or energy transfer generically drives $|\mathcal{Z}_0|^2 \to 0$, rendering this normalization ill defined [34].

In the CTP formulation, normalization is enforced instead by unitarity of real-time evolution. The closed contour structure guarantees that forward and backward evolution exactly cancel when no operator insertions are present, leading to the condition

$$Z[J_+ = J_-] = 1, \tag{1.36}$$

provided $\mathrm{Tr}\,\rho(t_0) = 1$. Thus, unitarity is preserved without reference to vacuum-to-vacuum amplitudes.

Another important point concerns causality. The GML theorem organizes perturbation theory in terms of time-ordered (Feynman) correlators. While suitable for scattering amplitudes, these correlators are not causal response functions and do not directly yield causal equations of motion in real time. As discussed earlier, this leads to acausal kernels when in-out effective actions are varied [53].

In contrast, the CTP formalism naturally separates different real-time correlators. Retarded response functions emerge as specific linear combinations of contour-ordered propagators, e.g.

$$G_R(x, y) = G^{++}(x, y) - G^{+-}(x, y) = \theta(x^0 - y^0)\,\langle[\phi(x), \phi(y)]\rangle, \tag{1.37}$$

ensuring manifest causality. This structural distinction between time ordering and response is absent in the GML framework but is built into the CTP formulation from the outset.

A further limitation is associated with secular growth and memory effects. Perturbative expansions based on the GML theorem generically develop secular terms in non-equilibrium backgrounds, reflecting the breakdown of an expansion around a stationary vacuum state. Such terms signal long-time memory effects and the failure of vacuum-based perturbation theory [68].

The CTP formalism does not assume relaxation toward a vacuum and instead treats time evolution as an initial-value problem. As a result, memory kernels and non-Markovian effects arise naturally in the equations of motion derived from the CTP effective action, without leading to inconsistencies or secular divergences.

Summary and perspective

The breakdown of the Gell-Mann-Low theorem thus points to a deeper requirement: quantum field theory must be formulated directly in terms of real-time evolution from a finite initial state. The Closed Time Path formalism provides precisely such a reformulation. By replacing vacuum correlators with contour-ordered expectation values, vacuum normalization with unitarity on a closed contour, and time-ordered amplitudes with causal response functions, the CTP framework resolves the conceptual obstructions identified in the previous chapter.

In the next subsection, we introduce the generating functional on the closed time path and develop the practical machinery needed to compute real-time Green's functions and effective equations of motion.

1.5 Generating functional and one-particle irreducible effective action

Having established the closed time contour and the associated doubling of fields, we now introduce the generating functional of the Closed Time Path (CTP) formalism. This object provides a unified framework for computing real-time expectation values and correlation functions in the presence of a general initial density matrix, without reference to asymptotic in- and out-states.

CTP generating functional

Consider a quantum field theory specified at an initial time t_0 by a density matrix $\rho(t_0)$. Introducing independent external sources $J_+(x)$ and $J_-(x)$ coupled to the fields on the forward and backward branches of the contour, the CTP generating functional is defined as

$$Z[J_+, J_-] = \mathrm{Tr}\Big[U_{J_+}(+\infty, t_0)\,\rho(t_0)\,U^\dagger_{J_-}(+\infty, t_0)\Big]\,, \tag{1.38}$$

where

$$U_{J_\pm}(+\infty, t_0) = \mathcal{T} \exp\left[-i \int_{t_0}^{+\infty} dt \int d^3\mathbf{x} \left(\mathcal{H}_I(x) - J_\pm(x)\phi(x)\right)\right]. \tag{1.39}$$

Here, $\mathcal{T}$ denotes time ordering along the corresponding branch of the closed time contour. The fields appearing in U_{J_+} and $U_{J_-}^\dagger$ are independent copies of the same Heisenberg operator, associated with the forward and backward branches of the contour. All real-time expectation values and correlation functions follow from functional differentiation with respect to the sources.

A key property of the CTP generating functional follows from unitarity of time evolution. When the sources on the two branches are set equal, $J_+(x) = J_-(x)$, one finds

$$Z[J, J] = \mathrm{Tr}\, \rho(t_0) = 1, \tag{1.40}$$

provided the density matrix is properly normalized. This identity ensures cancellation of disconnected vacuum diagrams and guarantees that expectation values are properly normalized, in contrast to the in–out formalism where vacuum persistence amplitudes appear explicitly [34, 69].

Beyond generating correlation functions, the CTP formalism admits a natural generalization of the one-particle-irreducible (1PI) effective action [34, 70]. Defining the generating functional of connected diagrams as

$$W[J_+, J_-] = -i \ln Z[J_+, J_-], \tag{1.41}$$

the classical fields on the contour are introduced as

$$\phi_a(x) = \frac{\delta W}{\delta J_a(x)}, \qquad a \in \{+, -\}. \tag{1.42}$$

The CTP effective action is then defined by the Legendre transform

$$\Gamma[\phi_+, \phi_-] = W[J_+, J_-] - \sum_{a=\pm} \int d^4x\, J_a(x)\phi_a(x). \tag{1.43}$$

The two fields ϕ_+ and ϕ_- are treated as independent variables in the Legendre transform; physical observables are obtained only after imposing the physical limit $\phi_+(x) = \phi_-(x)$.

Functional variation of Γ yields the exact real-time equations of motion,

$$\frac{\delta \Gamma}{\delta \phi_a(x)} = 0, \tag{1.44}$$

which, when evaluated in the physical limit $\phi_+(x) = \phi_-(x)$, are causal by construction and valid for arbitrary initial density matrices [34].

The second functional derivatives of the CTP effective action define the exact inverse propagators,

$$\frac{\delta^2\Gamma}{\delta\phi_a(x)\delta\phi_b(y)} = \left[G^{-1}\right]^{ab}(x,y), \tag{1.45}$$

which form a 2×2 matrix in contour space reflecting the doubling of fields on the closed time path. From these relations, Dyson equations on the closed time path follow. The self-energy $\Pi^{ab}(x,y)$ is identified as the interaction-induced part of the inverse propagator,

$$\left[G^{-1}\right]^{ab} = \left[G_0^{-1}\right]^{ab} - \Pi^{ab}, \tag{1.46}$$

where G_0 denotes the free propagator determined by the initial density matrix (vacuum or thermal), whose explicit form will be given in Sec. 2.6. In this sense, the self-energy encodes the effect of interactions on real-time propagation and provides the link between microscopic dynamics and macroscopic phenomena such as dissipation and particle production [34, 70].

This effective-action viewpoint provides the formal foundation for the Dyson and Kadanoff-Baym equations introduced in the following sections. In the next section, we make this structure explicit by introducing real-time Green's functions and their physical combinations.

1.6 Real-Time Green's Functions and Physical Observables

The doubling of fields in the Closed Time Path (CTP) formalism implies that real-time two-point functions naturally acquire a 2×2 matrix structure in contour space. This matrix structure encodes both the causal and statistical properties of quantum fields and provides the natural language for describing finite-temperature and non-equilibrium dynamics [34, 46, 54, 67]. In this subsection, we introduce the corresponding set of CTP propagators.

The basic CTP propagators for a real scalar field ϕ are defined as

$$\Delta^{ab}(x,y) \equiv -i\,\langle T_{\mathcal{C}}\,\phi_a(x)\phi_b(y)\rangle, \qquad a,b \in \{+,-\}, \tag{1.47}$$

where $T_{\mathcal{C}}$ denotes ordering along the closed time contour. Explicitly, one has

$$\Delta^{++}(x,y) = -i\,\langle T\,\phi(x)\phi(y)\rangle, \tag{1.48}$$
$$\Delta^{--}(x,y) = -i\,\langle \tilde{T}\,\phi(x)\phi(y)\rangle, \tag{1.49}$$
$$\Delta^{+-}(x,y) = -i\,\langle \phi(y)\phi(x)\rangle \equiv \Delta^{<}(x,y), \tag{1.50}$$
$$\Delta^{-+}(x,y) = -i\,\langle \phi(x)\phi(y)\rangle \equiv \Delta^{>}(x,y), \tag{1.51}$$

where T and $\tilde{T}$ denote time and anti-time ordering, respectively.

The time-ordered and anti-time-ordered propagators can be expressed in terms of the lesser and greater functions,

$$\Delta^{++}(x,y) = \theta(x^0-y^0)\Delta^{>}(x,y) + \theta(y^0-x^0)\Delta^{<}(x,y), \tag{1.52}$$
$$\Delta^{--}(x,y) = \theta(y^0-x^0)\Delta^{>}(x,y) + \theta(x^0-y^0)\Delta^{<}(x,y). \tag{1.53}$$

It is often convenient to introduce the spectral and statistical functions,

$$\rho(x,y) = i\big(\Delta^{>}(x,y) - \Delta^{<}(x,y)\big), \tag{1.54}$$
$$F(x,y) = \frac{1}{2}\big(\Delta^{>}(x,y) + \Delta^{<}(x,y)\big), \tag{1.55}$$

together with the retarded and advanced propagators,

$$\Delta^{R}(x,y) = -i\,\theta(x^0-y^0)\langle[\phi(x),\phi(y)]\rangle, \tag{1.56}$$
$$\Delta^{A}(x,y) = +i\,\theta(y^0-x^0)\langle[\phi(x),\phi(y)]\rangle. \tag{1.57}$$

The spectral function encodes the causal response of the system, while the statistical propagator contains information about occupation numbers and correlations.

For a thermal state at temperature T, the free scalar propagators in momentum space take the form

$$\Delta^{++}(p) = \frac{i}{p^2-m_\phi^2+i\eta} + 2\pi f_B(|p_0|)\,\delta(p^2-m_\phi^2), \tag{1.58}$$
$$\Delta^{--}(p) = -\frac{i}{p^2-m_\phi^2-i\eta} + 2\pi f_B(|p_0|)\,\delta(p^2-m_\phi^2), \tag{1.59}$$
$$\Delta^{+-}(p) = 2\pi f_B(|p_0|)\,\delta(p^2-m_\phi^2), \tag{1.60}$$
$$\Delta^{-+}(p) = 2\pi\big[1+f_B(|p_0|)\big]\,\delta(p^2-m_\phi^2), \tag{1.61}$$

where

$$f_B(\omega) = \frac{1}{e^{\beta\omega} - 1} \tag{1.62}$$

is the Bose–Einstein distribution.

Free fermionic CTP propagators

For a Dirac fermion ψ of mass m_ψ, the free lesser and greater propagators are

$$S_0^>(p) = -2\pi i\,(\not{p} + m_\psi)\left[1 - f_F(|p_0|)\right]\delta(p^2 - m_\psi^2), \tag{1.63}$$

$$S_0^<(p) = +2\pi i\,(\not{p} + m_\psi)\,f_F(|p_0|)\,\delta(p^2 - m_\psi^2), \tag{1.64}$$

where $f_F(\omega) = (e^{\beta\omega} + 1)^{-1}$ is the Fermi–Dirac distribution.

The corresponding time-ordered and anti-time-ordered propagators read

$$S_\psi^{++}(p) = \frac{i(\not{p} + m_\psi)}{p^2 - m_\psi^2 + i\eta} - 2\pi\,(\not{p} + m_\psi)\,f_F(|p_0|)\,\delta(p^2 - m_\psi^2), \tag{1.65}$$

$$S_\psi^{--}(p) = -\frac{i(\not{p} + m_\psi)}{p^2 - m_\psi^2 - i\eta} - 2\pi\,(\not{p} + m_\psi)\,f_F(|p_0|)\,\delta(p^2 - m_\psi^2), \tag{1.66}$$

$$S_\psi^{+-}(p) = -2\pi\,(\not{p} + m_\psi)\,f_F(|p_0|)\,\delta(p^2 - m_\psi^2), \tag{1.67}$$

$$S_\psi^{-+}(p) = -2\pi\,(\not{p} + m_\psi)\left[1 - f_F(|p_0|)\right]\delta(p^2 - m_\psi^2). \tag{1.68}$$

For fermions, the overall structure mirrors the bosonic case, with Pauli blocking and relative minus signs dictated by anticommutation relations.

Interpretation. The CTP propagator structure provides a clean separation between vacuum dynamics and medium effects. While Δ^{++}/S^{++} and Δ^{--}/S^{--} combine both contributions, the physically transparent building blocks are the retarded and advanced propagators, which encode causal response, and the lesser and greater propagators, which encode the statistical state of the system. This separation is essential for identifying dissipation and particle production in real-time dynamics.

1.7 Dyson equations and self-energies on the closed time path

The real-time Green's functions introduced in the previous subsection encode the kinematic and statistical properties of quantum fields in a non-equilibrium setting. To relate these quantities to microscopic interactions, one must introduce self-energies and establish the corresponding Dyson equations on the closed time path. This subsection presents these structures in a general form, emphasizing their causal content and physical interpretation [32–34, 54].

On the closed time path $\mathcal{C}$, the full two-point function satisfies a Dyson–Schwinger equation of the form

$$\Delta(x,y) = \Delta_0(x,y) + \int_{\mathcal{C}} d^4z \int_{\mathcal{C}} d^4z' \; \Delta_0(x,z)\,\Pi(z,z')\,\Delta(z',y), \tag{1.69}$$

where Δ_0 is the free contour-ordered propagator and Π denotes the contour self-energy, defined as the sum of one-particle-irreducible (1PI) two-point diagrams on the contour. Equivalently, the self-energy may be identified with the second functional derivative of the CTP effective action introduced in Sec. 2.5. The integrals are taken along the closed time path, and all products are understood as contour-ordered convolutions.

Equation (1.69) is formally identical to the Dyson equation in equilibrium field theory, but its interpretation is fundamentally different: it governs real-time evolution with general initial conditions and incorporates memory effects through the nonlocal structure of the self-energy [34, 71].

As a consequence of the contour formulation, the self-energy inherits the same 2×2 matrix structure as the propagator,

$$\Pi^{ab}(x,y), \qquad a, b \in \{+,-\}, \tag{1.70}$$

with components Π^{++}, Π^{--}, Π^{+-}, and Π^{-+} corresponding to different operator orderings on the contour, in direct analogy with the propagators defined in Sec. 1.6 [33, 34, 54].

It is convenient to introduce the lesser and greater self-energies,

$$\Pi^{<}(x,y) \equiv \Pi^{+-}(x,y), \qquad \Pi^{>}(x,y) \equiv \Pi^{-+}(x,y), \tag{1.71}$$

as well as the retarded and advanced combinations,

$$\Pi^{R}(x,y) = \Pi^{++}(x,y) - \Pi^{+-}(x,y), \qquad \Pi^{A}(x,y) = \Pi^{++}(x,y) - \Pi^{-+}(x,y). \tag{1.72}$$

These combinations ensure that $\Pi^{R,A}$ vanish outside the causal domain.

Projecting the contour Dyson equation (1.69) onto physical components yields a hierarchy of coupled equations. Of particular importance are the equations for the retarded propagator and for the lesser Green's function.

The retarded propagator satisfies

$$\Delta^R(x,y) = \Delta_0^R(x,y) + \int d^4z \int d^4z'\, \Delta_0^R(x,z)\, \Pi^R(z,z')\, \Delta^R(z',y), \tag{1.73}$$

which is manifestly causal: all time integrals involve only past times due to the retarded structure of Δ_0^R and Π^R [34, 53]. The imaginary part of Π^R governs damping, relaxation, and dissipation, while its real part induces medium-dependent mass and dispersion corrections.

The lesser propagator obeys a Kadanoff–Baym–type equation

$$\Delta^< = \Delta^R \star \Pi^< \star \Delta^A + (1 + \Delta^R \star \Pi^R) \star \Delta_0^< \star (1 + \Pi^A \star \Delta^A), \tag{1.74}$$

where $\star$ denotes convolution in spacetime. This equation makes explicit that $\Delta^<$ is sourced both by the lesser self-energy $\Pi^<$, encoding microscopic gain and loss processes, and by the initial statistical correlations contained in $\Delta_0^<$ [70–72]. Equation (1.74) is fully nonlocal in time and exact; kinetic or Boltzmann equations emerge only after further approximations, discussed below.

Physical interpretation

The decomposition of the Dyson equations highlights the distinct roles played by different self-energy components:

- The retarded self-energy Π^R controls the causal response of the system and determines dissipation rates, relaxation times, and effective masses.
- The lesser and greater self-energies $\Pi^{<,>}$ encode microscopic gain and loss processes, such as particle production, absorption, and scattering in a medium.

In equilibrium, these quantities are related by fluctuation–dissipation relations. Out of equilibrium, however, $\Pi^<$ and $\Pi^>$ are independent functions that carry detailed information about the processes driving the system away from equilibrium [34, 54].

Connection to later applications

In subsequent sections, explicit expressions for the self-energies $\Pi^{R,<,>}$ will be computed for interaction Lagrangians relevant to reheating and dark matter production. In this context, the imaginary part of Π^R will be directly related to dissipation rates, while $\Pi^<$ will determine particle production and collision terms. The general structure established here therefore provides the link between microscopic quantum dynamics and macroscopic observables.

Finally, the Dyson equations on the closed time path naturally lead to evolution equations for the spectral and statistical functions, known as the Kadanoff–Baym equations. These will be introduced in the next subsection, where their role in describing memory effects and the emergence of kinetic descriptions will be discussed [70, 72].

1.8 Kadanoff-Baym equations and memory effects

The Dyson equations on the closed time path can be reformulated as coupled evolution equations for the spectral and statistical propagators introduced in Sec. 1.6. These equations, known as the Kadanoff–Baym (KB) equations, provide a causal and non-perturbative description of real-time quantum dynamics and make explicit the role of memory effects and non-Markovian behavior in non-equilibrium systems [34, 70–72].

Starting from the Dyson equations for $\Delta^{R,A}$ and $\Delta^{<}$, and expressing all quantities in terms of the spectral function ρ and the statistical propagator F, one obtains two coupled integro-differential equations of motion. For a scalar field, these may be written schematically as

$$[\Box_x + m^2]\,\rho(x,y) = \int_{y^0}^{x^0} d^4z\; \Pi^{\rho}(x,z)\,\rho(z,y), \tag{1.75}$$

$$[\Box_x + m^2]\,F(x,y) = \int_{t_0}^{x^0} d^4z\; \Pi^{\rho}(x,z)\,F(z,y) - \int_{t_0}^{y^0} d^4z\; \Pi^{F}(x,z)\,\rho(z,y), \tag{1.76}$$

where the spectral and statistical self-energies are defined as

$$\Pi^{\rho} \equiv i(\Pi^{>} - \Pi^{<}), \qquad \Pi^{F} \equiv \tfrac{1}{2}(\Pi^{>} + \Pi^{<}). \tag{1.77}$$

These equations are exact and manifestly causal: the integration limits ensure that the evolution at time x^0 depends only on earlier times [34, 70, 71].

A key feature of the Kadanoff–Baym equations is the presence of memory integrals over the full history of the system since the initial time t_0. Unlike local equations of motion, the evolution of $F(x, y)$ and $\rho(x, y)$ depends on their values at all intermediate times through convolution with the self-energies. This nonlocality reflects the persistence of correlations generated by interactions in quantum field theory. In non-equilibrium settings, such memory effects can become important when interaction rates are comparable to the timescale of the macroscopic evolution [34, 70].

When treated perturbatively, the memory integrals can generate secular terms that grow with time, typically as powers of $(t - t_0)$. Such behavior signals a breakdown of naive perturbation theory and indicates that the system retains sensitivity to its initial conditions over long timescales [60, 70]. Physically, these terms arise from repeated scattering and decay processes that are not resummed at fixed perturbative order. The CTP framework makes this structure explicit and provides a systematic starting point for controlled resummations or for deriving effective descriptions in appropriate limits.

In situations where a separation of scales exists between microscopic interaction times and macroscopic evolution times, the Kadanoff–Baym equations can be simplified. After performing a Wigner transformation and a gradient expansion, and assuming a quasiparticle form for the spectral function, one obtains effective kinetic equations of Boltzmann type [70–72]. Schematically, the evolution of a phase-space distribution function $f(\mathbf{k}, t)$ takes the form

$$\partial_t f(\mathbf{k}, t) \;\sim\; \Pi^<(\mathbf{k}, t) - \Pi^>(\mathbf{k}, t), \tag{1.78}$$

where the lesser and greater self-energies act as gain and loss terms, respectively. The validity of this reduction relies on assumptions such as the existence of quasiparticles and a clear separation of scales, which will be specified more precisely in later applications.

The Kadanoff–Baym equations therefore provide a general framework that connects microscopic quantum dynamics to effective descriptions. Even when not solved explicitly, their structure clarifies the origin of dissipation, the role of memory and initial conditions, and the regime of validity of kinetic approaches. In this work, they serve as the conceptual bridge between the CTP formulation and the effective descriptions used in the analysis of reheating and dark matter production.

Outlook. In the next subsection, we discuss how physical processes such as decays, scatterings, and Landau damping are encoded in the self-energies $\Pi^{<,>}$ through cutting rules in a medium, providing a direct connection between CTP diagrams and particle production mechanisms [34, 54].

1.9 Cutting rules in a medium and physical processes

The lesser and greater self-energies introduced in the previous sections encode the microscopic processes responsible for dissipation, particle production, and equilibration in non-equilibrium quantum field theory. In this section, we clarify their physical interpretation by discussing cutting rules in a medium and their relation to decay, scattering, and absorption processes. This provides a direct link between CTP self-energies and the effective kinetic descriptions employed in later chapters [32–34, 54].

In the CTP formalism, the lesser and greater self-energies,

$$\Pi^{<}(x,y), \qquad \Pi^{>}(x,y), \tag{1.79}$$

play a role analogous to collision kernels in kinetic theory. When inserted into the Kadanoff–Baym equations, they act as source and sink terms for the statistical propagator and, in suitable limits, for phase-space distribution functions [70–72]. In particular, after a Wigner transformation and under quasiparticle assumptions, the evolution of an occupation number $f(\mathbf{k},t)$ takes the schematic form

$$\partial_t f(\mathbf{k},t) \;\sim\; \Pi^{<}(\mathbf{k},t) - \Pi^{>}(\mathbf{k},t), \tag{1.80}$$

where $\Pi^{<}$ describes gain processes (particle production or emission into the mode), while $\Pi^{>}$ describes loss processes (decay, absorption, or scattering out of the mode). This identification follows directly from the CTP structure, while its interpretation in terms of phase-space distributions relies on additional quasiparticle and gradient-expansion assumptions [34, 54].

Diagrammatically, $\Pi^{<}$ and $\Pi^{>}$ are obtained by applying cutting rules to self-energy diagrams, generalizing the Cutkosky rules of vacuum field theory to real-time, finite-density environments [34, 73, 74]. In contrast to the vacuum case, cuts in a medium do not correspond solely to on-shell particle production, but also account for absorption and stimulated processes due to the presence of background occupation numbers. Operationally, the CTP cutting prescription amounts to assigning propagators on opposite sides of the cut to $\Delta^<$ or $\Delta^>$, summing over all allowed cuts consistent with the contour structure, and including statistical factors associated with the medium. As a result, a given diagram generally contributes to both $\Pi^<$ and $\Pi^>$, corresponding to inverse processes related by crossing and, in equilibrium, by detailed balance [54, 74].

The physical content of these cutting rules can be illustrated with simple interaction topologies. For instance, in a theory with trilinear interactions, the same self-energy diagram may describe spontaneous decay in vacuum, inverse decay in a populated medium, or scattering processes involving bath excitations. Within the CTP formulation, these processes are not treated separately but are encoded in a unified manner in the same self-energy. Their relative importance is determined by kinematics and by the statistical factors appearing in the Wightman propagators, which incorporate Bose enhancement or Pauli blocking effects [34, 59].

A characteristic feature of cutting rules in a medium is the emergence of processes with no vacuum analogue, such as Landau damping. These arise from cuts involving space-like momentum exchange, which can place internal lines on shell due to the presence of a thermal distribution, even when on-shell decays are kinematically forbidden in vacuum [34, 59, 60]. In this way, the medium opens additional channels for energy transfer and dissipation that are absent at zero temperature.

The cutting interpretation is closely related to the analytic structure of the retarded self-energy. Defining the spectral self-energy

$$\Pi^\rho(x,y) = i\big(\Pi^>(x,y) - \Pi^<(x,y)\big), \tag{1.81}$$

one finds that it determines the imaginary part of Π^R in momentum space and hence the damping rate of quasiparticle excitations. While $\Pi^<$ and $\Pi^>$ separately encode gain and loss processes, their difference controls dissipation through $\mathrm{Im}\,\Pi^R$ [34, 54]. In equilibrium, these quantities are related by detailed balance, whereas out of equilibrium they remain independent, reflecting the absence of local balance between production and absorption processes.

Taken together, the CTP cutting rules provide a unified and physically transparent interpretation of self-energies in non-equilibrium quantum field theory.

They allow loop-level calculations to be directly mapped onto physical processes such as decays, inverse decays, scatterings, and medium-induced effects. This connection forms the basis for extracting particle production rates and dissipative coefficients from first-principles quantum field theory.

1.10 Summary and Outlook

In this chapter, we developed a real-time, non-equilibrium formulation of quantum field theory based on the Closed Time Path (CTP) formalism. Starting from the limitations of the in–out and Euclidean approaches, as well as the breakdown of the Gell–Mann–Low construction in time-dependent and open systems, we motivated the need for a framework capable of describing finite-time expectation values, causal response, and dissipative dynamics. The CTP contour, together with the doubling of fields and sources, provides such a formulation and ensures unitarity and causality at the level of real-time correlation functions, without relying on equilibrium assumptions or analytic continuation.

We introduced the CTP generating functional, the associated 2×2 matrix structure of Green's functions, and their physically relevant combinations. Dyson equations and self-energies on the closed time path were shown to encode dissipation, particle production, and memory effects in a unified manner, with the self-energies providing the link between microscopic interactions and macroscopic evolution. Reformulating these equations in terms of spectral and statistical propagators led naturally to the Kadanoff–Baym equations, which make explicit the non-Markovian character of quantum evolution and clarify the emergence of kinetic descriptions in suitable limits. Finally, we discussed how cutting rules in a medium provide a direct physical interpretation of the lesser and greater self-energies in terms of microscopic gain and loss processes.

The formalism developed in this chapter provides the theoretical foundation for the applications discussed in the remainder of this thesis. In the following chapters, we apply the CTP framework to concrete cosmological settings in which time-dependent and non-equilibrium effects play a central role. In particular, we will use this formalism to compute dissipation rates from first principles, analyze particle production processes in a thermal medium, and study the resulting abundance evolution in dark matter freeze-in scenarios. These applications illustrate how the general non-equilibrium structures introduced here translate into quantitative predictions for physically measurable quantities in the early Universe.

Chapter 2

Inflation and Reheating Kinematics

The dynamics of reheating are governed by the transfer of energy from the inflaton field to other degrees of freedom, leading to the formation of a thermal plasma in the early Universe [56, 75]. At a microscopic level, this process is controlled by the interaction of the inflaton with a surrounding medium and is therefore intrinsically a non-equilibrium phenomenon. A consistent description of these dynamics requires a real-time quantum field-theoretic framework capable of capturing particle production, dissipation, and medium effects [34, 54].

A quantitative understanding of reheating relies on identifying the kinematic quantities that characterize particle propagation and interactions in a thermal environment. In this context, spectral functions and self-energies provide a unified framework to describe quasiparticle properties, decay rates, and interaction processes in a medium [58, 76]. In particular, the retarded self-energy encodes both dispersive effects, through its real part, and dissipative dynamics, through its imaginary part, which determines relaxation and particle production rates [5, 34].

Recent work has further clarified the role of thermal corrections and non-equilibrium effects in reheating and particle production, particularly in the context of dark matter generation and its sensitivity to the thermal history of the Universe [57, 77]. These developments highlight the importance of combining first-principles quantum field theory with cosmological dynamics in order to obtain reliable predictions.

In this chapter, we introduce the kinematic framework underlying the analysis of reheating and particle production in a thermal bath. We begin by defining spectral functions and self-energies within the Closed Time Path formalism and discuss their physical interpretation in terms of quasiparticle excitations and interaction rates. These concepts provide the basis for the computation of decay rates, dissipation coefficients, and particle production processes that will be carried out in the following sections.

2.1 Spectral Functions and Self-Energies

We consider inflationary scenarios in which the inflaton field ϕ interacts weakly with additional degrees of freedom forming a thermal bath. In this work, we focus on interactions that are linear in the inflaton field, which in an effective field theory description can be written as

$$\mathcal{L}_{\rm int} = \phi\, \mathcal{O}[\chi_i], \tag{2.1}$$

where $\mathcal{O}[\chi_i]$ denotes a composite operator constructed from the bath fields χ_i. Such a structure arises naturally in many models, for instance after integrating out heavy mediator fields or in portal-type interactions between the inflaton and the thermal sector. Depending on the microscopic particle physics realization of the bath, the operator $\mathcal{O}[\chi_i]$ may contain products of scalar fields, fermion bilinears, or gauge-invariant combinations of gauge fields.

Throughout this work we assume that the inflaton self-interactions are negligible compared to the interactions with the bath, and that the inflaton–bath coupling is sufficiently weak to justify a perturbative treatment. Under these assumptions, the dissipation of the inflaton energy into the thermal plasma can be studied systematically using finite-temperature field theory.

Within the Closed Time Path (CTP) formalism developed in Chapter 2, the inflaton self-energy can be expressed entirely in terms of correlation functions of the bath operator $\mathcal{O}$. For the linear interaction $\mathcal{L}_{\rm int} = \phi\, \mathcal{O}$, the leading-order contribution to the inflaton self-energy is determined by the two-point correlator of $\mathcal{O}$. The greater and lesser self-energies are given by

$$\Pi^{>}(x_1, x_2) = \langle \mathcal{O}(x_1)\mathcal{O}(x_2)\rangle, \qquad \Pi^{<}(x_1, x_2) = \langle \mathcal{O}(x_2)\mathcal{O}(x_1)\rangle, \tag{2.2}$$

where expectation values are defined with respect to the density matrix ρ,

$$\langle A\rangle = \mathrm{Tr}(\rho\, A)\,. \tag{2.3}$$

A useful quantity is the *spectral self-energy*, defined as

$$\Pi^{-}(x_1, x_2) \equiv \Pi^{>}(x_1, x_2) - \Pi^{<}(x_1, x_2), \tag{2.4}$$

which determines the retarded self-energy according to

$$\Pi^R(x_1, x_2) = \theta(t_1 - t_2)\, \Pi^-(x_1, x_2). \tag{2.5}$$

As discussed in Chapter 2, the spectral combination Π^- governs dissipative effects and relaxation processes, while the symmetric combination $\Pi^> + \Pi^<$ encodes dispersive corrections to the inflaton propagation [34, 54].

Following the strategy adopted in Ref. [44], we restrict attention to the regime in which the bath fields remain in thermal equilibrium. In this case, translational invariance implies that the self-energies depend only on the relative coordinate $x_1 - x_2$. We therefore introduce the Fourier transform

$$\Pi^-_{\mathbf{q}}(\omega) = \int d^4(x_1 - x_2)\, e^{i\omega(t_1 - t_2) - i\mathbf{q}\cdot(\mathbf{x}_1 - \mathbf{x}_2)} \Pi^-(x_1 - x_2). \tag{2.6}$$

In this framework, thermal masses and widths of the bath fields are incorporated perturbatively [44].

The inflaton spectral function is defined through the commutator

$$\Delta^-(x_1, x_2) \equiv i\langle[\phi(x_1), \phi(x_2)]\rangle, \tag{2.7}$$

with the corresponding spectral density

$$\rho_{\mathbf{q}}(\omega) = -i \int d^4(x_1 - x_2)\, e^{i\omega(t_1 - t_2) - i\mathbf{q}\cdot(\mathbf{x}_1 - \mathbf{x}_2)} \Delta^-(x_1 - x_2). \tag{2.8}$$

A convenient representation of the spectral density, obtained from the retarded self-energy, is given by [44]

$$\rho_{\mathbf{q}}(\omega) = \frac{-2\,\mathrm{Im}\,\Pi^R_{\mathbf{q}}(\omega) + 2\omega\epsilon}{\big(\omega^2 - \mathbf{q}^2 - m^2 - \mathrm{Re}\,\Pi^R_{\mathbf{q}}(\omega)\big)^2 + \big(\mathrm{Im}\,\Pi^R_{\mathbf{q}}(\omega) + \omega\epsilon\big)^2}, \tag{2.9}$$

where $\epsilon \to 0^+$ implements the causal prescription.

The properties of excitations in the thermal medium are encoded in the analytic structure of the spectral density $\rho_{\mathbf{q}}(\omega)$ in the complex ω plane. In particular, poles of $\rho_{\mathbf{q}}(\omega)$ correspond to propagating quasiparticle modes. Denoting such a pole by $\hat{\Omega}_{\mathbf{q}}$, we define the quasiparticle energy and width as

$$\Omega_{\mathbf{q}} \equiv \mathrm{Re}\,\hat{\Omega}_{\mathbf{q}}, \qquad \Gamma_{\mathbf{q}} \equiv 2\,\mathrm{Im}\,\hat{\Omega}_{\mathbf{q}}. \tag{2.10}$$

Both quantities inherit a temperature dependence through the retarded self-energy $\Pi^R_{\mathbf{q}}(\omega)$.

For weak interactions, the imaginary part of the pole position is much smaller than its real part,

$$\Gamma_{\mathbf{q}} \ll \Omega_{\mathbf{q}}, \tag{2.11}$$

so that the spectral density exhibits narrow peaks around the quasiparticle energies $\omega \simeq \pm\Omega_{\mathbf{q}}$. These peaks admit a quasiparticle interpretation, corresponding to screened single-particle excitations or collective modes of the plasma [38, 78]. In the zero-temperature limit, the screened excitation continuously approaches the vacuum dispersion relation $\Omega_{\mathbf{q}} \to \sqrt{\mathbf{q}^2 + m^2}$.

In this regime, the quasiparticle dispersion relation is determined predominantly by the real part of the retarded self-energy through the on-shell condition

$$\omega^2 - \mathbf{q}^2 - m^2 - \mathrm{Re}\,\Pi^R_{\mathbf{q}}(\omega) = 0, \tag{2.12}$$

while the imaginary part $\mathrm{Im}\,\Pi^R_{\mathbf{q}}(\omega)$ controls the thermal width of the excitation [5]. In general, $\Omega_{\mathbf{q}}$ exhibits a nontrivial momentum dependence; only in special cases can it be parameterized in terms of a momentum-independent thermal mass [76].

Near the quasiparticle pole, the dominant contribution to the spectral density admits a Breit-Wigner type approximation,

$$\rho^{\mathrm{BW}}_{\mathbf{q}}(\omega) = \frac{2Z_{\mathbf{q}}\,\omega\,\Gamma_{\mathbf{q}}}{(\omega^2 - \Omega^2_{\mathbf{q}})^2 + (\omega\Gamma_{\mathbf{q}})^2} + \rho^{\mathrm{cont}}_{\mathbf{q}}(\omega), \tag{2.13}$$

where $\rho^{\mathrm{cont}}_{\mathbf{q}}(\omega)$ denotes the continuum contribution associated with multi-particle states and medium-induced processes [76]. The residue is given by

$$Z_{\mathbf{q}} = \left[1 - \frac{1}{2\Omega_{\mathbf{q}}}\frac{\partial}{\partial\omega}\mathrm{Re}\,\Pi^R_{\mathbf{q}}(\omega)\right]^{-1}_{\omega=\Omega_{\mathbf{q}}}. \tag{2.14}$$

This formulation provides the basis for computing inflaton decay rates and dissipative coefficients under different approximations to the bath spectral density, which will be explored in the following sections.

Using the relation between the spectral and retarded self-energies,

$$\Pi^-_{\mathbf{q}}(\omega) = 2i\,\mathrm{Im}\,\Pi^R_{\mathbf{q}}(\omega), \tag{2.15}$$

the thermal width of the inflaton excitation can be written as

$$\Gamma_{\mathbf{q}} = Z_{\mathbf{q}}\,\frac{i}{2\Omega_{\mathbf{q}}}\,\Pi^-_{\mathbf{q}}(\Omega_{\mathbf{q}}). \tag{2.16}$$

For the inflaton field ϕ, the residue may be set to $Z_{\mathbf{q}} \simeq 1$ due to the smallness of the inflaton coupling. For the bath scalar fields χ_i, however, this factor must in general be retained. The quantity $\Gamma_{\mathbf{q}}$ represents the total relaxation (or damping) rate of the inflaton mode with momentum $\mathbf{q}$ [44]. When the occupation number of this mode lies below its equilibrium value, $\Gamma_{\mathbf{q}}$ plays the role of a particle production rate, whereas for overoccupied modes it describes dissipative energy loss, as is relevant during reheating.

More generally, the total rate can be decomposed into gain and loss contributions,

$$\Gamma_{\mathbf{q}} = \Gamma_{\mathbf{q}}^{>} - \Gamma_{\mathbf{q}}^{<}, \tag{2.17}$$

with

$$\Gamma_{\mathbf{q}}^{\gtrless} = Z_{\mathbf{q}} \frac{i}{2\Omega_{\mathbf{q}}} \Pi_{\mathbf{q}}^{\gtrless}(\Omega_{\mathbf{q}}), \tag{2.18}$$

where $\Gamma^{<}$ and $\Gamma^{>}$ encode microscopic gain and loss processes, respectively [34, 54]. The relaxation rate of the coherent inflaton zero mode corresponds to $\Gamma = \Gamma_{\mathbf{q}=0}$.

Owing to the very weak inflaton coupling assumed throughout this work, thermal corrections to the inflaton dispersion relation are negligible. As a result, only a single type of inflaton quasiparticle is relevant, with dispersion relation

$$\Omega_{\mathbf{q}} \simeq \sqrt{\mathbf{q}^2 + m^2}, \tag{2.19}$$

while medium-induced corrections to the thermal width $\Gamma_{\mathbf{q}}$ remain important.

In the models discussed in the following sections, the inflaton couples to additional scalar fields χ_i. The spectral densities for these fields are defined in complete analogy to the inflaton case. For scalars, one has

$$\begin{aligned} \rho_{\chi_i}(p_0, \mathbf{p}) = \int d^4(x_1 - x_2)\, e^{ip_0(t_1 - t_2) - i\mathbf{p}\cdot(\mathbf{x}_1 - \mathbf{x}_2)} \\ \times \left(\langle \chi_i(x_1)\chi_i(x_2) \rangle - \langle \chi_i(x_2)\chi_i(x_1) \rangle \right), \end{aligned} \tag{2.20}$$

where the expectation values are taken with respect to the thermal density matrix.

The corresponding scalar self-energies $\Pi^{\pm}_{\chi_i}$ are defined in complete analogy to the inflaton case, but include all interaction channels present in the bath. In weakly coupled scalar theories at high temperature, transport phenomena are typically dominated by a single quasiparticle excitation [8], which justifies the use of a one-pole approximation for the scalar spectral density,

$$\rho^{\text{pole}}_{\chi_i}(p_0,\mathbf{p}) = \frac{2Z_{\chi_i}\,\Omega_{\chi_i}\,\Gamma_{\chi_i}}{(p_0^2-\Omega^2_{\chi_i})^2+(p_0\Gamma_{\chi_i})^2}. \tag{2.21}$$

Here, $\Omega_{\chi_i} = \mathrm{Re}\,\hat{\Omega}_{\chi_i}$ and $\Gamma_{\chi_i} = 2\,\mathrm{Im}\,\hat{\Omega}_{\chi_i}$ denote the quasiparticle energy and thermal width for χ_i excitations with spatial momentum $\mathbf{p}$. In the simplest case, the dispersion relation can be parameterized as

$$\Omega_{\chi_i} \simeq \sqrt{\mathbf{p}^2 + M_i^2(T)}, \tag{2.22}$$

with momentum-independent thermal masses $M_i(T)$.

Beyond the isolated quasiparticle pole, the scalar spectral density generally contains a broader structure associated with interactions and multi-particle processes. In the vicinity of the pole, the dominant contribution can be written in the Breit–Wigner form

$$\rho^{\text{BW}}_{\chi_i}(p_0,\mathbf{p}) = \frac{2Z_{\chi_i}\,p_0\,\Gamma_{\chi_i}}{(p_0^2-\Omega^2_{\chi_i})^2+(p_0\Gamma_{\chi_i})^2} + \rho^{\text{cont}}_{\chi_i}(p_0,\mathbf{p}), \tag{2.23}$$

where Ω_{χ_i} denotes the quasiparticle dispersion relation, Γ_{χ_i} is the thermal width that characterizes the damping of the excitation in the medium, and Z_{χ_i} is the wave-function renormalization factor that measures the residue of the pole. The Breit–Wigner structure describes a quasiparticle peak centered around the on-shell condition $p_0^2 = \Omega^2_{\chi_i}$, whose width is controlled by Γ_{χ_i}. Physically, the finite width arises from interactions with the surrounding medium, which allow the excitation to decay or scatter and therefore limit its lifetime.

In the limit where the interactions become very weak, the width becomes parametrically small and the quasiparticle becomes long-lived. In this zero-width limit the Breit–Wigner peak collapses to a delta function, recovering the familiar pole contribution

$$\rho^{\text{pole}}_{\chi_i}(p_0,\mathbf{p}) = 2\pi Z_{\chi_i}\,\mathrm{sign}(p_0)\,\delta(p_0^2-\Omega^2_{\chi_i}) + \rho^{\text{cont}}_{\chi_i}(p_0,\mathbf{p}). \tag{2.24}$$

This expression explicitly separates the sharp quasiparticle pole from the remaining spectral weight contained in the continuum.

The continuum contribution $\rho^{\text{cont}}_{\chi_i}$ originates from multi-particle intermediate states and off-shell processes. These include, for instance, scattering states and Landau damping contributions that do not correspond to a single well-defined quasiparticle excitation. In weakly coupled theories, however,

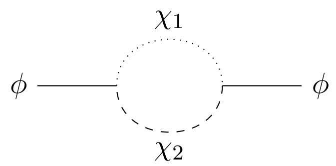

Figure 2.1: One-loop self-energy diagram for the scalar field ϕ in the trilinear interaction $g\,\phi\chi_1\chi_2$. The loop is formed by χ_1 (dotted line) and χ_2 (dashed line) propagators.

the spectral weight is typically dominated by the quasiparticle pole, while the continuum part is parametrically suppressed [76]. For this reason, many practical calculations employ the quasiparticle approximation and neglect $\rho^{\rm cont}_{\chi_i}$, retaining only the pole contribution to the spectral density.

In the following section we apply the formalism developed above to a specific particle physics realization and derive the corresponding inflaton decay and dissipation rates in a thermal plasma.

2.2 Effect of Thermal Masses on Tree Level Decay Rate

To investigate how thermal corrections affect inflaton dissipation during reheating, we now apply the formalism developed in the previous subsection to a simple particle physics model in which the inflaton decays into bosonic degrees of freedom in a thermal plasma.

We focus on a scenario in which the interactions of the inflaton field ϕ are dominated by its coupling to two additional scalar fields χ_i ($i = 1, 2$), described by the Lagrangian

$$\mathcal{L} = \frac{1}{2}(\partial_\mu\phi)^2 - \frac{1}{2}m^2\phi^2 + \sum_{j=1,2}\left[\frac{1}{2}(\partial_\mu\chi_j)^2 - \frac{1}{2}m_j^2\chi_j^2 - \frac{\lambda_j}{4!}\chi_j^4\right] - g\,\phi\,\chi_1\chi_2 + \mathcal{L}_{\rm bath}, \tag{2.25}$$

where $\mathcal{L}_{\rm bath}$ denotes additional interactions responsible for thermalizing the χ_i fields through couplings to other bath degrees of freedom that do not directly interact with the inflaton.

At leading order in the coupling g, the inflaton self-energy is given by the one-loop diagram shown in Fig. 2.1 (see also Ref. [79]). Evaluating the diagram in the rest frame of the external inflaton, $q^\mu = (m, \mathbf{0})$, and using the definitions introduced in the previous section for the self-energy and the full spectral densities, the imaginary part of the retarded inflaton self-energy reads

$$\Pi_\phi(m) = -ig^2 \int \frac{d^4p}{(2\pi)^4} \left[1 + f_B(p_0) + f_B(m - p_0)\right] \times \rho_1(p_0, \mathbf{p})\, \rho_2(m - p_0, -\mathbf{p}), \tag{2.26}$$

where

$$f_B(p_0) = \frac{1}{e^{\beta p_0} - 1} \tag{2.27}$$

is the Bose-Einstein distribution function, and ρ_j denote the full spectral densities of the χ_j fields.

We work in the zero-width (quasiparticle) limit, in which the χ_j excitations are described by free spectral densities. Using the definition of the free spectral function given in Eq. (2.24), the imaginary part of the retarded inflaton self-energy can be expressed in the form

$$\begin{aligned}\mathrm{Im}\,\Pi^R_{\boldsymbol{q}}(m) = &-\frac{g^2}{8} \int \frac{d^3p}{(2\pi)^2} \frac{1}{\omega_1\omega_2} \\ &\times \Bigg\{ (1 + f_1 + f_2) \left[\delta(m - \omega_1 - \omega_2) - \delta(m + \omega_1 + \omega_2)\right] \\ &+ (f_2 - f_1) \left[\delta(m - \omega_1 + \omega_2) - \delta(m + \omega_1 - \omega_2)\right] \Bigg\},\end{aligned} \tag{2.28}$$

where $\omega_i = \sqrt{\boldsymbol{p}^2 + m_i^2}$ are the on-shell quasiparticle energies and $f_i \equiv f_B(\omega_i)$ denote the corresponding Bose–Einstein distribution functions.

This expression admits a clear physical interpretation. The term proportional to $(1 + f_1 + f_2)\, \delta(m - \omega_1 - \omega_2)$ describes the decay of an inflaton quantum into two bosonic excitations, $\phi \to \chi_1 + \chi_2$, including Bose enhancement from the thermal population of the final states. The accompanying term $\delta(m + \omega_1 + \omega_2)$ corresponds to the unphysical process in which all energies flow into the vertex with the same sign and therefore vanishes identically, since $\omega_i > 0$ and no on-shell kinematics can satisfy this condition.

The second structure, proportional to $(f_2 - f_1)$, encodes scattering (Landau damping) processes in the thermal medium, in which the inflaton exchanges energy with the bath through absorption and emission, $\phi + \chi_1 \leftrightarrow \chi_2$ and $\phi + \chi_2 \leftrightarrow \chi_1$. These contributions are purely thermal in origin and vanish in the vacuum limit, reflecting the fact that they arise from interactions with pre-existing excitations in the plasma, as first emphasized in the finite-temperature analysis of self-energies in Ref. [5]. Such thermal scattering contributions to the imaginary part of self-energies were first systematically analyzed in the seminal work of Weldon [5].

The imaginary part of the self-energy therefore, directly encodes the microscopic dissipation channels of the inflaton: vacuum decay, Bose-enhanced thermal decay, and thermal scattering processes.

Including thermal mass corrections $m_i^2 \to M_i^2(T)$ in the quasiparticle dispersion relations, the momentum integral in Eq. (2.28) can be evaluated analytically in the zero-width limit. Specializing to the rest frame of the inflaton, $\boldsymbol{q} = 0$, one finds

$$\begin{aligned}\mathrm{Im}\,\Pi^R_{\boldsymbol{q}=0}(m) = -\frac{g^2}{8\pi m}\sqrt{\bar{\omega}_1^2 - M_1^2}\left[1 + f_B(\bar{\omega}_1) + f_B(\bar{\omega}_2)\right] \\ \times \Big[\theta\,(m - M_1 - M_2) - \theta(M_1 - m - M_2) - \theta\,(M_2 - m - M_1)\Big],\end{aligned} \tag{2.29}$$

where the on-shell energies are given by

$$\bar{\omega}_1 = \frac{m^2 + M_1^2 - M_2^2}{2m}, \qquad \bar{\omega}_2 = \frac{m^2 - M_1^2 + M_2^2}{2m}, \tag{2.30}$$

and M_i denote the thermal masses of the χ_i quasiparticles.

The square-root factor $\sqrt{\bar{\omega}_1^2 - M_1^2}$ arises from the phase-space integration and encodes the kinematic threshold for inflaton decay in the medium. The step functions implement the kinematic constraints implied by energy–momentum conservation and determine which physical processes contribute for a given hierarchy of masses.

The structure of Eq. (2.29) naturally separates the decay and inverse decay regimes. The first term,

$$\theta(m - M_1 - M_2),$$

corresponds to the standard decay channel $\phi \to \chi_1 + \chi_2$, which is open only if the inflaton mass exceeds the sum of the thermal quasiparticle masses. In this regime, the thermal factors $1 + f_B(\bar{\omega}_1) + f_B(\bar{\omega}_2)$ account for Bose enhancement from the population of the final states in the plasma.

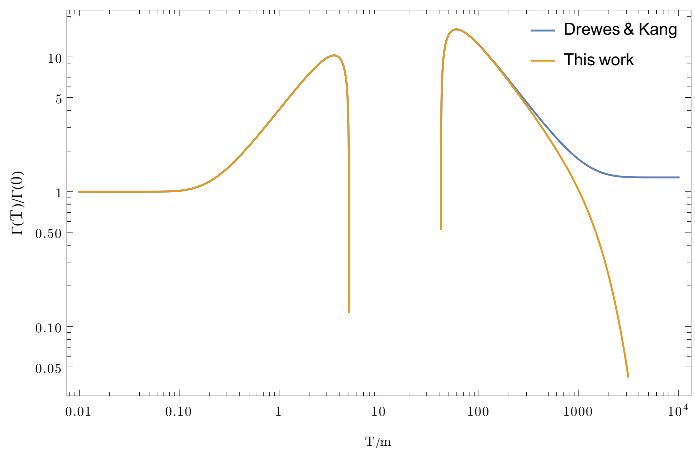

Figure 2.2: Comparison of the normalized inflaton dissipation rate $\Gamma(T)/\Gamma(0)$ as a function of the temperature ratio T/m. The blue curve shows the result obtained by Drewes and Kang [80], while the orange curve corresponds to the result derived in this work. Thermal masses are included according to $M_i^2(T) = m_i^2 + \lambda_i T^2/24$, with parameter choices $m_1 = 0.2\,m, m_2 = 0.4\,m$, $\lambda_1 = 0.11$, and $\lambda_2 = 0.2$. At high temperatures, the result presented here deviates from the earlier approximation and exhibits a qualitatively different behavior, reflecting the improved treatment of thermal effects.

The remaining step functions,

$$\theta(M_1 - m - M_2), \qquad \theta(M_2 - m - M_1),$$

enter with opposite sign and encode the complementary kinematic regions in which direct decay is forbidden but inverse decay processes become possible. In these regimes, a thermal quasiparticle from the bath can participate in the process, effectively converting a χ_i excitation into an inflaton and the other species.

Whether these channels are open depends sensitively on the temperature through the thermal masses $M_i(T)$. As the temperature increases, the growth of M_i shifts the kinematic thresholds and can either open or close specific dissipation channels relative to the vacuum case.

A detailed derivation of Eq. (2.29), including the treatment of the delta functions and kinematic constraints, is presented in Appendix A. The main steps involved in handling the delta functions and deriving the relevant kinematic constraints for Eq. (2.29) are presented in Appendix A.

In Fig. 2.2 we compare the inflaton dissipation rate obtained from Eq. (2.29) with the result of Drewes & Kang [80], adopting exactly the same parameter choices as in their analysis. In particular, the thermal masses are taken as

$$M_i^2(T) = m_i^2 + \frac{\lambda_i}{24} T^2, \tag{2.31}$$

with $\lambda_1 = 0.01$, $\lambda_2 = 1$, and $m_1 = m_2 = 10^{-3} m$. This ensures a direct, like-for-like comparison between the two approaches.

At low and intermediate temperatures the two results are in good agreement. In this regime, the dissipation rate is dominated by the vacuum decay channel $\phi \to \chi_1 \chi_2$ together with moderate thermal corrections, and both treatments correctly reproduce the expected enhancement from Bose statistics, and agree on the onset of thermal effects.

A qualitative difference emerges in the high-temperature regime. While the result of Drewes & Kang approaches a constant, the dissipation rate obtained here exhibits a pronounced suppression at large T. The origin of this discrepancy lies in the implementation of the kinematic constraints governing the microscopic processes that contribute to the imaginary part of the self-energy.

In the analysis of Drewes & Kang, the dissipation rate is controlled by step functions proportional to

$$\theta(\omega - M_1 - M_2), \qquad \theta(-\omega - M_1 + M_2),$$

which encode the decay process $\phi \to \chi_1 \chi_2$ and the inverse decay process $\chi_2 \to \phi \chi_1$, respectively. However, the complementary kinematic constraint

$$\theta(M_1 - \omega - M_2),$$

corresponding to the inverse process $\chi_1 \to \phi \chi_2$, is not included.

In the present work all kinematically allowed channels are treated on equal footing. Although the additional inverse channel contributes only in restricted regions of parameter space, its inclusion modifies the behavior in the high-temperature regime. As the temperature increases, the thermal masses grow as $M_i^2 \sim \lambda_i T^2$, and the relevant on-shell energies entering the inverse decay conditions shift accordingly. This modifies the high-temperature scaling of the dissipation rate.

The suppression observed in Fig. 2.2 reflects this altered kinematic structure. A detailed analysis of the large-temperature scaling and its physical origin will be presented in the following subsection.

To further elucidate the role of these kinematic effects and their dependence on the thermal mass hierarchy, we now extend the analysis to a broader scan over the coupling λ_2.

Figure 2.3 shows the inflaton dissipation rate for several values of the coupling λ_2, while keeping all other parameters fixed to $m_1 = 0.2\,m$, $m_2 = 0.9\,m$, and $\lambda_1 = 10^{-3}$. In this comparison only the thermal mass of χ_2 is varied, whereas χ_1 is kept parametrically lighter throughout. This choice is deliberate and is motivated by the structure of the kinematic constraints entering the dissipation rate in the analysis of Drewes & Kang, allowing for a meaningful comparison in the regime where inverse decay processes are expected to contribute.

As in Fig. 2.2, both calculations agree at low and intermediate temperatures. In this regime the dissipation rate is dominated by the vacuum decay channel together with moderate thermal corrections, and its dependence on λ_2 is mild.

The differences become pronounced at high temperature. In the result of Drewes & Kang the dissipation rate generically approaches a constant value, with only weak dependence on λ_2. In contrast, the result obtained in the present work exhibits a suppression at large T, whose onset and strength depend sensitively on the value of λ_2.

This behavior is directly tied to the temperature dependence of the thermal mass $M_2^2(T) = m_2^2 + \lambda_2 T^2/24$. Varying λ_2 changes how rapidly M_2 grows with temperature and therefore shifts the kinematic thresholds that control the inverse decay channels. For smaller λ_2, the growth of M_2 with T is slower, and the temperature at which the inverse decay kinematics begin to probe parametrically large on-shell energies is correspondingly delayed. This results in a visible shift of the suppression region toward higher temperatures.

In the present treatment all kinematically allowed inverse decay channels are included consistently. Their contribution modifies the asymptotic temperature dependence of the dissipation rate once thermal masses dominate over the vacuum masses. By contrast, the Drewes & Kang result effectively retains a more restricted set of kinematic constraints, which leads to a qualitatively different high-temperature behavior.

The systematic dependence on λ_2 visible in Fig. 2.3 highlights the central role of thermal mass growth in shaping the asymptotic regime. A quantitative

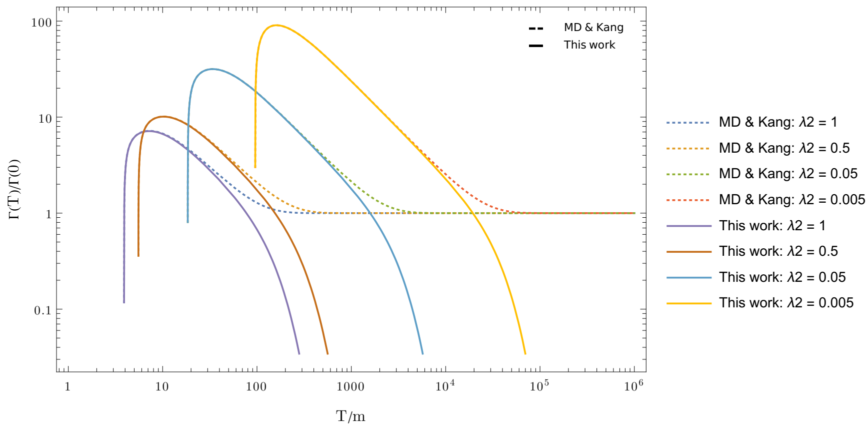

Figure 2.3: Comparison of the normalized inflaton dissipation rate $\Gamma(T)/\Gamma(0)$ as a function of the temperature ratio T/m for different choices of the coupling λ_2. Dashed curves correspond to the results of Drewes & Kang, while solid curves show the results obtained in this work. The remaining parameters are fixed to their vacuum values, with $m_1 = 0.2\,m$, $m_2 = 0.9\,m$, and $\lambda_1 = 10^{-3}$. Thermal masses are included according to $M_i^2(T) = m_i^2 + \lambda_i T^2/24$. Varying λ_2 highlights the sensitivity of the dissipation rate to the thermal mass of χ_2, particularly in the high-temperature regime.

understanding of this large-temperature scaling will be developed in the next subsection.

Figure 2.4 provides a compact summary of the differences between the dissipation rate obtained in this work and that of Drewes & Kang by displaying the ratio

$$\Gamma_{\rm MA}(T)/\Gamma_{\rm MDK}(T)$$

for the same set of parameter choices shown in Fig. 2.3.

At low temperatures the ratio approaches unity for all values of λ_2, confirming that both approaches agree in the vacuum-dominated regime and in the presence of moderate thermal corrections. This agreement is consistent with the behavior observed in the previous figures.

As the temperature increases, however, the ratio departs systematically from unity. In particular, for sufficiently large T the dissipation rate obtained in the present work becomes increasingly suppressed relative to the result of Drewes & Kang. The onset and strength of this suppression depend sensitively on λ_2: larger values of λ_2 lead to an earlier departure from unity, while smaller values delay the deviation to higher temperatures.

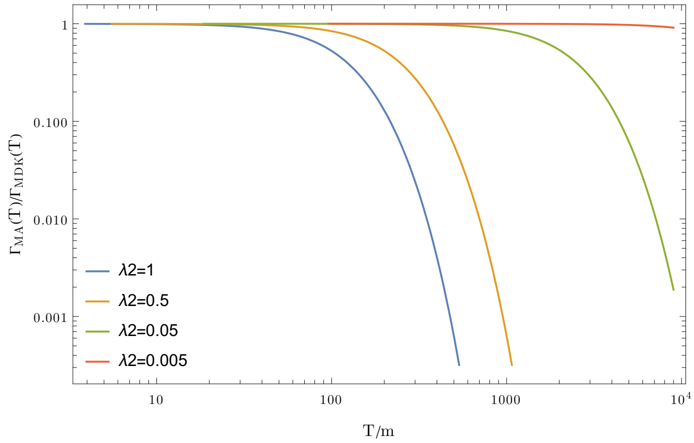

Figure 2.4: Ratio of the inflaton dissipation rates obtained in this work, $\Gamma_{\mathrm{MA}}(T)$, to those of Drewes & Kang, $\Gamma_{\mathrm{MDK}}(T)$, as a function of the temperature ratio T/m, shown for several values of the coupling λ_2. All other parameters are fixed to $m_1 = 0.2\,m$, $m_2 = 0.9\,m$, and $\lambda_1 = 10^{-3}$, with thermal masses given by $M_i^2(T) = m_i^2 + \lambda_i T^2/24$. This ratio highlights the growing discrepancy between the two results in the high-temperature regime as λ_2 is varied.

This behavior makes explicit the trend already visible in Fig. 2.3. The difference between the two approaches is not confined to a specific parameter choice, but instead reflects a systematic modification of the asymptotic high-temperature behavior once all kinematically allowed inverse channels are included consistently.

The ratio plot therefore isolates the regime in which the kinematic structure of the self-energy becomes crucial. In the following subsection we analyze the large-temperature scaling in detail and show how the growth of thermal masses and the associated on-shell conditions lead to the suppression observed here.

Asymptotic High-Temperature Behavior

The ratio plot in Fig. 2.4 suggests that the dissipation rate exhibits a qualitatively different asymptotic scaling at large temperature. We now analyze this regime analytically.

At high temperature, the thermal masses dominate over the vacuum masses,

$$M_i^2(T) \simeq \frac{\lambda_i}{24} T^2, \qquad T \gg m_i. \tag{2.32}$$

In this limit, and for the hierarchy of the parameters $\lambda_2 > \lambda_1$ and $m_2 > m_1$; the on-shell energies entering Eq. (2.29) behave parametrically as

$$\bar{\omega}_2 = \frac{m^2 - M_1^2 + M_2^2}{2m} \sim \frac{M_2^2}{2m} \propto \lambda_2 T^2, \qquad \bar{\omega}_1 \sim -\frac{M_2^2}{2m} \propto -\lambda_2 T^2. \tag{2.33}$$

Therefore, in the high-temperature limit $T \to \infty$, one finds

$$e^{\bar{\omega}_2/T} \sim e^{\lambda_2 T} \to \infty, \qquad e^{\bar{\omega}_1/T} \sim e^{-\lambda_2 T} \to 0. \tag{2.34}$$

The Bose-Einstein distributions thus behave as

$$f_B(\bar{\omega}_2) = \frac{1}{e^{\bar{\omega}_2/T} - 1} \sim e^{-\bar{\omega}_2/T} \sim e^{-\lambda_2 T}, \tag{2.35}$$

while

$$f_B(\bar{\omega}_1) = \frac{1}{e^{\bar{\omega}_1/T} - 1} \longrightarrow -1. \tag{2.36}$$

Substituting this into Eq. (2.29), we obtain parametrically

$$\Pi_0^-(m) \sim \frac{(ig)^2}{8\pi m} e^{-\bar{\omega}_2/T} \sqrt{\bar{\omega}_2^2 - M_2^2}. \tag{2.37}$$

Although the phase-space factor $\sqrt{\bar{\omega}_2^2 - M_2^2}$ grows polynomially with T, this growth is overwhelmed by the exponential suppression arising from the distribution function evaluated at $\bar{\omega}_2/T \sim \lambda_2 T \gg 1$. Consequently,

$$\Pi_0^-(m) \propto e^{-\bar{\omega}_2/T} \sim e^{-\lambda_2 T}, \tag{2.38}$$

which vanishes exponentially for large T.

Physical interpretation. The origin of this suppression can be understood in simple physical terms. At temperature T, the bulk of the thermal population consists of quanta with energies $\omega \sim T$. However, the kinematics of the present contribution require an X_2 particle with energy

$$\bar{\omega}_2 \sim \lambda_2 T^2, \tag{2.39}$$

so that

$$\frac{\bar{\omega}_2}{T} \sim \lambda_2 T \gg 1. \tag{2.40}$$

Thus, the relevant mode lies far in the ultraviolet tail of the Bose–Einstein distribution. In this regime the distribution reduces to its Boltzmann form,

$$f_B(\omega) \simeq e^{-\omega/T}, \tag{2.41}$$

and the occupation number of such hard quanta is exponentially small. The suppression is therefore statistical in origin.

It is instructive to compare this with the behavior of ordinary scattering processes in a thermal plasma. Scattering rates are typically dominated by particles with $\omega \sim T$, since these modes are abundant in the bath. Their temperature dependence is therefore governed by powers of T arising from phase space and thermal masses.

By contrast, the contribution under consideration is effectively controlled by an inverse decay channel: the on-shell condition fixes the participating X_2 particle to carry a very specific energy that grows parametrically as T^2. The process cannot proceed unless the plasma supplies a quantum with precisely this large energy. Since such quanta lie deep in the ultraviolet tail of the distribution, their abundance is exponentially suppressed.

In summary, the exponential suppression of $\Pi_0^-(m)$ at high temperature is not due to a dynamical cancellation in the amplitude, but rather reflects the scarcity of sufficiently energetic X_2 quanta in the thermal bath. The plasma simply does not contain enough hard excitations to efficiently trigger the inverse process at large T.

The analysis above relied on the quasiparticle approximation, in which the spectral densities of the bath fields are treated as infinitely narrow and localized on their on-shell dispersion relations. In the following section we relax this assumption and investigate how finite-width effects modify the inflaton self-energy.

2.3 Finite-Width Effects and Resummed Propagators

In the previous section we evaluated the inflaton self-energy in the zero-width (quasiparticle) limit, in which the spectral densities of the χ_i fields were approximated by delta functions localized on their on-shell dispersion rela-

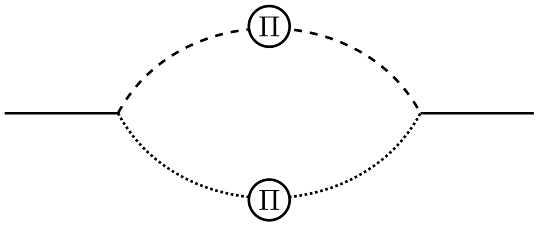

Figure 2.5: Leading-order contribution to $\Gamma_{\boldsymbol{q}}$ in the model 2.63. Solid lines denote ϕ, while dashed and dotted lines represent χ_1 and χ_2. Self-energy corrections to χ_i are depicted as circular insertions labeled Π.

tions. This approximation reduces the loop integral to a purely kinematic problem and isolates the contributions from decay and inverse decay processes with sharply defined energies.

While this treatment captures the leading-order structure of dissipation, it neglects an important physical effect: in a thermal medium, quasiparticles are not infinitely long-lived. Interactions with the surrounding plasma generate a finite lifetime, which manifests itself as a nonvanishing imaginary part of the retarded self-energy and leads to a broadening of the spectral function [5]. As a consequence, the strict on-shell kinematic constraints enforced by the delta functions are relaxed, and processes that are kinematically forbidden in the zero-width limit can acquire nonzero support.

To consistently incorporate these effects, one must resum self-energy insertions in the internal χ_i propagators. Diagrammatically, this corresponds to replacing the free propagators in the loop by fully dressed propagators, represented by the circled self-energy in Fig. 2.5.

The dressed propagator summarizes the geometric series of repeated self-energy insertions shown explicitly in Fig. 2.5. These insertions encode medium-induced scattering processes, including Landau-damping contributions, through the imaginary part of the retarded self-energy.

The resulting full propagator modifies the spectral density according to Eq. (2.44). Near the quasiparticle pole, the imaginary part can be interpreted in terms of a thermal width Γ_i, while away from the pole it describes continuum (Landau-damping) contributions.

The corresponding spectral densities are then determined by the full retarded propagator,

$$\rho_i(p_0, \mathbf{p}) = -2\,\mathrm{Im}\, D_i^R(p_0, \mathbf{p}), \tag{2.42}$$

with

$$D_i^R(p_0,\mathbf{p}) = \frac{1}{p_0^2 - \mathbf{p}^2 - m_i^2 - \Pi^R_{i,\mathbf{p}}(p_0)}. \tag{2.43}$$

In explicit form, the fully resummed spectral densities are derived in Ref. [44] and take the general form given in Eq. (2.9). In the following we work with the re-normalized spectral densities

$$\rho_i^r(p_0,\mathbf{p}) = Z_i^{-1}\frac{-2\,\mathrm{Im}\,\Pi^R_{i,\mathbf{p}}(p_0) + 2p_0\epsilon}{\left[p_0^2 - \Omega^2_{i,\mathbf{p}} - \mathrm{Re}\,\Pi^R_{i,\mathbf{p}}(p_0)\right]^2 + \left[\mathrm{Im}\,\Pi^R_{i,\mathbf{p}}(p_0) - p_0\epsilon\right]^2}, \tag{2.44}$$

where $\Pi^R_{i,\mathbf{p}}$ denotes the retarded self-energy of the χ_i field and $\Omega^2_{i,\mathbf{p}} = \mathbf{p}^2 + m_i^2$. The wave-function renormalization factor is given by

$$Z_i^{-1} = 1 - \frac{d}{dp_0^2}\mathrm{Re}\,\Pi^R_{i,\mathbf{p}}(p_0)\bigg|_{p_0=\bar{\omega}_{i,\mathbf{p}}}, \tag{2.45}$$

with $\bar{\omega}_{i,\mathbf{p}}$ denoting the quasiparticle pole. No assumption has been made at this stage about the specific functional form of the self-energy; in particular, the result is more general than a Breit–Wigner approximation and allows for arbitrary frequency dependence of $\mathrm{Re}\,\Pi_i^R$ and $\mathrm{Im}\,\Pi_i^R$.

Including a finite width modifies the imaginary part of the inflaton self-energy in two important ways. First, the sharp kinematic thresholds present in the zero-width limit become smeared. Second, off-shell contributions associated with scattering processes in the medium can acquire support once the internal lines are broadened. In particular, Landau-damping–type contributions, which were suppressed by strict on-shell kinematics in the previous section, can now contribute continuously over a range of energies.

In the following, we evaluate the inflaton self-energy using the fully resummed spectral densities and analyze how finite-width effects modify the dissipation rate across different temperature regimes.

The inflaton self-energy evaluated with the fully resummed spectral densities of the χ_i fields is represented diagrammatically in Fig. 2.5 and is given by

$$\Pi_0^-(\omega) = -ig^2\int\frac{d^4p}{(2\pi)^4}\left[1 + f_B(p_0) + f_B(\omega - p_0)\right]\rho^r_{1,\mathbf{p}}(p_0)\,\rho^r_{2,-\mathbf{p}}(\omega - p_0), \tag{2.46}$$

where the renormalized spectral densities $\rho^r_{i,\mathbf{p}}(p_0)$ are defined in Eq. (2.44). For $p_0 > 0$, the spectral function is positive definite, $\rho^r_{i,\mathbf{p}}(p_0) > 0$.

Quasiparticle approximation and pole expansion. We now work in the quasiparticle regime, where the retarded propagator is dominated by isolated poles in the narrow-width limit,

$$\Gamma_{i,\mathbf{p}} \ll \Omega_{i,\mathbf{p}}. \tag{2.47}$$

To analyze the structure of the integral, it is convenient to make the coordinate change from $(p^2, p.u)$ to $(p_0^2, \boldsymbol{p}^2)$, and expand the real and imaginary parts of the retarded self-energy $\Pi^R_i(p_0, \mathbf{p})$ as functions of p_0^2 around the quasiparticle pole $\mathcal{W}_{ir,\mathbf{p}}$, defined implicitly by

$$\mathcal{W}^2_{ir,\mathbf{p}} = \Omega^2_{i,\mathbf{p}} + \operatorname{Re}\Pi^R_{i,\mathbf{p}}\big(\mathcal{W}^2_{ir,\mathbf{p}}\big). \tag{2.48}$$

Performing a first-order Taylor expansion around this pole yields

$$\operatorname{Re}\Pi^R_{i,\mathbf{p}}(p_0) = \operatorname{Re}\Pi^R_{i,\mathbf{p}}\big(\mathcal{W}_{ir,\mathbf{p}}\big) + \big(p_0^2 - \mathcal{W}^2_{ir,\mathbf{p}}\big)\, \frac{d}{dp_0^2}\operatorname{Re}\Pi^R_{i,\mathbf{p}}(p_0^2)\bigg|_{p_0^2=\mathcal{W}^2_{ir,\mathbf{p}}}, \tag{2.49}$$

$$\operatorname{Im}\Pi^R_{i,\mathbf{p}}(p_0) = \operatorname{Im}\Pi^R_{i,\mathbf{p}}\big(\mathcal{W}_{ir,\mathbf{p}}\big) + \big(p_0^2 - \mathcal{W}^2_{ir,\mathbf{p}}\big)\, \frac{d}{dp_0^2}\operatorname{Im}\Pi^R_{i,\mathbf{p}}(p_0^2)\bigg|_{p_0^2=\mathcal{W}^2_{ir,\mathbf{p}}}. \tag{2.50}$$

At leading order in the coupling governing the χ_i width ($\mathcal{O}(g_i^2)$), the dressed propagator exhibits four complex poles,

$$p_0 = \pm\hat{\Omega}_{i,\mathbf{p}}, \qquad p_0 = \pm\hat{\Omega}^*_{i,\mathbf{p}}, \tag{2.51}$$

with

$$\hat{\Omega}_{j,\mathbf{p}} = \Omega_{j,\mathbf{p}} + \frac{i}{2}\Gamma_{j,\mathbf{p}}. \tag{2.52}$$

where $j = 1, 2$, and $\Omega_{i,\mathbf{p}}$ denotes the real quasiparticle dispersion relation and $\Gamma_{i,\mathbf{p}}$ the corresponding thermal width.

At the leading order in the coupling $\mathcal{O}(g_i^2)$, the thermal width is determined from the imaginary part of the retarded self-energy evaluated at the pole,

$$\Gamma_{i,\boldsymbol{p}} = \mathcal{Z}_{i,\boldsymbol{p}}\left(\frac{i\,\Pi^-_{i,\boldsymbol{p}}\left(\Omega_{i,\boldsymbol{p}}\right)}{2\Omega_{i,\boldsymbol{p}}} + \epsilon\right), \tag{2.53}$$

where we used the relation $\Pi^-_{i,\mathbf{p}}(\Omega_{i,\mathbf{p}}) = 2i\,\mathrm{Im}\,\Pi^R_{i,\mathbf{p}}(\Omega_{i,\mathbf{p}})$. A detailed derivation is provided in Appendix B.

Keeping the derivative of the imaginary part in the pole expansion induces a correction to the residue of the propagator. To keep track of the sign structure associated with the positive- and negative-frequency poles, we introduce a bookkeeping parameter $\alpha = \pm 1$, where $\alpha = +1$ corresponds to expansion near $p_0 \simeq +\Omega_{i,\mathbf{p}}$ and $\alpha = -1$ near $p_0 \simeq -\Omega_{i,\mathbf{p}}$.

The generalized residue factor then reads

$$\mathcal{Z}^{-1}_{i\alpha} = 1 - \frac{d}{d(p_0^2)}\mathrm{Re}\,\Pi^R_{i,\mathbf{p}}(p_0^2)\bigg|_{p_0^2=\mathcal{W}^2_{i,\mathbf{p}}} - \alpha\, i\,\frac{d}{d(p_0^2)}\mathrm{Im}\,\Pi^R_{i,\mathbf{p}}(p_0^2)\bigg|_{p_0^2=\mathcal{W}^2_{i,\mathbf{p}}}. \tag{2.54}$$

Neglecting the derivative of the imaginary part reduces $\mathcal{Z}_{i\alpha}$ to the standard wave-function renormalization factor appearing in the Breit–Wigner approximation.

Using these definitions, the renormalized spectral density Eq. (2.44) can be written in the explicit four-pole form

$$\rho^r_{i,\mathbf{p}}(p_0) = \mathcal{Z}_{i\alpha}\,\frac{-2\,\mathrm{Im}\,\Pi^R_{i,\mathbf{p}}(p_0) + 2p_0\epsilon}{\left(p_0 - \hat{\Omega}_{i,\mathbf{p}}\right)\left(p_0 - \hat{\Omega}^*_{i,\mathbf{p}}\right)\left(p_0 + \hat{\Omega}_{i,\mathbf{p}}\right)\left(p_0 + \hat{\Omega}^*_{i,\mathbf{p}}\right)}. \tag{2.55}$$

Performing the p_0 integration in Eq. (2.46) by closing the contour in the upper half-plane and summing the residues yields

$$\begin{aligned}
\Pi^-_0(\omega) = &-i\frac{g^2}{2}\int\frac{d^3p}{(2\pi)^3} \\
&\times\Bigg\{\frac{1}{\hat{\Omega}_{1,\mathbf{p}}}\left[1 + f_B(\hat{\Omega}_{1,\mathbf{p}}) + f_B(\omega - \hat{\Omega}_{1,\mathbf{p}})\right]\rho^r_{2,\mathbf{p}}(\omega - \hat{\Omega}_{1,\mathbf{p}}) \\
&+\frac{1}{\hat{\Omega}^*_{1,\mathbf{p}}}\left[f_B(\hat{\Omega}^*_{1,\mathbf{p}}) - f_B(\omega + \hat{\Omega}^*_{1,\mathbf{p}})\right]\rho^r_{2,\mathbf{p}}(\omega + \hat{\Omega}^*_{1,\mathbf{p}}) \\
&+\frac{1}{\hat{\Omega}_{2,\mathbf{p}}}\left[f_B(\hat{\Omega}_{2,\mathbf{p}}) - f_B(\omega + \hat{\Omega}_{2,\mathbf{p}})\right]\rho^r_{1,\mathbf{p}}(\omega + \hat{\Omega}_{2,\mathbf{p}}) \\
&+\frac{1}{\hat{\Omega}^*_{2,\mathbf{p}}}\left[1 + f_B(\hat{\Omega}^*_{2,\mathbf{p}}) + f_B(\omega - \hat{\Omega}^*_{2,\mathbf{p}})\right]\rho^r_{1,\mathbf{p}}(\omega - \hat{\Omega}^*_{2,\mathbf{p}})\Bigg\}.
\end{aligned} \tag{2.56}$$

Here the Bose–Einstein distribution is analytically continued to complex arguments when evaluated at the pole positions.

Using the definition of the thermal width Γ_i in Eq. (2.53) we can rewrite the four-pole spectral density $\rho_i(\omega)$ Eq. (2.55), as

$$\rho^{r}_{i,\boldsymbol{p}}(\omega \pm p_0) = \mathcal{Z}_i \frac{i\,\Pi^{-}_{i,\mathbf{p}}(\omega \pm p_0) + 2(\omega \pm p_0)\epsilon}{\left((\omega \pm p_0)^2 - \Omega^2_{i,\mathbf{p}}\right)^2 + \mathcal{Z}_i^2 \left(\frac{i}{2}\Pi^{-}_{i,\mathbf{p}}(\Omega_{i,\mathbf{p}}) + \epsilon\Omega_{i,\mathbf{p}}\right)^2} \tag{2.57}$$

So, the leading-order $\mathcal{O}(\Gamma_i)$ results of the full self-energy expression in Eq. (2.56), can be written as follows

$$\begin{aligned}
\Pi^{-}_0(\omega) = \frac{g^2}{2}\int \frac{d^3p}{(2\pi)^3} \\
\times\Bigg\{ &\frac{\mathcal{Z}_2}{\Omega_1} \frac{\left(\Pi^{-}_2(\omega - \Omega_1) - 2i(\omega - \Omega_1)\epsilon\right)\left(1 + f_B(\Omega_1) + f_B(\omega - \Omega_1)\right)}{\left((\omega - \hat{\Omega}_1)^2 - \Omega_2^2\right)^2 + \mathcal{Z}_2^2\left(\frac{i}{2}\Pi^{-}_2(\Omega_2) + \epsilon\Omega_2\right)^2} \\
&+ \frac{\mathcal{Z}_2}{\Omega_1} \frac{\left(\Pi^{-}_2(\omega + \Omega_1) - 2i(\omega + \Omega_1)\epsilon\right)\left(f_B(\Omega_1) - f_B(\omega + \Omega_1)\right)}{\left((\omega + \hat{\Omega}^*_1)^2 - \Omega_2^2\right)^2 + \mathcal{Z}_2^2\left(\frac{i}{2}\Pi^{-}_2(\Omega_2) + \epsilon\Omega_2\right)^2} \\
&+ \frac{\mathcal{Z}_1}{\Omega_2} \frac{\left(\Pi^{-}_1(\omega + \Omega_2) - 2i(\omega + \Omega_2)\epsilon\right)\left(f_B(\Omega_2) - f_B(\omega + \Omega_2)\right)}{\left((\omega + \hat{\Omega}_2)^2 - \Omega_1^2\right)^2 + \mathcal{Z}_1^2\left(\frac{i}{2}\Pi^{-}_1(\Omega_1) + \epsilon\Omega_1\right)^2} \\
&+ \frac{\mathcal{Z}_1}{\Omega_2} \frac{\left(\Pi^{-}_1(\omega - \Omega_2) - 2i(\omega - \Omega_2)\epsilon\right)\left(1 + f_B(\Omega_2) + f_B(\omega - \Omega_2)\right)}{\left((\omega - \hat{\Omega}^*_2)^2 - \Omega_1^2\right)^2 + \mathcal{Z}_1^2\left(\frac{i}{2}\Pi^{-}_1(\Omega_1) + \epsilon\Omega_1\right)^2}\Bigg\}.
\end{aligned} \tag{2.58}$$

2.4 The Breit–Wigner Approximation

Within the Breit–Wigner (BW) approximation, the renormalized spectral density in Eq. (2.44) reduces, in the narrow-width regime $\Gamma_{i,\mathbf{p}} \ll \Omega_{i,\mathbf{p}}$, to the familiar Lorentzian form

$$\rho^{\mathrm{BW}}_{i,\mathbf{p}}(p_0) = 2\,\mathcal{Z}_{i,\mathbf{p}} \frac{p_0\,\Gamma_{i,\mathbf{p}}}{\left(p_0^2 - \Omega^2_{i,\mathbf{p}}\right)^2 + \left(p_0\,\Gamma_{i,\mathbf{p}}\right)^2}. \tag{2.59}$$

Here $\Omega_{i,\mathbf{p}}$ denotes the quasiparticle dispersion relation, $\Gamma_{i,\mathbf{p}}$ the corresponding thermal width, and $\mathcal{Z}_{i,\mathbf{p}}$ the wave-function renormalization factor.

Substituting Eq. (2.59) into the full expression for the inflaton self-energy, Eq. (2.46), one obtains

$$\Pi_0^-(\omega) = -ig^2 \int \frac{d^4p}{(2\pi)^4}\,[1 + f_B(p_0) + f_B(\omega - p_0)]\,\rho_{1,\mathbf{p}}^{\mathrm{BW}}(p_0)\,\rho_{2,-\mathbf{p}}^{\mathrm{BW}}(\omega - p_0). \tag{2.60}$$

Performing the p_0 integration and retaining the leading contributions in Γ_i yields an expression structurally analogous to Eq. (2.56),

$$\begin{aligned}\Pi_0^-(\omega) = &-i\frac{g^2}{2}\int \frac{d^3p}{(2\pi)^3} \\ &\times \Bigg\{ \frac{\mathcal{Z}_{2,\mathbf{p}}}{\Omega_{1,\mathbf{p}}}\,[1 + f_B(\Omega_{1,\mathbf{p}}) + f_B(\omega - \Omega_{1,\mathbf{p}})]\,\rho_{2,\mathbf{p}}^{\mathrm{BW}}(\omega - \Omega_{1,\mathbf{p}}) \\ &+ \frac{\mathcal{Z}_{2,\mathbf{p}}}{\Omega_{1,\mathbf{p}}}\,[f_B(\Omega_{1,\mathbf{p}}) - f_B(\omega + \Omega_{1,\mathbf{p}})]\,\rho_{2,\mathbf{p}}^{\mathrm{BW}}(\omega + \Omega_{1,\mathbf{p}}) \\ &+ \frac{\mathcal{Z}_{1,\mathbf{p}}}{\Omega_{2,\mathbf{p}}}\,[f_B(\Omega_{2,\mathbf{p}}) - f_B(\omega + \Omega_{2,\mathbf{p}})]\,\rho_{1,\mathbf{p}}^{\mathrm{BW}}(\omega + \Omega_{2,\mathbf{p}}) \\ &+ \frac{\mathcal{Z}_{1,\mathbf{p}}}{\Omega_{2,\mathbf{p}}}\,[1 + f_B(\Omega_{2,\mathbf{p}}) + f_B(\omega - \Omega_{2,\mathbf{p}})]\,\rho_{1,\mathbf{p}}^{\mathrm{BW}}(\omega - \Omega_{2,\mathbf{p}}) \Bigg\}.\end{aligned} \tag{2.61}$$

Relation to the generalized pole expansion. It is instructive to clarify the relation between the Breit–Wigner approximation and the generalized pole expansion adopted in Sec. 2.3. In the latter, both the real and imaginary parts of the retarded self-energy are expanded to first order in p_0^2 around the quasiparticle pole. The derivative of the real part determines the usual wave-function renormalization factor $\mathcal{Z}_{i,\mathbf{p}}$, while the imaginary part evaluated on shell defines the thermal width $\Gamma_{i,\mathbf{p}}$.

In addition, the derivative of $\mathrm{Im}\,\Pi_{i,\mathbf{p}}^R(p_0)$ contributes to the residue of the complex pole. As a result, the wave-function renormalization factor becomes, in general, complex. This correction is of higher order in the narrow-width expansion and does not modify the pole position at leading order; rather, it refines the normalization of the propagator near the pole.

The Breit–Wigner form in Eq. (2.59) is recovered upon neglecting the frequency dependence of $\mathrm{Im}\,\Pi_{i,\mathbf{p}}^R(p_0)$ in the vicinity of the pole, i.e.

$$\mathrm{Im}\,\Pi_{i,\mathbf{p}}^R(p_0) \;\simeq\; \mathrm{Im}\,\Pi_{i,\mathbf{p}}^R(\Omega_{i,\mathbf{p}}), \tag{2.62}$$

while retaining only the linear correction from $\mathrm{Re}\,\Pi^R_{i,\mathbf{p}}$. In this limit, the residue becomes purely real and the spectral density reduces to the familiar Lorentzian characterized by a constant width $\Gamma_{i,\mathbf{p}}$.

The generalized expansion employed in this work therefore operates in the same quasiparticle regime as the Breit–Wigner approximation, but systematically retains subleading corrections to the residue arising from the frequency dependence of $\mathrm{Im}\,\Pi^R_{i,\mathbf{p}}$. The Breit–Wigner expression can thus be viewed as a controlled special case of the more general pole representation.

2.5 Model Setup and Thermal Masses

We consider the dissipation of a real scalar inflaton field ϕ into bosonic degrees of freedom. As an effective description of the relevant interactions, we adopt the model defined by the Lagrangian

$$\mathcal{L} = \frac{1}{2}\partial_\mu\phi\partial^\mu\phi - \frac{1}{2}m^2\phi^2 - g\,\phi\,\chi_1\chi_2 + \frac{1}{2}\partial_\mu\xi\partial^\mu\xi - \frac{1}{2}m_\xi^2\xi^2 + \sum_{i=1}^{2}\left(\frac{1}{2}\partial_\mu\chi_i\partial^\mu\chi_i - \frac{1}{2}m_i^2\chi_i^2 - g_i\,\chi_i\xi^2 - \frac{\lambda_i}{4!}\chi_i^4\right) + \mathcal{L}_{\mathrm{bath}}, \tag{2.63}$$

where χ_i are scalar fields with $m_i \ll m$, $\lambda_i \gg g_i$, and $\mathcal{L}_{\mathrm{bath}}$ represents all other degrees of freedom in the primordial plasma that maintain thermal equilibrium. The field ξ is another real scalar which we introduce as an additional bath degree of freedom coupled to χ_i. While the thermal masses of the χ_i fields are primarily generated by their quartic self-interactions, the coupling to ξ provides a microscopic origin for the self-energy corrections that give rise to a finite thermal width of the χ_i quasiparticles. The field ξ is assumed to be light and in thermal equilibrium, thereby serving as a simple effective description of the surrounding radiation bath.

Thermal masses and dispersion relations

We compute the dissipation rate Γ using the real-time formalism of thermal field theory. At leading order in the quartic coupling λ_i, the real part of the χ_i self-energy generates a thermal mass correction. Neglecting higher-order corrections to the residue (i.e. taking $\mathcal{Z}_{i,\mathbf{p}} \simeq 1$ at this order), the quasiparticle dispersion relation becomes [30, 57]

$$\Omega_{i,\mathbf{p}}^2 = \mathbf{p}^2 + m_{ir}^2 + \frac{\lambda_i}{2}\varphi^2 + \frac{\lambda_i}{4!}T^2, \tag{2.64}$$

where $\varphi \equiv \langle\phi\rangle$ denotes the background inflaton field and m_{ir} is the renormalized vacuum mass. It is convenient to introduce the effective thermal mass

$$M_i^2 = m_{ir}^2 + \frac{\lambda_i}{2}\varphi^2 + \frac{\lambda_i}{4!}T^2, \tag{2.65}$$

so that the quasiparticle poles take the standard form

$$\Omega_{i,\mathbf{p}} = \sqrt{\mathbf{p}^2 + M_i^2}. \tag{2.66}$$

Imaginary part of the χ_i self-energy

In the model (2.63), the imaginary part of the retarded χ_i self-energy was computed in Ref. [57] and is given by

$$\begin{aligned}\Pi_{i,\mathbf{p}}^-(p_0) = \frac{g_i^2}{16 i\pi|\mathbf{p}|}\Bigg[& -\theta(-p^2)\left(p_0 + T\log\left(\frac{f_B(p_0-\omega^+)f_B(-\omega^-)}{f_B(-\omega^+)f_B(p_0-\omega^-)}\right)\right) \\ & + \theta\big(p^2-(2m_\xi)^2\big)\,T\log\left(\frac{f_B(p_0-\omega^+)f_B(-\omega^-)}{f_B(-\omega^+)f_B(p_0-\omega^-)}\right)\Bigg],\end{aligned} \tag{2.67}$$

where the Bose–Einstein distribution is written as

$$f_B(p_0) = \frac{1}{e^{p_0/T}-1}, \tag{2.68}$$

and

$$\omega^\pm = \frac{p_0}{2} \pm \mathrm{sign}(p^2)\frac{|\mathbf{p}|}{2}\sqrt{1-\frac{(2m_\xi)^2}{p^2}}. \tag{2.69}$$

Numerical Evaluation of the Dissipation Rate

We now evaluate the inflaton self-energy in Eq. (2.58) using the temperature-dependent dispersion relations $\Omega_{i,\mathbf{p}} = \sqrt{\mathbf{p}^2 + M_i^2}$ and the analytic expression for the imaginary part of the χ_i self-energies derived above. All temperature dependence is thus incorporated consistently through the quasiparticle masses and the thermal self-energies.

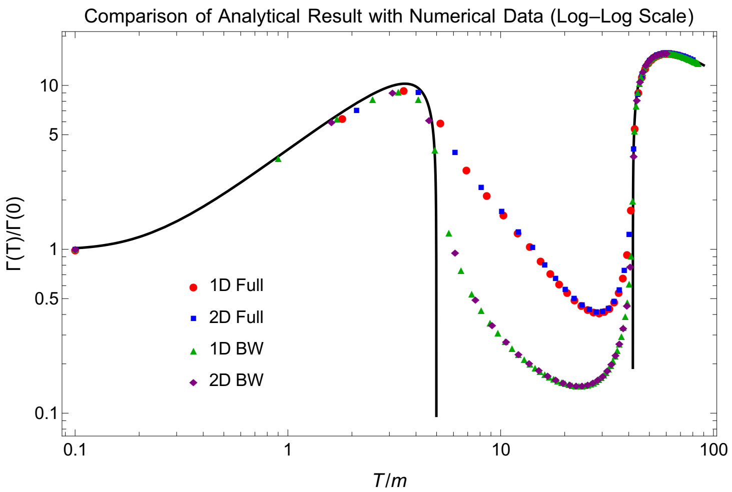

Figure 2.6: Temperature dependence of the decay rate, normalized to its vacuum value, as a function of T/m. The solid black curve shows the analytical result Eq. 2.29, while the markers correspond to numerical evaluations obtained using different approximations: full result in one and two dimensions (1D Full Eq. 2.58, 2D Full Eq. 2.26), and the Breit–Wigner (BW) approximation in one and two dimensions (1D BW Eq. 2.61, 2D BW Eq. 2.60). The parameters are chosen as $m_1 = 0.2\,m$, $m_2 = 0.4\,m$, $m_z = 0.03\,m$, $\lambda_1 = 0.11$, $\lambda_2 = 0.2$, and $\varphi = 0.1$.

The resulting three-momentum integral is computed numerically for fixed model parameters and varying temperature. This allows us to determine the temperature dependence of the dissipation rate and to compare the behavior obtained from the generalized pole expansion with the Breit–Wigner approximation discussed in the previous section.

The numerical results are shown in Fig. 2.6, where we plot the decay rate Γ (or equivalently the self energy $\Pi_0^-(\omega)$) as a function of T/m.

2.6 Comparison Between Full and Breit–Wigner Results

Figure 2.6 compares the inflaton self-energy computed using the fully resummed spectral densities and the Breit–Wigner approximation. For each case, we evaluate the expression in two independent ways: (i) by performing the full two-dimensional integral over $(p_0, \mathbf{p})$ directly [Eqs. (2.46) and (2.60)], and (ii) by first carrying out the p_0 integration analytically and subsequently evaluating the remaining three-momentum integral [Eqs. (2.58) and (2.61)].

In the kinematically allowed regions, all four computations — 2D-Full, 1D-Full, 2D-BW, and 1D-BW — show excellent agreement with each other and with the analytic zero-width result where applicable. This confirms both the numerical consistency of the implementation and the validity of the quasiparticle approximation in these regimes.

In the kinematically forbidden region, however, differences between the Breit–Wigner and fully resummed treatments become visible. While the direct two-dimensional evaluation with the full spectral densities provides the reference result, the reduced one-dimensional expression derived from the full pole expansion [Eq. (2.58)] reproduces it more accurately than the corresponding Breit–Wigner approximation. This indicates that retaining the full frequency dependence of the self-energy in the generalized pole expansion improves the description in regions where off-shell effects become relevant.

Overall, the comparison demonstrates that the generalized pole representation provides a controlled extension of the Breit–Wigner approximation, preserving agreement in the allowed regions while yielding a more reliable result when kinematic suppression or off-shell contributions dominate.

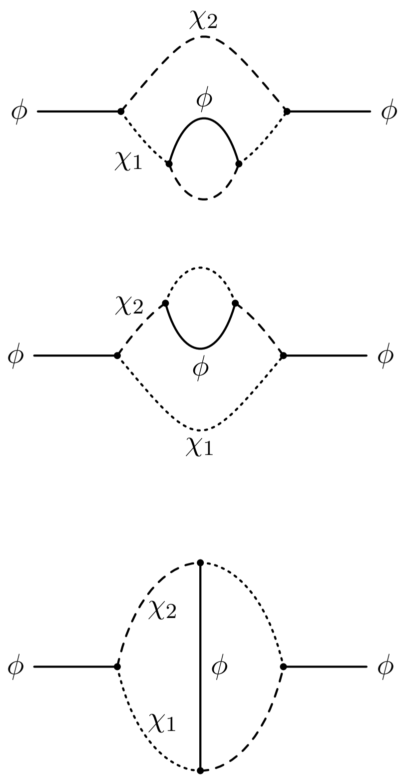

Figure 2.7: Two-loop contributions to the ϕ self-energy in the trilinear model $\mathcal{L}_{\rm int} = g\,\phi\chi_1\chi_2$: (top) one-loop self-energy insertion on the χ_1 propagator; (middle) one-loop self-energy insertion on the χ_2 propagator, and the genuine two-loop vertex correction (bottom). Solid, dashed, and dotted lines represent ϕ, χ_2, and χ_1, respectively.

2.7 Two-Loop Self-Energy at Finite Temperature

In this section, we compute the next-to-leading order (NLO) contributions to the ϕ self-energy arising from the trilinear interaction

$$\mathcal{L}_{\rm int} = g\,\phi\chi_1\chi_2\,, \tag{2.70}$$

introduced in Eq. 2.25, focusing on the finite-temperature effects relevant for the thermal plasma generated after inflation. At this order, corresponding to two-loop corrections, three distinct topologies contribute to the inflaton self-energy $\Pi^-_\phi(\omega)$: the genuine vertex correction, as well as the self-energy insertions on the internal χ_1 and χ_2 propagators, as shown in Fig. 2.7. Although these diagrams differ in topology, they all contribute at the same order in the coupling expansion, $\mathcal{O}(g^4)$, and must therefore be treated on equal footing.

From a physical perspective, these contributions encode complementary effects of the thermal medium. The vertex correction captures, among others, genuine two-loop scattering processes, while the propagator corrections account for the dressing of the intermediate χ_i states due to their interactions with the plasma. At finite temperature, this dressing manifests itself through the emergence of thermal widths, which can significantly modify the kinematics and open up qualitatively new channels, such as Landau damping.

In what follows, we evaluate each of these contributions within the closed-time-path (CTP) formalism, expressing the results in terms of thermal propagators and spectral densities. Particular emphasis will be placed on the imaginary part of the retarded self-energy, $\mathrm{Im}\,\Pi^R$, which governs dissipation and particle production rates in the thermal bath.

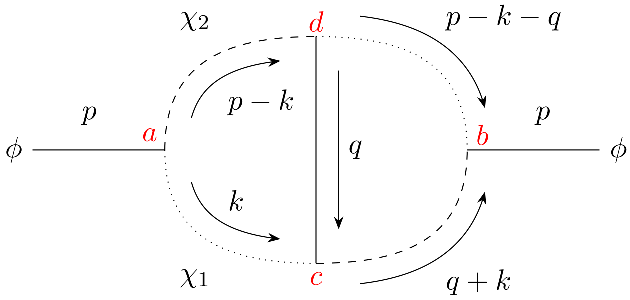

Figure 2.8: Two-loop self-energy correction to ϕ mediated by χ_1 and χ_2, showing the momentum routing. Solid lines denote ϕ, dashed lines χ_2, and dotted lines χ_1.

2.7.1 Two-loop Vertex Correction

We begin by evaluating the two-loop contribution to the self-energy of the scalar field ϕ arising from the trilinear interaction in Eq. 2.70. The corresponding vertex diagram is shown in Fig. 2.8, where we indicate the Keldysh contour indices and specify the momentum routing.

Within the Schwinger–Keldysh (closed-time-path) formalism, the self-energy is given by

$$\Pi^{-ab}_{\phi,p}(\omega) = -ig^4 \int \frac{d^4k}{(2\pi)^4}\frac{d^4q}{(2\pi)^4} \times \\ \times \sum_{cd} cd\, \Delta_1^{ac}(k)\Delta_2^{ad}(p-k)\Delta_\phi^{dc}(q)\Delta_1^{db}(p-k-q)\Delta_2^{cb}(q+k)\,. \tag{2.71}$$

We are primarily interested in the lesser component of the self-energy,

$$\mathrm{Im}\Pi^R_{\phi,\mathbf{p}}(\omega) \equiv \frac{-i\Pi^<_{\phi,\mathbf{p}}(\omega)}{2f_B(\omega)}\,,$$

which can be written as

$$\mathrm{Im}\Pi^R_{\phi,\mathbf{0}}(\omega) = -\frac{g^4}{2} f_B^{-1}(\omega) \int \frac{d^4k}{(2\pi)^4}\frac{d^4q}{(2\pi)^4}\, I\,. \tag{2.72}$$

For convenience, we define the integrand as

$$I = \sum_{a=1}^{4} I_a = \sum_{cd} cd\, \Delta_1^{+c}(k)\Delta_2^{+d}(p-k)\Delta_\phi^{dc}(q)\Delta_1^{d-}(p-k-q)\Delta_2^{c-}(q+k)\,, \tag{2.73}$$

where the four contributions correspond to the possible assignments of contour indices,

$$\begin{aligned}
I_1 &= \Delta_1^{++}(k)\Delta_2^{++}(p-k)\Delta_\phi^{++}(q)\Delta_1^{<}(p-k-q)\Delta_2^{<}(q+k)\,,\\
I_2 &= -\Delta_1^{<}(k)\Delta_2^{++}(p-k)\Delta_\phi^{<}(q)\Delta_1^{<}(p-k-q)\Delta_2^{--}(q+k)\,,\\
I_3 &= -\Delta_1^{++}(k)\Delta_2^{<}(p-k)\Delta_\phi^{>}(q)\Delta_1^{--}(p-k-q)\Delta_2^{<}(q+k)\,,\\
I_4 &= +\Delta_1^{<}(k)\Delta_2^{<}(p-k)\Delta_\phi^{--}(q)\Delta_1^{--}(p-k-q)\Delta_2^{--}(q+k)\,.
\end{aligned} \tag{2.74}$$

The four terms I_1–I_4 in Eq. (2.74) correspond to the distinct cut structures of the two-loop self-energy diagram shown in Fig. 2.8.

The terms I_1 and I_4 contain two Wightman propagators and correspond to vertical cuts through the diagram. Physically, these describe $1 \to 2$ decay processes of the external ϕ mode, dressed by an additional loop correction. In these contributions, the remaining internal lines appear as time-ordered (Δ^{++}) or anti-time-ordered (Δ^{--}) propagators. These propagators can themselves be decomposed into dispersive and on-shell pieces (see Eq. (2.87)), allowing further cut-like contributions once the delta-function part is isolated. We will analyze these "opened" contributions in detail when discussing off-diagonal cuts in Section 2.

The terms I_2 and I_3 correspond to diagonal and anti-diagonal (reverse-diagonal) cuts of the diagram. These encode scattering and inverse decay processes and will generate additional kinematic structures that differ from the vertical cuts discussed above.

Using the identity

$$\Delta_a^{--}(p) = \left[\Delta_a^{++}(p)\right]^*\,, \tag{2.75}$$

and performing the change of variables

$$k \to p-k-q\,, \tag{2.76}$$

one finds that both I_2 and I_3 are real, while the remaining two contributions satisfy

$$I_1^* = I_4\,. \tag{2.77}$$

Since we are computing the lesser self-energy $\Pi^<(\omega)$, which is a real quantity (it is directly related to the decay width and therefore must be real-valued), it follows that only the combination

$$I = 2\,\mathrm{Re}(I_1) + I_2 + I_3 \tag{2.78}$$

needs to be evaluated explicitly.

Next, we exploit the symmetry properties of the propagators. Under momentum reversal, the Wightman functions interchange,

$$\Delta^<(-p) = \Delta^>(p)\,, \tag{2.79}$$

whereas the time-ordered propagator is invariant,

$$\Delta^{++}(-p) = \Delta^{++}(p)\,. \tag{2.80}$$

Using these relations, we can establish a connection between the I_2 and I_3 contributions. Performing the transformation $q \to -q$ in I_3, we obtain

$$I_{3\,[q\to -q]} = -\Delta_1^{++}(k)\Delta_2^<(p-k)\Delta_\phi^<(q)\Delta_1^{--}(p-k+q)\Delta_2^<(k-q)\,. \tag{2.81}$$

We now perform the change of variables

$$k \to p-k\,, \tag{2.82}$$

and relabel the internal species $1 \leftrightarrow 2$. This yields

$$\tilde{I}_3 = -\Delta_2^{++}(p-k)\Delta_1^<(k)\Delta_\phi^<(q)\Delta_2^{--}(k+q)\Delta_1^<(p-k-q)\,. \tag{2.83}$$

We therefore conclude that, after the appropriate change of variables and relabeling,

$$\tilde{I}_3 = I_2\,. \tag{2.84}$$

In practice, this implies that to compute the full lesser self-energy of the vertex diagram in Fig. 2.8, it is sufficient to evaluate $\mathrm{Re}(I_1)$ and I_2. The contribution from I_3 then follows directly by symmetry.

Before proceeding to the explicit evaluation of the remaining contributions, we can implement further simplifications. In particular, we decompose the Feynman propagator as

$$\Delta_\phi^{++}(p) = \frac{i}{p^2 - m_\phi^2 + i\eta} + 2\pi f_B(|p_0|)\,\delta(p^2 - m_\phi^2) \tag{2.85}$$

$$= i\,\mathcal{P}\left(\frac{1}{p^2 - m_\phi^2}\right) + \pi\,(1 + 2f_B(|p_0|))\,\delta(p^2 - m_\phi^2) \tag{2.86}$$

$$= \Delta_\phi^{\mathcal{P}}(p) + \Delta_\phi^{\delta}(p)\,, \tag{2.87}$$

where $\mathcal{P}(\cdots)$ denotes the principal value. The term $\Delta_\phi^{\mathcal{P}}(p)$ represents the principal (dispersive) part of the propagator and constitutes the purely imaginary contribution, while $\Delta_\phi^{\delta}(p)$ denotes the on-shell delta-function piece, which is real and contains the thermal contribution.

Since the lesser self-energy $\Pi^<(\omega)$ must be real and positive (it is directly related to the decay width), only specific combinations of propagators can contribute to I_1 and I_2. In particular, non-vanishing contributions arise from either:

- fully real combinations, where Wightman propagators $\Delta^{>,<}$ multiply only the delta parts Δ^δ of the Feynman propagators, or
- combinations containing an even number of imaginary principal-value pieces $\Delta^{\mathcal{P}}$, such that the overall contribution remains real.

With this decomposition, the diagonal contribution I_2 can be written as

$$\begin{aligned} I_2 = {} & -\Delta_1^<(k)\Delta_\phi^<(q)\Delta_1^<(p-k-q) \\ & \times \Big[\Delta_2^\delta(p-k)\,\Delta_2^\delta(q+k) + \Delta_2^{\mathcal{P}}(p-k)\,\Delta_2^{\mathcal{P}}(q+k)\Big]\,. \end{aligned} \tag{2.88}$$

Similarly, the off-diagonal contribution $\mathrm{Re}(I_1)$ becomes

$$\begin{aligned} \mathrm{Re}(I_1) = 2\Big\{ & \Delta_1^\delta(k)\Delta_2^\delta(p-k)\Delta_\phi^\delta(q)\Delta_1^<(p-k-q)\Delta_2^<(q+k) \\ & + \Delta_1^\delta(k)\Delta_2^{\mathcal{P}}(p-k)\Delta_\phi^{\mathcal{P}}(q)\Delta_1^<(p-k-q)\Delta_2^<(q+k) \\ & + \Delta_1^{\mathcal{P}}(k)\Delta_2^\delta(p-k)\Delta_\phi^{\mathcal{P}}(q)\Delta_1^<(p-k-q)\Delta_2^<(q+k) \\ & + \Delta_1^{\mathcal{P}}(k)\Delta_2^{\mathcal{P}}(p-k)\Delta_\phi^\delta(q)\Delta_1^<(p-k-q)\Delta_2^<(q+k)\Big\}\,. \end{aligned} \tag{2.89}$$

The purely real contributions in both $\mathrm{Re}(I_1)$ and I_2 are proportional to the following product of delta functions:

$$\begin{aligned} I_{1,2}^{\delta} \sim & \, \delta(k^2 - m_1^2)\delta\big((p-k)^2 - m_2^2\big)\, \delta(q^2 - m_\phi^2) \\ & \times \delta\big((p-k-q)^2 - m_1^2\big)\, \delta\big((q+k)^2 - m_2^2\big) \ . \end{aligned} \tag{2.90}$$

Let us analyze the kinematic constraints implied by these delta functions. From the first and third delta functions, the χ_1 and ϕ propagators are placed on shell,

$$k^2 = m_1^2\,, \qquad q^2 = m_\phi^2\,. \tag{2.91}$$

The remaining delta functions impose the additional conditions

$$(p-k)^2 = m_2^2 \ \Rightarrow \ 2p{\cdot}k = m_\phi^2 + m_1^2 - m_2^2\,, \tag{2.92}$$

$$(p-k-q)^2 = m_1^2 \ \Rightarrow \ 2p{\cdot}q - 2q{\cdot}k = m_\phi^2 + m_2^2 - m_1^2\,, \tag{2.93}$$

$$(q+k)^2 = m_2^2 \ \Rightarrow \ m_1^2 + m_\phi^2 + 2q{\cdot}k = m_2^2\,. \tag{2.94}$$

Combining these relations yields

$$p{\cdot}k + q{\cdot}k = 0\,, \tag{2.95}$$

$$2p{\cdot}k = m_\phi^2 + m_1^2 - m_2^2\,, \tag{2.96}$$

$$p{\cdot}q = m_2^2 - m_1^2\,. \tag{2.97}$$

We now specialize to the rest frame of the external inflaton, $|\boldsymbol{p}| = 0$, so that $p^\mu = (m_\phi, \mathbf{0})$. The above constraints then imply

$$k_0 = \frac{m_\phi^2 + m_1^2 - m_2^2}{2m_\phi} = \frac{1}{2}(m_\phi + q_0)\,, \tag{2.98}$$

$$q_0 = \frac{m_2^2 - m_1^2}{m_\phi}\,. \tag{2.99}$$

Using the on-shell relation

$$q_0 = \pm\sqrt{|\mathbf{q}|^2 + m_\phi^2}\,,$$

we must consider two possible cases.

Case 1: $q_0 \geq m_\phi$.

In this case,

$$q_0 = \frac{m_2^2 - m_1^2}{m_\phi} \geq m_\phi \;\Rightarrow\; m_2^2 \geq m_\phi^2 + m_1^2 \,. \tag{2.100}$$

However, from the expression for k_0 we simultaneously obtain

$$k_0 \geq m_\phi \;\Rightarrow\; m_1^2 \geq m_\phi^2 + m_2^2 \,. \tag{2.101}$$

These two inequalities cannot both be satisfied, leading to a contradiction.

Case 2: $q_0 \leq -m_\phi$.
Then

$$q_0 = \frac{m_2^2 - m_1^2}{m_\phi} \leq -m_\phi \;\Rightarrow\; m_1^2 \geq m_\phi^2 + m_2^2 \,. \tag{2.102}$$

But consistency of k_0 now requires

$$k_0 \leq 0 \;\Rightarrow\; m_2^2 \geq m_\phi^2 + m_1^2 \,, \tag{2.103}$$

which again contradicts the previous condition.

We therefore conclude that the set of on-shell constraints imposed by the five delta functions cannot be satisfied simultaneously. Consequently, the purely real (fully cut) contributions in $\mathrm{Re}(I_1)$ and I_2 do not contribute to the inflaton lesser self-energy $\Pi^<_{\phi,0}(\omega)$.

Therefore, for the diagonal cut I_2, only the contribution involving the principal-value parts survives, and we are left with

$$I_2 = -\Delta_1^<(k)\,\Delta_\phi^<(q)\,\Delta_1^<(p-k-q)\,\Delta_2^{\mathcal{P}}(p-k)\,\Delta_2^{\mathcal{P}}(q+k)\,. \tag{2.104}$$

Similarly, for the off-diagonal contribution to I_1, we obtain

$$\begin{aligned}\mathrm{Re}(I_1) = \Delta_1^<(p-k-q)\,\Delta_2^<(q+k)\Big\{&\Delta_1^\delta(k)\,\Delta_2^{\mathcal{P}}(p-k)\,\Delta_\phi^{\mathcal{P}}(q)\\ &+\Delta_1^{\mathcal{P}}(k)\,\Delta_2^\delta(p-k)\,\Delta_\phi^{\mathcal{P}}(q)\\ &+\Delta_1^{\mathcal{P}}(k)\,\Delta_2^{\mathcal{P}}(p-k)\,\Delta_\phi^\delta(q)\Big\}\,.\end{aligned} \tag{2.105}$$

In the following sections, we analyze these two cut structures in detail and provide their explicit evaluation.

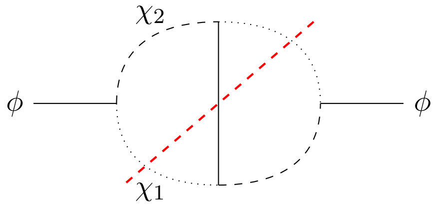

Figure 2.9: Diagonal cut of the two-loop self-energy diagram contributing to $\Pi^<(\omega)$. The three propagators intersected by the cut are placed on shell, while the remaining propagators appear as principal-value terms.

Diagonal Cut

We begin by evaluating the contribution from the diagonal cut I_2, shown in Fig. (2.9). This cut corresponds to the case where the three propagators on the right-hand side of the diagram are placed on shell, while the remaining propagators appear as principal-value contributions.

The corresponding contribution to the lesser self-energy can be written as

$$\mathrm{Im}\Pi_2^R(\omega) = \frac{g^4}{2} f_B^{-1}(\omega) \int \frac{d^4k}{(2\pi)^4} \frac{d^4q}{(2\pi)^4} \times \\ \times \Delta_2^{\mathcal{P}}(p-k)\Delta_2^{\mathcal{P}}(q+k)\Delta_1^<(k)\Delta_\phi^<(q)\Delta_1^<(p-k-q), \tag{2.106}$$

where the superscript $\mathcal{P}$ denotes the principal-value part of the propagator, while the lesser propagators describe the on-shell thermal excitations of the fields circulating in the cut.

After inserting the explicit forms of the thermal propagators and rewriting the resulting delta functions in terms of the corresponding on-shell energies, the integrand can be written in a compact form. In particular, we obtain

$$I_2^{\mathcal{P}} = -\frac{\pi^3}{\omega_1 \tilde{\omega} \tilde{\omega}_1} \sum_{\{s\}} s\, s_1\, s_2\, \mathcal{F}(s, s_1, s_2)\, \mathcal{K}(s, s_1, s_2)\, \mathcal{D}^{\mathcal{P}}(s, s_1), \tag{2.107}$$

where the different factors encode the statistical distributions, the kinematic constraints, and the remaining principal-value propagators.

The statistical factors are collected in

$$\mathcal{F}(s, s_1, s_2) = f_B(s\tilde{\omega})\, f_B(s_1\omega_1)\, f_B(s_2\tilde{\omega}_1), \tag{2.108}$$

which arise from the thermal occupation numbers of the internal particles. The product of delta functions enforcing energy conservation along the cut is

$$\mathcal{K}(s, s_1, s_2) = \delta(q_0 - s\tilde{\omega})\,\delta(k_0 - s_1\omega_1)\,\delta(\omega - s_1\omega_1 - s\tilde{\omega} - s_2\tilde{\omega}_1)\,, \tag{2.109}$$

while the remaining propagators contribute

$$\mathcal{D}^{\mathcal{P}}(s, s_1) = \Delta_2^{\mathcal{P}}(s_1\omega_1)\,\Delta_2^{\mathcal{P}}(s\tilde{\omega} + s_1\omega_1). \tag{2.110}$$

For compactness, we introduced the shorthand notation

$$\sum_{\{s\}} \equiv \prod_{i=0}^{2} \sum_{s_i=\pm 1}\,, \tag{2.111}$$

with $s_0 \equiv s$. The sign variables arise from the decomposition of the spectral functions into positive- and negative-energy contributions.

The principal-value propagators appearing above take the form

$$\Delta_2^{\mathcal{P}}(s_1\omega_1) = \frac{i}{2\omega}\mathcal{P}\left(\frac{1}{\bar{\omega}_1 - s_1\omega_1}\right), \tag{2.112}$$

$$\Delta_2^{\mathcal{P}}(s\tilde{\omega} + s_1\omega_1) = \frac{i}{2\omega}\mathcal{P}\left(\frac{1}{(s\tilde{\omega} + s_1\omega_1) - \bar{\omega}_2}\right), \tag{2.113}$$

where $\bar{\omega}_{1,2}$ denote the tree-level energies defined in Eq. (2.30).

The kinematic constraints of the self-energy in Eq. (2.106) are encoded in the delta functions appearing in Eq. (2.109). However, not all possible combinations of the sign variables s_i lead to a physical contribution. Since all energies are positive definite, certain combinations lead to delta functions with strictly positive arguments and therefore vanish identically.

For example, choosing $s = s_1 = s_2 = -1$ gives

$$\delta(\omega + \omega_1 + \tilde{\omega} + \tilde{\omega}_1)\,, \tag{2.114}$$

which would correspond to processes in which four on-shell particles are simultaneously created from the vacuum, schematically $0 \to 4$, since all on-shell energies are strictly positive, such processes violate energy conservation and therefore cannot occur. Moreover, after a detailed analysis of the kinematic constraints (see Appendix B for details), we find that the following terms (which would correspond a $1 \to 3$ particle creation process) also do not contribute to the diagonal cut:

$$\delta(\omega - \omega_1 - \tilde{\omega} - \tilde{\omega}_1), \quad \delta(\omega + \omega_1 - \tilde{\omega} + \tilde{\omega}_1), \quad \delta(\omega + \omega_1 + \tilde{\omega} - \tilde{\omega}_1). \tag{2.115}$$

Using these results together with the delta functions in Eq. (2.109), the integrations over the energy variables k_0 and q_0 can be performed straightforwardly. The self-energy then reduces to an integral over the spatial momenta only,

$$\mathrm{Im}\Pi_2^R(\omega) = -\frac{g^4}{2} f_B^{-1}(\omega) \int \frac{d^3\mathbf{k}}{(2\pi)^3} \frac{d^3\mathbf{q}}{(2\pi)^3} \frac{\pi}{4\,\omega_1 \tilde{\omega} \tilde{\omega}_1} \sum_{i=1}^{3} \mathcal{C}_i(\mathbf{k}, \mathbf{q}) \tag{2.116}$$

where the three kinematically allowed contributions are

$$\mathcal{C}_1 = f_B(\tilde{\omega}) f_B(\omega_1) f_B(-\tilde{\omega}_1) \Delta_2^{\mathcal{P}}(\omega_1) \Delta_2^{\mathcal{P}}(\tilde{\omega} + \omega_1) \delta(\omega - \omega_1 - \tilde{\omega} + \tilde{\omega}_1), \tag{2.117}$$

$$\mathcal{C}_2 = f_B(\tilde{\omega}) f_B(-\omega_1) f_B(\tilde{\omega}_1) \Delta_2^{\mathcal{P}}(-\omega_1) \Delta_2^{\mathcal{P}}(\tilde{\omega} - \omega_1) \delta(\omega + \omega_1 - \tilde{\omega} - \tilde{\omega}_1), \tag{2.118}$$

$$\mathcal{C}_3 = f_B(-\tilde{\omega}) f_B(\omega_1) f_B(\tilde{\omega}_1) \Delta_2^{\mathcal{P}}(\omega_1) \Delta_2^{\mathcal{P}}(\omega_1 - \tilde{\omega}) \delta(\omega - \omega_1 + \tilde{\omega} - \tilde{\omega}_1). \tag{2.119}$$

Each of the contributions $\mathcal{C}_i$ corresponds to a distinct physical process involving interactions between the inflaton and the thermal χ particles in the plasma. In particular, the first two terms describe scattering processes in which an inflaton quantum interacts with one of the χ particles in the medium. These contributions arise from different kinematic channels of the same underlying interaction and correspond to the usual t- and s-channel scattering processes mediated by the intermediate propagators appearing in the principal-value terms.

The third contribution corresponds to processes in which two inflaton quanta annihilate into two χ particles, as well as the inverse process in which two χ quanta combine to produce two inflaton quanta. Such pair creation and annihilation processes are naturally captured by the thermal statistical factors appearing in the integrand.

The physical processes corresponding to the contributions $\mathcal{C}_1$, $\mathcal{C}_2$, and $\mathcal{C}_3$ are illustrated in Fig. 2.10.

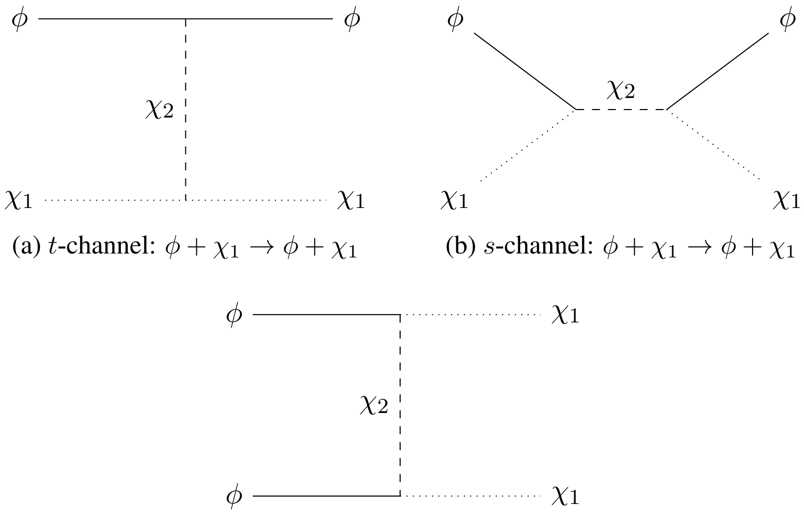

(a) t-channel: $\phi + \chi_1 \to \phi + \chi_1$ (b) s-channel: $\phi + \chi_1 \to \phi + \chi_1$

(c) $\phi + \phi \leftrightarrow \chi_1 + \chi_1$ (mediated by χ_2)

Figure 2.10: Representative $2 \to 2$ processes encoded in the kinematically allowed contributions $\mathcal{C}_i$ of Eq. (2.116). Panels (a) and (b) show χ_2-mediated scattering $\phi + \chi_1 \to \phi + \chi_1$ in the t- and s-channels, respectively, while panel (c) illustrates the χ_2-mediated pair annihilation (and inverse creation) process $\phi + \phi \leftrightarrow \chi_1 + \chi_1$.

Using the delta functions in $\mathcal{C}_1$–$\mathcal{C}_3$, the angular integrations can be carried out explicitly and the original six-dimensional momentum integral in Eq. (2.116) reduces to a two-dimensional integral over the on-shell energies ω_1 and $\tilde{\omega}$,

$$\mathrm{Im}\Pi^R_{\phi,\mathbf{0}}(\omega) = -\frac{g^4}{8(2\pi)^3} f_B^{-1}(\omega) \int d\omega_1\, d\tilde{\omega} \sum_{i=1}^{3} \Theta(\Omega_i)\, \Theta(1 - |x_i|)\, \mathcal{I}_i(\omega_1, \tilde{\omega}), \tag{2.120}$$

where the step functions encode the kinematic support of each channel, and the quantities x_i arise from the angular integration and can be interpreted as the cosine of the relative angle between $\mathbf{k}$ and $\mathbf{q}$. The three channels are defined by

$$\Omega_1 = \omega_1 + \tilde{\omega} - \omega, \quad \mathcal{I}_1 = f_B(\tilde{\omega})\, f_B(\omega_1)\, f_B(-\Omega_1)\, \Delta_2^{\mathcal{P}}(\omega_1)\, \Delta_2^{\mathcal{P}}(\tilde{\omega} + \omega_1), \tag{2.121}$$

$$\Omega_2 = \omega + \omega_1 - \tilde{\omega}, \quad \mathcal{I}_2 = f_B(\tilde{\omega})\, f_B(-\omega_1)\, f_B(\Omega_2)\, \Delta_2^{\mathcal{P}}(-\omega_1)\, \Delta_2^{\mathcal{P}}(\tilde{\omega} - \omega_1), \tag{2.122}$$

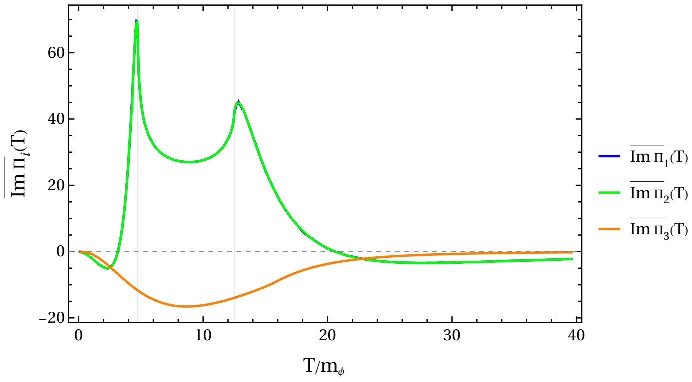

Figure 2.11: Diagonal-cut (scattering) contributions to imaginary part of the retarded self-energy, $\overline{\mathrm{Im}\,\Pi}(T) = -\mathrm{Im}\,\Pi^R(T)/g^4$, as a function of T/m_ϕ. The three curves correspond to the kinematic channels $\mathcal{I}_1$, $\mathcal{I}_2$, and $\mathcal{I}_3$. The parameters are $m_1 = 0.01\,m_\phi$, $m_2 = 0.1\,m_\phi$, $\lambda_1 = 0.1$, and $\lambda_2 = 0.5$, which determine the temperature-dependent masses.

$$\Omega_3 = \omega + \tilde{\omega} - \omega_1, \quad \mathcal{I}_3 = f_B(-\tilde{\omega})\, f_B(\omega_1)\, f_B(\Omega_3)\, \Delta_2^{\mathcal{P}}(\omega_1)\, \Delta_2^{\mathcal{P}}(\omega_1 - \tilde{\omega}). \tag{2.123}$$

The angular integrations further introduce the variables

$$x_1 = \frac{(\omega - \tilde{\omega})(\omega - \omega_1)}{|\mathbf{q}|\,|\mathbf{k}|}, \tag{2.124}$$

$$x_2 = \frac{(\omega - \tilde{\omega})(\omega + \omega_1)}{|\mathbf{q}|\,|\mathbf{k}|}, \tag{2.125}$$

$$x_3 = \frac{(\omega + \tilde{\omega})(\omega - \omega_1)}{|\mathbf{q}|\,|\mathbf{k}|}, \tag{2.126}$$

which correspond to the cosine of the angle between the loop momenta $\mathbf{k}$ and $\mathbf{q}$. The conditions $\Theta(1 - |x_i|)$ therefore enforce the physical constraint $|x_i| \leq 1$, ensuring that the corresponding kinematic configurations are realizable for real momenta.

The three channels correspond to χ_2-mediated scattering $\phi + \chi_1 \to \phi + \chi_1$ in different kinematic topologies and to χ_2-mediated pair annihilation and creation $\phi + \phi \leftrightarrow \chi_1 + \chi_1$, as illustrated in Fig. 2.10.

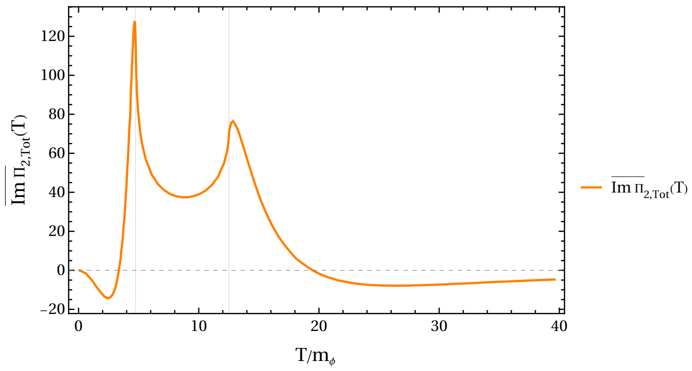

Figure 2.12: Total diagonal-cut contribution to the imaginary part of the retarded self-energy, $\overline{\text{Im}\,\Pi^R_{2,\text{tot}}}(T) = -\text{Im}\,\Pi^R_{2,\text{tot}}(T)/g^4$, as a function of T/m_ϕ, obtained by summing the contributions from the channels $\mathcal{I}_1$, $\mathcal{I}_2$, and $\mathcal{I}_3$. The parameters are $m_1 = 0.01\,m_\phi$, $m_2 = 0.1\,m_\phi$, $\lambda_1 = 0.1$, and $\lambda_2 = 0.5$.

Numerical results for the diagonal cut

The temperature dependence of the diagonal-cut contribution to the imaginary part of the retarded self-energy exhibits a nontrivial structure that can be understood in terms of the kinematic thresholds of the underlying processes.

In analogy with the discussion of decay and inverse-decay channels, one can identify two characteristic temperatures $T_{\text{th},1}$ and $T_{\text{th},2}$ as the solutions of

$$m_\phi = M_1(T_{\text{th},1}) + M_2(T_{\text{th},1}), \qquad m_\phi = \left|M_2(T_{\text{th},2}) - M_1(T_{\text{th},2})\right|, \tag{2.127}$$

or equivalently by the condition that the common on-shell momentum vanishes,

$$\bar{\omega}_1^2(T_{\text{th},i}) - M_1^2(T_{\text{th},i}) = 0, \qquad i = 1, 2. \tag{2.128}$$

The temperature $T_{\text{th},1}$ marks the closure of the decay channel $\phi \to \chi_1 + \chi_2$, while $T_{\text{th},2}$ corresponds to the opening of inverse-decay processes such as $\chi_1 \to \phi + \chi_2$ and $\chi_2 \to \phi + \chi_1$. Between these two temperatures, all $1 \leftrightarrow 2$ processes are kinematically forbidden due to thermal mass effects.

We now consider the numerical evaluation of the diagonal-cut contribution,

$$\overline{\text{Im}\,\Pi_2^R}(T) \equiv -\frac{\text{Im}\,\Pi_2^R(T)}{g^4}, \tag{2.129}$$

as a function of T/m_ϕ.

Figure 2.11 shows the individual contributions from the three channels $\mathcal{I}_1$, $\mathcal{I}_2$, and $\mathcal{I}_3$, which correspond to the processes depicted in Fig. 2.10: the t-channel scattering $\phi + \chi_1 \to \phi + \chi_1$ (a), the s-channel scattering $\phi + \chi_1 \to \phi + \chi_1$ (b), and the annihilation channel $\phi + \phi \leftrightarrow \chi_1 + \chi_1$ mediated by χ_2 (c), respectively. A noteworthy feature of Fig. 2.11 is that the channels $\mathcal{I}_1$ and $\mathcal{I}_2$ yield nearly identical positive contributions throughout the entire temperature range, while the annihilation channel $\mathcal{I}_3$ contributes with the opposite sign over most of the parameter space. The threshold structures near $T_{\mathrm{th},1}$ and $T_{\mathrm{th},2}$ are clearly visible in all channels and arise from the sensitivity of the phase-space integrals to the kinematic boundaries defined by $\Omega_i = 0$ and $|x_i| = 1$.

The total diagonal-cut contribution,

$$\overline{\operatorname{Im}\Pi^R_{2,\mathrm{tot}}}(T) = \sum_{i=1}^{3} \overline{\operatorname{Im}\Pi^R_{2,i}}(T), \tag{2.130}$$

shown in Fig. 2.12, results from a substantial cancellation between the positive scattering channels $\mathcal{I}_1$ and $\mathcal{I}_2$ and the negative annihilation contribution $\mathcal{I}_3$. This cancellation is a manifestation of the quantum structure of the self-energy and highlights an important difference between the thermal self-energy approach and a Boltzmann description based on individual reaction rates. While each channel can be associated with a well-defined scattering or annihilation process, their sum is not simply a sum of positive-definite transition probabilities. Consequently, the full diagonal-cut contribution cannot, in general, be interpreted as a classical reaction rate constructed from squared matrix elements, but rather reflects the coherent quantum-mechanical combination of several processes.

In the interval $T_{\mathrm{th},1} < T < T_{\mathrm{th},2}$, where all tree-level $1 \leftrightarrow 2$ processes are kinematically forbidden, the diagonal-cut contribution remains nonvanishing and provides the dominant contribution to $\operatorname{Im}\Pi^R$. This reflects the different kinematic nature of the underlying processes, which involve integrations over off-shell intermediate states and are not constrained by the same threshold conditions as the decay and inverse-decay channels.

The temperature dependence in this regime is governed by the interplay between the kinematic boundaries and the principal-value structure of the propagators, leading to a nontrivial integrand even in the absence of open tree-level channels. Outside this interval, the diagonal-cut contribution persists but does not qualitatively alter the dynamics, and its most significant role is to provide a

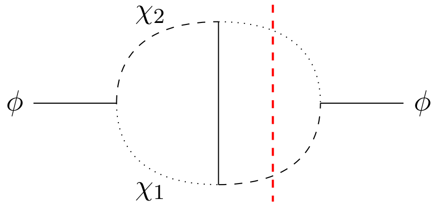

Figure 2.13: Off-diagonal cut of the two-loop self-energy diagram contributing to $\Pi^<(\omega)$. In this case, the two propagators on the right-hand side of the loop are placed on shell, while the remaining internal propagators contribute through their principal-value parts.

continuous, nonvanishing contribution across the kinematic gap separating the two tree-level regions.

Off-Diagonal Cut

We now evaluate the contribution from the off-diagonal cut I_1, shown in Fig. (2.13). This cut corresponds to the configuration in which the two $\chi_{1,2}$ propagators on the right-hand side of the diagram are placed on shell. As a result, the diagram effectively factorizes into a decay-like contribution together with a loop containing an opened leg, while the remaining two propagators in the loop appear as principal-value contributions.

Using Eq. (2.105), the corresponding contribution to the lesser self-energy can be written as

$$\begin{aligned}\mathrm{Im}\Pi_1^R(\omega) = -\frac{g^4}{2} f_B^{-1}(\omega) \int \frac{d^4k}{(2\pi)^4} \frac{d^4q}{(2\pi)^4}\, \Delta_1^<(p-k-q)\, \Delta_2^<(q+k) \\ \times \Big\{ \Delta_1^\delta(k)\, \Delta_2^\mathcal{P}(p-k)\, \Delta_\phi^\mathcal{P}(q) + \Delta_1^\mathcal{P}(k)\, \Delta_2^\delta(p-k)\, \Delta_\phi^\mathcal{P}(q) \\ + \Delta_1^\mathcal{P}(k)\, \Delta_2^\mathcal{P}(p-k)\, \Delta_\phi^\delta(q) \Big\}. \end{aligned} \tag{2.131}$$

Here the superscript $\mathcal{P}$ denotes the principal-value part of the propagator, while the lesser propagators describe the on-shell thermal excitations of the fields circulating in the cut.

After inserting the explicit expressions for the thermal propagators and rewriting the resulting delta functions in terms of the corresponding on-shell energies, the integrand can again be expressed in a compact form. In particular,

we obtain

$$I_1 = \frac{(2\pi)^3}{4\omega} \frac{\delta(x - \chi_2(\tilde{\omega}))}{\sqrt{(\tilde{\omega}^2 - \omega^2)(\omega_1^2 - m_1^2)}} \mathcal{S}(\omega, \bar{\omega}_1, \bar{\omega}_2)\, f_B(\bar{\omega}_1)\, f_B(\bar{\omega}_2)$$
$$\times \sum_{i=1}^{3} \frac{1 + 2f_B(E_i)}{2E_i} \sum_{s=\pm 1} \mathcal{K}_i(s)\, \mathcal{D}_i^{\mathcal{P}}(s), \tag{2.132}$$

where

$$\mathcal{S}(\omega, \bar{\omega}_1, \bar{\omega}_2) \equiv \theta(\bar{\omega}_2)\Big[2\theta(\bar{\omega}_1) - 1\Big] - \theta(\bar{\omega}_1)\theta(-\bar{\omega}_2), \tag{2.133}$$

collects the step functions that determine the kinematic support of the off-diagonal cut. The index $i = 1, 2, 3$ labels the three possible choices for the internal line that is placed on shell, with corresponding energies

$$E_1 = \omega_1, \qquad E_2 = \omega_2, \qquad E_3 = \tilde{\omega}. \tag{2.134}$$

The function

$$\chi_2(\tilde{\omega}) = \frac{\bar{\omega}_2^2 - \omega_2^2 - \tilde{\omega}^2 + \omega^2}{2\sqrt{(\tilde{\omega}^2 - \omega^2)(\omega_2^2 - m_2^2)}} \tag{2.135}$$

arises from rewriting one of the delta functions that enforces energy conservation in terms of the cosine of the angle between the loop momenta. In this way, the corresponding kinematic constraint can be expressed as $\delta(x - \chi_2(\tilde{\omega}))$, where $x = \cos\theta$ denotes the relative angle between the loop momenta $\mathbf{k}$ and $\mathbf{q}$.

The functions $\mathcal{K}_i(s)$ collect the products of delta functions that enforce the on-shell energy constraints in each channel. Explicitly, they are given by

$$\mathcal{K}_1(s) = \delta(k_0 - s\omega_1)\, \delta(q_0 + s\omega_1 - \bar{\omega}_2), \tag{2.136}$$

$$\mathcal{K}_2(s) = \delta(\omega - s\omega_2 - k_0)\, \delta(q_0 + \bar{\omega}_1 - s\omega_2), \tag{2.137}$$

$$\mathcal{K}_3(s) = \delta(q_0 - s\tilde{\omega})\, \delta(k_0 + s\tilde{\omega} - \bar{\omega}_2). \tag{2.138}$$

Similarly, the factors $\mathcal{D}_i^{\mathcal{P}}(s)$ contain the remaining principal-value propagators associated with each channel,

$$\mathcal{D}_1^{\mathcal{P}}(s) = \Delta_{\phi,\mathbf{q}}^{\mathcal{P}}(\bar{\omega}_2 - s\omega_1)\, \Delta_{2,\mathbf{p}_2}^{\mathcal{P}}(\omega - s\omega_1), \tag{2.139}$$

$$\mathcal{D}_2^{\mathcal{P}}(s) = \Delta_{\phi,\mathbf{q}}^{\mathcal{P}}(\bar{\omega}_1 - s\omega_2)\, \Delta_{1,\mathbf{k}}^{\mathcal{P}}(\omega - s\omega_2), \tag{2.140}$$

$$\mathcal{D}_3^{\mathcal{P}}(s) = \Delta_{1,\mathbf{k}}^{\mathcal{P}}(\bar{\omega}_2 - s\tilde{\omega})\, \Delta_{2,\mathbf{p}_2}^{\mathcal{P}}(\bar{\omega}_1 + s\tilde{\omega}). \tag{2.141}$$

In this representation, the off-diagonal contribution is naturally organized according to which internal line is placed on shell. The sum over $s = \pm 1$ accounts for the positive- and negative-energy branches of the corresponding on-shell condition, while the channel-dependent factors $\mathcal{K}_i(s)$ and $\mathcal{D}_i^{\mathcal{P}}(s)$ separate the kinematic constraints from the remaining principal-value structure. This compact form closely parallels the decomposition obtained for the diagonal cut and will prove convenient for performing the remaining integrations.

Using the delta functions appearing in the off-diagonal contribution, the angular integrations can again be performed explicitly, and the original six-dimensional momentum integral reduces to a sum of two-dimensional integrals over the on-shell energies. The result can be written in the compact form

$$\mathrm{Im}\Pi_1^R(\omega) = -\frac{g^4}{4(2\pi)^3\omega} f_B^{-1}(\omega)\, f_B(\bar{\omega}_1)\, f_B(\bar{\omega}_2)\, \mathcal{S}(\omega, \bar{\omega}_1, \bar{\omega}_2) \mathcal{J}(\omega), \quad (2.142)$$

where we defined the integral $\mathcal{J}(\omega)$ as

$$\mathcal{J}(\omega) \equiv \sum_{i=1}^{3} \mathcal{J}_i = \sum_{i=1}^{3} \int dE_i\, d\tilde{\omega}\; \mathcal{I}_i(E_i, \tilde{\omega}), \quad (2.143)$$

where the channel-dependent integrands are defined by

$$\mathcal{I}_1(\omega_1, \tilde{\omega}) = \Theta(1 - |\chi_2|)\, \tilde{\omega}\, \big(1 + 2f_B(\omega_1)\big) \sum_{s=\pm 1} \mathcal{D}_1^{\mathcal{P}}(s), \quad (2.144)$$

$$\mathcal{I}_2(\omega_2, \tilde{\omega}) = \Theta(1 - |\chi_2|)\, \tilde{\omega}\, \big(1 + 2f_B(\omega_2)\big) \sum_{s=\pm 1} \mathcal{D}_2^{\mathcal{P}}(s), \quad (2.145)$$

$$\mathcal{I}_3(\omega_2, \tilde{\omega}) = \Theta(1 - |\chi_2|)\, \omega_2\, \big(1 + 2f_B(\tilde{\omega})\big) \sum_{s=\pm 1} \mathcal{D}_3^{\mathcal{P}}(s). \quad (2.146)$$

The two–dimensional representation in Eq. (2.143) already provides a convenient starting point for numerical evaluation. However, the structure of the integrand allows one of the remaining integrations to be performed analytically. In particular, the angular constraint encoded in $\theta(1 - |\chi_2|)$ restricts the kinematic domain in a way that permits an explicit evaluation of the corresponding momentum integral. As a result, the channel contributions $\mathcal{J}_i$ can be reduced further to one–dimensional integrals, which are more suitable for numerical implementation.

Final one-dimensional representation

The two–dimensional representation in Eq. (2.143) can be reduced further by performing one of the integrations analytically. Introducing the momentum parametrization

$$k = \sqrt{\omega_i^2 - m_i^2}, \qquad \omega_i(k) = \sqrt{k^2 + m_i^2}, \qquad i = 1, 2, \tag{2.147}$$

the channel contributions $\mathcal{J}_1$ and $\mathcal{J}_2$ can be expressed as one–dimensional principal-value integrals over the momentum k,

$$\mathcal{J}_i = \frac{1}{2} \sum_{s=\pm 1} \mathcal{P} \int_0^\infty dk \, \frac{k}{\omega_i(k)} \frac{1 + 2 f_B(\omega_i(k))}{\bar{\omega}_i - s\,\omega_i(k)} \log \left| \frac{a_{i,s}(k) + 2k\lambda_i}{a_{i,s}(k) - 2k\lambda_i} \right|, \tag{2.148}$$

where $i = 1, 2$, and we defined

$$\lambda_i = \sqrt{\bar{\omega}_i^2 - m_i^2}, \tag{2.149}$$

$$a_{i,s}(k) = D_{i,s}(k) - k^2 - \lambda_i^2, \tag{2.150}$$

$$D_{i,s}(k) = \left(m - \bar{\omega}_i - s\,\omega_i(k)\right)^2 - m^2. \tag{2.151}$$

This representation is valid for $\bar{\omega}_i^2 > m_i^2$. If this condition is not satisfied, the constraint $\theta(1 - |\chi_2|)$ has no support and the corresponding contribution vanishes, implying $\Pi_i = 0$.

The remaining channel contribution $\mathcal{J}_3$ in Eq. (2.143) can be reduced in a similar way. Performing the k-integration analytically yields

$$\mathcal{J}_3 = \sum_{s=\pm 1} \int_0^\infty dq \, \frac{q}{\tilde{\omega}(q)} \frac{1 + 2 f_B(\tilde{\omega}(q))}{2\big(B_{1,s}(q) - B_{2,s}(q)\big)} \ln \left| \frac{(B_{1,s} - k_+^2)(B_{2,s} - k_-^2)}{(B_{1,s} - k_-^2)(B_{2,s} - k_+^2)} \right|. \tag{2.152}$$

Here we introduced

$$B_{1,s}(q) \equiv (\bar{\omega}_2 - s\tilde{\omega})^2 - m_1^2, \tag{2.153}$$

$$B_{2,s}(q) \equiv (\bar{\omega}_1 + s\tilde{\omega})^2 - m_2^2. \tag{2.154}$$

For $\Delta > 0$, defined as

$$\Delta \equiv \bar{\omega}_1^2 - m_1^2, \tag{2.155}$$

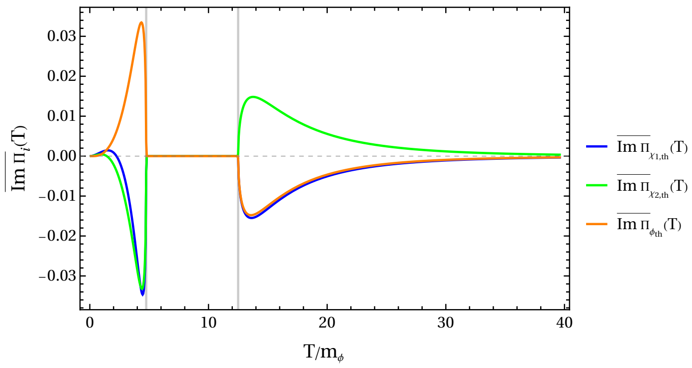

Figure 2.14: Off-diagonal contributions to the imaginary part of the retarded self-energy, $\overline{\mathrm{Im}\,\Pi_1^R}(T) = -\mathrm{Im}\,\Pi_1^R(T)/g^4$, as a function of T/m_ϕ. The three components correspond to the different choices of the propagator entering through its thermal on-shell part in the vertical-cut configuration. The parameters are $m_1 = 0.01\,m_\phi$, $m_2 = 0.1\,m_\phi$, $\lambda_1 = 0.1$, and $\lambda_2 = 0.5$.

the angular constraint $\theta(1-|\chi_2|)$ restricts the allowed values of the momentum k for fixed q to the interval

$$k \in [\,k_-(q),\, k_+(q)\,], \tag{2.156}$$

where

$$k_+(q) = q + \sqrt{\Delta}, \tag{2.157}$$
$$k_-(q) = \max\{0, |q - \sqrt{\Delta}|\}. \tag{2.158}$$

Equations above therefore provide a fully reduced one–dimensional representation of the off–diagonal contribution, which is particularly convenient for the numerical evaluation of the self-energy.

Numerical results for the off-diagonal cut

Before discussing the temperature dependence, it is important to clarify that in Figs. 2.14 and 2.15 we only display the thermal contribution to the off-diagonal self-energy results 2.148, and 2.152. More precisely, in the thermal factors appearing in the principal-value integrals we retain only the Bose-enhanced part proportional to $2f_B$, while the vacuum contribution associated with the constant term is omitted. The latter corresponds to the zero-temperature part of the loop correction and should be treated together with the appropriate renormal-

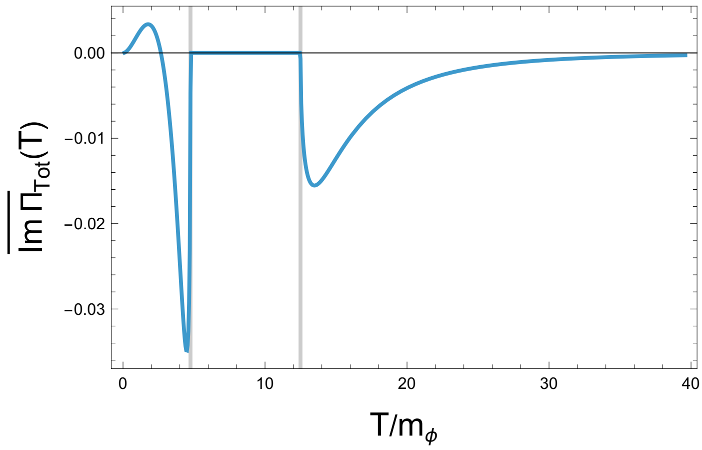

Figure 2.15: Total off-diagonal contribution to the imaginary part of the retarded self-energy, $\overline{\mathrm{Im}\,\Pi^R_{1,\mathrm{tot}}}(T) = -\mathrm{Im}\,\Pi^R_{1,\mathrm{tot}}(T)/g^4$, as a function of T/m_ϕ, obtained by summing the three components of the vertical cut. The parameters are $m_1 = 0.01\,m_\phi$, $m_2 = 0.1\,m_\phi$, $\lambda_1 = 0.1$, and $\lambda_2 = 0.5$.

ization procedure. Since our interest here is the finite-temperature modification of the self-energy, we focus exclusively on the thermal contribution.

We now turn to the physical interpretation of the numerical result for the off-diagonal contribution. As shown in Fig. 2.14, the temperature dependence exhibits a localized structure characterized by two distinct temperature scales.

The temperature dependence closely follows the same kinematic structure encountered in the tree-level analysis. At low temperatures, the condition($m_\phi > M_1(T)+M_2(T)$) is satisfied, so that the decay process ($\phi \to \chi_1+\chi_2$) remains kinematically allowed. Consequently, the off-diagonal contribution is already nonvanishing in this regime.

As the temperature increases, the thermal masses grow and eventually reach the threshold

$$T_{\mathrm{th},1}: \qquad m_\phi = M_1(T_{\mathrm{th},1}) + M_2(T_{\mathrm{th},1}), \tag{2.159}$$

at which the decay channel closes. Between $T_{\mathrm{th},1}$ and $T_{\mathrm{th},2}$, the kinematic constraints encoded in

$$\mathcal{S}(\omega, \bar{\omega}_1, \bar{\omega}_2) \tag{2.160}$$

together with $\Theta(1 - |\chi_2|)$ admit no solutions. The off-diagonal contribution therefore vanishes throughout this intermediate forbidden region, reproducing the same kinematic gap that appears in the tree-level decay and inverse-decay analysis.

As the temperature increases, the result rises and reaches a pronounced maximum near

$$T_{\rm th,2}: \qquad m_\phi = \big|M_2(T_{\rm th,2}) - M_1(T_{\rm th,2})\big|, \tag{2.161}$$

which marks the reopening of the available phase space through inverse-decay processes such as $\chi_1 \to \phi + \chi_2$ and $\chi_2 \to \phi + \chi_1$. In the vicinity of this threshold the overlap between the thermal distribution functions and the allowed phase-space region is maximal, producing the pronounced peak visible in Fig. 2.14.

The off-diagonal cut can be understood as an interference between the tree-level $1 \leftrightarrow 2$ processes and the corresponding one-loop correction. More precisely, the vertical cut selects configurations in which one internal propagator contributes through its thermal on-shell part, while the remaining propagators appear as principal-value terms. This structure is manifest in Eq. (2.131), where the different contributions correspond to the three possible choices of the propagator taken on shell.

A clear hierarchy is observed among these terms. The contribution associated with the thermal χ_2 propagator dominates over the full temperature range, while the χ_1 contribution is subleading. The term associated with the thermal ϕ propagator is smallest and can change sign, reflecting cancellations induced by the principal-value structure of the remaining propagators.

For $T > T_{\rm th,2}$, the off-diagonal contribution decreases smoothly. This behaviour is driven primarily by the thermal factors

$$f_B(\bar{\omega}_1)\, f_B(\bar{\omega}_2), \tag{2.162}$$

which suppress the result as the effective masses and on-shell energies grow with temperature, together with a reduced efficiency of the phase-space overlap away from the threshold region.

The total off-diagonal contribution,

$$\overline{\operatorname{Im}\Pi^R_{1,\rm tot}}(T) = \sum_{i=1}^{3} \overline{\operatorname{Im}\Pi^R_{1,i}}(T), \tag{2.163}$$

is shown in Fig. 2.15. It exhibits two kinematically allowed regions separated by the forbidden interval $T_{\rm th,1} < T < T_{\rm th,2}$. The low-temperature branch corresponds to the ordinary decay regime, while the high-temperature branch is associated with inverse decays and contains a pronounced peak near $T_{\mathrm{th},2}$.

In the summed result, the cancellations present in the individual contributions are largely reduced, yielding a positive and smooth temperature dependence. In particular, the sign-changing behaviour of the subleading ϕ contribution is suppressed once all channels are combined.

Overall, the off-diagonal contribution follows the same thermal kinematic structure as the tree-level process, consisting of a low-temperature decay regime, an intermediate forbidden region, and a high-temperature inverse-decay regime. The largest contribution arises near $T_{\mathrm{th},2}$, where the inverse-decay phase space first becomes available.

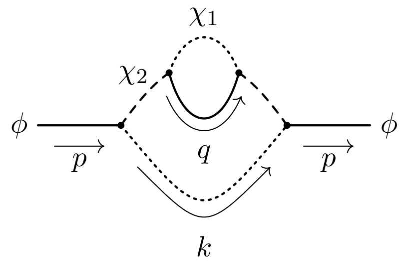

Figure 2.16: Two-loop contribution to the ϕ self-energy in the trilinear model $\mathcal{L}_{\rm int} = g\,\phi\chi_1\chi_2$, with a one-loop self-energy insertion on the χ_2 propagator. The external momentum is denoted by p, while k and q label the loop momenta flowing through the χ_1 and internal ϕ propagators, respectively.

2.7.2 Self-Energy Insertions

We now evaluate the two diagrams corresponding to one-loop self-energy insertions on the χ_i propagators, shown in panels (a) and (b) of Fig. 2.7. These two contributions are related by the exchange $\chi_1 \leftrightarrow \chi_2$, and are therefore identical up to relabeling. It is thus sufficient to compute the diagram with the insertion on the χ_2 line, shown in Fig. 2.16; the second contribution can then be obtained by symmetry.

In analogy with the vertex correction, the lesser component of the inflaton self-energy, $\Pi^< \equiv \Pi^{+-}$, is given by

$$\Pi^<_\phi(p) = -ig^4 \int \frac{d^4k}{(2\pi)^4}\frac{d^4q}{(2\pi)^4} \times \\ \times \sum_{a,b=\pm} ab\,\Delta_1^<(k)\,\Delta_2^{+a}(p-k)\,\Delta_\phi^{ab}(q)\,\Delta_1^{ab}(p-k-q)\,\Delta_2^{b-}(p-k)\,. \tag{2.164}$$

This expression can be reorganized by factorizing the inner loop involving the ϕ and χ_1 propagators. One obtains

$$\Pi^<_\phi(p) = -ig^2 \int \frac{d^4k}{(2\pi)^4}\,\Delta_1^<(k) \sum_{a,b=\pm} ab\,\Delta_2^{+a}(p-k) \\ \times \left[g^2 \int \frac{d^4q}{(2\pi)^4}\Delta_\phi^{ab}(q)\,\Delta_1^{ab}(p-k-q)\right]\Delta_2^{b-}(p-k)\,. \tag{2.165}$$

The quantity in square brackets is precisely the one-loop self-energy of the χ_2 field,

$$i\Pi_2^{ab}(p-k) = g^2 \int \frac{d^4q}{(2\pi)^4} \Delta_\phi^{ab}(q)\, \Delta_1^{ab}(p-k-q)\,. \tag{2.166}$$

Substituting this result back into $\Pi_\phi^<$ yields

$$\Pi_\phi^<(p) = g^2 \sum_{a,b=\pm} ab \int \frac{d^4k}{(2\pi)^4} \Delta_1^<(k)\, \Delta_2^{+a}(p-k)\, \Pi_2^{ab}(p-k)\, \Delta_2^{b-}(p-k)\,. \tag{2.167}$$

It is convenient to express this result in matrix form in Keldysh space. Defining

$$X(p-k) \equiv \tilde{\Delta}_2(p-k)\, \tilde{\Pi}_2(p-k)\, \tilde{\Delta}_2(p-k)\,, \tag{2.168}$$

the corresponding imaginary part, obtained by inserting the one-loop correction on χ_2, can be written as

$$\mathrm{Im}\Pi^{\mathrm{R}}_{\phi,2}(\omega) = -i\frac{g^2}{2} f_{\mathrm{B}}(\omega)^{-1} \int \frac{d^4k}{(2\pi)^4} \Delta_1^<(k)\, X^{+-}(p-k)\,. \tag{2.169}$$

The thermal propagator in the $(+,-)$ basis can be diagonalized as

$$\tilde{\Delta}(p) = U(p) \begin{pmatrix} \Delta_{f_B}(p) & 0 \\ 0 & -\Delta_F^*(p) \end{pmatrix} U(p)\,, \tag{2.170}$$

where $\Delta_{f_B}(p)$ denotes the vacuum Feynman propagator. The matrix $U(p)$ is given by

$$U(p) = \frac{1}{\sqrt{1+f_B(|p_0|)}} \begin{pmatrix} 1+f_B(|p_0|) & \mathrm{sgn}(p_0)\, f_B(|p_0|) \\ 1+\mathrm{sgn}(p_0)\, f_B(|p_0|) & 1+f_B(|p_0|) \end{pmatrix}, \tag{2.171}$$

with $f_B(p_0) = (e^{\beta p_0}-1)^{-1}$ the Bose–Einstein distribution.

Similarly, the self-energy matrix can be diagonalized as

$$\tilde{\Pi}(p) = U^{-1}(p) \begin{pmatrix} \pi(p) & 0 \\ 0 & -\pi^*(p) \end{pmatrix} U^{-1}(p)\,. \tag{2.172}$$

The scalar function $\pi(p)$ is related to the Keldysh components via

$$\mathrm{Re}\,\pi(p) = \mathrm{Re}\,\tilde{\Pi}^{++}(p)\,, \tag{2.173}$$

$$\mathrm{Im}\,\pi(p) = \frac{i\,\tilde{\Pi}^{-+}(p)}{2\left[\theta(p_0) + f_B(|p_0|)\right]} = \frac{i\,\tilde{\Pi}^{+-}(p)}{2\left[\theta(-p_0) + f_B(|p_0|)\right]}\,. \tag{2.174}$$

We now compute

$$X^{+-}(p-k) = \left(\tilde{\Delta}_2\,\tilde{\Pi}_2\,\tilde{\Delta}_2\right)^{+-}(p-k)\,. \tag{2.175}$$

Using the diagonal representation, one finds

$$X^{+-} = (UMU)^{+-} = -U^{++}U^{+-}\left[(\Delta_F^*)^2\pi^* + \Delta_F^2\pi\right]\,. \tag{2.176}$$

Using the definition of the Feynman propagator together with Eqs. (2.173) and (2.174), we can rewrite this expression as

$$\begin{aligned} X^{+-}(p-k) &= \mathcal{P}\left(\frac{1}{\left((p-k)^2 - m_2^2\right)^2}\right)\tilde{\Pi}_2^{<}(p-k) \\ &\quad + 2i\pi\delta'\left((p-k)^2 - m_2^2\right)\mathrm{sgn}(p_0-k_0)\,f_B(|p_0-k_0|)\,\mathrm{Re}\,\tilde{\Pi}_2^{++}(p-k)\,. \end{aligned} \tag{2.177}$$

Substituting this result into Eq. (2.169), we see that the self-energy naturally splits into two contributions, arising respectively from the principal-value term and the derivative of the delta function. We denote these contributions by $\mathrm{Im}\Pi_{\mathrm{L}}$ and $\mathrm{Im}\Pi_{\mathrm{Re}}$, respectively.

We begin with the contribution $\mathrm{Im}\Pi_{\mathrm{L}}$. After straightforward manipulations, we obtain

$$\begin{aligned} \mathrm{Im}\Pi_{\mathrm{L}} &= \frac{-ig^2}{8m_\phi(2\pi)^3} f_{\mathrm{B}}(m_\phi)^{-1}\int_{m_1}^{\infty} d\omega_1\sqrt{\omega_1^2 - m_1^2} \\ &\quad \times \sum_{s=\pm}\left[s\,f_B(s\omega_1)\,\tilde{\Pi}_{2,-\mathbf{k}}^{<}(m_\phi - s\omega_1)\,\mathcal{P}\left(\frac{1}{(s\omega_1 - \bar{\omega}_1)^2}\right)\right]. \end{aligned} \tag{2.178}$$

Similarly, the contribution proportional to $\mathrm{Re}\,\Pi_2$ reads

$$\mathrm{Im}\Pi_{\mathrm{Re}} = \frac{-g^2}{8m_\phi^2(2\pi)^2} f_{\mathrm{B}}(m_\phi)^{-1}\left\{\mathcal{A}(\bar{\omega}_1) - \mathcal{A}(-\bar{\omega}_1)\right\}, \tag{2.179}$$

where

$$\mathcal{A}(\bar{\omega}_1) = \theta(\bar{\omega}_1 - m_1)\sqrt{\bar{\omega}_1^2 - m_1^2}\,\mathrm{sgn}(m_\phi - \bar{\omega}_1)\, f_B(\bar{\omega}_1) f_B(|m_\phi - \bar{\omega}_1|) \\ \times \left\{ \left[\frac{\bar{\omega}_1}{\bar{\omega}_1^2 - m_1^2} - \frac{1}{T}\Big(f_B(m_\phi - \bar{\omega}_1) - f_B(\bar{\omega}_1) \Big) \right] \mathrm{Re}\Pi_{2,-\mathbf{k}}(m_\phi - \bar{\omega}_1) \right. \\ \left. + \frac{d}{d\omega_1} \mathrm{Re}\Pi_{2,-\mathbf{k}}(m_\phi - \omega_1) \Big|_{\omega_1 = \bar{\omega}_1} \right\}. \tag{2.180}$$

The real part of the self-energy can be expressed in terms of its imaginary part via the dispersion relation

$$\mathrm{Re}\Pi_{\boldsymbol{k}}(k_0) = \mathcal{P}\int \frac{d\omega}{\pi} \frac{\mathrm{Im}\,\Pi_{\boldsymbol{k}}(\omega)}{\omega - k_0}\,. \tag{2.181}$$

To further evaluate Eqs. (2.178) and (2.179), we make use of the known expression for the one-loop self-energy with general external momentum, as computed in [57],

$$\mathrm{Im}\,\Pi^R_{i,\boldsymbol{k}}(k_0) = \frac{-g^2}{16\pi|\mathbf{k}|} \Bigg\{ -\theta(-k^2)\, k_0 \\ + \Bigg[\Big(\theta\big(k^2 - (m_\phi + m_i)^2\big) - \theta\big(-k^2 + (m_\phi - m_i)^2\big) \Big) \\ \times T \log\left(\frac{f_B(k_0 - \omega_i^+) f_B(-\omega_i^-)}{f_B(-\omega_i^+) f_B(k_0 - \omega_i^-)} \right) \Bigg] \Bigg\}, \tag{2.182}$$

with

$$\omega_i^\pm = \frac{1}{2k^2} \Bigg[k_0 \left(m_\phi^2 - m_i^2 + k^2 \right) \\ \pm |\mathbf{k}| \sqrt{ m_i^4 + \left(m_\phi^2 - k^2 \right)^2 - 2m_i^2 \left(m_\phi^2 + k^2 \right) } \Bigg]. \tag{2.183}$$

Discussion

The decomposition of X^{+-} into a principal-value contribution and a term proportional to the derivative of the on-shell delta function admits a simple diagrammatic interpretation, illustrated in Fig. 2.17. The two contributions cor-

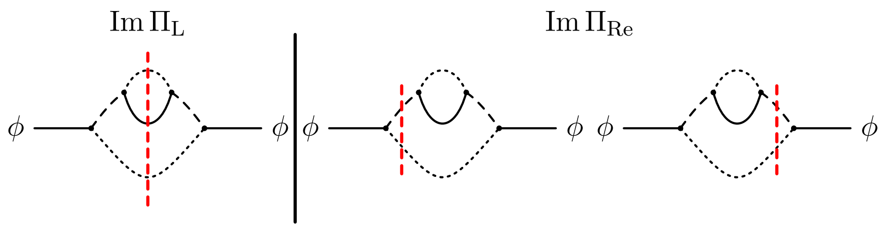

Figure 2.17: Diagrammatic interpretation of the two contributions to the imaginary part of the two-loop self-energy. The contribution $\mathrm{Im}\,\Pi_{\mathrm{L}}$ corresponds to cuts passing through the three propagators in the self-energy insertion. The contribution $\mathrm{Im}\,\Pi_{\mathrm{Re}}$ corresponds to cutting the two external χ_i lines while leaving the internal one-loop self-energy insertion uncut.

respond to different ways in which the self-energy insertion can participate in the cut diagram.

The contribution $\mathrm{Im}\,\Pi_{\mathrm{L}}$ originates from the term proportional to $\tilde{\Pi}_2^<$. Since $\tilde{\Pi}_2^<$ itself represents the cut one-loop self-energy of the χ_2 field, the corresponding diagrammatic interpretation is obtained by cutting through the three propagators that form the self-energy insertion. This is represented by the vertical cut shown in Fig. 2.17. Physically, this contribution describes processes in which the intermediate states contained in the one-loop self-energy insertion become on shell and therefore contribute directly to the imaginary part of the two-loop self-energy.

In contrast, the contribution $\mathrm{Im}\,\Pi_{\mathrm{Re}}$ is proportional to the real part of the one-loop self-energy and is accompanied by the derivative of the on-shell delta function, $\delta'\big((p-k)^2 - m_2^2\big)$. Diagrammatically, the self-energy insertion itself remains uncut, while the imaginary part is generated by cutting the two external χ_i propagators attached to the insertion. The two equivalent cuts shown in Fig. 2.17 correspond to the two possible placements of the cut through these propagators. Rather than cutting through the self-energy insertion itself, this contribution originates from the dispersive effect of the one-loop correction on the intermediate χ_2 propagator. This is encoded in the derivative of the on-shell delta function appearing in Eq. (2.177).

The two contributions, $\mathrm{Im}\,\Pi_{\mathrm{L}}$ and $\mathrm{Im}\,\Pi_{\mathrm{Re}}$, therefore correspond to distinct physical effects: on-shell processes encoded in the cut self-energy insertion and dispersive corrections arising from the real part of the one-loop self-energy. Together, they provide a complete description of the self-energy-insertion contribution at two-loop order.

2.8 Summary and Outlook

In this chapter, we have developed a self-contained kinematic and field-theoretic framework to describe reheating and particle production in a thermal environment. Working within real-time finite-temperature quantum field theory, we showed that spectral functions and self-energies provide a unified description of quasiparticle propagation, interaction rates, and dissipation.

Using a simple scalar model as a laboratory, we analysed how thermal effects modify inflaton decay and energy transfer to the plasma. At leading order, the imaginary part of the self-energy naturally decomposes into vacuum decay, Bose-enhanced decay, and purely thermal scattering (Landau-damping) contributions. Including thermal masses leads to temperature-dependent kinematic thresholds, which determine the opening and closing of decay and inverse decay channels.

A key result is that a consistent implementation of all kinematically allowed processes qualitatively modifies the high-temperature behavior of the dissipation rate. In particular, we find an exponential suppression at large temperature, which can be traced back to the statistical suppression of hard modes required by inverse decay kinematics. We further showed that going beyond the quasiparticle approximation by including finite-width effects smooths kinematic thresholds and introduces off-shell contributions. In this context, the generalized pole expansion provides an improved description compared to the Breit–Wigner approximation, especially near kinematic boundaries and in regimes where off-shell effects are relevant.

Beyond leading order, higher-order contributions encoded in two-loop self-energies introduce qualitatively new structures that are not captured by a simple quasiparticle decay picture. We analysed both the diagonal and off-diagonal cuts of the vertex correction and showed that they exhibit markedly different thermal behavior. The off-diagonal contribution closely follows the same kinematic pattern as the tree-level decay and inverse-decay processes, consisting of a low-temperature decay regime, an intermediate forbidden region, and a high-temperature inverse-decay regime. Its contribution follows the same kinematic structure as the tree-level $1 \leftrightarrow 2$ processes and remains nonvanishing throughout both the decay and inverse-decay regimes. The magnitude exhibits pronounced threshold features near $T_{\text{th},1}$ and $T_{\text{th},2}$, but extends over the entire kinematically allowed regions.

The diagonal contribution behaves very differently. In contrast to the decay and inverse-decay channels, it remains non-vanishing in the temperature interval where all tree-level $1 \leftrightarrow 2$ processes are kinematically forbidden. As a result, it provides the dominant contribution to the imaginary part of the self-energy in this regime. Moreover, the total diagonal-cut contribution arises from a nontrivial cancellation between scattering and annihilation channels, illustrating that thermal self-energies need not admit a simple interpretation in terms of positive-definite reaction rates. These results highlight the importance of quantum coherence and the analytic structure of multi-loop self-energies for a complete description of dissipation in a thermal medium.

We also analysed self-energy insertion diagrams and showed that their contribution naturally separates into a term associated with cuts through the self-energy insertion itself and a dispersive contribution proportional to the real part of the one-loop self-energy. This decomposition provides a simple diagrammatic interpretation of the corresponding two-loop corrections.

The analysis presented here is intended as a standalone investigation of in-medium kinematics and dissipation in scalar field theories. It highlights the interplay between thermal masses, quantum statistics, and the analytic structure of self-energies in shaping particle production rates in a hot plasma.

As an outlook, several important conceptual and technical questions remain to be addressed. In particular, it is natural to ask to what extent vacuum-based field-theoretic properties persist in a thermal environment. This includes, for instance, the investigation of Kinoshita–Lee–Nauenberg (KLN) cancellations and whether analogous mechanisms operate for inclusive observables in the presence of a thermal bath. Closely related is the issue of infrared (IR) safety of the models considered here, and whether medium effects regulate or modify potential IR sensitivities.

Another open direction concerns the physical interpretation of the different contributions to the self-energy, especially the various cut structures that appear in the real-time formalism. While some cuts can be related to on-shell intermediate states or dispersive corrections associated with lower-order self-energies, the interplay between the different multi-particle channels and the possibility of cancellations among them remains to be clarified. Developing a systematic interpretation of these structures in terms of physical processes in the medium is an important step toward a fully consistent picture.

Finally, the present analysis has been restricted to scalar degrees of freedom. A natural next step is to extend this framework to include fermionic fields, where quantum statistics, chiral structure, and additional interaction channels can lead to qualitatively new effects.

These questions will be addressed in a forthcoming work, where the framework developed in this chapter will be extended and applied to a broader class of theories, providing a more complete understanding of particle production and dissipation in thermal quantum field theory.

Chapter 3

Dark Matter production during and after reheating

We begin by recalling the physical picture underlying perturbative reheating and the associated production of Dark Matter during this stage. After inflation, the inflaton no longer slow-rolls but instead oscillates around the minimum of its potential, gradually transferring its energy into lighter degrees of freedom. At the macroscopic level, this energy loss can be captured by an effective equation of motion for the inflaton field of the form[1]

$$\ddot{\varphi} + (3H + \Gamma_\varphi)\dot{\varphi} + \mathcal{V}'(\varphi) = 0\,. \tag{3.1}$$

Here we use the notation $\dot{f} \equiv df/dt$ and $f' \equiv df/d\varphi$. The Hubble rate is defined as $H \equiv \dot{a}/a$, where a is the scale factor, and $\mathcal{V}(\varphi)$ denotes the effective inflaton potential. The damping (or effective friction) term is parametrized by the inflaton decay rate Γ_φ, which can be related to the imaginary part of the inflaton self-energy.

In the standard picture of cold single-field inflation, the evolution of the Universe proceeds through a sequence of qualitatively different regimes, separated by relatively short transition periods that we neglect in the following: (i) Initially, the energy density is dominated by the inflaton potential, leading to a phase of accelerated expansion with $\ddot{a} > 0$ and $\mathcal{V} \gg \rho_R$, which lasts for $\mathcal{O}(10)$ e-folds, denoted by $N_{\rm inf}$; (ii) as the inflaton exits the slow-roll regime, the expansion becomes decelerated ($\ddot{a} < 0$), while the potential energy still domi-

[1] From a microscopic perspective, the inflaton dynamics is in general non-local in time, involving memory kernels derived from the underlying quantum field theory. The use of a local, Markovian equation of the form (3.1) therefore relies on additional assumptions, such as a separation of time scales and the neglect of memory effects. These conditions are satisfied in the regime relevant for the present analysis; see Appendix C of [81].

nates over radiation, marking the reheating phase lasting for $N_{\rm reh}$ e-folds; (iii) eventually, the radiation energy density overtakes that of the inflaton, $\mathcal{V} < \rho_R$, and the Universe enters the radiation-dominated era, during which $\ddot{a} < 0$.

Reheating is typically assumed to commence when the slow-roll parameters,

$$\epsilon = \frac{M_{\rm pl}^2}{2}\left(\frac{\mathcal{V}'}{\mathcal{V}}\right)^2, \qquad \eta = M_{\rm pl}^2\frac{\mathcal{V}''}{\mathcal{V}}, \tag{3.2}$$

become of order unity[2], and it ends when the decay rate becomes comparable to the Hubble expansion rate, $\Gamma_\varphi \simeq H$.

If the reheating phase is sufficiently prolonged to leave observable imprints in the CMB, the inflaton undergoes many oscillations about the minimum of its potential. In this regime, it is convenient to describe its dynamics in terms of the oscillation-averaged energy density ρ_φ and effective isotropic pressure P_φ,

$$\rho_\varphi \equiv \frac{1}{2}\dot{\varphi}^2 + \mathcal{V}(\varphi), \tag{3.3}$$

$$P_\varphi \equiv \frac{1}{2}\dot{\varphi}^2 - \mathcal{V}(\varphi). \tag{3.4}$$

In this work, we consider the regime where the inflaton dissipates its energy mainly through perturbative decays[3] into relativistic particles. Under this assumption, the dynamics of the system can be described by a set of coupled equations governing the inflaton and radiation energy densities, ρ_φ and ρ_R.

These read

$$\dot{\rho}_\varphi + (3H + \Gamma_\varphi)(\rho_\varphi + P_\varphi) = 0\,, \tag{3.5}$$

$$\dot{\rho}_R + 4H\rho_R = \Gamma_\varphi\left(\rho_\varphi + P_\varphi\right)\,. \tag{3.6}$$

These equations are supplemented by the Friedmann constraint

$$\rho_\varphi + \rho_R = 3H^2 M_{\rm pl}^2\,. \tag{3.7}$$

[2]This criterion holds at leading order in the slow-roll expansion and is sufficient for our purposes; see Appendix B of [82].

[3]We use the term *perturbative* in a broad sense, referring to quantities that can be computed as an expansion in a small parameter, irrespective of whether this expansion takes the form of a simple power series. This includes, in particular, resummed and time-dependent perturbative approaches.

If the interactions in the plasma are sufficiently strong to ensure rapid kinetic equilibration [83–88] instantaneously —that is, on time scales much shorter than all other relevant dynamical scales— the particle distributions can be described by an effective temperature T. In this case, the radiation energy density can be written as

$$\rho_R = \frac{\pi^2}{30} g_\star T^4 \,, \tag{3.8}$$

where $g_\star$ characterises the effective number of relativistic degrees of freedom contributing to the energy density of the thermal bath.

We further assume that the dark matter species X is produced from this thermal bath. Its number density n_X obeys the Boltzmann equation

$$\dot{n}_X + 3Hn_X = \mathcal{C}_X \,, \tag{3.9}$$

where $\mathcal{C}_X$ is the collision term encoding production and depletion processes. For the class of models considered here, it is convenient to express it as [89]

$$\mathcal{C}_X = \int \Gamma_X \left(f_X^{\text{eq}} - f_X \right) \,, \tag{3.10}$$

with Γ_X an effective interaction rate, in general depending on the phase-space distribution f_X. In situations where the dark matter sector comprises only a small number of degrees of freedom compared to the radiation bath, its back-reaction on ρ_R can be safely neglected.

For numerical convenience, it is useful to reformulate the system in terms of dimensionless variables. We introduce

$$x \equiv m_\varphi a \,, \quad \Phi \equiv \frac{\rho_\varphi a^3}{m_\varphi} = \frac{\rho_\varphi x^3}{m_\varphi^4} \,, \quad R \equiv \rho_R a^4 = \frac{\rho_R x^4}{m_\varphi^4} \,, \quad X \equiv n_X a^3 = \frac{n_X x^3}{m_\varphi^3} \,, \tag{3.11}$$

where m_φ denotes the inflaton mass at the minimum of its potential. The normalization is chosen such that $x = 1$ at the onset of reheating.

The inflaton mass is defined by expanding the potential around its minimum,

$$\mathcal{V}(\varphi) = \sum_n \frac{v_n}{n!} \frac{\varphi^n}{\Lambda^{n-4}} = \frac{1}{2} m_\varphi^2 \varphi^2 + \frac{g_\varphi}{3!} \varphi^3 + \frac{\lambda_\varphi}{4!} \varphi^4 + \dots \,, \tag{3.12}$$

with Λ an appropriate effective field theory scale.

In terms of the dimensionless variables, the evolution equations take the form

$$\frac{\mathrm{d}\Phi}{\mathrm{d}x} = -\frac{\Gamma_\varphi}{Hx}\Phi\,, \tag{3.13}$$

$$\frac{\mathrm{d}R}{\mathrm{d}x} = \frac{\Gamma_\varphi}{H}\Phi\,, \tag{3.14}$$

$$\frac{\mathrm{d}X}{\mathrm{d}x} = \frac{\mathcal{C}_X x^2}{H m_\varphi^3}\,. \tag{3.15}$$

The Hubble rate and temperature are determined self-consistently from

$$H = \frac{m_\varphi^2}{\sqrt{3}m_{\mathrm{pl}}}\left(\frac{R}{x^4} + \frac{\Phi}{x^3} + \frac{X}{x^2}\frac{m_X}{m_\varphi}\right)^{1/2}\,, \tag{3.16a}$$

$$T = \frac{m_\varphi}{x}\left(\frac{30R}{\pi^2 g_\star}\right)^{1/4}\,. \tag{3.16b}$$

where $m_{\mathrm{Pl}} \approx 2.43 \cdot 10^{18}$ GeV is the reduced Planck mass.

In Eq. (3.16a), we have assumed that the inflaton condensate redshifts as non-relativistic matter, corresponding to an effective equation-of-state parameter $w = 0$. This approximation is justified when the inflaton potential is approximately quadratic in the vicinity of its minimum.[4]

Furthermore, we fix the effective number of relativistic degrees of freedom to its Standard Model value, $g_\star = 106.75$. Under these assumptions, the system of equations (3.13) and (3.16) forms a closed set, whose solution determines both the expansion history and the thermal evolution of the Universe.

Two quantities of particular interest are the maximal temperature reached during reheating, T_{max}, and the temperature at the onset of radiation domination, T_{re}. The latter is commonly referred to as the *reheating temperature* and is defined as the value of T at the time when the radiation and inflaton energy densities become equal for the last time,

$$\rho_R = \rho_\varphi \quad \text{at} \quad T = T_{\mathrm{re}}\,. \tag{3.17}$$

[4]The validity of this assumption will be ensured by imposing the condition (3.22b) below. More generally, describing the post-inflationary Universe as a combination of components with fixed equations of state $w = 0$ and $w = 1/3$ constitutes an idealisation; see, e.g., [90–93].

This temperature can be related to the duration of reheating through the standard redshifting relation

$$T_{\rm re} = \exp\left[-\frac{3(1+\bar{w}_{\rm reh})}{4}N_{\rm reh}\right]\left(\frac{40\,V_{\rm end}}{\pi^2 g_\star}\right)^{1/4}\,, \tag{3.18}$$

where $\mathcal{V}_{\rm end}$ denotes the inflaton potential evaluated at the end of inflation, $\bar{w}_{\rm reh}$ is the averaged equation-of-state parameter during reheating, and $\rho_{\rm end} \simeq \frac{4}{3}\mathcal{V}_{\rm end}$ accounts for the non-negligible kinetic contribution at that time.

Relating a specific dark matter interaction—potentially testable in collider experiments—to the observed relic abundance requires detailed knowledge of the thermal history during reheating. Within the framework adopted here, information about $T_{\rm re}$ can be inferred by connecting the quantities appearing on the right-hand side of Eq. (3.18) to CMB observables. These are typically expressed in terms of the scalar amplitude A_s, the spectral index n_s, and the tensor-to-scalar ratio r, using the standard relations summarised in Appendix D.

Since these observations provide at most three independent constraints, they can only fix a limited number of model parameters. In most viable inflationary scenarios, the inflaton potential $\mathcal{V}$ depends on at least two parameters [94]. For instance, in the examples discussed in Appendix F.2—namely α-T, RGI, and MHI—these correspond to the overall scale M of the potential and a parameter α controlling the ratio m_φ/M. As a consequence, at most one additional parameter, such as a coupling g, can be constrained using CMB data alone.

The extent to which the full thermal history during reheating can be reconstructed from CMB observations depends on the strength of the inflaton coupling. Following Ref. [95], one can distinguish three qualitatively different regimes:

1. For sufficiently small values of the coupling g, non-perturbative particle production mechanisms—such as parametric resonance, tachyonic instabilities, or fragmentation of the inflaton condensate—are either absent or negligible. If the potential $\mathcal{V}$ is approximately quadratic near its minimum, the inflaton dynamics reduces to that of a weakly perturbed harmonic oscillator [96]. In addition, the expansion of the Universe keeps occupation numbers in the radiation bath low, such that their backreaction on Γ_φ can be neglected. In this regime, Γ_φ can be computed

perturbatively throughout reheating from the inflaton mass m_φ and the coupling g.

Assuming a constant decay rate, the system of equations (3.13) and (3.16) admits an analytic solution [17], leading to

$$T_{\rm re} \approx \sqrt{\Gamma_\varphi m_{\rm Pl}} \left(\frac{90}{\pi^2 g_\star}\right)^{1/4} \Big|_{\Gamma_\varphi = H}, \tag{3.19}$$

and

$$T_{\rm max} \approx 0.9 \left(\Gamma_\varphi^2 m_{\rm Pl}^2 \mathcal{V}_{\rm end}/g_\star^2\right)^{1/8}, \tag{3.20}$$

where we approximate the inflaton potential at the onset of reheating by its value $\mathcal{V}_{\rm end}$ at the end of inflation.

In this case, observational bounds on $T_{\rm re}$ can be translated directly into constraints on the decay rate,

$$\Gamma_\varphi \approx \frac{T_{\rm re}^2}{m_{\rm Pl}} \frac{\sqrt{g_\star}}{3}, \tag{3.21}$$

which can in turn be expressed in terms of m_φ and g.

2. For intermediate values of g, non-linear effects and backreaction from the produced particles influence Γ_φ during the early stages of reheating, without significantly affecting the time at which $\Gamma_\varphi = H$. As a result, the expansion history remains essentially unchanged, while the thermal history can be modified. In particular, $T_{\rm re}$ continues to be described by Eq. (3.19), whereas $T_{\rm max}$ may deviate substantially from Eq. (3.20).

   Although Γ_φ at the end of reheating can still be inferred from Eq. (3.21), reconstructing the full thermal history requires modelling the effects of instabilities and backreaction. These effects generally depend not only on $\mathcal{V}$ and g, but also on the properties and interactions of the produced particles,[5] introducing a dependence on a large set of microphysical parameters that cannot be constrained by the limited set of observables $\{A_s, n_s, r\}$. Reconstruction remains feasible only in simplified scenarios where the dominant effects depend on a small subset of parameters

[5] For example, the occupation numbers of particles produced in inflaton decays depend both on their interactions with each other and on their couplings to additional species. These interactions determine their decay rates into secondary products, their thermalisation timescales, and their effective masses, which in turn influence the available phase space for inflaton decays.

from the set $\{\mathrm{g}, \mathrm{v}_i\}$, or, if the leading effects come from quantum statistics alone.

3. For large values of the coupling g, non-linear effects and backreaction become sufficiently strong to modify both the thermal and the expansion histories. While it is in principle conceivable that these effects depend only on a small number of parameters of the set $\{\mathrm{g}, \mathrm{v}_i\}$, which could be infered from observation, in practice it is difficult to restrict their impact to such a limited set once they significantly affect T_{re}. As a result, Γ_φ cannot be computed reliably over the entire reheating epoch without additional assumptions about the underlying model even if the same inflaton coupling g dominates the whole reheating process, and the thermal history cannot be reconstructed in a model-independent manner throughout reheating.[6]

From a methodological perspective, different regimes require different computational approaches for determining Γ_φ. In regime 1, it is well approximated by the vacuum decay rate when the interaction is linear in φ, and can otherwise be computed using time-dependent perturbation theory [102]. Corrections can be incorporated systematically using multi-scale perturbation theory [96].

In regime 2, an important question is whether the decay products thermalise faster than the oscillation time scale of the inflaton. If this is the case,[7] thermal corrections to Γ_φ can be computed within finite-temperature quantum field theory [57, 103, 104], and the system of equations (3.13) can still be treated analytically [105]. Otherwise, one must solve a set of coupled quantum kinetic equations, for instance derived within the Closed Time Path (CTP) formalism [106].

In regime 3, perturbative methods break down altogether. A first-principles treatment would require solving the coupled dynamics of the condensate and correlation functions in nonequilibrium quantum field theory [107–110], or employing analogue systems [111, 112]. In practice, these dynamics are often approximated using classical lattice simulations, see e.g. [113–117]. Apart

[6] In regime 3, a reconstruction of the thermal history may still be feasible in minimal models with only a few (or no) additional free parameters beyond $\mathcal{V}$ and g. Examples include Starobinsky inflation [97], Higgs inflation [98] (see [99, 100]), and QCD-driven warm inflation [101].

[7] More generally, it is sufficient that thermalisation occurs on a time scale shorter than $1/\Gamma_\varphi$ once effective masses are dominated by forward scattering rather than interactions with the condensate.

from the computational challenges, this regime also faces a conceptual limitation: the thermal history depends on a large number of microphysical parameters that cannot be fully constrained by observations, even within a specific inflationary model.

The boundary between regimes 2 and 3 can be estimated by requiring that perturbation theory remains valid. For a general interaction of the form $\mathrm{g}\varphi^j\Lambda^{4-D}\mathcal{O}[\{\mathcal{X}_i\}]$, this leads to the conservative conditions [81]

$$|\mathrm{g}| \ll \left(\frac{m_\varphi}{\varphi_{\mathrm{end}}}\right)^{j-\frac{1}{2}} \min\left(\sqrt{\frac{m_\phi}{m_{\mathrm{Pl}}}}, \sqrt{\frac{m_\phi}{\phi_{\mathrm{end}}}}\right)\left(\frac{m_\varphi}{\Lambda}\right)^{4-D}, \tag{3.22a}$$

$$|v_j| \ll \left(\frac{m_\varphi}{\varphi_{\mathrm{end}}}\right)^{j-\frac{5}{2}} \min\left(\sqrt{\frac{m_\phi}{m_{\mathrm{Pl}}}}, \sqrt{\frac{m_\phi}{\phi_{\mathrm{end}}}}\right)\left(\frac{m_\varphi}{\Lambda}\right)^{4-j}, \tag{3.22b}$$

where $\mathcal{O}[\{\mathcal{X}_i\}]$ denotes a generic operator of mass dimension $D - j$ constructed from fields $\mathcal{X}_i$ of arbitrary spin. The first condition constrains the inflaton coupling g, while the second ensures that self-interactions of the inflaton do not induce strong backreaction effects such as fragmentation.

In Ref. [20], it was demonstrated that, for a fixed inflationary setup and a specified dark matter model, collider signatures can be inferred by combining CMB observations with the measured relic abundance, provided the dynamics lie within regime 1.[8] This approach relies on the fact that in regime 1 the decay rate Γ_φ can be approximated as constant, allowing the full thermal history during reheating to be reconstructed from Eq. (3.21), once T_{re} has been determined by relating the right-hand side of Eq. (3.18) to CMB observables (see appendix D). In the present work, we investigate to what extent this strategy can be extended beyond regime 1. In general, reconstructing the thermal history based solely on the limited set of observables $\{A_s, n_s, r\}$ is not feasible in regime 3.

The relevant physical scales entering this analysis are the characteristic scale M of the inflaton potential, the inflaton mass m_φ, and the energy density at the end of reheating, which we parameterise in terms of T_{re} via Eq. (3.18). The scale M is determined by the tensor-to-scalar ratio r. In plateau-type

[8]Although the analysis in [20] employs sufficiently small values of g to justify a perturbative treatment, the cases with potentials of the form $\mathcal{V}(\varphi) \propto \varphi^j$ with $j > 2$ violate the condition (3.22b). This indicates that inflaton fragmentation may lead to additional uncertainties that are not accounted for [118, 119].

models, one finds[9]

$$M \approx m_{\rm Pl} \left(\frac{3\pi^2}{2} A_s r \right)^{1/4} \lesssim 1.5 \cdot 10^{16}\ \text{GeV}\,, \tag{3.23}$$

where we used $A_s \approx 2 \cdot 10^{-9}$ and the current bound $r \lesssim 0.03$ [120, 121].

As shown in appendix F.1, we derived a general estimate for the inflaton mass scale in two-parameter inflationary models in the form Eq.(F.1)

$$m_\varphi \approx \frac{\sqrt{24\pi^2 A_s}}{N_{\rm k}} m_{\rm Pl} \approx 10^{13}\ \text{GeV}\,, \tag{3.24}$$

see Eq. (F.5), this relation holds in particular for α-attractor models, and remains a good approximation for several other models, though it can be violated for certain parameter choices. This is consistent with the explicit treatment of several benchmark models presented in appendix F.2. Here $N_{\rm k}$ denotes the number of e-folds between horizon exit of the CMB modes and the end of inflation. Using Eq. (3.24), the inflaton energy density at the onset of reheating can be expressed as

$$\Phi = \frac{\mathcal{V}}{m_\varphi^4} \approx \frac{r N_{\rm k}^4}{384\pi^2 A_s}\,. \tag{3.25}$$

Given the observational bound $r \lesssim 0.03$, this implies $\Phi \lesssim 9 \cdot 10^{10}$ within the regime of validity of Eq. (3.24).

Constraints on $T_{\rm re}$ can be extracted from CMB data using the standard procedure summarised in appendix D. Future sensitivity to the tensor-to-scalar ratio r is expected to improve significantly with upcoming experiments such as the extended Simons Observatory [122] and the Japanese LiteBIRD satellite [123]. While the current configuration of the Chinese AliCPT-1 array's [124, 125] is less competitive in probing reheating [95], it offers complementary coverage due to its location in the Northern Hemisphere and may be upgraded in the future. In the following, we adopt LiteBIRD as our benchmark experiment. The projected sensitivities to $T_{\rm re}$ listed in Tab. 3.1 are obtained using the analytic framework of [126], which has been validated against Monte Carlo Markov Chain forecasts in [82]. Further details are provided in appendix D.

[9] This general relation follows from Eq. (D.4) in the appendix; explicit expressions for the examples considered here are given in Eqs. (F.27), (F.47), and (F.60).

benchmark	model	α	$\bar{n}_s$	σ_{n_s}	$\bar{r}$	σ_r	$\log_{10}(\frac{T_{\rm re}}{\rm GeV})$
A	α-T	2	0.9651	0.002	0.00696	0.001	$13.7^{+1.2}_{-2.0}$
B	RGI	20	0.9607	0.002	0.0265	0.00175	$-0.8^{+1.5}_{-1.0}$
C	MHI	2	0.9623	0.002	0.00947	0.0013	$6.8^{+3.0}_{-2.7}$

Table 3.1: Projected 1σ sensitivities of LiteBIRD to the reheating temperature $T_{\rm re}$ for the three benchmark scenarios A–C. These estimates are obtained following the method of [126], using the projected LiteBIRD sensitivities reported in [123].

If Γ_φ is constant, as assumed in [20], the information contained in Tab. 3.1 can be translated directly into knowledge of the rate Γ_φ entering (3.13), and therefore into a reconstruction of the thermal history during reheating. In general, however, the assumption of constant Γ_φ can only be justified in regime 1. Nevertheless, as long as Γ_φ remains calculable in terms of the parameters in $\mathcal{V}$ and the coupling g alone, a constraint on $T_{\rm re}$ can still be converted into information on g in regime 2. This in turn makes it possible to compute $\Gamma_\varphi(T)$ throughout reheating. This motivates the following two questions:

- In Sec. 3.1, we examine whether the strategy employed in [20] can be extended into regime 2, namely whether there exists a parameter range in which thermal corrections to Γ_φ are both relevant for dark matter production and calculable. More specifically, we ask whether within regime 2 there is a region of parameter space where $\Gamma_\varphi(T)$ can be determined from m_φ and g alone using finite-temperature Quantum Field Theory (QFT).

- Thermal corrections to the DM rate Γ_X may be relevant in all three regimes. In particular, they can substantially modify Γ_X during epochs in which the temperature greatly exceeds the masses of the particles involved. In Sec. 3.2, we therefore study whether such thermal corrections can significantly affect the relic abundance in the range of parameters where they can be computed within finite-temperature QFT.

We find that, in regime 2, thermal corrections to both Γ_φ and Γ_X generically induce only subleading modifications of the dark matter relic abundance. In Sec. 3.3, we discuss three exceptions to this general conclusion.

3.1 Thermal effects on the inflaton decay rate and related DM abundance

Predicting the relic abundance of thermally produced dark matter (DM) requires a detailed understanding of the thermal history during the epoch in which production occurs. In what follows, we consider scenarios where the dissipation of energy from the inflaton condensate into other degrees of freedom is governed throughout reheating by a single microphysical coupling constant. Given that realistic inflationary models typically involve two parameters in the potential $\mathcal{V}$ – denoted here by M and α – the set of observables $\{A_s, n_s, r\}$ can at most determine one additional parameter, namely the coupling g.

Extending the framework of [20] to regime 2, and assessing how finite-temperature corrections to the inflaton decay rate influence the DM relic abundance, requires three conditions to be satisfied.

1. To begin with, one must ensure that the system does not lie in regime 1, where thermal corrections to Γ_φ, by construction, have a negligible impact on the DM relic density and the results of [20] remain applicable. This requirement translates into a lower bound on g, given in (3.27).

   For a thermal plasma, a simple estimate for the transition between regimes 1 and 2 is obtained from the condition $T_{\max} = m_\varphi$. Assuming that dissipation in regime 1 is dominated by perturbative inflaton decays, the decay rate can be parametrised as[10]

   $$\Gamma_\varphi = \mathrm{g}^2 m_\varphi / \mathrm{c} \,, \tag{3.26}$$

   where c denotes a numerical factor. Using (3.20), one obtains the condition

   $$\mathrm{g} > \sqrt{c g_\star \frac{m_\varphi}{m_{\mathrm{Pl}}}} \frac{m_\varphi}{\mathcal{V}_{\mathrm{end}}^{1/4}} \tag{3.27}$$

   in order to be in regime 2.

   For the plateau potentials considered here, one typically has $\mathcal{V}_{\mathrm{end}} \approx M^4$ and $M \approx 10^{16}$ GeV (see (3.23)). Assuming a radiation bath dominated

[10] In plateau models, φ_{end} may be of order m_{Pl} (see appendix F), implying that decay products acquire large time-dependent masses through their coupling to the oscillating inflaton condensate. Although this formally challenges the use of the vacuum decay rate, Eq. (3.26) nevertheless provides a reasonable estimate of the averaged decay rate in regime 1 [115, 127].

by Standard Model degrees of freedom ($g_\star = 106.75$), this implies[11]

$$\mathsf{g} \gtrsim 1.5 \cdot 10^{-4} \left(\frac{m_\varphi}{10^{13}\ \text{GeV}}\right)^{3/2} \tag{3.28}$$

for thermal effects to become relevant. Combining this with Eq. (3.24) yields

$$\mathsf{g} \gtrsim 1.5 \cdot 10^{-4}. \tag{3.29}$$

2. In addition, avoiding regime 3 requires that the conditions (3.22a) and (3.22b) are satisfied. For plateau models, these approximately reduce to [81]

$$|\mathsf{v}_j| \ll \left(3\pi^2 r A_s\right)^{(j-2)/2}, \qquad |\mathsf{g}| \ll \left(3\pi^2 r A_s\right)^{j/2}. \tag{3.30}$$

Using $A_s \approx 2 \cdot 10^{-9}$ and $r < 0.03$, this leads to the upper bound

$$\mathsf{g} \lesssim 10^{-4}. \tag{3.31}$$

This appears to be in tension with (3.29). However, this apparent inconsistency should not be overinterpreted: the derivation of (3.30) neglects numerical prefactors, and the conditions (3.22a) and (3.22b) are conservative estimates. Nonetheless, one can conclude that the parameter region of g in which thermal corrections to Γ_φ significantly impact the DM abundance, while still allowing for a perturbative treatment without additional assumptions, is rather narrow.[12]

3. Finally, thermal corrections to Γ_φ can only influence the DM relic density if a substantial fraction of DM is produced during the phase of reheating where such effects are relevant.

For renormalisable interactions in the radiation-dominated epoch, it is well known [128] that the DM abundance is predominantly generated at late times, since $\Gamma_X \propto T$ while $H \propto T^2$, implying an increasing ratio Γ_X/H. This regime is referred to as *infrared (IR) dominated freeze-in*. If freeze-in terminates due to Boltzmann suppression of a mediator or threshold effects, thermal corrections to Γ_X are typically small because T is already well below the relevant mass scales.

[11] Even in a minimal scenario with $g_\star = 1$, the bound is only weakened by roughly a factor of three.

[12] This conclusion is supported, for instance, by lattice simulations shown in figure 4 of [115].

Achieving *ultraviolet (UV) dominated freeze-in*, where production is dominated at early times, requires the production rate to grow sufficiently rapidly with temperature. In radiation domination, this implies $\Gamma_X \propto T^{2+\delta}$ with $\delta > 0$.

During reheating, however, the situation is more subtle due to the modified equation of state $w_{\rm re}$. Even for higher-dimensional operators ($d > 4$), whose interaction strength increases with temperature, DM production may still fail to be UV-dominated, i.e., particles generated around $T_{\rm max}$ contribute negligibly to the final DM abundance..

For an operator of dimension d, one expects $\Gamma_X \propto T^{2(d-4)+1}$ and

$$\mathcal{C}_X \propto \Gamma_X n_X^{\rm eq} \propto T^{2(d-4)+4} \tag{3.32}$$

in the relativistic regime.

Taking $\bar{w}_{\rm re}$ to be the averaged equation-of-state parameter during reheating, the dimensionless inflaton energy density Φ follows the scaling

$$\Phi \sim x^{-3\bar{w}_{\rm re}}, \tag{3.33}$$

leading to

$$H \sim \sqrt{\frac{\Phi}{x^3}} \sim x^{-3(1+\bar{w}_{\rm re})/2}. \tag{3.34}$$

Using Eq. (3.13), one finds

$$R \sim x^{(5-3\bar{w}_{\rm re})/2}, \qquad T \sim x^{-3(1+\bar{w}_{\rm re})/8}. \tag{3.35}$$

Finally, working under the assumption that Γ_φ is temperature-independent in regime 1, and combining Eqs. (3.32), (3.34) and (3.35), we get

$$\frac{\mathrm{d}}{\mathrm{d}x} X \propto x^{(20-3d-3\bar{w}_{\rm re}(d-4))/4}. \tag{3.36}$$

Thus, DM production is UV-dominated if[13]

$$d \geq \frac{4(2+\bar{w}_{\rm re})}{1+\bar{w}_{\rm re}}. \tag{3.37}$$

[13]The criterion (3.37) assumes that w does not vary strongly during reheating and remains close to its average value $\bar{w}_{\rm re}$.

For a monomial potential $\mathcal{V}(\varphi) \propto \varphi^j$, one has $\bar{w}_{\rm re} = (j-2)/(j+2)$ [129], which implies $d \geq 6+4/j$. In particular, for a quadratic potential ($\bar{w}_{\rm re} = 0$), this gives $d \geq 8$ [130], while for a quartic potential ($\bar{w}_{\rm re} = 1/3$), one finds $d \geq 7$.

The physical origin of point 3 lies in the modified temperature evolution during reheating. For instance, in the simple case $\bar{w}_{\rm re} = 0$, one might expect that the slower expansion rate ($H \propto x^{-3/2}$ rather than x^{-2}) enhances early-time production by reducing dilution. However, this effect is offset by the altered relation between time t and temperature T: since T redshifts more slowly than in radiation domination, DM production occurring at later times–corresponding to lower temperatures–plays a comparatively larger role than in the radiation-dominated case. This behaviour is captured by the scaling $\mathcal{C}_X \propto T^{2(d-4)+4} \propto x^{-3(d-2)/4}$, rather than $x^{-2(d-2)}$ in the radiation-dominated case, cf. (3.36). Furthermore, once freeze-in has ceased ($\Gamma_X \ll H$), the DM density undergoes additional dilution relative to the radiation bath, since the inflaton continues to inject energy into the latter—an effect absent during radiation domination.

Enhancing UV production therefore requires either faster temperature redshifting or an increased decay rate Γ_φ at early times. Thermal effects can provide such an enhancement, particularly for bosonic couplings due to induced emission, whereas fermionic couplings lead to suppression via Pauli blocking [57]. However, combining the bounds (3.29) and (3.31) shows that, for bosonic interactions, regime 2 is either extremely restricted or absent. Consequently, the parameter space (g-values) in which thermal corrections to Γ_φ both affect the DM relic abundance and can be quantified from next generation CMB observations is extremely limited.

We therefore conclude that feedback effects from produced particles on Γ_φ typically do not play a significant role for the DM relic density in the regime where they can be reliably calculated by means of resummed thermal field theory. Even if such effects enhance Γ_φ at early times of reheating, they either act too briefly to overcome late-time production, or they are subdominant compared to the non-perturbative dynamics characteristic of regime 3.

In Sec. 3.3, we present three scenarios that evade this conclusion, all based on UV-dominated freeze-in realised in different ways:

- ⋆ Sec. 3.3.1: Production via operators with high dimension $d \geq 9$.
- ⋆ Sec. 3.3.2: Production of super-heavy DM with Boltzmann suppression during reheating.

⋆ Sec. 3.3.3: Threshold effects induced by screening that suppress decays below a critical temperature.

More elaborate inflationary setups beyond the minimal two-parameter models considered here may also alter this conclusion. In addition, warm inflation scenarios [131], characterised by significant dissipative effects, modify the standard relation (3.20) and can lead to different CMB scaling relations, see [132]. This is particularly relevant in models with very few parameters, where g could potentially be constrained directly by observations [101].

3.2 Impact of thermal effects on the Dark Matter production rate

We begin by analyzing how thermal corrections influence the Dark Matter production rate itself, while deliberately ignoring finite-temperature effects associated with the inflaton sector. Under this simplification, the inflaton dynamics can be fully characterized by its decay width Γ_φ, or equivalently by the reheating temperature $T_{\rm re}$. Consequently, there is no need to commit to a specific form of the inflaton potential in this section. The only requirement we impose is that, near the minimum, the potential is approximately quadratic so that reheating proceeds perturbatively. In practical terms, this corresponds to treating the inflaton as a damped harmonic oscillator during the reheating phase.

For concrete realizations within fully specified inflationary models, we refer the reader to Sec. 3.1 and appendix F.2. Anticipating the results, we find that thermal effects modify the final Dark Matter abundance only mildly, typically at the level of a few tens of percent. This magnitude of correction is consistent with expectations from standard freeze-in production scenarios occurring during radiation domination.

3.2.1 Dark Matter production via scalar decays

As a first illustrative setup, we consider the scenario analysed in Ref. [20], in which Dark Matter is generated through the decay of a scalar mediator P. This particle interacts with a (Majorana) Dark Matter fermion X and a right-handed Standard Model lepton f_R through a Yukawa interaction of the form

$$\mathcal{L}_X \supset y_X \, P \, \bar{f}_R X \, . \tag{3.38}$$

In the limit where the decay products are much lighter than the parent particle, $m_X, m_{f_R} \ll m_P$, the decay width of P in its rest frame is given by

$$\Gamma_P = \frac{y_X^2}{16\pi}\, m_P\,. \tag{3.39}$$

This quantity is, in principle, accessible experimentally, for instance through collider searches targeting long-lived particles. Representative sensitivity projections for such searches (within a specific realisation of the model) are displayed in Fig. 3.2.

In the early Universe, the scalar P may either remain in thermal equilibrium or depart from it, depending on the strength of its interactions [133, 134]. In both regimes, thermal effects can be treated consistently using the Closed-Time-Path (CTP) formalism [135]. Here, we focus on the case where P is part of the thermal bath. Additionally, we assume that the occupation number of Dark Matter is always small, $f_X \ll 1$, which allows us to neglect both quantum-statistical effects and inverse decay processes involving X.

Under these assumptions, the momentum-resolved production rate of Dark Matter, including thermal corrections, reads [136, 137]

$$\Gamma_X(q) = y_X^2 \frac{m_P^2 T}{8\pi|\mathbf{q}|q_0} \ln\left[\frac{\sinh(E_{\rm max}/2T)}{\sinh(E_{\rm min}/2T)}\frac{\cosh((q_0 - E_{\rm min})/2T)}{\cosh((q_0 - E_{\rm max})/2T)}\right], \tag{3.40}$$

where q denotes the four-momentum of the Dark Matter particle. The kinematic endpoints are defined as

$$E_{\rm max\,/\,min} = \frac{q_0 \pm |\mathbf{q}|}{2}\left(\frac{m_P}{m_X}\right)^2. \tag{3.41}$$

Since our primary interest lies in the evolution of the total number density, it is sufficient to consider the momentum-integrated collision term. This is obtained by averaging over the phase-space distribution,

$$\mathcal{C}_X = \int \frac{\mathrm{d}^3\mathbf{q}}{(2\pi)^3}\, \Gamma_X(q)\, f_X^{\rm eq}(q)\,. \tag{3.42}$$

Adopting the Maxwell–Boltzmann approximation, in which quantum-statistical factors are neglected, the collision term can be expressed directly in terms of the vacuum decay width Γ_P. One finds

$$\mathcal{C}_X = m_P \frac{g_P}{2\pi^2}\Gamma_P \int_0^\infty \mathrm{d}p\, \frac{p^2}{E} e^{-E/T} = \frac{\Gamma_P}{\pi^2} m_P^2 T\, K_1\!\left(\frac{m_P}{T}\right), \tag{3.43}$$

where K_1 denotes the modified Bessel function of the second kind.

We illustrate in Fig. 3.1 the difference between employing the full momentum-dependent expression in Eq. (3.40) and its Maxwell–Boltzmann approximation given in Eq. (3.43). The comparison is performed for a representative set of parameters, namely fixed values of the coupling y_X and masses m_P, m_X, and m_{f_R}.

The comparison shows that thermal corrections modify the final Dark Matter abundance only mildly, with deviations typically at the level of 10–20%. This behaviour is consistent with previous estimates and can be understood from the fact that, for processes that are not infrared dominated (i.e. those satisfying $\langle p \rangle \ll \pi T$), the ratio between the Fermi–Dirac and Maxwell–Boltzmann distributions remains close to unity. More precisely, one finds

$$0.95 \lesssim \frac{f_{\rm F}(E)}{f_{\rm MB}(E)} \leq 1\,. \tag{3.44}$$

It is also instructive to examine the temperature range that dominantly contributes to Dark Matter production. In the left panel of Fig. 3.1, the production rate is maximal for temperatures

$$T \in [m_P/5,\, m_P/2] = [100,\, 250]\ \text{GeV}\,, \tag{3.45}$$

which occurs well after the end of reheating (here $T_{\rm re} = 10^4$ GeV) and during the radiation-dominated epoch.

If instead a lower reheating temperature is considered, for instance $T_{\rm re} = 20$ GeV as shown in the right panel of Fig. 3.1, Dark Matter production effectively takes place during the reheating phase itself. In this regime, thermal corrections become even less significant. This is because the continued decay of the inflaton condensate shifts the production towards lower temperatures compared to standard freeze-in scenarios. Since the relevant temperatures are smaller, the Maxwell–Boltzmann approximation becomes increasingly accurate.

This trend is further supported by Fig. 3.2, where a broader range of scalar masses is explored. In particular, one can compare the yellow solid and dotted curves to see the reduced impact of thermal effects.

We next present in Fig. 3.2 the predicted decay length $c\tau$ of the parent particle P (evaluated in its rest frame), under the assumption that the produced X particles account for the observed Dark Matter abundance. We compare results obtained with the full treatment of quantum statistics to those derived

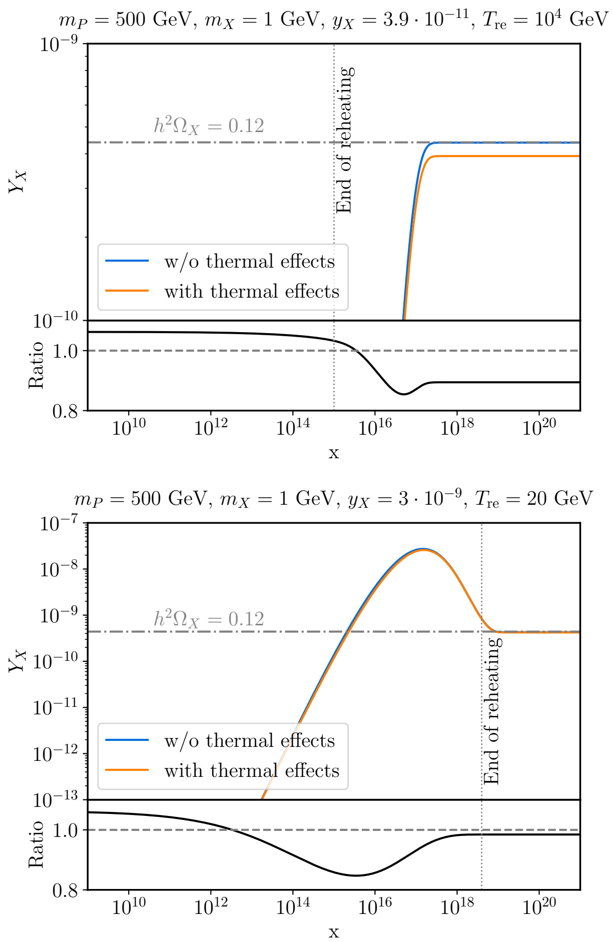

Figure 3.1: Comparison of thermal effects on the final Dark Matter abundance for $T_{\rm re} = 10^4$ GeV (upper panel) and $T_{\rm re} = 20$ GeV (lower panel). The lower panels show the ratio of the yield obtained using the fully momentum-dependent rate in Eq. (3.40) to that computed with the Maxwell–Boltzmann approximation in Eq. (3.43) (blue curve). The orange curve corresponds to the case where momentum dependence is neglected but quantum statistics are retained. The parameter choices are indicated in the figure. We set $m_{f_R} = 0$. In the right panel, the dashed horizontal line marks the observed Dark Matter abundance today, while the vertical dotted line indicates the end of reheating.

within the Maxwell–Boltzmann approximation, restricting our attention to the region of parameter space relevant for collider searches.

A notable feature is that the relevance of thermal corrections decreases as the reheating temperature is lowered, in particular once $T_{\rm re} \lesssim m_P$. In this regime, the late-time decay of the inflaton condensate shifts Dark Matter production towards temperatures satisfying $m_P/T > 1$, where thermal effects are suppressed relative to earlier epochs.

We also emphasise that freeze-in production typically occurs in the range $m_P/T \sim$ 2–5. In this regime, corrections arising from thermal masses are generally subleading compared to those induced by quantum statistics.

Finally, we comment on the interpretation of collider constraints. The bounds shown above usually rely on additional electroweak interactions of the scalar P, which enable its efficient production at colliders. Although such interactions could, in principle, introduce additional channels for Dark Matter production (for instance via scattering processes),[15] we neglect them here in order to isolate the role of thermal effects. A complete phenomenological analysis of specific models should nevertheless include these contributions.

Given that thermal corrections have only a modest impact, it is worth noting that other commonly used approximations can lead to significantly larger deviations. A typical example is the use of the condition $\Gamma = H$ as a proxy for defining the reheating temperature in Eq. (3.17), which avoids solving the full system of Boltzmann equations in Eq. (3.13). This approach allows for an analytic estimate of $T_{\rm re}$ [17, 105], but generally leads to an overestimate of the true reheating temperature, especially at low $T_{\rm re}$.

As an illustration, consider a benchmark point with $m_P = 500$ GeV and $T_{\rm re} = 100$ GeV, where the reheating temperature is assumed to be independently determined from CMB observations [82]. Using the approximate expression instead of the exact definition results in an overestimation of $T_{\rm re}$ by roughly 30%, which in turn enhances the predicted Dark Matter abundance by about a factor of two. Equivalently, this corresponds to underestimating the decay length relevant for collider searches by a similar factor.

[14] More recent analyses have refined these bounds, see e.g. [146, 147]. Incorporating these updates would require a dedicated recast following the methodology of [138], which lies beyond the scope of this work. In any case, such refinements are not expected to qualitatively alter the conclusions drawn here.

[15] Dark Matter can also be generated through scatterings mediated by the right-handed lepton f_R. However, for $m_P/T \gg 1$ these processes suffer from the same Boltzmann suppression as the dominant $1 \to 2$ decay channel and are therefore expected to be subleading.

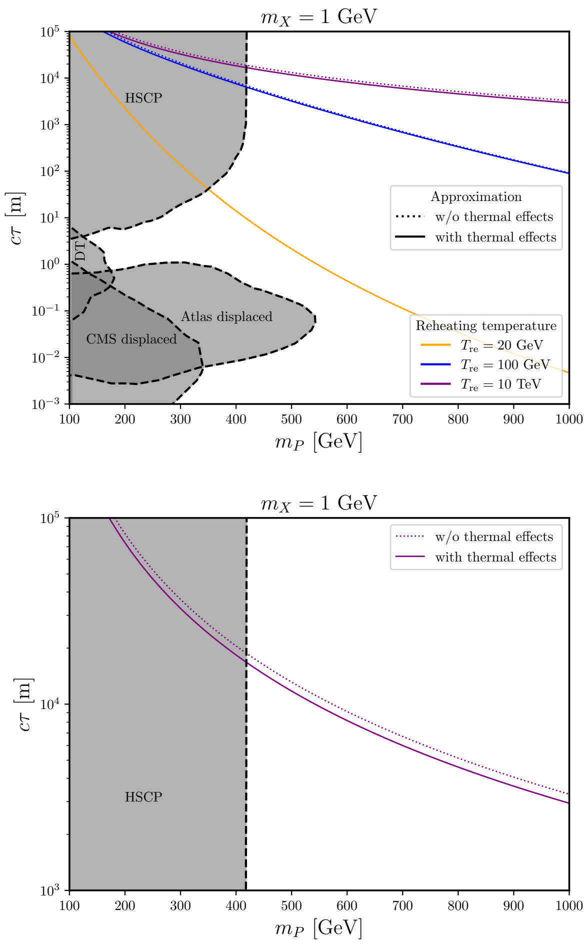

Figure 3.2: *Upper panel*: The contours compare the values of the rest frame decay length $c\tau$ and mass m_P accounting for the observed DM relic abundance without and with thermal corrections, based on (3.43) and (3.42) with (3.40). We compare different choices of the reheating temperature, chosen as in [20], and the expected decay length with and without accounting for quantum statistical effects in the DM production rate. *Lower panel*: We zoom in on the results for $T_{\rm re} = 10$ TeV to highlight more clearly the impact of said thermal effects. In gray, we highlight the parameter space region excluded for a muophilic DM candidate X in the muonphilic Majorana DM model [138], including searches for heavy stable charged particles (HSCP) at ATLAS [139], searches for disappearing tracks (DT) at ATLAS [140] and CMS [141, 142] as well as searches for displaced leptons at Atlas [143] and CMS [144, 145].[14]

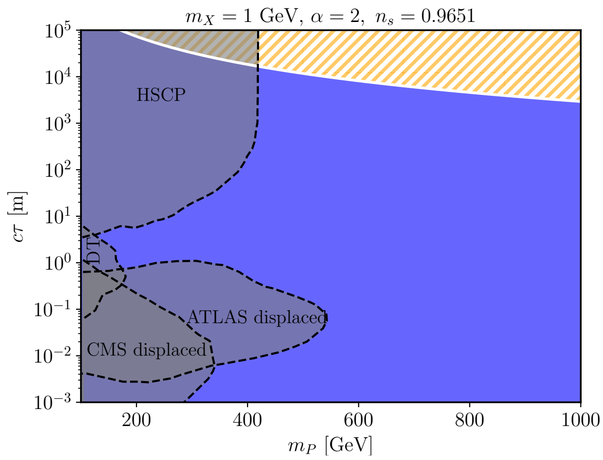

Figure 3.3: Forecast for constraints set on the model parameter space displayed in Fig. 3.2 by the next-generation CMB experiment LiteBIRD in scenario A, see Tab. 3.2. In dark blue shaded, we display the region that would be disfavoured at 3σ or more. Since $m_P \ll T_{\rm re}$, the DM production is essentially insensitive to the reheating epoch, and the region consistent with CMB observation at the 2σ level is compressed into the immediate proximity of the region with instant reheating ($N_{\rm re} = 0$) indicated by the white line, making it indistinguishable from DM production in the radiation dominated epoch. The orange hatched area represents the parameter space region where the observed DM abundance can never be achieved independently of the value of the reheating temperature.[20]

Moreover, even when adopting the definition in Eq. (3.17), one should keep in mind that the Universe is not yet in a state of perfect radiation domination at that stage. Since this assumption underlies the connection between $T_{\rm re}$ and CMB observables [82], small corrections are expected. Comparable effects may also arise in non-standard cosmological histories, such as scenarios featuring an early matter-dominated phase.

Collider predictions from CMB observations

We conclude this subsection by emphasizing, as illustrated in Figs. 3.3–3.5, the complementarity between constraints from future CMB observations—most notably from LiteBIRD—and those obtained from laboratory experiments.

[20]The reason is simply that, within the chosen setup for reheating, a low reheating temperature can only dilute the produced DM abundance but never enhance it.

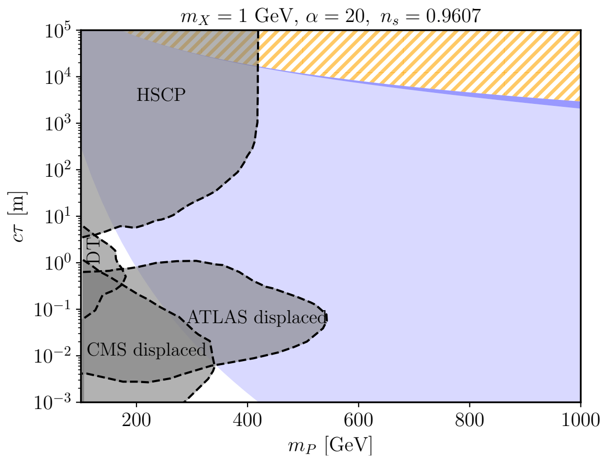

Figure 3.4: Constraints set on the model parameter space displayed in Fig. 3.2 by the next-generation CMB experiment LiteBIRD in scenario B, see Tab. 3.2. The white, light blue and darker blue areas correspond to the regions consistent with such observation at the 1σ, 2σ and 3σ level. Similarly to the previous figure, the orange hatched area represents the parameter space region where the observed DM abundance can never be achieved independently of the value of the reheating temperature.

Our analysis is performed for the three benchmark scenarios introduced in Table 3.1. The corresponding posteriors for $T_{\rm re}$ are derived using the method of [126], cf. (D.9) in the appendix.

Figure 3.3 demonstrates that LiteBIRD observations could shrink the viable parameter space of inflationary scenario A to an approximately one-dimensional band in the mediator mass–lifetime plane. A portion of this region is within reach of heavy stable charged particle (HSCP) searches [139] in the muonphilic Majorana DM model [138]. It is important to note, however, that in this scenario the DM production mechanism is largely insensitive to the details of reheating. This is because the relevant parameter space lies in the regime $m_P \ll T_{\rm re}$, where production predominantly occurs during radiation domination. Consequently, the improvement expected from LiteBIRD over current bounds from Planck and BICEP/Keck is rather modest. These existing measurements already imply $T_{\rm re} > 10^4$ GeV even when α is treated as a free parameter [95]. Moreover, neither current constraints nor those anticipated from LiteBIRD constitute a genuine measurement of the reheating temperature, in the sense of providing both upper and lower observational bounds. The uncertainty quoted in Table 3.1 instead arises from combining a lower observational limit with the theoretical consistency condition $N_{\rm re} \geq 0$. As a result, the

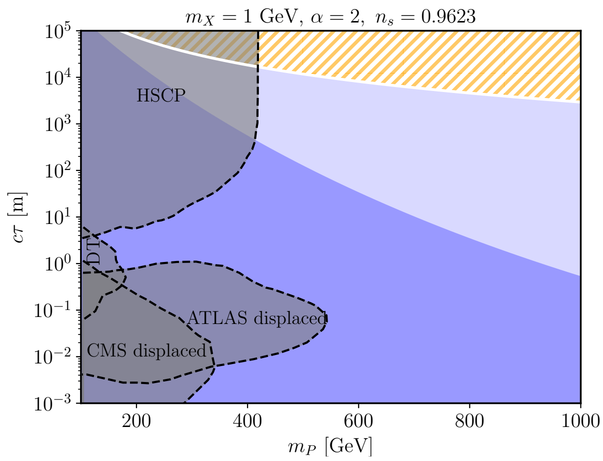

Figure 3.5: Constraints set on the model parameter space displayed in Fig. 3.2 by the next-generation CMB experiment LiteBIRD in scenario C, see Tab. 3.2. The white, light blue and darker blue areas correspond to the regions consistent with such observation at the 1σ, 2σ and 3σ level. As in Fig. 3.3, the 1σ region is compressed into the immediate vicinity of the region with instant reheating ($N_{\rm re} = 0$) indicated by the white line, making it indistinguishable from DM production in the radiation dominated epoch. However, in scenario C the 2σ region is distinguishable from instant reheating. Similarly to the previous figures, the orange hatched area represents the parameter space region where the observed DM abundance can never be achieved independently of the value of the reheating temperature.

posterior distribution is highly non-Gaussian and asymmetric, rendering the interpretation of the quoted error on $T_{\rm re}$ nontrivial.

A qualitatively different situation arises in scenario B, as shown in Fig. 3.4. Here, the posterior distribution of $T_{\rm re}$ is well approximated by a Gaussian, allowing for a determination $\log_{10}(T_{\rm re}/\text{GeV}) = -0.8^{+1.5}_{-1.0}$, which places the coupling y_φ firmly within region 1. This scenario corresponds to inflation occurring in a hidden or secluded sector that interacts only very weakly with the Standard Model. In this case, DM production is dominated by processes during reheating. LiteBIRD observations could therefore constrain the model parameter space at the 1σ level to a region accessible to long-lived particle searches at the HL-LHC, given that the sensitivity to the decay length $c\tau$ is expected to scale approximately linearly with the integrated luminosity [148].[21] At the 2σ level, however, a substantial portion of the allowed parameter space remains beyond collider reach. This limitation could potentially be alleviated by incorporating additional constraints on the spectral index n_s, for instance from the EUCLID mission or future 21 cm observations [126].

Finally, Fig. 3.5 indicates that in scenario C the parameter space favored by LiteBIRD spans regions where collider-accessible DM is produced both during reheating and during radiation domination. Within the 1σ range of $T_{\rm re}$, DM production relevant for collider phenomenology necessarily occurs during radiation domination, since $m_P \lesssim 1\,\text{TeV} < T_{\rm re}$ in this regime. At the 2σ level, the lower bound on the reheating temperature relaxes to $T_{\rm re} \gtrsim 40\,\text{GeV}$, opening the possibility for collider-accessible DM production during reheating. We note that parts of this parameter space can be probed by HSCP searches at the LHC.

3.2.2 Dark Matter production from an effective four-fermion interaction

As a second example, we turn to Dark Matter production mediated by higher-dimensional operators, and examine how thermal effects modify the corresponding rates. For concreteness, we consider an effective interaction described by the Lagrangian

$$\mathcal{L}_{X,\text{int}} = 2\sqrt{2}\,\mathcal{G}\,(P\gamma_\mu P_R X)(\Psi_1\gamma^\mu P_R\Psi_2)\,, \tag{3.46}$$

[21] The analytic sensitivity estimates in [148] are most reliable for lepton colliders, but still provide reasonable order-of-magnitude estimates for the HL-LHC, see Fig. 8 of [149].

where P and Ψ_2 are taken to be massless fermions, X denotes the Dark Matter particle with mass m_X, and Ψ_1 is a distinct fermion with mass[22] $m_{\Psi_1} = m_X$.

The coupling $\mathcal{G} = \frac{g^2}{4\sqrt{2}m_{Z'}^2}$ represents an effective Fermi constant arising after integrating out a heavy neutral gauge boson Z', which sets the cutoff scale of the theory. In realistic ultraviolet completions, such as Left–Right symmetric models or $U(1)_{B-L}$ extensions, several interaction channels involving X are typically present. However, since our aim is solely to isolate the role of thermal effects, we refrain from specifying a complete UV realisation leading to Eq. (3.46).

Within this framework, Dark Matter is predominantly generated via scattering processes in the thermal bath. The full thermal interaction rate in a Fermi-like theory Eq. (3.46) can be written as [150]

$$
\begin{aligned}
\Gamma_X(q) =& \frac{8\mathcal{G}^2}{q_0} f_F^{-1}(-q_0) \int \frac{\mathrm{d}^3\mathbf{p}_1}{(2\pi)^3 2E_1} \int \frac{\mathrm{d}^3\mathbf{p}_2}{(2\pi)^3 2E_2} \int \frac{\mathrm{d}^3\mathbf{p}_3}{(2\pi)^3 2E_3} \\
&\times \Bigg\{ (2\pi)^4 \delta^4(p_1 + p_2 + p_3 - q) \\
&\qquad \times \big(1 - f_F(E_1)\big)\big(1 - f_F(E_2)\big)\big(1 - f_F(E_3)\big)\, \mathcal{T}(m_1, -m_2, m_3) \\
&\quad + (2\pi)^4 \delta^4(p_1 + p_2 - p_3 - q) \\
&\qquad \times \big(1 - f_F(E_1)\big)\big(1 - f_F(E_2)\big) f_F(E_3)\, \mathcal{T}(m_1, -m_2, -m_3) \\
&\quad + (2\pi)^4 \delta^4(p_1 + p_3 - p_2 - q) \\
&\qquad \times \big(1 - f_F(E_1)\big) f_F(E_2) \big(1 - f_F(E_3)\big)\, \mathcal{T}(m_1, m_2, m_3) \\
&\quad + (2\pi)^4 \delta^4(p_2 + p_3 - p_1 - q) \\
&\qquad \times f_F(E_1)\big(1 - f_F(E_2)\big)\big(1 - f_F(E_3)\big)\, \mathcal{T}(-m_1, -m_2, m_3) \\
&\quad + (2\pi)^4 \delta^4(p_3 - p_1 - p_2 - q) \\
&\qquad \times f_F(E_1) f_F(E_2) \big(1 - f_F(E_3)\big)\, \mathcal{T}(-m_1, m_2, m_3) \\
&\quad + (2\pi)^4 \delta^4(p_2 - p_1 - p_3 - q) \\
&\qquad \times f_F(E_1)\big(1 - f_F(E_2)\big) f_F(E_3)\, \mathcal{T}(-m_1, -m_2, -m_3) \\
&\quad + (2\pi)^4 \delta^4(p_1 - p_2 - p_3 - q) \\
&\qquad \times \big(1 - f_F(E_1)\big) f_F(E_2) f_F(E_3)\, \mathcal{T}(m_1, m_2, -m_3) \Bigg\},
\end{aligned} \tag{3.47}
$$

[22] This mass choice is made for simplicity, as it avoids the need to include decay processes explicitly. In practice, an exact degeneracy is not required; a small mass splitting, potentially lifted by thermal corrections, would lead to qualitatively similar results.

For comparison, we also employ the Maxwell–Boltzmann approximation, in which the quantum statistical factors are replaced by their classical exponential form. In this case, the production rate simplifies to

$$\begin{aligned}
\Gamma_X(q) = \frac{8\mathcal{G}^2}{q_0}\, f_F^{-1}(-q_0) \int \frac{\mathrm{d}^3\mathbf{p}_1}{(2\pi)^3 2E_1} \int \frac{\mathrm{d}^3\mathbf{p}_2}{(2\pi)^3 2E_2} \int \frac{\mathrm{d}^3\mathbf{p}_3}{(2\pi)^3 2E_3} \Bigg\{ \\
& (2\pi)^4\delta^4(p_1+p_2+p_3-q)\, \mathcal{T}(m_1,-m_2,m_3) \\
& + (2\pi)^4\delta^4(p_1+p_2-p_3-q)\, e^{-E_3/T}\, \mathcal{T}(m_1,-m_2,-m_3) \\
& + (2\pi)^4\delta^4(p_1+p_3-p_2-q)\, e^{-E_2/T}\, \mathcal{T}(m_1,m_2,m_3) \\
& + (2\pi)^4\delta^4(p_2+p_3-p_1-q)\, e^{-E_1/T}\, \mathcal{T}(-m_1,-m_2,m_3) \\
& + (2\pi)^4\delta^4(p_3-p_1-p_2-q)\, e^{-(E_1+E_2)/T}\, \mathcal{T}(-m_1,m_2,m_3) \\
& + (2\pi)^4\delta^4(p_2-p_1-p_3-q)\, e^{-(E_1+E_3)/T}\, \mathcal{T}(-m_1,-m_2,-m_3) \\
& + (2\pi)^4\delta^4(p_1-p_2-p_3-q)\, e^{-(E_2+E_3)/T}\, \mathcal{T}(m_1,m_2,-m_3) \Bigg\}, \qquad (3.48)
\end{aligned}$$

where the masses are specified as $m_1 = m_X$ and $m_2 = m_3 = 0$. The function $\mathcal{T}$ encodes the spin-summed matrix element and is given by

$$\begin{aligned}
\mathcal{T}(m_1,m_2,m_3) &\equiv \mathrm{Tr}\Big[(\not{q} + m_X)\gamma^\mu P_R(\not{p}_3 + m_3)\gamma^\nu P_R\Big] \\
&\quad \times \mathrm{Tr}\Big[(\not{p}_2 + m_2)\gamma_\mu P_R(\not{p}_1 + m_1)\gamma_\nu P_R\Big] \\
&= 8\Big[(p_2\cdot p_3)(p_1\cdot q) + (p_1\cdot p_3)(p_2\cdot q)\Big]. \qquad (3.49)
\end{aligned}$$

The impact of quantum statistical effects is illustrated in Fig. 3.6, where we compare the final Dark Matter abundance obtained using the full expression (shown in orange) with the result derived within the Maxwell–Boltzmann approximation. The parameters of both the inflaton and Dark Matter sectors are indicated in the figure and have been chosen such that Dark Matter production is maximal during the reheating phase, while ensuring that the effective field theory description remains valid throughout.

As can be seen, even in this setup where production occurs predominantly during reheating, the size of thermal corrections remains modest, at the level of $\mathcal{O}(10\%)$. This is consistent with the expectation from Eq. (3.44), since the process is not dominated by infrared contributions.

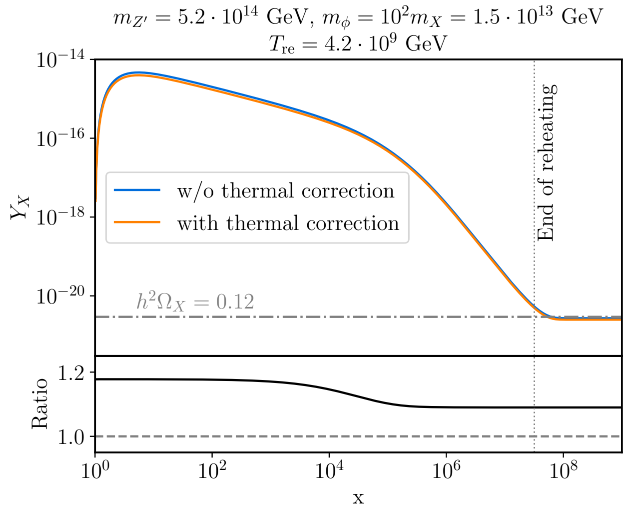

Figure 3.6: Effect of quantum statistical corrections on the Dark Matter yield for a Fermi-type interaction. In the right panel, the dashed horizontal line indicates the observed present-day Dark Matter abundance, while the vertical dotted line marks the end of the reheating period.

3.2.3 General picture

In the two examples discussed above, thermal corrections turn out to be small. This naturally raises the question of how generic this result is and motivates a closer look at the underlying physical reasons.

A central assumption in both cases is that the DM particle is the only species out of thermal equilibrium. In the scenario considered in Sec. 3.2.1, freeze-in production ceases once the parent particle P undergoes freeze-out, i.e., when its abundance becomes Boltzmann suppressed. This behaviour is typical for renormalisable interactions, where dimensional analysis implies $\Gamma_X \propto T$ in the regime $T \gg m_P$. As a consequence, Γ_X decreases more slowly than the Hubble rate (3.16a). Therefore, the dominant contribution to freeze-in arises at temperatures $T < m_P$ – in the present model roughly for $m_P/T \sim$ 2–5 – where quantum statistical effects are generally subdominant [135].

Screening effects tend to be even less relevant in this regime. Indeed, thermal corrections to particle dispersion relations scale as $\sim gT$ and only exceed the vacuum mass m_P when $T \gtrsim m_P/g$. Although thermal corrections to Γ_X can become large at higher temperatures, their impact on the final DM abundance is suppressed for the reasons discussed at the end of Sec. 3.1: the temperature decreases more slowly than in radiation domination, and the DM produced at early times is subsequently diluted by particles generated in inflaton decays at later times. In the second example of Sec. 3.2.2, the stronger temperature dependence $\Gamma_X \sim \mathcal{G}^2 T^5$ is still insufficient to overcome these effects, as anticipated from Eq. (3.36). Moreover, the bound (3.44) further constrains the role of quantum statistical effects for non-IR-enhanced thermal DM production, even in the ultra-relativistic regime.

We therefore conclude, combining the results of this section with the arguments presented in Sec. 3.1, that thermal corrections to both Γ_X and Γ_φ do not significantly alter the DM relic abundance in a broad class of scenarios.

There are, however, several ways in which this conclusion can be circumvented:

- ⋆ If DM is predominantly produced from light particles through sufficiently high-dimensional operators, freeze-in becomes UV-dominated without additional tuning (cf. Eq. (3.37) and Sec. 3.3.1), thereby increasing the sensitivity of the final DM abundance to thermal corrections to Γ_φ.
- ⋆ If DM production involves particles with large effective masses, Boltzmann suppression of coannihilating species or phase-space suppression can enforce UV-dominated freeze-in (cf. Secs. 3.3.2 and 3.3.3). As in the previous case, this enhances the relevance of thermal effects in Γ_φ.
- ⋆ A temperature- or field-dependent effective coupling or mixing angle can lead to resonant conversion, as realised for instance in sterile neutrino DM [14, 151] or dark photon DM [152].
- ⋆ If the parent particles or mediators involved in DM production are themselves out of equilibrium, the evolution of Γ_X is controlled by their dynamics rather than the bath temperature T, potentially making thermal effects relevant at the time of peak DM production.
- ⋆ If DM is produced non-thermally from a condensate (such as, but not limited to, the inflaton), the production mechanism depends primarily on the evolution of that condensate rather than on T, and may include non-perturbative processes such as parametric or tachyonic resonance.

Nevertheless, for standard thermal histories with thermally produced DM, the general expectation is that thermal corrections to both Γ_φ and Γ_X remain small in regimes 1 and 2. In the following section, we present explicit examples that evade this behaviour, focusing on the first two mechanisms listed above.

3.3 Counterexamples to the standard lore

In Secs. 3.1 and 3.2, we have argued on general grounds that thermal corrections to the inflaton decay rate Γ_φ and the DM production rate Γ_X do not significantly modify the final relic abundance in the regime where these quantities can be computed within perturbative finite-temperature field theory. This conclusion was explicitly illustrated with two examples in Sec. 3.2. A key reason is that, in most scenarios, the dominant contribution to the DM abundance is generated towards the end of reheating or during radiation domination.

In the following, we construct explicit counterexamples based on *UV-dominated freeze-in*, in which a substantial fraction of the DM abundance is produced at early times, rendering it sensitive to the thermal history during reheating. We stress that these examples are deliberately engineered to evade the general arguments presented earlier and therefore do not invalidate their applicability in typical situations.

All examples discussed in this section share the same inflationary background. For definiteness, we adopt the α-attractor T-model potential

$$\mathcal{V}(\varphi) = M^4 \tanh^2 \left[\frac{\varphi}{\sqrt{6\alpha} m_{\rm Pl}} \right] , \tag{3.50}$$

although our conclusions are not specific to this choice, it serves as a representative example of plateau-type inflation. As shown in appendix F.1, many phenomenologically viable plateau models share the same qualitative inflationary dynamics. We have furthermore verified in appendix F.2 that radion gauge inflation and mutated hilltop inflation exhibit analogous behaviour for suitable choices of their parameters.

Constraints from CMB observations tightly constrain the inflationary scale. In the α-attractor benchmark considered here, and as illustrated in Fig. 3.7, this implies an inflaton mass of approximately

$$m_\varphi \simeq 1.5 \cdot 10^{13}\,\text{GeV}, \tag{3.51}$$

in agreement with the general estimate (3.24). We choose the initial inflaton energy density as $\Phi = 2 \cdot 10^{10}$, close to the maximal value allowed by the upper bound on the tensor-to-scalar ratio, cf. (3.25). This enhances the impact of thermal effects during reheating, which is essential for the counterexamples discussed below.

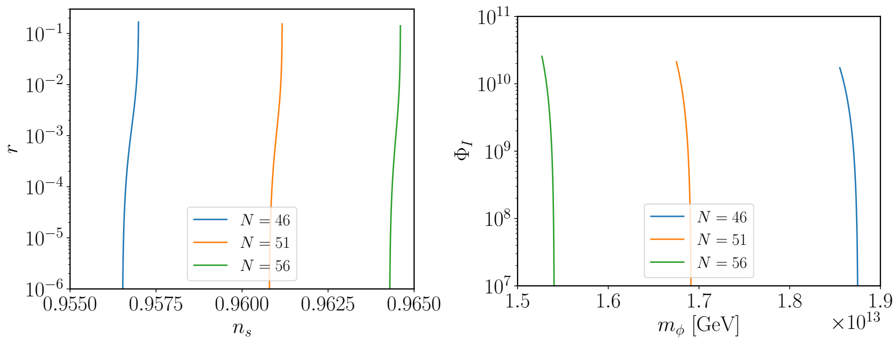

Figure 3.7: (*Left*) Tensor-to-scalar ratio r as a function of the spectral index n_s for the α-attractor T-model and fixed values of the number of e-folds N_k, consistent with the Planck and BICEP/Keck data. The blue, orange and green lines correspond to $N_\mathrm{k} = 46$, $N_\mathrm{k} = 51$, and $N_\mathrm{k} = 56$, respectively. (*Right*) Inflaton energy density Φ_I at the beginning of reheating as a function of the inflaton mass m_φ assuming the same choices for the number of e-folds and inflationary scenario. The colour scheme is identical to the left panel.

Reheating is assumed to proceed dominantly via a fermionic channel described by the Yukawa interaction

$$\mathcal{L}_\varphi \supset y_\varphi\, \varphi \bar{\Psi}\Psi\,. \tag{3.52}$$

As argued in [95], based on earlier works [108, 153–155], fermionic reheating can extend the regime of validity of perturbative treatments beyond the bound (3.30). The underlying reason is that Pauli blocking suppresses the build-up of large occupation numbers, thereby preventing strong feedback effects such as parametric resonance. Provided that the condition (3.22b) is satisfied to avoid early inflaton fragmentation [118, 119], the decay rate Γ_φ can therefore be approximated by the perturbative expression (3.26) with $\{\mathrm{g}, \mathrm{c}\} = \{y_\varphi, 8\pi\}$.

Taking into account the lower bound (3.28), we adopt the benchmark value

$$y_\varphi = 5 \cdot 10^{-3}. \tag{3.53}$$

In this regime, the perturbative description is expected to provide a reasonable approximation, although its precise range of validity remains uncertain [115].

The fermionic dispersion relation can in general be momentum dependent in the presence of gauge interactions [156]. For simplicity, we approximate the fermionic dispersion relation by

$$M_\Psi^2 \simeq (m_\Psi + y_\varphi \varphi)^2 + \left(\frac{g_\Psi T}{2}\right)^2\,, \tag{3.54}$$

which is a good approximation as long as, at any given time, one of the two contributions dominates the effective mass. In the following, we neglect the vacuum mass, $m_\Psi \ll m_\varphi$, and adopt $g_\Psi = 0.5$ as a representative value.

At early stages of reheating, the contribution induced by the inflaton condensate, $y_\varphi \varphi$, typically provides the dominant mass term. This is because $\varphi_{\rm end}$ can be of order $m_{\rm Pl}$, cf. (F.15), whereas the maximal temperature $T_{\rm max}$ is only moderately larger than m_φ. As the system evolves and the temperature increases relative to the field amplitude, the thermal contribution $\sim g_\Psi T/2$ becomes increasingly relevant.

A more quantitative estimate can be obtained in regime 2. Using $\rho_R \sim \rho_\varphi \sim m_\varphi^2 \varphi^2$ together with (3.19), one finds that near the end of reheating the field amplitude scales as $\varphi \sim y_\varphi^2 m_{\rm Pl}$, while the reheating temperature behaves as $T_{\rm re} \sim y_\varphi \sqrt{m_\varphi m_{\rm Pl}}$. This implies that, for $y_\varphi \lesssim 10^{-2}$, the thermal contribution in (3.54) generically dominates over the inflaton-induced term during the late stages of reheating.

Including thermal corrections, the inflaton decay rate takes the form [57]

$$\Gamma_\varphi = \frac{y_\varphi^2}{8\pi} M_\varphi \left(1 - 2\left(\frac{M_\Psi}{M_\varphi}\right)^2\right)^{1/2} \left(1 - 2 f_{\rm F}(M_\varphi/2)\right) , \tag{3.55}$$

where $M_\varphi^2 = m_\varphi^2 + \lambda_\phi T^2/24 + \lambda_\phi \varphi^2/2$ denotes the effective inflaton mass.

In regime 1, this expression reduces to the perturbative result (3.26), which can be used to reconstruct the thermal history via (3.13). However, at early times the time-dependent mass $y_\varphi \varphi$ can lead to kinematic suppression of the decay. This effect is conveniently characterised by the parameter [127]

$$\mathcal{R} = 4 y_\varphi^2 \frac{\varphi^2}{m_\varphi^2} \, . \tag{3.56}$$

When $\mathcal{R} \ll 1$, the standard perturbative expression applies, while for $\mathcal{R} \gg 1$ the decay rate is suppressed. This can be accounted for by introducing an effective Yukawa coupling [127]

$$y_{\rm eff}^2 = \begin{cases} y_\varphi^2 & \text{if } \mathcal{R} \ll 1 \\ 0.38\, y_\varphi^2/\sqrt{\mathcal{R}} & \text{if } \mathcal{R} \gg 1 \end{cases} , \tag{3.57}$$

with a smooth interpolation around $\mathcal{R} \sim 1/7$.

The effective coupling in (3.57) is derived within time-dependent perturbation theory and does not capture non-perturbative fermion production. Interestingly, it has been observed that for sufficiently small couplings, e.g. $y_\varphi =$

Parameter	m_φ [GeV]	Φ	y_φ	α	M [GeV]	n_s	r
Value	$1.5 \cdot 10^{13}$	$2 \cdot 10^{10}$	$5 \cdot 10^{-3}$	2	$9.46 \cdot 10^{15}$	0.965	$6.96 \cdot 10^{-3}$

Table 3.2: Parameters characterising the benchmark inflationary scenario used in this section.

10^{-4}, neglecting the time-dependent contribution $y_\varphi \varphi$ can yield a better estimate for $T_{\max}$ than including it, when compared to non-perturbative results, see Fig. 6 in [115]. However, both the perturbative framework underlying (3.57) and the non-perturbative analysis of [115] neglect gauge interactions of the fermions. Such interactions can significantly affect the reheating dynamics, for instance by redistributing the injected energy into additional degrees of freedom or by generating effective masses through forward scatterings that may terminate non-perturbative particle production.

These considerations highlight that a quantitatively reliable description of fermionic reheating in realistic settings is still incomplete. Although this does not contradict the conclusion of [95] that regime 2 can be extended to couplings beyond the bound (3.22a) in the fermionic case, it suggests that computing Γ_φ perturbatively during the early stages of reheating becomes questionable once (3.22a) is violated. This, in turn, introduces an intrinsic uncertainty in predictions for observables such as DM relic abundances or gravitational wave spectra that rely on the detailed thermal history.

In the following, we therefore compare the solutions of (3.13) obtained using the decay rate (3.55) with and without the effective coupling (3.57). While neither description is fully reliable, the comparison suffices to demonstrate that the early-time thermal evolution in regime 2 can have a non-negligible impact on the final DM abundance. At the same time, the spread between the two results provides a useful proxy for the theoretical uncertainty associated with fermionic reheating.

All parameters defining the benchmark inflationary setup are summarised in Tab. 3.2.[23] For practical purposes, we set $M_\varphi \simeq m_\varphi$. Moreover, we assume that DM production proceeds via particles in the thermal bath that are not directly coupled to the inflaton, such that inflaton-induced mass corrections do not affect the production mechanism itself.

[23] We choose $\alpha \gtrsim 0.25$ to avoid non-perturbative fragmentation of the inflaton field induced by higher-order terms in the potential [81].

3.3.1 UV-dominated freeze-in from a dimension-9 operator

As a first counter-example, we consider a scenario in which Dark Matter is predominantly produced via a higher-dimensional interaction. Specifically, we assume that the production is mediated by a dimension-9 operator involving only relativistic degrees of freedom, such that all particles in the plasma—except for the Dark Matter—can be treated as effectively massless over the relevant temperature range.

A representative interaction takes the form

$$\mathcal{L} \supset y_X \left(\bar{X}\Psi_1\right) \left(\bar{\Psi}_2\Psi_3\right) \left(\bar{\Psi}_4\Psi_5\right) \ , \tag{3.58}$$

where y_X denotes the effective coupling and the Ψ_i are massless fermions in the thermal bath.

In this setup, the Dark Matter production rate is strongly dominated by UV scatterings and can be parametrised, at the level of momentum-averaged rates, as

$$\Gamma_X = c\, y_X^2 \frac{T^{2(d-4)+1}}{\Lambda^{2(d-4)}} = c\, y_X^2 \frac{T^{11}}{\Lambda^{10}} \ , \tag{3.59}$$

where c encodes the phase-space and loop suppression factors. For concreteness, we adopt

$$y_X = 3.8 \cdot 10^{-2} \qquad \text{and} \qquad c = 10^{-3}. \tag{3.60}$$

The Dark Matter mass is fixed to $m_X = m_\varphi/10^4$, while the cutoff scale is chosen as $\Lambda = 10\, m_\varphi$, ensuring the validity of the effective field theory throughout the reheating epoch.

Impact of thermal effects. The resulting Dark Matter abundance as a function of temperature is shown in Fig. 3.8. Within the benchmark defined in Sec. 3.3, the relatively large Yukawa coupling y_φ implies that quantum statistical effects—most notably Pauli blocking—significantly modify the reheating dynamics. In particular, the maximal temperature reached by the plasma is reduced by a factor of $\mathcal{O}(2)$ once these effects are taken into account.

While this reduction may appear moderate, it has a dramatic impact on the Dark Matter abundance. Indeed, because the production rate scales as $\Gamma_X \propto T^{11}$, the mechanism is intrinsically UV-dominated, and therefore highly sensitive to the highest temperatures attained during reheating. As a result,

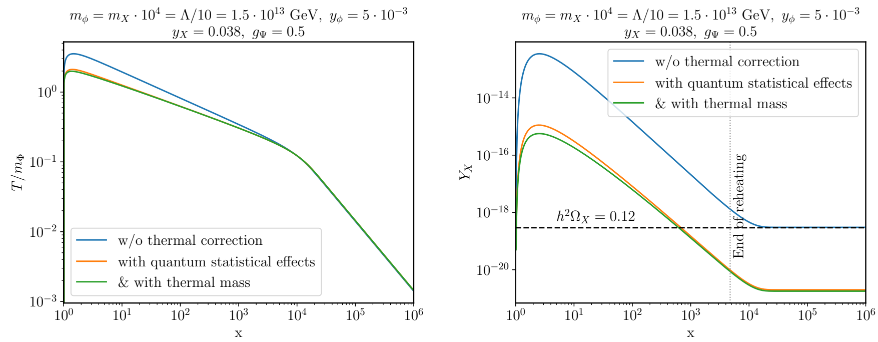

Figure 3.8: Time evolution (as a function of the scale factor $x = am_\varphi$) of the plasma temperature (left) and the Dark Matter yield (right) for production via a dimension-9 operator, cf. Eq. (3.59). In the right panel, the dashed horizontal line indicates the observed present-day Dark Matter abundance, while the dotted vertical line marks the end of reheating.

even an $\mathcal{O}(1)$ suppression of the maximal temperature translates into orders-of-magnitude differences in the final Dark Matter yield, as illustrated in the right panel of Fig. 3.8.

We also observe that thermal corrections to the dispersion relations of the fermions, encoded in $\mathbf{m}_\Psi(T)$, lead to comparatively mild effects on the final abundance. Their impact becomes relevant only when approaching the strong (non-perturbative) regime, where the simple perturbative description of reheating begins to break down.

However, Fig. 3.9 demonstrates that the inflaton-induced contribution $y_\varphi\varphi$ to the effective mass in (3.54) can play an even more prominent role than quantum statistical effects. The pronounced difference between the results obtained using the fundamental Yukawa coupling y_φ and the effective coupling y_{eff} defined in (3.57) reflects a substantial modelling uncertainty in the description of fermionic reheating.

This leads to two main observations. First, thermal effects in Γ_φ – here exemplified by Pauli blocking – can become important and modify the DM relic abundance by several orders of magnitude in scenarios with UV-dominated freeze-in. Second, the theoretical uncertainty associated with the treatment of fermionic reheating can be even larger, and thus constitutes a dominant source of uncertainty in the predicted relic density.

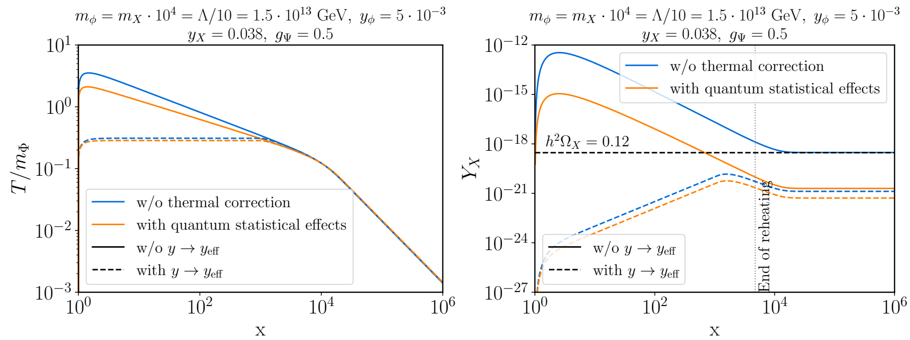

Figure 3.9: Time evolution of the radiation bath's temperature and DM yield assuming a production from a dimension-9 operator, see Eq. (3.59). The solid lines are identical to Fig. 3.8, the dashed lines use the effective Yukawa coupling (3.57).

3.3.2 UV-dominated freeze-in due to Boltzmann suppression

As a second counter-example, we consider Dark Matter production mediated by a Fermi-like four-fermion interaction, following the setup introduced in Sec. 3.2.2, cf. Eq. (3.46). In contrast to the previous example, the production mechanism in this case is controlled by both kinematics and Boltzmann suppression effects. The possibility of achieving UV-dominated freeze-in via Boltzmann suppression has previously been pointed out in renormalisable models, see [17, 157].

In order for the production to be most efficient at early times, i.e. close to the maximal temperature reached during reheating, we require the Dark Matter particle to be heavy, $m_X \gtrsim m_\varphi$. We further impose $m_{\Psi_1} = m_X$, which forbids vacuum decays of the Dark Matter particle. This choice also eliminates potential contributions from three-body decays of Ψ_1, thereby isolating the thermal production channel and enhancing the sensitivity to reheating dynamics.

For definiteness, we adopt the parameter values

$$m_{Z'} \simeq 1.5 \cdot 10^{17}\ \text{GeV} \gg T\ , \tag{3.61}$$

$$m_X = m_{\Psi_1} = 10\, m_\varphi\ . \tag{3.62}$$

The heavy mediator Z' can thus be integrated out, leading to an effective Fermi-like interaction.

A crucial ingredient in this setup is the presence of an additional heavy fermion Ψ_1 that is distinct from X but remains in thermal equilibrium with

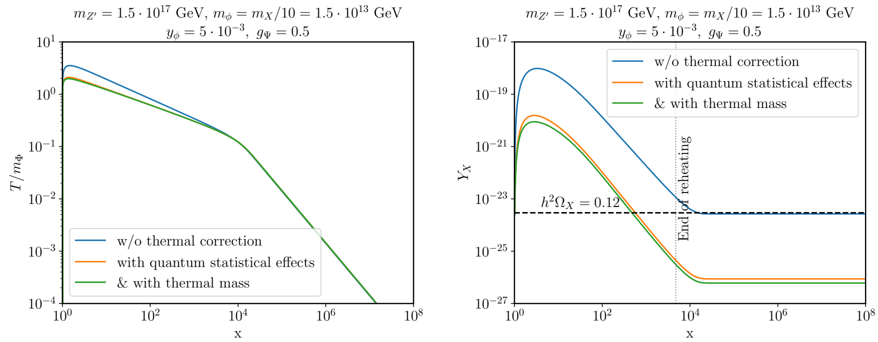

Figure 3.10: Time evolution (as a function of the scale factor $x = am_\varphi$) of the plasma temperature (left) and Dark Matter yield (right) for production via a Fermi-like interaction. The production rates are given in Eq. (**??**). In the right panel, the dashed horizontal line corresponds to the observed Dark Matter abundance, while the dotted vertical line marks the end of reheating.

the plasma. This ensures that the production rate of Dark Matter inherits an exponential Boltzmann suppression at temperatures below m_X. If, instead, Ψ_1 were replaced by the out-of-equilibrium Dark Matter particle itself, this suppression would be significantly weakened, reducing the sensitivity to thermal effects during reheating.

Impact of thermal effects. The evolution of the Dark Matter abundance is shown in Fig. 3.10. In the present setup, the condition $m_X = m_{\Psi_1} \lesssim T_{\max}$ is satisfied, implying that the dominant production occurs at the highest temperatures achieved during reheating. As in the previous example, the mechanism is therefore effectively UV-dominated.

This feature makes the final Dark Matter abundance particularly sensitive to modifications of the reheating dynamics. Including quantum statistical effects in the inflaton decay rate leads to a reduction of the maximal temperature by a factor of $\mathcal{O}(2)$. Despite its modest size, this effect translates into a substantial suppression of the Dark Matter yield, typically by about two orders of magnitude, as can be seen in the right panel of Fig. 3.10.

Model-building considerations. It is important to note that the strong sensitivity to thermal effects in this example relies on a specific set of assumptions. In particular, the heavy fermion Ψ_1 must remain in thermal equilibrium despite having a mass comparable to that of the Dark Matter particle. This

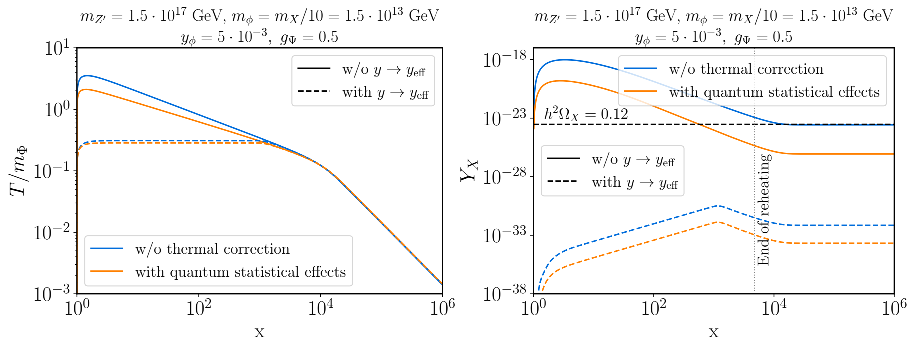

Figure 3.11: Time evolution (as function of the scale factor $x = am_\varphi$) of the radiation bath's temperature T and DM yield Y_X assuming a production from a Fermi-like interaction, see Eq. (**??**). The solid lines are identical to Fig. 3.8, the dashed lines use the effective Yukawa coupling (3.57).

requires the existence of additional interactions capable of efficiently coupling Ψ_1 to the plasma.

Such interactions, for instance of the form $(\bar{\Psi}_1 \ell)\,\varphi$, where ℓ and φ are lighter degrees of freedom (with ℓ a fermion and φ a scalar), may introduce new phenomenological complications. They can open additional production channels for Dark Matter or even jeopardise its stability through higher-order decay processes such as $X \to \Psi_2 + \ell + \varphi + \cdots$. Although it may be possible to suppress these effects in a carefully constructed model, this example illustrates that achieving a large impact of thermal corrections within a fully consistent UV completion can be non-trivial.

This observation reinforces the broader point of this section: while thermal effects can, in principle, induce sizable modifications to the Dark Matter abundance during perturbative reheating, constructing realistic scenarios in which these effects dominate requires non-trivial model-building ingredients.

3.3.3 UV-dominated freeze-in from threshold effects

As a final counterexample, we consider a situation in which UV-dominated DM production arises from kinematic threshold effects that are sensitive to screening in the thermal plasma. We work with the renormalisable model introduced in Eq. (3.38). In order for the parent particle P to thermalise, it must have additional interactions beyond those responsible for DM production. These interactions modify the in-medium dispersion relation of P, an effect which we neglected in Sec. 3.2.1. In the simplest approximation, this can be described by a momentum-independent thermal mass M_P.

Thermal corrections to the parent mass can have an important impact on the production rate Γ_X, as discussed in Sec. 3 of [135]. When DM production is dominated by the decay $P \to X f_R$, increasing M_P reduces the lifetime of the parent particle and can therefore enhance the production rate. If the thermal mass originates from gauge interactions, however, at least one of the decay products must be charged under the same gauge group and will also acquire a comparable thermal mass. In that case, the phase space for $P \to X f_R$ can become suppressed at high temperature, and scattering processes may become increasingly important for $T > m_P$.

This conclusion can be avoided if the large thermal correction to M_P is mainly generated by scalar self-interactions, such as $(P^\dagger P)^2$, or by additional Yukawa interactions with other fields. Then the thermal mass of P can be larger than those of the decay products, so that the decay channel remains the dominant contribution to Γ_X even for $T > m_P$. In such a setup, the decay may be forbidden in vacuum,

$$m_P < m_X + m_{f_R}, \tag{3.63}$$

but become allowed in the plasma once the masses are replaced by their thermal counterparts,

$$M_P > M_X + M_{f_R}. \tag{3.64}$$

This provides a simple way to realise UV-dominated freeze-in.

For illustration, we use the parametrisation

$$M_P^2 = m_P^2 + \frac{\lambda_P T^2}{24}, \tag{3.65}$$

and choose

$$m_P = m_\varphi/5 \ \ , m_{f_R} = m_\varphi/8 \ \ , m_X = m_\varphi/10 \ \ , y_X = 6 \cdot 10^{-7} \ \ , \lambda_P = 0.25 \, . \tag{3.66}$$

The DM production rate is computed using the full thermal expression in Eq. (3.40).

The resulting temperature evolution and DM yield are shown in Fig. 3.12. The left panel shows that DM production shuts off during reheating once the decay $P \to X f_R$ becomes kinematically forbidden. Consequently, when Pauli

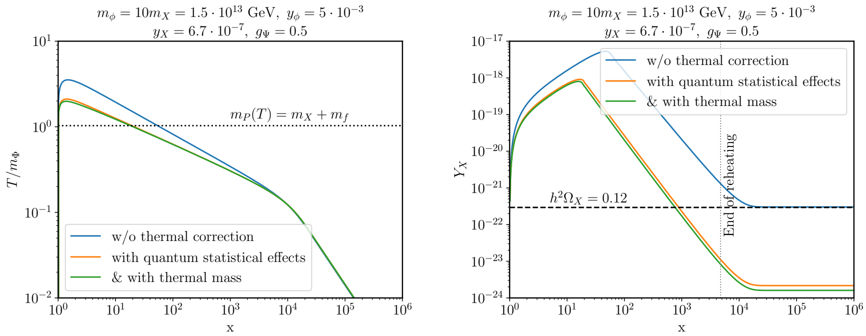

Figure 3.12: Time evolution, as a function of the scale factor $x = am_\varphi$, of the radiation bath temperature T and the DM yield Y_X. The dotted line in the left panel denotes the threshold temperature below which DM production is kinematically forbidden. In the right panel, the dashed horizontal line represents the observed present-day DM yield, while the dotted vertical line marks the end of reheating.

blocking is included systematically in the inflaton decay rate, the maximal temperature is reduced, the decay channel closes earlier, and the DM abundance freezes in sooner. The produced abundance then undergoes a longer period of dilution, leading to a suppression of the final yield by more than two orders of magnitude.

In this example, the sensitivity of the relic abundance to thermal effects arises from the combination of Pauli blocking in Γ_φ and the screening correction to the parent-particle mass. However, as in the previous counterexamples, the uncertainty associated with modelling fermionic reheating is even larger than the thermal correction itself. Indeed, Fig. 3.12 was obtained by computing Γ_φ using (3.55); if instead the effective coupling (3.57) is used, the temperature never becomes large enough for M_P to exceed the threshold required for P-decays into DM, and no DM is produced through this channel.

Finally, we stress that this simplified setup neglects scatterings mediated by P and f_R, which could either enhance or deplete the final DM abundance. Although scatterings are usually subdominant to decays in the regime studied in Sec. 3.2.1, this need not remain true once the decay channel becomes kinematically inaccessible. Moreover, interactions strong enough to generate a sizeable thermal mass for P will generally also induce scattering processes, which may dominate unless the thermal correction to M_P mainly originates from self-interactions [135]. A quantitative treatment of these effects is left for future work. This reinforces the broader point that constructing a complete

UV model of DM production during perturbative reheating in which thermal effects significantly modify the relic abundance is highly non-trivial.

3.4 Discussion and conclusion

In this chapter, we have investigated the role of finite-temperature effects in Dark Matter production during cosmic reheating. Our analysis focused on the impact of quantum statistical corrections and screening effects in the primordial plasma, which modify both the inflaton dissipation rate Γ and the Dark Matter production rate Γ_X. A key motivation for this study lies in the prospect of constraining the thermal history of the Universe during reheating with future CMB observations, thereby enabling connections between cosmological measurements and laboratory searches for Dark Matter.

The main result of our analysis, presented in Secs. 3.1 and 3.2, is that finite-temperature corrections to Γ and Γ_X generally have a limited impact on the predicted Dark Matter relic abundance in regimes where they can be reliably computed within finite-temperature quantum field theory. This behaviour is illustrated in Figs. 3.1 and 3.6. In particular, these corrections remain subdominant in scenarios where the reheating dynamics is sufficiently simple such that the thermal history can be reconstructed from a small set of parameters constrained by observations.

We further demonstrated in Figs. 3.2 and 3.3–3.5 how cosmological observations, especially from next-generation CMB experiments, can provide constraints that are complementary to those obtained from collider searches. In certain scenarios, such as the one shown in Fig. 3.4, CMB data have the potential to exclude regions of parameter space that are beyond the reach of current and near-future laboratory experiments.

In Sec. 3.3, we discussed a number of scenarios in which thermal effects can significantly alter the Dark Matter relic abundance, in some cases by several orders of magnitude (see Figs. 3.8–3.12). However, these cases do not contradict the general conclusion stated above, as they typically lie outside the regime where a perturbative treatment of reheating is fully reliable. Indeed, our analysis indicates that even in scenarios such as fermionic reheating, where perturbative methods are often assumed to be applicable, the determination of the thermal history can be subject to substantial theoretical uncertainties. These uncertainties can exceed the quantitative impact of finite-temperature corrections themselves, thereby limiting the predictive power of perturbative approaches for relic density computations. This observation highlights the need for a more robust and quantitative understanding of reheating dynamics in realistic particle physics models.

Finally, we derive the estimate (3.24) for the inflaton mass scale in a general two-parameter inflationary models of the form Eq.(F.1) see (F.5), this relation holds in particular for α-attractor models, and remains indicative for several other models (though it can be violated for certain parameter choices).

Chapter 4

General Summary and Conclusions

The transition from inflation to the hot Big Bang, known as cosmic reheating, is one of the least understood epochs in the history of the Universe. During this period, the energy stored in the inflaton field is transferred to a thermal plasma, setting the initial conditions for the subsequent evolution of the Universe and determining the production of relic particles such as Dark Matter. A quantitative description of this process requires understanding particle production in a hot and evolving medium, where interactions are modified by thermal effects, collective phenomena, and non-equilibrium dynamics.

In this thesis, we investigate particle production during cosmic reheating using the framework of real-time non-equilibrium quantum field theory. We develop the theoretical tools required to describe particle production and dissipation in thermal environments, with particular emphasis on the Closed Time Path formalism and the role of spectral functions and self-energies in determining in-medium interaction rates. This framework provides a unified description of quasiparticle propagation, dissipation, and particle production, and allows medium effects to be systematically incorporated from first principles.

We then study the impact of thermal effects on inflaton dissipation and particle production rates. Using scalar field theories as a laboratory, we investigate the role of thermal masses, modified dispersion relations, finite-width effects, and higher-order corrections. We show how the spectral structure of thermal self-energies determines the kinematics of particle production in a medium and governs the transfer of energy from the inflaton to the plasma. In particular, thermal masses can kinematically suppress or completely block tree-level decay channels, while finite-width effects can smooth otherwise sharp thermal thresholds and reopen regions of phase space that are forbidden in the quasiparticle limit through off-shell contributions. We further show that going beyond the quasiparticle approximation is essential near kinematic boundaries, where a generalized pole expansion provides a more accurate description of the spectral density than the commonly used Breit–Wigner approximation. At next-to-leading order, scattering and other medium-induced processes can remain active even when tree-level decay channels are blocked by thermal masses, thereby providing additional channels for energy transfer to the plasma. More generally, we find that the thermal medium blurs the distinction between processes that are separate in vacuum, causing different contributions to become intertwined and allowing interference effects to play an important role in determining the net particle production rate. These results demonstrate that the dynamics of reheating cannot always be understood in terms of vacuum decay rates alone and highlight the importance of the full in-medium spectral structure.

We further investigate the implications of thermal effects for the production of Dark Matter during and after reheating in freeze-in scenarios. We quantify how thermal corrections modify particle production rates and assess their impact on the resulting relic abundance. We find that finite-temperature effects generally lead to modest corrections when perturbative calculations remain reliable, but we also identify scenarios in which thermal thresholds, Boltzmann suppressions, or higher-dimensional interactions can substantially alter the predicted Dark Matter abundance. These results clarify when simplified treatments of reheating are sufficient and when a detailed description of the thermal history becomes essential for reliable Dark Matter predictions.

Finally, we explore the connection between reheating, Dark Matter production, and cosmological observables. We show how future measurements of the Cosmic Microwave Background can constrain the reheating history and provide information complementary to laboratory probes of particle physics.

Overall, this thesis develops a systematic framework for studying particle production in thermal environments and clarifies the role of medium effects in cosmic reheating, inflaton dissipation, and Dark Matter generation. By combining real-time quantum field theory with cosmological applications, it identifies the physical mechanisms that govern energy transfer in the early Universe and determines how they influence the production of Dark Matter and the interpretation of cosmological observations.

Appendix A

Tree-Level Result

A.1 Reduction of the Energy Delta Functions

In the rest frame of the inflaton we set $\omega = m$. The quasiparticle energies are

$$\omega_1 = \sqrt{\boldsymbol{p}^2 + m_1^2}, \qquad \omega_2 = \sqrt{\boldsymbol{p}^2 + m_2^2}. \tag{A.1}$$

It is convenient to eliminate the momentum in favor of ω_1, which gives

$$\omega_2 = \sqrt{\omega_1^2 - m_1^2 + m_2^2}. \tag{A.2}$$

The delta functions appearing in the self-energy integrals constrain the energies of the intermediate quasiparticles. Their reduction can be performed using the identity

$$\delta(f(x)) = \sum_i \frac{\delta(x - x_i)}{|f'(x_i)|}, \tag{A.3}$$

where x_i are the roots of $f(x)$.

A.2 Combined reduction of $\delta(\omega - \omega_1 \pm \omega_2)$

The two delta functions

$$\delta(\omega - \omega_1 - \omega_2), \qquad \delta(\omega - \omega_1 + \omega_2), \tag{A.4}$$

can be treated simultaneously. To this end, define

$$g_\pm(\omega_1) = \omega - \omega_1 \pm \omega_2 = \omega - \omega_1 \pm \sqrt{\omega_1^2 - m_1^2 + m_2^2}. \tag{A.5}$$

The corresponding root is obtained from the condition

$$g_\pm(\omega_1) = 0 \qquad \Longrightarrow \qquad \omega - \omega_1 = \mp \omega_2. \tag{A.6}$$

Squaring both sides yields in both cases

$$(\omega - \omega_1)^2 = \omega_1^2 - m_1^2 + m_2^2, \tag{A.7}$$

so that the solution is

$$\omega_1 = \bar{\omega}_1 = \frac{\omega^2 + m_1^2 - m_2^2}{2\omega}, \qquad \bar{\omega}_2 = \frac{\omega^2 - m_1^2 + m_2^2}{2\omega}. \tag{A.8}$$

The derivative of $g_\pm$ is

$$g'_\pm(\omega_1) = -1 \pm \frac{\omega_1}{\omega_2}. \tag{A.9}$$

Evaluating at the root gives

$$|g'_\pm(\bar{\omega}_1)| = \frac{\omega}{\bar{\omega}_2}, \tag{A.10}$$

where the sign information is encoded in the kinematic domain of the root.

Using the identity Eq. (A.3), we therefore obtain the unified expression

$$\delta(\omega - \omega_1 \pm \omega_2) = \frac{\bar{\omega}_2}{\omega}\, \delta(\omega_1 - \bar{\omega}_1)\, \theta\big(\pm(\omega - \omega_1)\big). \tag{A.11}$$

Equivalently, writing the two cases separately,

$$\delta(\omega - \omega_1 - \omega_2) = \frac{\bar{\omega}_2}{\omega}\, \delta(\omega_1 - \bar{\omega}_1)\, \theta(\omega - \omega_1), \tag{A.12}$$

$$\delta(\omega - \omega_1 + \omega_2) = \frac{\bar{\omega}_2}{\omega}\, \delta(\omega_1 - \bar{\omega}_1)\, \theta(\omega_1 - \omega). \tag{A.13}$$

The two step functions distinguish the kinematic regions corresponding to the decay process $\phi \to \chi_1 + \chi_2$ and the inverse-decay process $\chi_1 \to \phi + \chi_2$, depending on whether the inflaton energy is larger or smaller than the energy of the intermediate quasiparticle.

Equations (A.12) and (A.13) allow the energy integrals in the self-energy to be carried out analytically, leaving only the kinematic constraints encoded by the step functions.

A.3 Contribution from $\delta(\omega + \omega_1 - \omega_2)$

Finally we consider the delta function

$$\delta(\omega + \omega_1 - \omega_2). \tag{A.14}$$

Defining

$$\varrho(\omega_1) = \omega + \omega_1 - \omega_2, \tag{A.15}$$

the constraint $\varrho(\omega_1) = 0$ implies

$$\omega_2 = \omega + \omega_1. \tag{A.16}$$

Squaring both sides yields

$$(\omega + \omega_1)^2 = \omega_1^2 - m_1^2 + m_2^2. \tag{A.17}$$

Solving for ω_1 gives

$$\omega_1 = \frac{m_2^2 - \omega^2 - m_1^2}{2\omega} \equiv \tilde{\omega}_1. \tag{A.18}$$

This solution can be written in terms of the root obtained previously as $\tilde{\omega}_1 = -\bar{\omega}_1$. Eq: A.8. The derivative of ϱ is

$$\varrho'(\omega_1) = 1 - \frac{\omega_1}{\omega_2}. \tag{A.19}$$

Evaluating this at the root gives

$$|\varrho'(\tilde{\omega}_1)| = \frac{\omega}{\omega_2}. \tag{A.20}$$

Applying the delta-function identity then yields

$$\delta(\omega + \omega_1 - \omega_2) = \frac{\omega_2|_{\tilde{\omega}_1}}{\omega}\, \delta(\omega_1 - \tilde{\omega}_1)\, \theta(\omega_2 - \omega). \tag{A.21}$$

The step function reflects the kinematic condition $\omega_2 > \omega$ required by the constraint $\omega + \omega_1 - \omega_2 = 0$.

Appendix B

Four-Pole form of the spectral density

We will start from the renormalized spectral density Eq. 2.44, which reads

$$\rho_r = Z^{-1}\frac{-2\mathrm{Im}\Pi^R + 2p_0\epsilon}{\left(p_0^2 - \Omega_{\mathbf{p}}^2 - \mathrm{Re}\Pi^R\right)^2 + \left(\mathrm{Im}\Pi^R - p_0\epsilon\right)^2} \tag{B.1}$$

and derive its four-pole form given in Eq. (2.55). In the following, we suppress the index i, since the derivation applies identically to both spectral densities in Eq. (2.44). We work in the upper half-plane, corresponding to closing the contour for positive values of p_0. For $p_0 > 0$, the spectral function is positive definite, $\rho^r_{\boldsymbol{p}}(p_0) > 0$. We make the coordinate change from $(p^2, p.u)$ to $(p_0^2, \boldsymbol{p}^2)$ and expand the real and imaginary parts of Π^R as functions of p_0^2, around the pole $\mathcal{W}_{r\mathbf{p}}$

$$\mathcal{W}_{ir\mathbf{p}}^2 = \Omega_{i\mathbf{p}}^2 + Re\Pi_{i\boldsymbol{p}}^R(\mathcal{W}_{ir\mathbf{p}}^2) \tag{B.2}$$

as follows

$$\mathrm{Re}\Pi_{\boldsymbol{p}}^R(p_0) = \mathrm{Re}\Pi_{\boldsymbol{p}}^R\left(\mathcal{W}_{r\mathbf{p}}\right) + \left(p_0^2 - \mathcal{W}_{r\mathbf{p}}^2\right)\frac{d}{dp_0^2}\mathrm{Re}\Pi_{\boldsymbol{p}}^R(p_0^2)|_{p_0^2=\mathcal{W}_{r\mathbf{p}}^2} \tag{B.3}$$

$$\mathrm{Im}\Pi_{\boldsymbol{p}}^R(p_0) = \mathrm{Im}\Pi_{\boldsymbol{p}}^R(\mathcal{W}_{r\mathbf{p}}) + \left(p_0^2 - \mathcal{W}_{r\mathbf{p}}^2\right)\frac{d}{dp_0^2}\mathrm{Im}\Pi_{\boldsymbol{p}}^R(p_0^2)|_{p_0^2=\mathcal{W}_{r\mathbf{p}}^2} \tag{B.4}$$

We need to solve

$$p_0^2 - \Omega_{\mathbf{p}}^2 - Re\Pi_{\boldsymbol{p}}^R(p_0) = \alpha i\left(\mathrm{Im}\Pi_{\boldsymbol{p}}^R(p_0) - p_0\epsilon\right) \tag{B.5}$$

where $\alpha = \pm$. Substituting the Taylor expansions (B.3)–(B.4), this equation can be brought into the quadratic form

$$p_0^2 + i\alpha\tilde{\epsilon}_\alpha p_0 - B_\alpha = 0 \tag{B.6}$$

Where

$$B_\alpha = \mathcal{W}_{r\boldsymbol{p}}^2 + i\alpha\mathcal{Z}_\alpha \,\mathrm{Im}\,\Pi^R(\mathcal{W}_{r\boldsymbol{p}})\,, \tag{B.7}$$

$$\tilde{\epsilon}_\alpha = \mathcal{Z}_\alpha\,\epsilon\,, \qquad \mathcal{Z}_\alpha = \mathcal{R} + i\alpha\mathcal{D}\,. \tag{B.8}$$

Here we have introduced

$$\mathcal{R} = \frac{1 - \frac{d}{d(p_0^2)}\mathrm{Re}\Pi_{\boldsymbol{p}}^R(p_0^2)\Big|_{p_0^2=\mathcal{W}_{r\mathbf{p}}^2}}{\left(1 - \frac{d}{d(p_0^2)}\mathrm{Re}\Pi_{\boldsymbol{p}}^R(p_0^2)\Big|_{p_0^2=\mathcal{W}_{r\mathbf{p}}^2}\right)^2 + \left(\frac{d}{dp_0^2}\mathrm{Im}\Pi_{\boldsymbol{p}}^R(p_0^2)\Big|_{p_0^2=\mathcal{W}_{r\mathbf{p}}^2}\right)^2} \tag{B.9}$$

$$\mathcal{D} = \frac{\frac{d}{dp_0^2}\mathrm{Im}\Pi_{1\boldsymbol{p}}^R(p_0^2)\Big|_{p_0^2=\mathcal{W}_{r\mathbf{p}}^2}}{\left(1 - \frac{d}{d(p_0^2)}\mathrm{Re}\Pi_{\boldsymbol{p}}^R(p_0^2)\Big|_{p_0^2=\mathcal{W}_{r\mathbf{p}}^2}\right)^2 + \left(\frac{d}{dp_0^2}\mathrm{Im}\Pi_{\boldsymbol{p}}^R(p_0^2)\Big|_{p_0^2=\mathcal{W}_{r\mathbf{p}}^2}\right)^2} \tag{B.10}$$

We denote the two solutions of Eq.B.6 by $p_0 = \hat{\Omega}_{\pm\alpha}$, which, using the definitions above, can be written as

$$\hat{\Omega}_{\pm\alpha} = \frac{1}{2}\tilde{\epsilon} \pm \left(\mathcal{W}_{r\mathbf{p}} - \frac{1}{2}\mathcal{D}\frac{\mathrm{Im}\Pi_{\boldsymbol{p}}^R(\mathcal{W}_{r\mathbf{p}})}{\mathcal{W}_{r\mathbf{p}}}\right) + \frac{i\alpha}{2}\left(-\epsilon \pm \mathcal{R}\frac{\mathrm{Im}\Pi_{\boldsymbol{p}}^R(\mathcal{W}_{r\mathbf{p}})}{\mathcal{W}_{r\mathbf{p}}}\right) \tag{B.11}$$

For $p_0 > 0$, the physical poles are given by

$$\hat{\Omega} = \left(\mathcal{W}_{r\mathbf{p}} - \frac{\mathcal{D}}{2}\left(\frac{\mathrm{Im}\Pi_{\boldsymbol{p}}^R(\mathcal{W}_{r\mathbf{p}})}{\mathcal{W}_{r\mathbf{p}}} - \epsilon\right)\right) - \frac{i}{2}\mathcal{R}\left(\frac{\mathrm{Im}\Pi_{\boldsymbol{p}}^R(\mathcal{W}_{r\mathbf{p}})}{\mathcal{W}_{r\mathbf{p}}} - \epsilon\right) \tag{B.12}$$

$$\hat{\Omega}^* = \left(\mathcal{W}_{r\mathbf{p}} - \frac{\mathcal{D}}{2}\left(\frac{\mathrm{Im}\Pi_{\boldsymbol{p}}^R(\mathcal{W}_{r\mathbf{p}})}{\mathcal{W}_{r\mathbf{p}}} - \epsilon\right)\right) + \frac{i}{2}\mathcal{R}\left(\frac{\mathrm{Im}\Pi_{\boldsymbol{p}}^R(\mathcal{W}_{r\mathbf{p}})}{\mathcal{W}_{r\mathbf{p}}} - \epsilon\right) \tag{B.13}$$

where we defined $\Omega_{-+} \equiv \hat{\Omega}$, and $\Omega_{++} \equiv \hat{\Omega}^*$. For $\mathcal{W}_{r\mathbf{p}} \gg \mathrm{Im}\Pi_{\boldsymbol{p}}^R(\mathcal{W}_{r\mathbf{p}})$ and working at $\mathcal{O}(g^2)$ we find

$$\hat{\Omega} = \Omega + \frac{i}{2}\Gamma \tag{B.14}$$

In the coupling expansion both $\mathrm{Im}\Pi^R_{\boldsymbol{p}}, \mathcal{D}_2 \sim \mathcal{O}(g^2)$, and we get

$$\Omega = \mathcal{W}_{r\mathbf{p}} \tag{B.15}$$

$$\Gamma = -\mathcal{Z}\left(\frac{\mathrm{Im}\Pi^R_{\boldsymbol{p}}(\Omega)}{\Omega} - \epsilon\right) \tag{B.16}$$

Therefore, for $p_0 > 0$ we get

$$\rho^r_{\boldsymbol{p}}(p_0)\Big|_{p_0>0} = Z^{-1}\frac{\left(-2\mathrm{Im}\Pi^R_{\boldsymbol{p}}(p_0) + 2p_0\epsilon\right)\mathcal{X}}{\left(p_0 - \hat{\Omega}\right)\left(p_0 - \hat{\Omega}^*\right)} \tag{B.17}$$

where, $\mathcal{X}(p_0)$ is smooth at the pole positions.

Using the antisymmetry property $\rho^r_{\boldsymbol{p}}(p_0) = -\rho^r_{\boldsymbol{p}}(-p_0)$, the poles for $p_0 < 0$ are located at

$$p_0 = -\hat{\Omega}, \quad -\hat{\Omega}^*\,. \tag{B.18}$$

Requiring regularity at $p_0 = 0$ fixes the structure of the numerator functions and leads to the full four-pole representation

$$\rho^r_{\boldsymbol{p}}(p_0) = Z^{-1}C\,\frac{-2\,\mathrm{Im}\,\Pi^R(p_0) + 2p_0\epsilon}{(p_0 - \hat{\Omega})(p_0 - \hat{\Omega}^*)(p_0 + \hat{\Omega})(p_0 + \hat{\Omega}^*)}\,. \tag{B.19}$$

The constant C is fixed by the normalization condition $\int_{-\infty}^{\infty}\frac{dp_0}{2\pi}p_0\rho^r(p_0) = 1$ which yield $C_1 = Z_1\mathcal{R}_1$. At leading Order in the coupling $\mathcal{O}(g^2)$ we can write

$$\rho^r_{\boldsymbol{p}}(p_0) = \mathcal{Z}\,\frac{-2\,\mathrm{Im}\,\Pi^R(p_0) + 2p_0\epsilon}{(p_0 - \hat{\Omega})(p_0 - \hat{\Omega}^*)(p_0 + \hat{\Omega})(p_0 + \hat{\Omega}^*)}\,, \tag{B.20}$$

which is the desired 4-pole representation Eq. (2.55).

Appendix C

Derivation of the Diagonal-Cut Integrand

In this appendix we derive the explicit form of the integrand appearing in the diagonal-cut contribution discussed in Sec. 2.7.1. Starting from Eq. (2.106), the relevant combination of propagators is

$$I_2^{\mathcal{P}} = -\Delta_1^{<}(k)\Delta_2^{\mathcal{P}}(p-k)\Delta_\phi^{<}(q)\Delta_1^{<}(p-k-q)\Delta_2^{\mathcal{P}}(q+k). \tag{C.1}$$

The three propagators intersected by the cut appear as Wightman propagators, while the remaining propagators contribute through their principal-value parts.

Insertion of Wightman propagators

Using the definition of the Wightman,

$$\Delta^{<}(k) = 2\pi\,\mathrm{sign}(k_0)\,f(k_0)\,\delta(k^2-m^2), \tag{C.2}$$

we obtain

$$\begin{aligned} I_2^{\mathcal{P}} = -\Delta_2^{\mathcal{P}}(p-k)\Delta_2^{\mathcal{P}}(q+k)\,\delta(k^2-m_1^2)\delta(q^2-m_\phi^2)\delta((p-k-q)^2-m_1^2) \\ \times (2\pi)^3\mathrm{sign}(k_0)\mathrm{sign}(q_0)\mathrm{sign}(\omega-k_0-q_0)f(k_0)f(q_0)f(\omega-k_0-q_0). \end{aligned} \tag{C.3}$$

The three delta functions enforce the on-shell conditions for the particles crossing the cut.

Decomposition of the on-shell delta functions

The first delta function can be written as

$$\delta(k^2 - m_1^2) = \frac{1}{2\omega_1}\left[\delta(k_0 - \omega_1) - \delta(k_0 + \omega_1)\right], \tag{C.4}$$

where $\omega_1 = \sqrt{\mathbf{k}^2 + m_1^2}$. Substituting this expression into the integrand yields

$$\begin{aligned} I_2^{\mathcal{P}} = &-\frac{(2\pi)^3}{2\omega_1}\mathrm{sign}(q_0) f(q_0)\delta(q_0^2 - \tilde{\omega}^2) \\ &\times \Bigg\{ \delta(k_0 - \omega_1) f(\omega_1)\Delta_2^{\mathcal{P}}(p-k)\Delta_2^{\mathcal{P}}(q+k) \\ &\qquad \times \mathrm{sign}(\omega - \omega_1 - q_0) f(\omega - \omega_1 - q_0)\delta((m_\phi - \omega_1 - q_0)^2 - \tilde{\omega}_1^2) \\ &- (\omega_1 \to -\omega_1)\Bigg\}. \end{aligned} \tag{C.5}$$

The delta function $\delta(q^2 - m_\phi^2)$ can be decomposed similarly,

$$\delta(q_0^2 - \tilde{\omega}^2) = \frac{1}{2\tilde{\omega}}\left[\delta(q_0 - \tilde{\omega}) - \delta(q_0 + \tilde{\omega})\right], \tag{C.6}$$

where $\tilde{\omega} = \sqrt{\mathbf{q}^2 + m_\phi^2}$.
After inserting this expression we obtain

$$\begin{aligned} I_2^{\mathcal{P}} = &-\frac{(2\pi)^3}{4\omega_1\tilde{\omega}}\Bigg\{ f(\tilde{\omega})\delta(q_0 - \tilde{\omega}) \\ &\times \Big[\delta(k_0 - \omega_1) f(\omega_1)\Delta_2^{\mathcal{P}}(p-k)\Delta_2^{\mathcal{P}}(q+k) \\ &\times \mathrm{sign}(\omega - \omega_1 - \tilde{\omega}) f(\omega - \omega_1 - \tilde{\omega})\delta((m_\phi - \omega_1 - \tilde{\omega})^2 - \tilde{\omega}_1^2) \\ &- (\omega_1 \to -\omega_1)\Big] - (\tilde{\omega} \to -\tilde{\omega})\Bigg\}. \end{aligned} \tag{C.7}$$

Energy conservation along the cut

The remaining delta function can be decomposed as

$$\delta((m_\phi - \omega_1 - \tilde{\omega})^2 - \tilde{\omega}_1^2) = \frac{1}{2\tilde{\omega}_1}\Big[\delta(m_\phi - \omega_1 - \tilde{\omega} - \tilde{\omega}_1) \\ - \delta(m_\phi - \omega_1 - \tilde{\omega} + \tilde{\omega}_1)\Big], \qquad \text{(C.8)}$$

which enforces energy conservation across the cut. After collecting all factors we obtain

$$I_2^{\mathcal{P}} = -\frac{\pi^3}{\omega_1 \tilde{\omega} \tilde{\omega}_1}\Bigg\{ f(\tilde{\omega})\delta(q_0 - \tilde{\omega})\Big[\Big\{\delta(k_0 - \omega_1)\delta(m_\phi - \omega_1 - \tilde{\omega} - \tilde{\omega}_1) \\ \times f(\omega_1) f(\tilde{\omega}_1) \Delta_2^{\mathcal{P}}(p-k)\Delta_2^{\mathcal{P}}(q+k) - (\tilde{\omega}_1 \to -\tilde{\omega}_1)\Big\} \\ - (\omega_1 \to -\omega_1)\Big] - (\tilde{\omega} \to -\tilde{\omega})\Bigg\}. \qquad \text{(C.9)}$$

Principal-value propagators

We now evaluate the two propagators that are not intersected by the cut. These appear through their principal-value parts.

We first introduce the on-shell energies associated with the internal momenta,

$$\omega_1 = \sqrt{\mathbf{k}^2 + m_1^2}, \qquad \text{(C.10)}$$

$$\omega_2 = \sqrt{\mathbf{p}_2^2 + m_2^2}, \qquad \text{(C.11)}$$

where $\mathbf{p}_2 = \mathbf{p} - \mathbf{k}$ denotes the spatial momentum flowing through the propagator $\Delta_2(p-k)$.

Using these definitions, the principal-value propagator can be written as

$$\Delta_2^{\mathcal{P}}(p-k) = i\,\mathcal{P}\left(\frac{1}{(m_\phi - \omega_1)^2 - \omega_2^2}\right). \qquad \text{(C.12)}$$

Expanding the denominator yields

$$\Delta_2^{\mathcal{P}}(p-k) = i\,\mathcal{P}\left(\frac{1}{m_\phi^2 + m_1^2 - m_2^2 - 2m_\phi\omega_1}\right). \qquad \text{(C.13)}$$

It is convenient to introduce the quantities

$$\bar{\omega}_1 = \frac{m_\phi^2 + m_1^2 - m_2^2}{2m_\phi}, \tag{C.14}$$

$$\bar{\omega}_2 = \frac{m_\phi^2 - m_1^2 + m_2^2}{2m_\phi}, \tag{C.15}$$

which satisfy

$$\bar{\omega}_1 + \bar{\omega}_2 = m_\phi. \tag{C.16}$$

These quantities correspond to the tree-level energies of the particles in the decay process $\phi \to \chi_1\chi_2$ evaluated in the rest frame of the parent particle.

Using this notation the principal-value propagator becomes

$$\Delta_2^{\mathcal{P}}(p-k) = \frac{i}{2m_\phi}\mathcal{P}\left(\frac{1}{\bar{\omega}_1 - \omega_1}\right). \tag{C.17}$$

A similar expression is obtained for the second propagator,

$$\Delta_2^{\mathcal{P}}(q+k) = \frac{i}{2m_\phi}\mathcal{P}\left(\frac{1}{\omega_1 + \tilde{\omega} - \bar{\omega}_2}\right). \tag{C.18}$$

We therefore see that the poles of the principal-value propagators occur at

$$\omega_1 = \bar{\omega}_1, \qquad \omega_1 + \tilde{\omega} = \bar{\omega}_2, \tag{C.19}$$

The appearance of these poles has a simple physical interpretation. The quantities $\bar{\omega}_1$ and $\bar{\omega}_2$ correspond to the tree-level energies of the particles produced in the decay $\phi \to \chi_1\chi_2$ in the rest frame of the parent particle. The principal-value propagators therefore exhibit poles precisely at the tree-level kinematic configuration of this process. In the present diagram these poles do not correspond to additional on-shell particles, since the corresponding propagators are not intersected by the cut. Instead, they reflect the analytic structure of the virtual propagators that mediate the interaction, while the cut propagators enforce the on-shell conditions of the physical excitations circulating in the thermal plasma.

For compactness, we introduce the shorthand notation

$$\Delta_2^{\mathcal{P}}(\omega_1) \equiv \frac{i}{2m_\phi}\mathcal{P}\left(\frac{1}{\bar{\omega}_1 - \omega_1}\right), \tag{C.20}$$

$$\Delta_2^{\mathcal{P}}(\omega_1 + \tilde{\omega}) \equiv \frac{i}{2m_\phi}\mathcal{P}\left(\frac{1}{\omega_1 + \tilde{\omega} - \bar{\omega}_2}\right). \tag{C.21}$$

Substituting these expressions into Eq. (C.9) yields the compact representation used in the main text.

C.1 Analysis of Kinematic Support

We now determine which of the delta functions appearing in Eq. (C.9) have kinematic support. This amounts to checking whether the corresponding energy-conservation conditions can be satisfied for any values of the loop momenta $\boldsymbol{k}$ and $\boldsymbol{q}$.

We use the on-shell energies

$$\omega_1 = \sqrt{\boldsymbol{k}^2 + m_1^2}, \tag{C.22}$$

$$\tilde{\omega} = \sqrt{\boldsymbol{q}^2 + m_\phi^2}, \tag{C.23}$$

$$\tilde{\omega}_1 = \sqrt{(\boldsymbol{q}+\boldsymbol{k})^2 + m_1^2}, \tag{C.24}$$

which satisfy the inequalities

$$\omega_1 \geq |\boldsymbol{k}|, \qquad \tilde{\omega} \geq |\boldsymbol{q}|, \qquad \tilde{\omega}_1 \geq |\boldsymbol{q}+\boldsymbol{k}|. \tag{C.25}$$

1) $\delta(m_\phi - \omega_1 - \tilde{\omega} - \tilde{\omega}_1)$ This delta function requires

$$m_\phi = \omega_1 + \tilde{\omega} + \tilde{\omega}_1. \tag{C.26}$$

However, since all three energies are positive and satisfy

$$\omega_1 \geq m_1, \qquad \tilde{\omega}_1 \geq m_1, \qquad \tilde{\omega} \geq m_\phi, \tag{C.27}$$

we obtain

$$\omega_1 + \tilde{\omega} + \tilde{\omega}_1 \geq m_\phi + 2m_1. \tag{C.28}$$

Therefore this equality cannot be satisfied, and the delta function $\delta(m_\phi - \omega_1 - \tilde{\omega} - \tilde{\omega}_1)$ has no kinematic support.

2) $\delta(m_\phi + \omega_1 - \tilde{\omega} + \tilde{\omega}_1)$ This delta function requires

$$\tilde{\omega} = m_\phi + \omega_1 + \tilde{\omega}_1. \tag{C.29}$$

To analyze this condition we first note that

$$\omega_1 = \sqrt{\boldsymbol{k}^2 + m_1^2} > |\boldsymbol{k}|, \tag{C.30}$$

$$\tilde{\omega}_1 = \sqrt{(\boldsymbol{q}+\boldsymbol{k})^2 + m_1^2} \geq |\boldsymbol{q}+\boldsymbol{k}|. \tag{C.31}$$

Therefore

$$\omega_1 + \tilde{\omega}_1 \geq |\boldsymbol{k}| + |\boldsymbol{q}+\boldsymbol{k}|. \tag{C.32}$$

Using the triangle inequality,

$$|\boldsymbol{q}| = |(\boldsymbol{q}+\boldsymbol{k}) - \boldsymbol{k}| \leq |\boldsymbol{q}+\boldsymbol{k}| + |\boldsymbol{k}|, \tag{C.33}$$

we obtain

$$\omega_1 + \tilde{\omega}_1 \geq |\boldsymbol{q}|. \tag{C.34}$$

On the other hand,

$$\tilde{\omega} = \sqrt{\boldsymbol{q}^2 + m_\phi^2} \leq |\boldsymbol{q}| + m_\phi. \tag{C.35}$$

Combining these relations gives

$$m_\phi + \omega_1 + \tilde{\omega}_1 > m_\phi + |\boldsymbol{q}| \geq \tilde{\omega}. \tag{C.36}$$

Hence the equality required by the delta function cannot be satisfied, and $\delta(m_\phi + \omega_1 - \tilde{\omega} + \tilde{\omega}_1)$ also has no kinematic support.

3) $\delta(m_\phi + \omega_1 + \tilde{\omega} - \tilde{\omega}_1)$ This delta function requires

$$\tilde{\omega}_1 = m_\phi + \omega_1 + \tilde{\omega}. \tag{C.37}$$

From the definitions of the energies we have

$$\tilde{\omega}_1^2 - \omega_1^2 = (\boldsymbol{q}+\boldsymbol{k})^2 - \boldsymbol{k}^2. \tag{C.38}$$

Using this relation one finds

$$\tilde{\omega}_1 - \omega_1 = \frac{(|\boldsymbol{q}+\boldsymbol{k}| - |\boldsymbol{k}|)(|\boldsymbol{q}+\boldsymbol{k}| + |\boldsymbol{k}|)}{\tilde{\omega}_1 + \omega_1}. \tag{C.39}$$

Since

$$|\boldsymbol{q}+\boldsymbol{k}| - |\boldsymbol{k}| \leq |\boldsymbol{q}|, \tag{C.40}$$

we obtain

$$\tilde{\omega}_1 - \omega_1 \leq |\boldsymbol{q}|. \tag{C.41}$$

This implies

$$\tilde{\omega}_1 \leq |\boldsymbol{q}| + \omega_1. \tag{C.42}$$

However, since $\tilde{\omega} \geq |\boldsymbol{q}|$, we have

$$m_\phi + \omega_1 + \tilde{\omega} > |\boldsymbol{q}| + \omega_1 \geq \tilde{\omega}_1. \tag{C.43}$$

Therefore the equality in Eq. (C.37) cannot be satisfied for any values of $\boldsymbol{k}$ and $\boldsymbol{q}$, and the delta function $\delta(m_\phi + \omega_1 + \tilde{\omega} - \tilde{\omega}_1)$ does not have kinematic support.

We conclude that the following delta functions do not contribute to the integral,

$$\begin{aligned} &\delta(m_\phi - \omega_1 - \tilde{\omega} - \tilde{\omega}_1), \quad \delta(m_\phi + \omega_1 - \tilde{\omega} + \tilde{\omega}_1), \\ &\delta(m_\phi + \omega_1 + \tilde{\omega} - \tilde{\omega}_1), \quad \delta(m_\phi + \omega_1 + \tilde{\omega} + \tilde{\omega}_1), \end{aligned} \tag{C.44}$$

since the corresponding energy-conservation conditions cannot be satisfied for any kinematically allowed configuration of the loop momenta.

Physical interpretation. The absence of kinematic support for the delta functions discussed above has a simple physical interpretation. Each delta function corresponds to a particular assignment of energy flow through the three on-shell lines crossed by the cut. The combinations that do not contribute would require the external particle ϕ to produce or absorb a set of excitations whose total energy exceeds the available energy m_ϕ, or whose energy balance would require negative-energy particles.

For example, the condition

$$m_\phi = \omega_1 + \tilde{\omega} + \tilde{\omega}_1 \tag{C.45}$$

would correspond to a process in which the single particle ϕ decays into three on-shell excitations. Since the minimal energy of these particles satisfies

$$\omega_1 + \tilde{\omega} + \tilde{\omega}_1 \geq m_\phi + 2m_1, \tag{C.46}$$

such a decay is kinematically forbidden.

Similarly, the conditions

$$\tilde{\omega} = m_\phi + \omega_1 + \tilde{\omega}_1, \qquad \tilde{\omega}_1 = m_\phi + \omega_1 + \tilde{\omega}, \tag{C.47}$$

would correspond to processes in which the plasma would need to absorb an amount of energy larger than that carried by the available on-shell excitations. In other words, these terms represent scattering channels that violate energy conservation once the positive-energy dispersion relations of the particles are taken into account.

Consequently, these delta functions correspond to unphysical energy-flow assignments and do not contribute to the diagonal cut. Only the remaining delta functions correspond to kinematically allowed processes, which represent physical interactions of the ϕ particle with on-shell excitations in the thermal plasma.

C.2 Kinematic Constraints from the Allowed Delta Functions

We now analyze the delta functions that remain after eliminating the kinematically forbidden contributions discussed in the previous section. Each of these delta functions fixes the relative angle between the loop momenta $\mathbf{k}$ and $\mathbf{q}$ and therefore reduces the original six-dimensional momentum integral to an integral over the on-shell energies ω_1 and $\tilde{\omega}$.

The angular dependence enters through

$$\tilde{\omega}_1^2 = (\mathbf{q} + \mathbf{k})^2 + m_1^2 = \omega_1^2 + \tilde{\omega}^2 - m_\phi^2 + 2|\mathbf{q}||\mathbf{k}|x, \tag{C.48}$$

where

$$x \equiv \cos\theta \tag{C.49}$$

is the cosine of the angle between the momenta $\mathbf{k}$ and $\mathbf{q}$. The angular integration therefore enforces the physical constraint

$$|x| \leq 1. \tag{C.50}$$

Below we determine how each allowed delta function fixes x and restricts the integration domain in the $(\omega_1, \tilde{\omega})$ plane.

First Channel: $\delta(m_\phi - \omega_1 - \tilde{\omega} + \tilde{\omega}_1)$

Solving the delta function condition

$$m_\phi - \omega_1 - \tilde{\omega} = -\tilde{\omega}_1 \tag{C.51}$$

and squaring both sides yields

$$m_\phi^2 + \omega_1^2 + \tilde{\omega}^2 - 2m_\phi\tilde{\omega} + 2\tilde{\omega}\omega_1 - 2m_\phi\omega_1 = \omega_1^2 + \tilde{\omega}^2 - m_\phi^2 + 2|\mathbf{q}||\mathbf{k}|x. \tag{C.52}$$

Solving for the angular variable x yields

$$x = \frac{(m_\phi - \tilde{\omega})(m_\phi - \omega_1)}{|\mathbf{q}||\mathbf{k}|} \equiv x_1. \tag{C.53}$$

Since the angular variable must satisfy $|x| \leq 1$, we obtain the condition

$$|(m_\phi - \tilde{\omega})(m_\phi - \omega_1)| \leq |\mathbf{q}||\mathbf{k}|. \tag{C.54}$$

Using

$$|\mathbf{q}|^2 = \tilde{\omega}^2 - m_\phi^2, \qquad |\mathbf{k}|^2 = \omega_1^2 - m_1^2, \tag{C.55}$$

this becomes

$$(m_\phi - \tilde{\omega})^2(m_\phi - \omega_1)^2 \leq (\tilde{\omega}^2 - m_\phi^2)(\omega_1^2 - m_1^2). \tag{C.56}$$

Introducing

$$R_1(\omega_1) = \frac{\omega_1^2 - m_1^2}{(m_\phi - \omega_1)^2}, \tag{C.57}$$

For $\tilde{\omega} > m_\phi$, the inequality Eq. (C.56) can be written as

$$\tilde{\omega} - m_\phi \leq R_1(\omega_1)(\tilde{\omega} + m_\phi). \tag{C.58}$$

Equivalently,

$$\tilde{\omega}\left[1 - R_1(\omega_1)\right] \leq m_\phi\left[1 + R_1(\omega_1)\right]. \tag{C.59}$$

Therefore, if

$$1 - R_1(\omega_1) > 0, \tag{C.60}$$

we obtain the finite upper bound

$$\tilde{\omega} \leq m_\phi \frac{1 + R_1(\omega_1)}{1 - R_1(\omega_1)}. \tag{C.61}$$

Thus

$$\tilde{\omega}_{\max}(\omega_1) = m_\phi \frac{(m_\phi - \omega_1)^2 + \omega_1^2 - m_1^2}{(m_\phi - \omega_1)^2 - \omega_1^2 + m_1^2}. \tag{C.62}$$

The condition $1 - R_1(\omega_1) > 0$ is equivalent to

$$(m_\phi - \omega_1)^2 - \omega_1^2 + m_1^2 > 0, \tag{C.63}$$

or

$$\omega_1 < \frac{m_\phi^2 + m_1^2}{2m_\phi} \equiv \mathcal{Q}. \tag{C.64}$$

Hence, for $\omega_1 < \mathcal{Q}$, the allowed domain is

$$m_\phi \leq \tilde{\omega} \leq \tilde{\omega}_{\max}(\omega_1). \tag{C.65}$$

For $\omega_1 \geq \mathcal{Q}$, the angular constraint does not give a finite upper bound on $\tilde{\omega}$.

Second Channel: $\delta(m_\phi + \omega_1 - \tilde{\omega} - \tilde{\omega}_1)$

Repeating the same procedure for

$$m_\phi + \omega_1 - \tilde{\omega} = \tilde{\omega}_1 \tag{C.66}$$

yields

$$x = \frac{(m_\phi - \tilde{\omega})(m_\phi + \omega_1)}{|\mathbf{q}||\mathbf{k}|} \equiv x_2. \tag{C.67}$$

The requirement $|x_2| \leq 1$ gives

$$(m_\phi - \tilde{\omega})^2(m_\phi + \omega_1)^2 \leq (\tilde{\omega}^2 - m_\phi^2)(\omega_1^2 - m_1^2), \tag{C.68}$$

which again leads to an upper bound on $\tilde{\omega}$,

$$\tilde{\omega} \leq \tilde{\omega}_{\max}(\omega_1), \tag{C.69}$$

with

$$\tilde{\omega}_{\max}(\omega_1) = m_\phi \frac{1 + R(\omega_1)}{1 - R(\omega_1)}, \tag{C.70}$$

where

$$R(\omega_1) = \frac{\omega_1^2 - m_1^2}{(m_\phi + \omega_1)^2}. \tag{C.71}$$

Third Channel: $\delta(m_\phi - \omega_1 + \tilde{\omega} - \tilde{\omega}_1)$

Finally, solving

$$m_\phi - \omega_1 + \tilde{\omega} = \tilde{\omega}_1 \tag{C.72}$$

gives

$$x = \frac{(m_\phi + \tilde{\omega})(m_\phi - \omega_1)}{|\mathbf{q}||\mathbf{k}|} \equiv x_3. \tag{C.73}$$

The constraint $|x_3| \leq 1$ now produces a lower bound on $\tilde{\omega}$,

$$\tilde{\omega} \geq \tilde{\omega}_{\min}(\omega_1). \tag{C.74}$$

Introducing again

$$\mathcal{Q} = \frac{m_\phi^2 + m_1^2}{2m_\phi}, \tag{C.75}$$

the allowed region separates into two cases:

- For

  $$m_1 \leq \omega_1 < \mathcal{Q}, \tag{C.76}$$

  the lower bound reduces to

  $$\tilde{\omega} \geq m_\phi. \tag{C.77}$$

- For

  $$\omega_1 \geq \mathcal{Q}, \tag{C.78}$$

  the lower bound becomes

  $$\tilde{\omega} \geq \tilde{\omega}_{\min}(\omega_1). \tag{C.79}$$

Resulting Integration Domain

Combining the constraints obtained above, the allowed kinematic region in the $(\omega_1, \tilde{\omega})$ plane is determined by

$$\tilde{\omega}_{\min}(\omega_1) \leq \tilde{\omega} \leq \tilde{\omega}_{\max}(\omega_1), \tag{C.80}$$

with

$$\omega_1 \geq m_1. \tag{C.81}$$

These bounds determine the region of phase space where the scattering and pair creation processes mediated by the virtual χ_2 particle are kinematically allowed. Inserting these limits into the reduced integral leads directly to the compact representation in Eq. (2.120).

Appendix D

Relation between $T_{\rm re}$ and CMB observables

The connection between $T_{\rm re}$ and CMB observables is well established and has been extensively discussed in the literature. For completeness, we summarise the relevant relations following [158]. The number of e-folds during reheating, $N_{\rm re}$, can be expressed in terms of the number of e-folds $N_{\rm k}$ between the horizon crossing of a perturbation mode with wave number k and the end of inflation as

$$\begin{aligned}N_{\rm re} = \frac{4}{3\bar{w}_{\rm re}-1}\Bigg[N_{\rm k} + \ln\left(\frac{k}{a_0 T_0}\right) + \frac{1}{4}\ln\left(\frac{40}{\pi^2 g_\star}\right) + \frac{1}{3}\ln\left(\frac{11 g_\star}{43}\right) \\ - \frac{1}{2}\ln\left(\frac{\pi^2 m_{\rm Pl}^2 r A_s}{2\sqrt{\mathcal{V}_{\rm end}}}\right)\Bigg].\end{aligned} \tag{D.1}$$

This expression assumes that the effective numbers of relativistic degrees of freedom contributing to the energy and entropy densities are equal and approximately constant, i.e., $g_\rho(T) = g_s(T) = g_\star$. Here, $T_0 = 2.725$ K denotes the present CMB temperature and a_0 is the current scale factor.

The quantity $N_{\rm k}$ is given by

$$N_{\rm k} = \ln\left(\frac{a_{\rm end}}{a_k}\right) = \int_{\phi_k}^{\phi_{\rm end}} \frac{H\mathrm{d}\phi}{\dot{\phi}} \approx \frac{1}{m_{\rm Pl}^2}\int_{\phi_{\rm end}}^{\phi_k} \mathrm{d}\phi \frac{\mathcal{V}}{\partial_\phi \mathcal{V}}, \tag{D.2}$$

where ϕ_k and H_k denote the values of the inflaton field and Hubble parameter at horizon crossing of the scale k. The field value ϕ_k can be determined in terms of the observables n_s and r by solving

$$n_s = 1 - 6\epsilon_k + 2\eta_k\ , \quad r = 16\epsilon_k. \tag{D.3}$$

In the slow-roll approximation, $\epsilon, \eta \ll 1$, the Hubble scale at horizon crossing is

$$H_k^2 = \frac{\mathcal{V}(\phi_k)}{3m_{\rm Pl}^2} = \pi^2 m_{\rm Pl}^2 \frac{r A_s}{2}. \tag{D.4}$$

Substituting (D.1) together with (D.2) into (3.18), one can express $T_{\rm re}$ in terms of the observables $\{A_s, n_s, r\}$. The value of ϕ_k is obtained by solving (D.3), while $\mathcal{V}_{\rm end}$ and $\phi_{\rm end}$ follow from the condition $\epsilon = 1$.

Using (D.3), one finds

$$\epsilon_k = \frac{r}{16}\,, \quad \eta_k = \frac{n_s - 1 + 3r/8}{2}. \tag{D.5}$$

Combining these relations with the definitions of ϵ and η yields

$$\frac{\partial_\phi \mathcal{V}}{\mathcal{V}}\bigg|_{\phi_k} = \sqrt{\frac{r}{8m_{\rm Pl}^2}}\,, \quad \frac{\partial_\phi^2 \mathcal{V}}{\mathcal{V}}\bigg|_{\phi_k} = \frac{n_s - 1 + 3r/8}{2m_{\rm Pl}^2}. \tag{D.6}$$

Together with (D.4), these expressions provide three independent relations linking the inflaton potential and its derivatives to the observables $\{A_s, n_s, r\}$. This allows one to express $\bar{w}_{\rm re}$ and $N_{\rm re}$ appearing in (D.1) and (3.21) in terms of measurable quantities.

In practice, fixing A_s to its best-fit value provides an excellent approximation [82]. The information gain on $X = \log_{10}(T_{\rm re}/\mathrm{GeV})$ from observational data $\mathcal{D} = \{n_s, r\}$ can then be quantified through the posterior distribution

$$P(X|\mathcal{D}) = \frac{P(\mathcal{D}|X)P(X)}{P(\mathcal{D})}, \tag{D.7}$$

where

$$P(\mathcal{D}) = \int dX\, P(\mathcal{D}|X)P(X)\,, \tag{D.8}$$

and the likelihood is approximated by

$$P(\mathcal{D}|X) = C_2 \mathcal{N}(n_s, r|\bar{n}_s, \sigma_{n_s}; \bar{r}, \sigma_r)\theta(r). \tag{D.9}$$

The normalization constant C_2 is fixed by imposing $\int P(\mathcal{D}|X) d\mathcal{D} = 1$. The function $\mathcal{N}(n_s, r|\bar{n}_s, \sigma_{n_s}; \bar{r}, \sigma_r)$ is well approximated by a two-dimensional Gaussian [82], characterised by the experimental sensitivities σ_{n_s} and σ_r around the fiducial values $n_s = \bar{n}_s$ and $r = \bar{r}$.

Expressing $T_{\rm re}$ and $N_{\rm re}$ in terms of X, we adopt a flat prior

$$P(X) = \theta(N_{\rm re})\theta(T_{\rm re} - T_{\rm BBN}), \tag{D.10}$$

with $T_{\rm BBN} = 5.96\,$MeV to ensure successful Big Bang nucleosynthesis [159].[1]

[1]The precise lower bound on $T_{\rm re}$ depends on the details of the inflaton couplings to the Standard Model. The quoted bound assumes no coupling to the hadronic sector; relaxing this assumption is expected to slightly weaken the constraint, see e.g. [160–163] for further discussion.

Appendix E

Effective damping equation from the CTP effective action

In this appendix we briefly outline how a local damping equation for a scalar background field can be derived from nonequilibrium quantum field theory. We follow the general strategy of Ref. [164], where the effective equation of motion is obtained from the Closed-Time-Path (CTP) effective action and subsequently reduced to a local Markovian form.

We consider a real scalar field ϕ and define its expectation value $\varphi(t) \equiv \langle\phi(t)\rangle$. For a homogeneous and isotropic system, the dynamics is entirely encoded in the time evolution of $\varphi(t)$. Quantum fluctuations around the expectation value are described by a field η,

$$\phi(x) = \varphi(t) + \eta(x). \tag{E.1}$$

The central assumption is that the background evolves slowly compared to the microscopic interaction time scales of the system. Physically, this means that the expectation value $\varphi(t)$ changes only slightly during a single microscopic interaction. Under this condition, one may expand the background field around a given time t as

$$\varphi(t')^n = \varphi(t)^n + n(t'-t)\dot{\varphi}(t)\varphi(t)^{n-1} + \mathcal{O}(\ddot{\varphi}). \tag{E.2}$$

Inside loop integrals, the field $\varphi(t')$ always appears convoluted with correlation functions. These correlation functions are strongly suppressed when the time separation $|t-t'|$ becomes much larger than the characteristic microscopic interaction time $\tau_{\rm int}$. They therefore act as effective window functions that restrict the dominant contribution of the memory integrals to the region $|t-t'| \lesssim \tau_{\rm int}$. As a result, the nonlocal dynamics admits a derivative expansion and can be described by equations that are effectively local in time.

In the following, we discuss how such an effective quantum kinetic equation can be derived from the CTP effective action. Under the assumption of a slowly evolving background, the resulting evolution equation takes the form

$$\ddot{\varphi} + \sum_n \Gamma_\varphi^{(n)}\, \dot{\varphi}^{(n)} + \frac{\partial \mathcal{V}_\varphi}{\partial \varphi} = 0, \tag{E.3}$$

where $\mathcal{V}_\varphi$ denotes the effective potential and the friction coefficients $\Gamma_\varphi^{(n)}$ encode dissipative effects arising from interactions with the surrounding medium.

To derive Eq. (E.3) systematically, we begin with the CTP generating functional. For generality, we consider a theory containing a set of real scalar fields Φ_a. Throughout the derivation, we only assume that the couplings of the fields Φ_a are sufficiently weak for perturbation theory to be applicable, but we make no further assumptions about the specific form of their interactions. Following Ref. [164], we assume that only one of the fields Φ_a acquires a non-vanishing expectation value; we denote this field by ϕ. Generalizing the discussion to several fields with non-vanishing expectation values is straightforward, but would considerably complicate the notations.

Introducing a local source $J_a(x)$ and a bilocal source $R_{ab}(x, y)$, the CTP generating functional is defined as

$$\begin{aligned} Z[J, R] = \int \mathcal{D}\Phi \, \exp \Bigg\{ & iS[\Phi] + i \int_{\mathcal{C}} d^4x \, J_a(x)\Phi_a(x) \\ & + \frac{i}{2} \int_{\mathcal{C}} d^4x \, d^4y \, \Phi_a(x) R_{ab}(x, y) \Phi_b(y) \Bigg\}, \end{aligned} \tag{E.4}$$

where repeated field indices are summed over, and all time integrations are performed along the closed-time contour $\mathcal{C}$. Here, $\Phi \equiv \{\Phi_a\}$, and $S[\Phi]$ is the classical action which we assume is written with the canonical kinetic terms, $S[\Phi] = \frac{1}{2} (\partial_\mu \Phi_a)^2 - V(\Phi)$, here interaction terms are included in the potential $V(\Phi)$.

The two-particle irreducible (2PI) effective action is obtained by a double Legendre transform of the generating functional $W[J, R] = -i \ln Z[J, R]$,

$$\begin{aligned} \Gamma[\varphi, \Delta] = W[J,R] & - \int_x \varphi_a(x) J_a(x) \\ & - \frac{1}{2} \int_{xy} \varphi_a(x) \varphi_b(y) R_{ab}(x, y) - \frac{1}{2} \mathrm{Tr}[\Delta R] \, , \end{aligned} \tag{E.5}$$

where

$$\mathrm{Tr}[AB] \equiv \sum_{a,b} \int_{xy} A_{ab}(x,y) B_{ba}(y,x). \tag{E.6}$$

The expectation values and connected propagators are defined by

$$\varphi_a(x) = \frac{\delta W[J,R]}{\delta J_a(x)}, \tag{E.7}$$

$$\Delta_{ab}(x,y) = 2\frac{\delta W[J,R]}{\delta R_{ba}(y,x)} - \varphi_a(x)\varphi_b(y). \tag{E.8}$$

The physical theory is recovered after setting the external sources to zero,

$$J_a(x) = 0, \qquad R_{ab}(x,y) = 0. \tag{E.9}$$

The physical configurations therefore satisfy the stationarity conditions

$$\frac{\delta\Gamma[\varphi,\Delta]}{\delta\varphi_a(x)} = 0, \tag{E.10}$$

$$\frac{\delta\Gamma[\varphi,\Delta]}{\delta\Delta_{ab}(x,y)} = 0. \tag{E.11}$$

It is convenient to decompose the effective action into a tree-level contribution $S[\varphi]$, a one-loop contribution $\Gamma_1[\varphi,\Delta]$, and a remainder containing all two-particle irreducible diagrams with two or more loops $\Gamma_2[\varphi,\Delta]$, so we write

$$\Gamma[\varphi,\Delta] = S[\varphi] + \Gamma_{\mathrm{loop}}[\varphi,\Delta] = S[\varphi] + \Gamma_1[\varphi,\Delta] + \Gamma_2[\varphi,\Delta]. \tag{E.12}$$

The one-loop contribution is given by

$$\Gamma_1[\varphi,\Delta] = \frac{i}{2}\mathrm{Tr}\ln\Delta^{-1} + \frac{i}{2}\mathrm{Tr}\left[G_0^{-1}[\varphi]\,\Delta\right], \tag{E.13}$$

where

$$iG^{-1}_{0,ab}[\varphi](x,y) = \left.\frac{\delta^2 S[\Phi]}{\delta\Phi_a(x)\delta\Phi_b(y)}\right|_{\langle\Phi\rangle} \tag{E.14}$$

denotes the inverse tree-level propagator evaluated in the background configuration.

The equation of motion for the expectation value follows from Eq. (E.10),

$$\frac{\delta\Gamma[\varphi,\Delta]}{\delta\varphi_a(x)} = -\Box\varphi_a(x) - \frac{\delta V[\varphi]}{\delta\varphi_a(x)} + \frac{\delta\Gamma_{\mathrm{loop}}[\varphi,\Delta]}{\delta\varphi_a(x)} = 0, \tag{E.15}$$

Similarly, the equation for the propagator follows from Eq. (E.11). Using Eq. (E.13), one finds

$$\Delta^{-1}_{ab}(x,y) = G^{-1}_{0,ab}[\varphi](x,y) - \Pi_{ab}[\varphi,\Delta](x,y), \tag{E.16}$$

with self-energy

$$\Pi_{ab}[\varphi,\Delta](x,y) = 2i\frac{\delta\Gamma_2[\varphi,\Delta]}{\delta\Delta_{ab}(x,y)}. \tag{E.17}$$

Equation (E.16) is the Schwinger–Dyson equation for the full propagator.

Equations (E.15) and (E.16) form a coupled system for the one- and two-point functions. Solving Eq. (E.16) determines the propagator as a functional of the background field,

$$\Delta = \Delta[\varphi]. \tag{E.18}$$

Substituting this solution into Eq. (E.15) yields an effective equation for the expectation value alone,

$$\left.\frac{\delta\Gamma[\varphi,\Delta]}{\delta\varphi_a(x)}\right|_{\Delta=\Delta[\varphi]} = 0. \tag{E.19}$$

Although Eq. (E.19) is formally exact, it remains difficult to evaluate because the loop contribution depends on the full propagator $\Delta[\varphi]$. In principle, determining the exact evolution would require solving the coupled equations for both φ and Δ. For the present discussion, however, we do not need the explicit solution $\Delta[\varphi]$. It is sufficient to use the fact that the resummed propagator can be regarded as a functional of the background field and that the latter evolves slowly compared to the microscopic interaction time scales of the system. Under these conditions, we can use the expansion (E.2) inside the loop integrals.

To make this idea explicit, we introduce a reference configuration $\bar{\varphi}$ and expand the loop-induced contribution around it as

$$\begin{aligned}\left.\frac{\partial\Gamma_{\mathrm{loop}}[\varphi,\Delta[\varphi]]}{\partial\varphi(x)}\right|_{\bar{\varphi}+\delta\varphi} &= \left.\frac{\partial\Gamma_{\mathrm{loop}}[\varphi,\Delta[\varphi]]}{\partial\varphi(x)}\right|_{\bar{\varphi}} \\ &\quad + \sum_{n=1}^{\infty}\frac{1}{n!}\prod_{i=1}^{n}\left[\int_{\mathcal{C}} dx_i^0 \int d^3x_i\,\delta\varphi(x_i)\right]\end{aligned}$$

$$\times \frac{\delta^n}{\delta\varphi(x_1)\cdots\delta\varphi(x_n)} \left(\frac{\partial\Gamma_{\rm loop}[\varphi,\Delta[\varphi]]}{\partial\varphi(x)} \right)\bigg|_{\bar\varphi}. \tag{E.20}$$

Here the functional derivative with respect to $\varphi(x)$ acts only on the explicit dependence of $\Gamma_{\rm loop}$ on φ, while the implicit dependence through $\Delta[\varphi]$ has already been accounted for by solving the propagator equation.

The kernels appearing in Eq. (E.20) are built from correlation functions. Since these correlation functions are strongly suppressed for time separations larger than the characteristic microscopic interaction time $\tau_{\rm int}$, the dominant contribution comes from the region $|x_i^0 - t| \lesssim \tau_{\rm int}$. We therefore choose the reference configuration to be the constant field equal to the instantaneous value of the solution at the time appearing in the equation of motion,

$$\bar\varphi = \varphi(t), \qquad t = x^0. \tag{E.21}$$

For a slowly varying background, the field can be expanded around the local time t as

$$\varphi(x_i^0) = \varphi(t) + (x_i^0 - t)\dot\varphi(t) + \frac{1}{2}(x_i^0 - t)^2\ddot\varphi(t) + \cdots . \tag{E.22}$$

Using $\bar\varphi = \varphi(t)$, the deviation from the reference background is

$$\delta\varphi(x_i) = \varphi(x_i^0) - \bar\varphi \simeq (x_i^0 - t)\dot\varphi(t), \tag{E.23}$$

where higher-order terms in the derivative expansion have been neglected. This approximation does not require the total field excursion to be small; it only requires the field to change little during one microscopic interaction time, namely $\tau_{\rm int}\dot\varphi/\varphi \ll 1$.

Substituting Eq. (E.23) into Eq. (E.20), the equation of motion becomes

$$\ddot\varphi + \sum_{n=1}^{\infty} \Gamma_\varphi^{(n)} \dot\varphi^{\,n} + \partial_\varphi \mathcal{V}_\varphi = 0, \tag{E.24}$$

The effective potential is defined by

$$\frac{\partial\mathcal{V}_\varphi}{\partial\varphi} = V'(\varphi(t)) - \frac{\partial\Gamma_{\rm loop}[\varphi,\Delta[\varphi]]}{\partial\varphi(x)}\bigg|_{\bar\varphi}, \tag{E.25}$$

and the friction coefficients are

$$\Gamma_{\varphi}^{(n)} = -\frac{1}{n!}\prod_{i=1}^{n}\left[\int_{\mathcal{C}} dx_i^0\,(x_i^0 - t)\int d^3x_i\right] \times \frac{\delta^n}{\delta\varphi(x_1)\cdots\delta\varphi(x_n)}\left(\frac{\partial\Gamma_{\mathrm{loop}}[\varphi,\Delta[\varphi]]}{\partial\varphi(x)}\right)\Bigg|_{\bar{\varphi}}. \tag{E.26}$$

This is the desired Markovian form of the equation of motion. Keeping only the leading dissipative term gives

$$\ddot{\varphi} + \Gamma_{\varphi}\dot{\varphi} + \frac{\partial\mathcal{V}_{\varphi}}{\partial\varphi} = 0, \qquad \Gamma_{\varphi} \equiv \Gamma_{\varphi}^{(1)}. \tag{E.27}$$

Finally, in an FLRW background, the classical equation also contains the Hubble friction term. The effective equation used in the main text is therefore

$$\ddot{\varphi} + (3H + \Gamma_{\varphi})\,\dot{\varphi} + \frac{\partial\mathcal{V}_{\varphi}}{\partial\varphi} = 0. \tag{E.28}$$

Appendix F

Plateau models of inflation

The general arguments given in the main text only require the estimates (3.23) and (3.24), which hold for a broad class of plateau-like inflationary potentials. The validity of (3.23) follows directly from (D.4), while (3.24) is justified below in Sec. F.1. However, relating the CMB observables to $T_{\rm re}$ and g requires specifying the inflationary model. In Sec. F.2, we collect the relevant relations for three explicit models and verify (3.23) and (3.24) in each case.

F.1 Inflaton mass in two-parameters plateau models

We consider an inflationary potential of the form

$$\mathcal{V}(\phi) = M^4 f\left(\frac{\phi}{m_{\rm CMB}}\right) \ , \tag{F.1}$$

where M and $m_{\rm CMB}$ denote two mass scales. Since the number of e-folds can be written as

$$N_{\rm k} = \frac{1}{m_{\rm Pl}} \int_{\phi_{\rm end}}^{\phi_k} {\rm d}\phi \frac{1}{\sqrt{2\epsilon}} \ , \tag{F.2}$$

we estimate $\phi_k \sim m_{\rm CMB}$, which gives

$$\epsilon_k \sim \frac{m_{\rm CMB}^2}{N_{\rm k}^2 m_{\rm Pl}^2} \ . \tag{F.3}$$

As the example below illustrates, this scaling is accurate up to logarithmic corrections. Using $\mathcal{V}/\epsilon_k = 24\pi^2 A_s m_{\rm Pl}^4$, cf. Eqs. (D.3) and (D.4), then fixes

$$\frac{M^2}{m_{\rm CMB}} \sim \frac{\sqrt{24\pi^2 A_s} m_{\rm Pl}}{N_{\rm k}} \ . \tag{F.4}$$

Consequently, expanding the potential around the origin gives

$$m_\phi \sim \sqrt{\partial_{\phi\phi}\mathcal{V}} \sim \frac{M^2}{m_{\text{CMB}}} \sim \frac{\sqrt{24\pi^2 A_s}m_{\text{Pl}}}{N_{\text{k}}} \ , \tag{F.5}$$

which reproduces Eq. (3.24) in the main text. It is worth stressing that the dimensionless prefactor in this estimate may vanish. In such cases, the inflaton is massless during reheating and Eq. (3.24) is not applicable. This happens, for instance, in α-attractor models, cf. Eq. (3.50), when the power of the hyperbolic tangent is larger than 2.

To illustrate how Eq. (F.5) emerges explicitly, let us consider the class of plateau potentials

$$\mathcal{V}(\phi) = M^4 \left(1 - c\,\exp\left(-\frac{\phi}{\sqrt{2}m_{\text{CMB}}}\right)\right)^2 \ , \tag{F.6}$$

where $c > 0$ is dimensionless. The quadratic power ensures that the inflaton acquires a mass during reheating. Using the approximation

$$\frac{\partial_\phi \mathcal{V}}{\mathcal{V}} \approx \frac{\sqrt{2}c}{m_{\text{CMB}}} \exp\left(-\frac{\phi}{\sqrt{2}m_{\text{CMB}}}\right) \ , \tag{F.7}$$

the field value at horizon crossing follows from Eq. (D.2) as

$$\exp\left(-\frac{\phi_k}{\sqrt{2}m_{\text{CMB}}}\right) \approx \frac{m_{\text{CMB}}^2}{cN_{\text{k}}m_{\text{Pl}}^2} \ . \tag{F.8}$$

The first slow-roll parameter, $\epsilon_k \equiv \frac{m_{\text{Pl}}^2}{2}\left(\frac{\partial_\phi \mathcal{V}}{\mathcal{V}}(\phi = \phi_k)\right)^2$, is therefore

$$\epsilon_k \approx \frac{c^2 m_{\text{Pl}}^2}{m_{\text{CMB}}^2} \exp\left(-\sqrt{2}\frac{\phi_k}{m_{\text{CMB}}}\right) \approx \frac{m_{\text{CMB}}^2}{N_{\text{k}}^2 m_{\text{Pl}}^2} \ . \tag{F.9}$$

Equations (D.3) and (D.4) then imply

$$\frac{M^2}{m_{\text{CMB}}} = \frac{\sqrt{24\pi^2 A_s}m_{\text{Pl}}}{N_{\text{k}}} \ . \tag{F.10}$$

Thus, we again recover Eq. (F.5), and hence Eq. (3.24) in the main text. As a useful cross-check, the α-attractor potential (3.50) corresponds to

$$c = 2 \ , \qquad m_{\text{CMB}} = \frac{\sqrt{3}}{2}\sqrt{\alpha}m_{\text{Pl}} \ , \tag{F.11}$$

so that Eq. (F.5) agrees with Eqs. (F.28), (F.48) and (F.62), derived in appendix F.2, and is consistent with the discussion in [165].

F.2 Useful relations for specific plateau models

In this appendix, we summarise the CMB constraints on several well-motivated two-parameter inflationary models. For the benchmark parameter choices considered here, the CMB normalization implies an inflaton mass of order $m_\phi \gtrsim \mathcal{O}(10^{13})$ GeV, providing a useful reference scale for the analysis in the main text.

α-Attractor T-Model Inflation

Originally introduced in [166], α-attractor models form a broad class of chaotic inflation scenarios [167]. Here we focus on the T-model realisation, whose potential is given by (3.50),

$$\mathcal{V}(\phi) = M^4 \tanh^2\left[\frac{\phi}{\sqrt{6\alpha} m_{\mathrm{Pl}}}\right] , \tag{F.12}$$

where M is a mass scale and $\alpha > 0$.

We begin by deriving the relevant inflationary relations. The slow-roll parameters are

$$\epsilon \equiv \frac{m_{\mathrm{Pl}}^2}{2}\left(\frac{\partial_\phi \mathcal{V}}{\mathcal{V}}\right)^2 = \frac{4}{3\alpha \sinh^2\left(\frac{\sqrt{2}\phi}{\sqrt{3\alpha} m_{\mathrm{Pl}}}\right)} , \tag{F.13}$$

$$\eta \equiv m_{\mathrm{Pl}}^2 \frac{\partial_{\phi\phi}\mathcal{V}}{\mathcal{V}} = -\frac{4\left(\cosh\left(\frac{\sqrt{2}\phi}{\sqrt{3\alpha} m_{\mathrm{Pl}}}\right) - 2\right)}{3\alpha \sinh^2\left(\frac{\sqrt{2}\phi}{\sqrt{3\alpha} m_{\mathrm{Pl}}}\right)} . \tag{F.14}$$

Solving $\epsilon = 1$ gives the approximate field value at the end of inflation,

$$\phi_{\mathrm{end}} = \sqrt{\frac{3\alpha}{2}} m_{\mathrm{Pl}} \,\mathrm{arcsinh}\left(\frac{2}{\sqrt{3\alpha}}\right) . \tag{F.15}$$

For $\alpha \gtrsim 1$, this gives $\phi_{\mathrm{end}} \approx \sqrt{2} m_{\mathrm{Pl}}$, while smaller values are possible for small α.

Evaluating the number of e-folds (D.2),

$$N_{\mathrm{k}} = \frac{3}{4}\alpha\left(\cosh\left(\frac{\sqrt{2}\phi_k}{\sqrt{3\alpha} m_{\mathrm{Pl}}}\right) - \sqrt{\frac{4}{3\alpha} + 1}\right) , \tag{F.16}$$

we obtain

$$\phi_k = \sqrt{\frac{3\alpha}{2}} m_{\rm Pl} \,\mathrm{arccosh}\left(\sqrt{\frac{4}{3\alpha}+1}+\frac{4N_{\rm k}}{3\alpha}\right) . \tag{F.17}$$

This immediately gives

$$\epsilon_k = \frac{3\alpha}{3\alpha + 4N_{\rm k}^2 + 2\alpha N_{\rm k}\sqrt{\frac{12}{\alpha}+9}} , \tag{F.18}$$

$$\eta_k = -\frac{4N_{\rm k} - \alpha\left(6-\sqrt{\frac{12}{\alpha}+9}\right)}{3\alpha + 4N_{\rm k}^2 + 2\alpha N_{\rm k}\sqrt{\frac{12}{\alpha}+9}} . \tag{F.19}$$

The CMB observables can therefore be expressed in terms of α and $N_{\rm k}$ as

$$r = 16\epsilon_k = \frac{48\alpha}{3\alpha + 4N_{\rm k}^2 + 2\alpha N_{\rm k}\sqrt{\frac{12}{\alpha}+9}} , \tag{F.20}$$

$$n_s = 1 - \frac{8}{4N_{\rm k} - 3\alpha + \alpha\sqrt{\frac{12}{\alpha}+9}} . \tag{F.21}$$

Over a large part of parameter space, these reduce to the approximate scalings

$$r \sim \frac{12\alpha}{N_{\rm k}^2} , \qquad 1-n_s \sim \frac{2}{N_{\rm k}} , \tag{F.22}$$

although we use the exact expressions in the numerical analysis. Matching to CMB observations [120],[1] the 2σ bound $n_s \gtrsim 0.957$ implies

$$N_{\rm k} \gtrsim 46 , \tag{F.23}$$

while the BICEP/Keck constraint [121] $r \lesssim 0.03$ gives

$$\alpha \lesssim 3 \cdot 10^{-3} N_{\rm k}^2 . \tag{F.24}$$

[1]Recent results from the Atacama Cosmology Telescope [168] and the South Pole Telescope [169] indicate a preference for larger values of n_s compared to Planck. However, it has recently been argued [170] that this shift is mainly driven by a tension between the CMB data and DESI BAO measurements. For this reason, we do not include these results here.

So far, the amplitude of scalar perturbations has not been used. Evaluating

$$\frac{\mathcal{V}}{\epsilon_k} = \frac{M^4\left(4N_\mathrm{k}^2 + 3\alpha + 2\alpha N_\mathrm{k}\sqrt{\frac{12}{\alpha}+9}\right)\tanh^2\left(\frac{1}{2}\mathrm{arcsech}\left(\frac{3\alpha}{4N_\mathrm{k}+\sqrt{\frac{12}{\alpha}+9\alpha}}\right)\right)}{3\alpha}\,, \tag{F.25}$$

and matching the observed value [120], $\mathcal{V}/\epsilon_k \approx 5\cdot 10^{-7} m_\mathrm{Pl}^4$, fixes M as a function of N_k and α. Together with $r \lesssim 0.03$, this gives the universal upper bound

$$N_\mathrm{k} \lesssim 56\,, \tag{F.26}$$

corresponding to instantaneous reheating. Using Eq. (D.4), M can be written explicitly as

$$M = m_\mathrm{Pl}\left(\frac{3\pi^2}{2}A_s r\right)^{1/4}\tanh^{-1}\left(\frac{\phi_k}{\sqrt{6\alpha}m_\mathrm{Pl}}\right)\,, \tag{F.27}$$

in agreement with (3.23).

Finally, the vacuum mass of the inflaton follows by expanding the potential (3.50),

$$m_\phi = \frac{M^2}{\sqrt{3\alpha}m_\mathrm{Pl}}\,. \tag{F.28}$$

This can again be regarded as a function of α and N_k. Since Eq. (F.25) shows that $M^2/\sqrt{\alpha}$ is approximately fixed by the CMB normalisation, there is little freedom to vary m_ϕ apart from changing N_k. We illustrate this in Fig. 3.7, where we show r as a function of n_s and $\Phi_I \equiv \mathcal{V}_\mathrm{end}/m_\phi^4$ as a function of m_ϕ. We have also checked numerically that the approximations used above are accurate. This is shown in Fig. F.1, which displays the full parameter space in the $\Phi_I - m_\phi$ plane consistent with the Planck and BICEP/Keck data at the 2σ level. The colour encodes the number of e-folds for each point.

Radion Gauge Inflation

Radion gauge inflation was originally introduced in [171] as a variation of gauge inflation [172–174]. Its potential is

$$\mathcal{V}(\phi) = M^4\left[\frac{(\phi/m_\mathrm{Pl})^2}{\alpha + (\phi/m_\mathrm{Pl})^2}\right]\,. \tag{F.29}$$

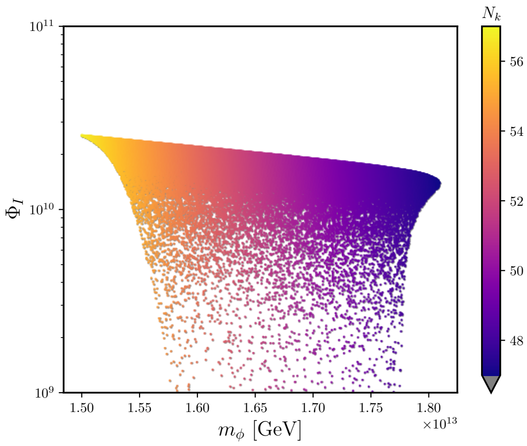

Figure F.1: Region of the α-attractor T-model parameter space in the $\Phi_I - m_\phi$ plane consistent with the Planck and BICEP/Keck data at the 2σ level. The colour indicates the number of e-folds N_k of inflation for a given parameter-space point.

Following the same steps as above, we find

$$\epsilon_k = \frac{2\alpha^2 m_{\mathrm{Pl}}^2}{\phi^2\left(\alpha + (\phi/m_{\mathrm{Pl}})^2\right)^2}\,, \tag{F.30}$$

$$\eta_k = \frac{2\alpha m_{\mathrm{Pl}}^2\left(\alpha - 3\,(\phi/m_{\mathrm{Pl}})^2\right)}{\phi^2\left(\alpha + (\phi/m_{\mathrm{Pl}})^2\right)^2}\,. \tag{F.31}$$

The condition $\epsilon = 1$ gives

$$\phi_{\text{end}} = m_{\mathrm{Pl}}\frac{\left(\alpha^2\tilde{\alpha}\right)^{1/3} - \alpha}{\sqrt{3}\left(\alpha^2\tilde{\alpha}\right)^{1/6}}\,, \tag{F.32}$$

where

$$\tilde{\alpha} \equiv \alpha + 3\left(\sqrt{6\alpha + 81} + 9\right)\,. \tag{F.33}$$

As in the α-attractor case, $\phi_{\text{end}} \approx \sqrt{2}m_{\mathrm{Pl}}$ for $\alpha \gtrsim 1$, while smaller values of α lead to smaller ϕ_{end}.

The number of e-folds is

$$N_\mathrm{k} = \frac{\phi_k^4 - \phi_{\text{end}}^4}{8\alpha} + \frac{\phi_k^2 - \phi_{\text{end}}^2}{4}\,, \tag{F.34}$$

which gives

$$\phi_k = 2m_{\rm Pl}\sqrt{\tilde{N}} \; , \tag{F.35}$$

with

$$\tilde{N} \equiv \frac{\alpha}{12}\left(\sqrt{\left(\frac{\alpha}{\tilde{\alpha}}\right)^{2/3} + 2\left(\frac{\alpha}{\tilde{\alpha}}\right)^{1/3} + 2\left(\frac{\tilde{\alpha}}{\alpha}\right)^{1/3} + \left(\frac{\tilde{\alpha}}{\alpha}\right)^{2/3} + \frac{72N_{\rm k}}{\alpha} + 3} - 3\right) \; . \tag{F.36}$$

For large α, one has $\tilde{N} \approx N_{\rm k}$, and hence $\phi_k \approx 2\sqrt{N_{\rm k}}m_{\rm Pl}$. The slow-roll parameters become

$$\epsilon_k = \frac{\alpha^2}{2\tilde{N}(\alpha + 4\tilde{N})^2} \; , \tag{F.37}$$

$$\eta_k = \frac{\alpha(\alpha - 12\tilde{N})}{2\tilde{N}(\alpha + 4\tilde{N})^2} \; , \tag{F.38}$$

leading to

$$r = \frac{8\alpha^2}{\tilde{N}(\alpha + 4\tilde{N})^2} \; , \tag{F.39}$$

$$n_s = 1 - \frac{2\alpha(\alpha + 6\tilde{N})}{\tilde{N}(\alpha + 4\tilde{N})^2} \; . \tag{F.40}$$

For large α, these reduce to

$$r \sim \frac{8}{N_{\rm k}^2} \; , \qquad 1 - n_s \sim \frac{2}{N_{\rm k}} \; . \tag{F.41}$$

Since the scaling of n_s is the same as in the α-attractor model, we again obtain

$$46 \lesssim N_{\rm k} \lesssim 56 \; . \tag{F.42}$$

For small α, instead,

$$r \sim \frac{\sqrt{2\alpha}}{N_{\rm k}^{3/2}} \; , \qquad 1 - n_s \sim \frac{3}{2N_{\rm k}} \; . \tag{F.43}$$

Thus, the observational range $0.957 \lesssim n_s \lesssim 0.973$ can be satisfied in the broader interval

$$35 \lesssim N_{\rm k} \lesssim 56 \; . \tag{F.44}$$

Hence, n_s and r do not directly bound α, although α affects the allowed range of $N_{\rm k}$.

The CMB amplitude fixes M through

$$\frac{\mathcal{V}}{\epsilon_k} = \frac{8M^4\tilde{N}^2(\alpha + 4\tilde{N})}{\alpha^2} \, . \tag{F.45}$$

The condition $M \lesssim m_{\rm Pl}$ gives the mild upper bound $\alpha \lesssim 10^{10}$, while for small α one obtains

$$\frac{\mathcal{V}}{\epsilon_k} \approx \frac{8\sqrt{2}M^4 N_{\rm k}^{3/2}}{\sqrt{\alpha}} \, . \tag{F.46}$$

Using Eq. (D.4), the mass scale M can be written as

$$M = m_{\rm Pl}\left(\frac{3\pi^2}{2} r A_s\left(1 + \alpha\frac{m_{\rm Pl}^2}{\phi_k^2}\right)\right)^{1/4} \, , \tag{F.47}$$

and expanding the potential around the origin gives

$$m_\phi = \frac{\sqrt{2}M^2}{\sqrt{\alpha}m_{\rm Pl}} \, . \tag{F.48}$$

For $\alpha \gtrsim 4N$, the CMB normalisation fixes $M^2/\sqrt{\alpha}$ and therefore also m_ϕ, as in the α-attractor case. Smaller values of α, however, allow different scalings and can lead to larger m_ϕ. In Fig. F.2, we show r as a function of n_s and Φ_I as a function of m_ϕ. Furthermore, Fig. F.3 displays the full parameter space in the $\Phi_I - m_\phi$ plane consistent with the Planck and BICEP/Keck data at the 2σ level. The colour indicates the corresponding number of e-folds. The agreement shows that the approximations used in this section work well.

Mutated Hilltop Inflation

Mutated hilltop inflation was originally proposed in [175, 176] as a refined version of hilltop inflation [177, 178]. Its potential is

$$\mathcal{V}(\phi) = M^4\left[1 - \frac{1}{\cosh\left(\frac{\phi}{\alpha m_{\rm Pl}}\right)}\right] \, . \tag{F.49}$$

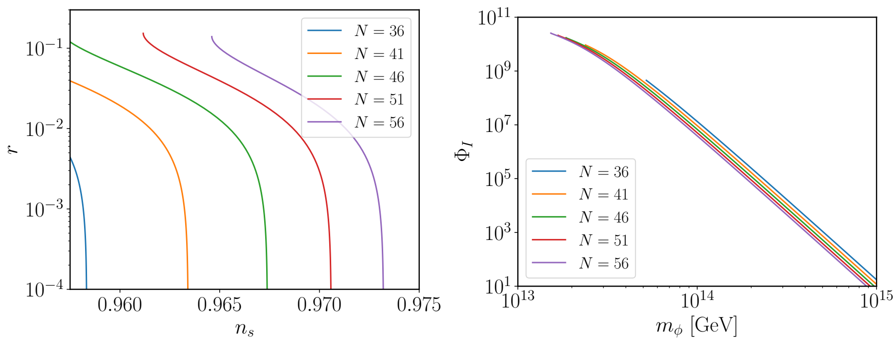

Figure F.2: (*Left*) Tensor-to-scalar ratio r as a function of the spectral index n_s for the radion gauge inflation model and fixed values of the number of e-folds N_k, consistent with the Planck and BICEP/Keck data. The purple, red, blue, orange and green lines correspond to $N_\mathrm{k} = 36$, $N_\mathrm{k} = 41$, $N_\mathrm{k} = 46$, $N_\mathrm{k} = 51$, and $N_\mathrm{k} = 56$, respectively. (*Right*) Inflaton energy density Φ_I at the beginning of reheating as a function of the inflaton mass m_ϕ for the same choices of N_k and inflationary scenario. The colour scheme is identical to the left panel.

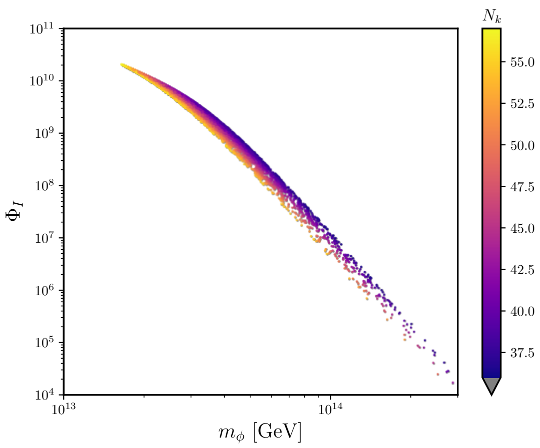

Figure F.3: Region of the radion gauge inflation model parameter space in the $\Phi_I - m_\phi$ plane consistent with the Planck and BICEP/Keck data at the 2σ level. The colour indicates the number of e-folds N_k of inflation for a given parameter-space point.

Repeating the previous analysis, one obtains

$$\epsilon_k = \frac{1}{2\alpha^2 \cosh^2\left(\frac{\phi}{\alpha m_{\rm Pl}}\right) \tanh^2\left(\frac{\phi}{2\alpha m_{\rm Pl}}\right)} \,, \tag{F.50}$$

$$\eta_k = -\frac{\cosh\left(\frac{\phi}{\alpha m_{\rm Pl}}\right) - 3}{4\alpha^2 \cosh^2\left(\frac{\phi}{\alpha m_{\rm Pl}}\right) \sinh^2\left(\frac{\phi}{2\alpha m_{\rm Pl}}\right)} \,, \tag{F.51}$$

and the condition $\epsilon = 1$ gives [82]

$$\phi_{\rm end} = \alpha m_{\rm Pl} \text{arccosh}\left(\frac{2^{2/3}\left(3+2\alpha^2\right) + 2^{1/3} b^{2/3} + 2\alpha b^{1/3}}{6\alpha b^{1/3}}\right) \,, \tag{F.52}$$

where

$$a = \sqrt{4\alpha^4 + 22\alpha^2 - 1}\,, \qquad b = 3\sqrt{6}a + 36\alpha + 4\alpha^3 \,. \tag{F.53}$$

The quantity b is real only for

$$\alpha_{\rm crit} = \frac{\sqrt{5\sqrt{5} - 11}}{2} \approx 0.21 \,. \tag{F.54}$$

In the following analytic discussion, we assume $\alpha > \alpha_{\rm crit}$. The number of e-folds is then

$$N_{\rm k} = \alpha^2 \left(2\ln\left(\cosh\left(\frac{\phi_{\rm end}}{2\alpha m_{\rm Pl}}\right) \text{sech}\left(\frac{\phi_k}{2\alpha m_{\rm Pl}}\right)\right) - \cosh\left(\frac{\phi_{\rm end}}{\alpha m_{\rm Pl}}\right) + \cosh\left(\frac{\phi_k}{\alpha m_{\rm Pl}}\right)\right) \,. \tag{F.55}$$

In contrast to the previous two models, solving for ϕ_k analytically requires an approximation. Since $\cosh(x) \gg 2\ln\cosh(x/2)$ for the relevant values of x, we neglect the logarithmic terms and obtain

$$\begin{aligned}\phi_k &\approx \alpha m_{\rm Pl} \text{arccosh}\left(\frac{N_{\rm k}}{\alpha^2} + \cosh\left(\frac{\phi_{\rm end}}{\alpha m_{\rm Pl}}\right)\right) \\ &= \alpha m_{\rm Pl} \text{arccosh}\left(\frac{N_{\rm k}}{\alpha^2} + \frac{2^{2/3}\left(3+2\alpha^2\right) + 2^{1/3} b^{2/3} + 2\alpha b^{1/3}}{6\alpha b^{1/3}}\right) \,.\end{aligned} \tag{F.56}$$

Substituting this expression into Eqs. (F.50) and (F.51) determines the slow-roll parameters as functions of $N_{\rm k}$. For $\alpha < 1$, one finds the approximate behaviour

$$r \sim \frac{8\alpha^2}{N_{\rm k}^2} \,, \qquad 1 - n_s \sim \frac{2}{N_{\rm k}} \,. \tag{F.57}$$

The scaling of n_s is therefore again the same as in the previous models, yielding

$$46 \lesssim N_{\rm k} \lesssim 56 \,. \tag{F.58}$$

Within the same small-α approximation, the amplitude of scalar perturbations is

$$\frac{\mathcal{V}}{\epsilon_k} = \frac{2M^4 N_{\rm k}^2}{\alpha^2} \,, \tag{F.59}$$

which fixes M as a function of α and $N_{\rm k}$. More explicitly, Eq. (D.4) gives

$$M = m_{\rm Pl} \sqrt[4]{\frac{3\pi^2 r A_s}{2[1 - 1/\cosh(\phi_k/(\alpha m_{\rm Pl}))]}} \,. \tag{F.60}$$

Expanding the potential around the origin gives the inflaton mass,

$$m_\phi = \frac{M^2}{\alpha m_{\rm Pl}} \,. \tag{F.61}$$

Thus, the CMB normalisation implies

$$m_\phi = \frac{1.2 \cdot 10^{15}\,\text{GeV}}{N_{\rm k}} \,, \tag{F.62}$$

so that, within the approximations used here, m_ϕ lies in the narrow interval between $2.1 \cdot 10^{13}$ GeV and $2.6 \cdot 10^{13}$ GeV. We therefore cannot reach small inflaton masses as long as $\alpha > \alpha_{\text{crit}}$. For this parameter region, Fig. F.4 shows r as a function of n_s and $\Phi_I \equiv \mathcal{V}_{\rm end}/m_\phi^4$ as a function of m_ϕ. As in the previous two examples, Fig. F.5 displays the full parameter space in the $\Phi_I - m_\phi$ plane consistent with the Planck and BICEP/Keck data at the 2σ level. The colour indicates the number of e-folds for each point. We note that the region with large Φ_I and relatively small m_ϕ, which appears to deviate from the analytical estimate in Fig. F.4, corresponds to large values $\alpha \gtrsim 1$, where the approximations used in this section are no longer expected to be accurate.

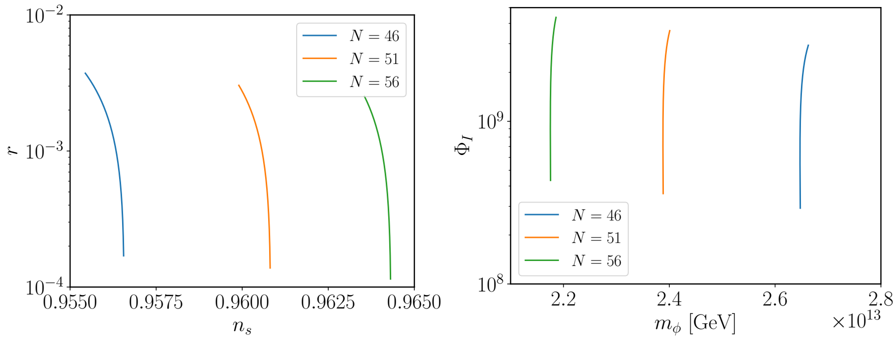

Figure F.4: (*Left*) Tensor-to-scalar ratio r as a function of the spectral index n_s for the mutated hilltop inflation model and fixed values of the number of e-folds N_k, consistent with the Planck and BICEP/Keck data. The blue, orange and green lines correspond to $N_\mathrm{k} = 46$, $N_\mathrm{k} = 51$, and $N_\mathrm{k} = 56$, respectively. (*Right*) Inflaton energy density Φ_I at the beginning of reheating as a function of the inflaton mass m_ϕ for the same choices of N_k and inflationary scenario. The colour scheme is identical to the left panel.

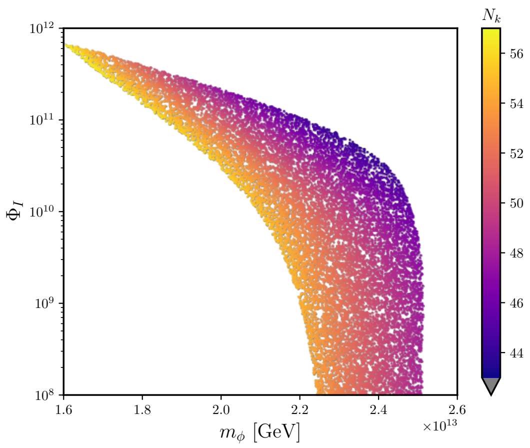

Figure F.5: Region of the mutated hilltop inflation model parameter space in the $\Phi_I - m_\phi$ plane consistent with the Planck and BICEP/Keck data at the 2σ level. The colour indicates the number of e-folds N_k of inflation for a given parameter-space point.

Appendix G

Fundamental coupling of α-attractors

In the original formulation of the α-attractor T-model, the fundamental action is given by [179]

$$S = \int \mathrm{d}^4x \sqrt{-g} \times \left[\frac{1}{12}(\chi^2 - \varphi^2)R + \frac{1}{2}\partial_\mu\chi\partial^\mu\chi - \frac{1}{2}\partial_\mu\varphi\partial^\mu\varphi - f\left(\frac{\varphi}{\chi}\right)\left(\chi^2 - \varphi^2\right)^2 \right] . \tag{G.1}$$

Here χ and φ are two scalar fields. The structure of the action is determined by two requirements: Weyl invariance and an $SO(1,1)$ symmetry acting on χ and φ, which is only weakly broken when $f(\varphi/\chi)$ is not constant. After imposing the gauge condition $\chi^2 - \varphi^2 = 6m_{\mathrm{Pl}}^2$, the action becomes

$$S = \int \mathrm{d}^4x \sqrt{-g} \times \left[\frac{1}{2}m_{\mathrm{Pl}}^2 R - \frac{1}{2}\frac{6m_{\mathrm{Pl}}^2}{\varphi^2 + 6m_{\mathrm{Pl}}^2}\partial_\mu\varphi\partial^\mu\varphi - 36m_{\mathrm{Pl}}^4 f\left(\frac{\varphi}{\sqrt{\varphi^2 + 6m_{\mathrm{Pl}}^2}}\right) \right] . \tag{G.2}$$

Introducing the canonically normalised field ϕ through

$$\phi = \sqrt{6}m_{\mathrm{Pl}}\,\mathrm{arcsinh}\left(\frac{\varphi}{\sqrt{6}m_{\mathrm{Pl}}}\right) , \tag{G.3}$$

one obtains

$$S = \int \mathrm{d}^4x \sqrt{-g} \left[\frac{1}{2}m_{\mathrm{Pl}}^2 R - \frac{1}{2}\partial_\mu\phi\partial^\mu\phi - 36m_{\mathrm{Pl}}^4 f\Big(\tanh\left(\frac{\phi}{\sqrt{6}m_{\mathrm{Pl}}}\right)\Big) \right] . \tag{G.4}$$

For the choice $f(x) = \lambda x^{2n}$, this leads to the inflaton potential

$$\mathcal{V} = M^4 \tanh^{2n}\left(\frac{\phi}{\sqrt{6}m_{\rm Pl}}\right) , \qquad M \equiv \lambda^{1/4}\sqrt{6}m_{\rm Pl} . \tag{G.5}$$

We recall that the parameter α was not present in the original construction of [179], but was introduced later in [166].

This formulation also makes clear how to couple the inflaton sector to a fermion. At the level of the action (G.1), we add

$$S \to S + \int \mathrm{d}^4x\,\sqrt{-g}\left[\left(i\bar{\Psi}\not{D}\Psi + \text{h.c.}\right) + y\sqrt{\chi^2 - \varphi^2}\, g\left(\frac{\varphi}{\chi}\right)\bar{\Psi}\Psi\right] . \tag{G.6}$$

After gauge fixing and transforming to the canonically normalised scalar field, the Einstein-frame action (G.4) is supplemented by

$$S \to S + \int \mathrm{d}^4x\,\sqrt{-g}\left[\left(i\bar{\Psi}\not{D}\Psi + \text{h.c.}\right) + \sqrt{6}y m_{\rm Pl}\, g\Big(\tanh\left(\frac{\phi}{\sqrt{6}m_{\rm Pl}}\right)\Big)\bar{\Psi}\Psi\right] . \tag{G.7}$$

To reproduce a Yukawa interaction, we choose $g(x) = x$, which gives

$$\mathcal{L}_\phi \supset \sqrt{6}y m_{\rm Pl}\tanh\left(\frac{\phi}{\sqrt{6}m_{\rm Pl}}\right)\bar{\Psi}\Psi . \tag{G.8}$$

By analogy with the generalisation of the inflaton potential to arbitrary α [166], this suggests[1]

$$\mathcal{L}_\phi \supset \sqrt{6\alpha}y m_{\rm Pl}\tanh\left(\frac{\phi}{\sqrt{6\alpha}m_{\rm Pl}}\right)\bar{\Psi}\Psi . \tag{G.9}$$

For the α-attractor model, condition (3.22b) requires sufficiently large α, namely $\alpha \gtrsim 0.25$. In this regime, the field value during reheating remains approximately sub-Planckian, $\phi \lesssim \phi_{\rm end} \simeq \sqrt{2}m_{\rm Pl}$, throughout reheating. Therefore, the $\tanh$ can be expanded around its minimum to good accuracy. The size of the higher-order corrections to the inflaton–fermion Yukawa coupling is controlled by the same parameter, $\phi_{\rm end}/\sqrt{6\alpha}m_{\rm Pl}$, that governs when reheating enters the non-perturbative regime. For instance, for the benchmark used in Sec. 3.3, with $\alpha = 2$, the relative difference between the full $\tanh$ expression and its leading-order expansion is of order 5%.

[1] We note that in inflationary models based on a non-minimal coupling to gravity, the matter sector is generically strongly modified by the conformal transformation required to obtain the Einstein-frame action [180, 181].

Bibliography

[1] Andreas Albrecht, Paul J. Steinhardt, Michael S. Turner, and Frank Wilczek, "Reheating an Inflationary Universe", *Phys. Rev. Lett.*, vol. 48, pp. 1437, 1982.

[2] A. D. Dolgov and D. P. Kirilova, "ON PARTICLE CREATION BY A TIME DEPENDENT SCALAR FIELD", *Sov. J. Nucl. Phys.*, vol. 51, pp. 172–177, 1990.

[3] Lev Kofman, Andrei D. Linde, and Alexei A. Starobinsky, "Reheating after inflation", *Phys. Rev. Lett.*, vol. 73, pp. 3195–3198, 1994.

[4] Lev Kofman, Andrei D. Linde, and Alexei A. Starobinsky, "Towards the theory of reheating after inflation", *Phys. Rev. D*, vol. 56, pp. 3258–3295, 1997.

[5] H. Arthur Weldon, "Simple rules for discontinuities in finite temperature field theory", *Phys. Rev. D*, vol. 28, pp. 2007, 1983.

[6] Eric Braaten and Robert D. Pisarski, "Simple effective lagrangian for hard thermal loops", *Phys. Rev. D*, vol. 45, pp. R1827, 1992.

[7] Eric Braaten and Robert D. Pisarski, "Soft amplitudes in hot gauge theories: A general analysis", *Nucl. Phys. B*, vol. 337, pp. 569–634, 1990.

[8] Sangyong Jeon, "Hydrodynamic transport coefficients in relativistic scalar field theory", *Phys. Rev. D*, vol. 52, pp. 3591–3642, 1995.

[9] Peter Arnold, Guy D. Moore, and Laurence G. Yaffe, "Photon emission from ultrarelativistic plasmas", *JHEP*, vol. 11, pp. 057, 2001.

[10] Peter Arnold, Guy D. Moore, and Laurence G. Yaffe, "Photon emission from quark gluon plasma: Complete leading order results", *JHEP*, vol. 12, pp. 009, 2001.

[11] Marco Cirelli, Alessandro Strumia, and Jure Zupan, "Dark Matter", 6 2024.

[12] Edward W. Kolb and Michael S. Turner, *The Early Universe*, vol. 69, Taylor and Francis, 5 2019.

[13] Gianfranco Bertone and Tim Tait, M. P., "A new era in the search for dark matter", *Nature*, vol. 562, no. 7725, pp. 51–56, 2018.

[14] Scott Dodelson and Lawrence M. Widrow, "Sterile-neutrinos as dark matter", *Phys. Rev. Lett.*, vol. 72, pp. 17–20, 1994.

[15] Lawrence J. Hall, Karsten Jedamzik, John March-Russell, and Stephen M. West, "Freeze-In Production of FIMP Dark Matter", *JHEP*, vol. 03, pp. 080, 2010.

[16] Daniel J. H. Chung, Edward W. Kolb, and Antonio Riotto, "Production of massive particles during reheating", *Phys. Rev. D*, vol. 60, pp. 063504, 1999.

[17] Gian Francesco Giudice, Edward W. Kolb, and Antonio Riotto, "Largest temperature of the radiation era and its cosmological implications", *Phys. Rev. D*, vol. 64, pp. 023508, 2001.

[18] James E. Lidsey, Andrew R. Liddle, Edward W. Kolb, Edmund J. Copeland, Tiago Barreiro, and Mark Abney, "Reconstructing the inflation potential : An overview", *Rev. Mod. Phys.*, vol. 69, pp. 373–410, 1997.

[19] Prudhvi N. Bhattiprolu, Gilly Elor, Robert McGehee, and Aaron Pierce, "Freezing-in hadrophilic dark matter at low reheating temperatures", *JHEP*, vol. 01, pp. 128, 2023.

[20] Mathias Becker, Emanuele Copello, Julia Harz, Jonas Lang, and Yong Xu, "Confronting dark matter freeze-in during reheating with constraints from inflation", *JCAP*, vol. 01, pp. 053, 2024.

[21] Basabendu Barman, Subhaditya Bhattacharya, Sahabub Jahedi, Dipankar Pradhan, and Abhik Sarkar, "Lepton collider as a window to reheating via freezing in dark matter detection. Part II", *JHEP*, vol. 07, pp. 157, 2025.

[22] Subhaditya Bhattacharya, Anupam Ghosh, Niloy Mondal, and Abhik Sarkar, "Lepton Collider as a Window to Reheating via Freezing Out Dark Matter Detection", 9 2025.

[23] Rajesh Mondal, Sourav Mondal, and Toshifumi Yamada, "Freeze-in and freeze-out production of Higgs portal Majorana fermionic dark matter during and after reheating", *Phys. Rev. D*, vol. 113, no. 2, pp. 023529, 2026.

[24] Geneviève Bélanger, Nicolás Bernal, and Alexander Pukhov, "Strongly interacting singlet scalar dark matter during reheating", 3 2026.

[25] Jerome Martin and Christophe Ringeval, "First CMB Constraints on the Inflationary Reheating Temperature", *Phys. Rev. D*, vol. 82, pp. 023511, 2010.

[26] Peter Adshead, Richard Easther, Jonathan Pritchard, and Abraham Loeb, "Inflation and the Scale Dependent Spectral Index: Prospects and Strategies", *JCAP*, vol. 02, pp. 021, 2011.

[27] Jakub Mielczarek, "Reheating temperature from the CMB", *Phys. Rev. D*, vol. 83, pp. 023502, 2011.

[28] Richard Easther and Hiranya V. Peiris, "Bayesian Analysis of Inflation II: Model Selection and Constraints on Reheating", *Phys. Rev. D*, vol. 85, pp. 103533, 2012.

[29] Liang Dai, Marc Kamionkowski, and Junpu Wang, "Reheating constraints to inflationary models", *Phys. Rev. Lett.*, vol. 113, pp. 041302, 2014.

[30] Marco Drewes, "What can the CMB tell about the microphysics of cosmic reheating?", *JCAP*, vol. 03, pp. 013, 2016.

[31] Marco Drewes, Yannis Georis, Mubarak A. S. Mohammed, and Sebastian Zell, "Thermal effects on Dark Matter production during cosmic reheating", 4 2026.

[32] Julian Schwinger, "Brownian motion of a quantum oscillator", *J. Math. Phys.*, vol. 2, pp. 407–432, 1961.

[33] Leonid V. Keldysh, "Diagram technique for nonequilibrium processes", *Zh. Eksp. Teor. Fiz.*, vol. 47, pp. 1515–1527, 1964, [Sov. Phys. JETP 20 (1965) 1018].

[34] Esteban A. Calzetta and Bei-Lok B. Hu, *Nonequilibrium Quantum Field Theory*, Cambridge University Press, Cambridge, 2008.

[35] Richard D. Jordan, "Effective field equations for expectation values", *Phys. Rev. D*, vol. 33, pp. 444–454, 1986.

[36] Bei-Lok Hu, Juan Pablo Paz, and Yuhong Zhang, "Quantum Brownian motion in a general environment", *Phys. Rev. D*, vol. 45, pp. 2843–2861, 1992.

[37] Mathias Garny, Jan Heisig, Fabian Lülf, and Stefan Vogl, "Coannihilation without chemical equilibrium", *Phys. Rev. D*, vol. 98, no. 9, pp. 095031, 2018.

[38] Pawel Danielewicz, "Quantum theory of nonequilibrium processes. i", *Annals Phys.*, vol. 152, pp. 239–304, 1984.

[39] Esteban Calzetta and Bei-Lok Hu, "Nonequilibrium quantum fields: Closed-time-path effective action", *Phys. Rev. D*, vol. 37, pp. 2878–2900, 1988.

[40] Jürgen Berges, "Introduction to nonequilibrium quantum field theory", *AIP Conf. Proc.*, vol. 739, pp. 3–62, 2004.

[41] Mustafa A. Amin, Mark P. Hertzberg, David I. Kaiser, and Johanna Karouby, "Nonperturbative dynamics of reheating after inflation: A review", *Int. J. Mod. Phys. D*, vol. 24, pp. 1530003, 2015.

[42] Masahiro Morikawa and Misao Sasaki, "Entropy production in the inflationary universe", *Prog. Theor. Phys.*, vol. 72, pp. 782, 1984.

[43] Arjun Berera, Ian G. Moss, and Rudnei O. Ramos, "Warm inflation and its microphysical basis", *Rept. Prog. Phys.*, vol. 72, pp. 026901, 2009.

[44] A. Anisimov, W. Buchmuller, M. Drewes, and S. Mendizabal, "Nonequilibrium Dynamics of Scalar Fields in a Thermal Bath", *Annals Phys.*, vol. 324, pp. 1234–1260, 2009.

[45] Julian Schwinger, "Brownian motion of a quantum oscillator", *J. Math. Phys.*, vol. 2, pp. 407–432, 1961.

[46] L. V. Keldysh, "Diagram technique for nonequilibrium processes", *Zh. Eksp. Teor. Fiz.*, vol. 47, pp. 1515–1527, 1964, [Sov. Phys. JETP 20 (1965) 1018].

[47] Jurgen Berges, "Introduction to nonequilibrium quantum field theory", *AIP Conf. Proc.*, vol. 739, pp. 3–62, 2004.

[48] Pawel Danielewicz, "Quantum theory of nonequilibrium processes, i", *Annals Phys.*, vol. 152, pp. 239–304, 1984.

[49] Tomislav Prokopec, Michael G. Schmidt, and Stefan Weinstock, "Transport equations for chiral fermions to order h-bar and electroweak baryogenesis", *Annals Phys.*, vol. 314, pp. 208–265, 2004.

[50] Alexei Kamenev, *Field Theory of Non-Equilibrium Systems*, Cambridge University Press, Cambridge, 2011.

[51] Steven Weinberg, *The Quantum Theory of Fields. Volume 1: Foundations*, Cambridge University Press, Cambridge, 1995.

[52] Michael E. Peskin and Daniel V. Schroeder, *An Introduction to Quantum Field Theory*, Westview Press, Boulder, 1995.

[53] Richard D. Jordan, "Effective field equations for expectation values", *Phys. Rev. D*, vol. 33, pp. 444–454, 1986.

[54] Alex Kamenev, *Field Theory of Non-Equilibrium Systems*, Cambridge Monographs on Mathematical Physics. Cambridge University Press, Cambridge, UK, 2011.

[55] Masahiro Morikawa, "Dissipation and fluctuation of quantum fields in expanding universes", *Phys. Rev. D*, vol. 33, pp. 3607–3614, 1986.

[56] Edward W. Kolb and Michael S. Turner, *The Early Universe*, vol. 69 of *Frontiers in Physics*, Addison-Wesley, 1990.

[57] Marco Drewes and Jin U Kang, "The Kinematics of Cosmic Reheating", *Nucl. Phys. B*, vol. 875, pp. 315–350, 2013, [Erratum: Nucl.Phys.B 888, 284–286 (2014)].

[58] Joseph I. Kapusta and Charles Gale, *Finite-Temperature Field Theory: Principles and Applications*, Cambridge University Press, 2 edition, 2006.

[59] Michel Le Bellac, *Thermal Field Theory*, Cambridge University Press, 1996.

[60] Daniel Boyanovsky and H. J. de Vega, "Dynamics of symmetry breaking out of equilibrium: From the early universe to laboratory experiments", *Phys. Rev. D*, vol. 70, pp. 063508, 2004.

[61] B. L. Hu, Juan Pablo Paz, and Yuhong Zhang, "Quantum brownian motion in a general environment: Exact master equation with nonlocal dissipation and colored noise", *Phys. Rev. D*, vol. 45, pp. 2843–2861, 1992.

[62] Paolo Gondolo and Graciela Gelmini, "Cosmic abundances of stable particles: Improved analysis", *Nucl. Phys. B*, vol. 360, pp. 145–179, 1991.

[63] Nicolás Bernal et al., "Dark matter production in the early universe: Beyond the thermal wimp paradigm", *Int. J. Mod. Phys. A*, vol. 36, pp. 2130023, 2021.

[64] Marcos A. G. Garcia, Yann Mambrini, Keith A. Olive, and Marco Peloso, "Enhancement of dark matter production during reheating", *Phys. Rev. D*, vol. 96, pp. 103510, 2017.

[65] Leo P. Kadanoff and Gordon Baym, *Quantum Statistical Mechanics*, Benjamin, 1962.

[66] G. Buldgen et al., "Kinetic theory of scalar fields in curved spacetime: A systematic derivation", *Journal of Cosmology and Astroparticle Physics*, vol. 2019, no. 06, pp. 021, 2019.

[67] Julian Schwinger, "Brownian motion of a quantum oscillator", *J. Math. Phys.*, vol. 2, pp. 407–432, 1961.

[68] Daniel Boyanovsky and H. J. de Vega, "Dynamics of symmetry breaking out of equilibrium: From the early universe to laboratory experiments", *Phys. Rev. D*, vol. 70, pp. 063508, 2004.

[69] Kuang-chao Chou, Zhao-bin Su, Bai-lin Hao, and Lu Yu, "Equilibrium and nonequilibrium formalisms made unified", *Phys. Rept.*, vol. 118, pp. 1–131, 1985.

[70] Jürgen Berges, "Introduction to nonequilibrium quantum field theory", *AIP Conf. Proc.*, vol. 739, pp. 3–62, 2004.

[71] Pawel Danielewicz, "Quantum theory of nonequilibrium processes. i", *Annals Phys.*, vol. 152, pp. 239–304, 1984.

[72] Leo P. Kadanoff and Gordon Baym, *Quantum Statistical Mechanics: Green's Function Methods in Equilibrium and Nonequilibrium Problems*, Benjamin, New York, 1962.

[73] R. E. Cutkosky, "Singularities and discontinuities of feynman amplitudes", *J. Math. Phys.*, vol. 1, pp. 429–433, 1960.

[74] Kuang-Chao Chou, Zhao-Bin Su, Bai-Lin Hao, and Lu Yu, "Equilibrium and nonequilibrium formalisms made unified", *Phys. Rept.*, vol. 118, pp. 1–131, 1985.

[75] Rouzbeh Allahverdi, Robert Brandenberger, Francis-Yan Cyr-Racine, and Anupam Mazumdar, "Reheating in Inflationary Cosmology: Theory and Applications", *Ann. Rev. Nucl. Part. Sci.*, vol. 60, pp. 27–51, 2010.

[76] Michel Le Bellac, *Thermal Field Theory*, Cambridge University Press, Cambridge, 1996.

[77] Marcos A. G. Garcia, Kunio Kaneta, Yann Mambrini, and Keith A. Olive, "Reheating and Post-inflationary Production of Dark Matter", *Phys. Rev. D*, vol. 101, no. 12, pp. 123507, 2020.

[78] Jürgen Berges, "Introduction to nonequilibrium quantum field theory", *AIP Conf. Proc.*, vol. 739, pp. 3–62, 2004.

[79] Marco Drewes, "On the role of quasiparticles and thermal masses in nonequilibrium processes in a plasma", *Int. J. Mod. Phys. E*, vol. 19, pp. 1–62, 2010.

[80] Marco Drewes and Björn Garbrecht, "Combining experimental and cosmological constraints on heavy neutrinos", *Nucl. Phys. B*, vol. 921, pp. 250–315, 2017.

[81] Marco Drewes, "Measuring the inflaton coupling in the CMB", *JCAP*, vol. 09, pp. 069, 2022.

[82] Marco Drewes, Lei Ming, and Isabel Oldengott, "LiteBIRD and CMB-S4 sensitivities to reheating in plateau models of inflation", *JCAP*, vol. 05, pp. 081, 2024.

[83] Juergen Berges, Alexander. Rothkopf, and Jonas Schmidt, "Non-thermal fixed points: Effective weak-coupling for strongly correlated systems far from equilibrium", *Phys. Rev. Lett.*, vol. 101, pp. 041603, 2008.

[84] Anupam Mazumdar and Bryan Zaldivar, "Quantifying the reheating temperature of the universe", *Nucl. Phys. B*, vol. 886, pp. 312–327, 2014.

[85] Keisuke Harigaya and Kyohei Mukaida, "Thermalization after/during Reheating", *JHEP*, vol. 05, pp. 006, 2014.

[86] Keisuke Harigaya, Masahiro Kawasaki, Kyohei Mukaida, and Masaki Yamada, "Dark Matter Production in Late Time Reheating", *Phys. Rev. D*, vol. 89, no. 8, pp. 083532, 2014.

[87] Kyohei Mukaida and Masaki Yamada, "Thermalization Process after Inflation and Effective Potential of Scalar Field", *JCAP*, vol. 02, pp. 003, 2016.

[88] Kyohei Mukaida and Masaki Yamada, "Perturbative reheating and thermalization of pure Yang-Mills plasma", *JHEP*, vol. 05, pp. 174, 2024.

[89] Marco Drewes, Sebastian Mendizabal, and Christoph Weniger, "The Boltzmann Equation from Quantum Field Theory", *Phys. Lett. B*, vol. 718, pp. 1119–1124, 2013.

[90] Kaloian D. Lozanov and Mustafa A. Amin, "Equation of State and Duration to Radiation Domination after Inflation", *Phys. Rev. Lett.*, vol. 119, no. 6, pp. 061301, 2017.

[91] Pankaj Saha, Sampurn Anand, and L. Sriramkumar, "Accounting for the time evolution of the equation of state parameter during reheating", *Phys. Rev. D*, vol. 102, no. 10, pp. 103511, 2020.

[92] Stefan Antusch, Daniel G. Figueroa, Kenneth Marschall, and Francisco Torrenti, "Energy distribution and equation of state of the early Universe: matching the end of inflation and the onset of radiation domination", *Phys. Lett. B*, vol. 811, pp. 135888, 2020.

[93] Stefan Antusch, Kenneth Marschall, and Francisco Torrenti, “Equation of state during (p)reheating with trilinear interactions”, *JCAP*, vol. 11, pp. 002, 2025.

[94] Jerome Martin, Christophe Ringeval, and Vincent Vennin, “Encyclopædia Inflationaris: Opiparous Edition”, *Phys. Dark Univ.*, vol. 5-6, pp. 75–235, 2014.

[95] Yang Liu, Lei Ming, Marco Drewes, and Hong Li, “AliCPT Sensitivity to Cosmic Reheating”, 3 2025.

[96] Wen-Yuan Ai, Marco Drewes, Dražen Glavan, and Jan Hajer, “Oscillating scalar dissipating in a medium”, *JHEP*, vol. 11, pp. 160, 2021.

[97] Alexei A. Starobinsky, “A New Type of Isotropic Cosmological Models Without Singularity”, *Phys. Lett. B*, vol. 91, pp. 99–102, 1980.

[98] Fedor L. Bezrukov and Mikhail Shaposhnikov, “The Standard Model Higgs boson as the inflaton”, *Phys. Lett. B*, vol. 659, pp. 703–706, 2008.

[99] Javier Rubio and Eemeli S. Tomberg, “Preheating in Palatini Higgs inflation”, *JCAP*, vol. 04, pp. 021, 2019.

[100] Frédéric Dux, Adrien Florio, Juraj Klarić, Andrey Shkerin, and Inar Timiryasov, “Preheating in Palatini Higgs inflation on the lattice”, *JCAP*, vol. 09, pp. 015, 2022.

[101] Kim V. Berghaus, Marco Drewes, and Sebastian Zell, “Warm Inflation with the Standard Model”, *Phys. Rev. Lett.*, vol. 135, no. 17, pp. 171002, 2025.

[102] Kazuhide Ichikawa, Teruaki Suyama, Tomo Takahashi, and Masahide Yamaguchi, “Primordial Curvature Fluctuation and Its Non-Gaussianity in Models with Modulated Reheating”, *Phys. Rev. D*, vol. 78, pp. 063545, 2008.

[103] Kyohei Mukaida and Kazunori Nakayama, “Dynamics of oscillating scalar field in thermal environment”, *JCAP*, vol. 01, pp. 017, 2013.

[104] Kyohei Mukaida and Kazunori Nakayama, “Dissipative Effects on Reheating after Inflation”, *JCAP*, vol. 03, pp. 002, 2013.

[105] Marco Drewes, "On finite density effects on cosmic reheating and moduli decay and implications for Dark Matter production", *JCAP*, vol. 11, pp. 020, 2014.

[106] Wen-Yuan Ai, Ankit Beniwal, Angelo Maggi, and David J. E. Marsh, "From QFT to Boltzmann: freeze-in in the presence of oscillating condensates", *JHEP*, vol. 02, pp. 122, 2024.

[107] Juergen Berges and Julien Serreau, "Parametric resonance in quantum field theory", *Phys. Rev. Lett.*, vol. 91, pp. 111601, 2003.

[108] J. Berges, D. Gelfand, and J. Pruschke, "Quantum theory of fermion production after inflation", *Phys. Rev. Lett.*, vol. 107, pp. 061301, 2011.

[109] Kyohei Mukaida, Kazunori Nakayama, and Masahiro Takimoto, "Fate of Z_2 Symmetric Scalar Field", *JHEP*, vol. 12, pp. 053, 2013.

[110] Kimmo Kainulainen, Sami Nurmi, and Olli Väisänen, "Tachyonic production of dark relics: classical lattice vs. quantum 2PI in Hartree truncation", *JHEP*, vol. 10, pp. 009, 2024.

[111] Aleksandr Chatrchyan, Kevin T. Geier, Markus K. Oberthaler, Jürgen Berges, and Philipp Hauke, "Analog cosmological reheating in an ultracold Bose gas", *Phys. Rev. A*, vol. 104, no. 2, pp. 023302, 2021.

[112] Jeff Steinhauer, Murad Abuzarli, Tangui Aladjidi, Tom Bienaimé, Clara Piekarski, Wei Liu, Elisabeth Giacobino, Alberto Bramati, and Quentin Glorieux, "Analogue cosmological particle creation in an ultracold quantum fluid of light", *Nature Commun.*, vol. 13, pp. 2890, 2022.

[113] Oleg Lebedev, Fedor Smirnov, Timofey Solomko, and Jong-Hyun Yoon, "Dark matter production and reheating via direct inflaton couplings: collective effects", *JCAP*, vol. 10, pp. 032, 2021.

[114] Aqeel Ahmed, Bohdan Grzadkowski, and Anna Socha, "Higgs boson induced reheating and ultraviolet frozen-in dark matter", *JHEP*, vol. 02, pp. 196, 2023.

[115] Marcos A. G. Garcia, Kunio Kaneta, Yann Mambrini, Keith A. Olive, and Sarunas Verner, "Freeze-in from preheating", *JCAP*, vol. 03, no. 03, pp. 016, 2022.

[116] Alexei H. Sopov, Carlos Tamarit, and Raymond R. Volkas, “The post-inflationary cosmology of the VISHν axion-majoron model”, 12 2025.

[117] Marcos A. G. Garcia, Wenqi Ke, Yann Mambrini, Keith A. Olive, and Sarunas Verner, “Scalar field fluctuations and the production of dark matter”, *JCAP*, vol. 08, pp. 039, 2025.

[118] Marcos A. G. Garcia, Mathieu Gross, Yann Mambrini, Keith A. Olive, Mathias Pierre, and Jong-Hyun Yoon, “Effects of fragmentation on post-inflationary reheating”, *JCAP*, vol. 12, pp. 028, 2023.

[119] Nabeen Bhusal, M. Ernesto Chávez M., Marcos A. G. Garcia, Adriana G. Menkara, and Mathias Pierre, “Fermion reheating with a quartic inflaton potential”, 12 2025.

[120] N. Aghanim et al., “Planck 2018 results. VI. Cosmological parameters”, *Astron. Astrophys.*, vol. 641, pp. A6, 2020, [Erratum: Astron.Astrophys. 652, C4 (2021)].

[121] P. A. R. Ade et al., “Improved Constraints on Primordial Gravitational Waves using Planck, WMAP, and BICEP/Keck Observations through the 2018 Observing Season”, *Phys. Rev. Lett.*, vol. 127, no. 15, pp. 151301, 2021.

[122] I. Abril-Cabezas et al., “The Simons Observatory: forecasted constraints on primordial gravitational waves with the expanded array of Small Aperture Telescopes”, 12 2025.

[123] E. Allys et al., “Probing Cosmic Inflation with the LiteBIRD Cosmic Microwave Background Polarization Survey”, *PTEP*, vol. 2023, no. 4, pp. 042F01, 2023.

[124] Hong Li et al., “Probing Primordial Gravitational Waves: Ali CMB Polarization Telescope”, *Natl. Sci. Rev.*, vol. 6, no. 1, pp. 145–154, 2019.

[125] Hong Li, Si-Yu Li, Yang Liu, Yong-Ping Li, and Xinmin Zhang, “Tibet’s window on primordial gravitational waves”, *Nature Astron.*, vol. 2, no. 2, pp. 104–106, 2018.

[126] Marco Drewes and Lei Ming, “Connecting Cosmic Inflation to Particle Physics with LiteBIRD, CMB-S4, EUCLID, and SKA”, *Phys. Rev. Lett.*, vol. 133, no. 3, pp. 031001, 2024.

[127] Marcos A. G. Garcia, Kunio Kaneta, Yann Mambrini, and Keith A. Olive, "Inflaton Oscillations and Post-Inflationary Reheating", *JCAP*, vol. 04, pp. 012, 2021.

[128] Farinaldo Elahi, Christopher Kolda, and James Unwin, "Ultraviolet freeze-in", *JHEP*, vol. 03, pp. 048, 2015.

[129] Michael S. Turner, "Coherent Scalar Field Oscillations in an Expanding Universe", *Phys. Rev. D*, vol. 28, pp. 1243, 1983.

[130] Shao-Long Chen and Zhaofeng Kang, "On UltraViolet Freeze-in Dark Matter during Reheating", *JCAP*, vol. 05, pp. 036, 2018.

[131] Arjun Berera, "Warm inflation", *Phys. Rev. Lett.*, vol. 75, pp. 3218–3221, 1995.

[132] Katherine Freese, Gabriele Montefalcone, and Barmak Shams Es Haghi, "Dark Matter Production during Warm Inflation via Freeze-In", *Phys. Rev. Lett.*, vol. 133, no. 21, pp. 211001, 2024.

[133] Alexander Merle and Maximilian Totzauer, "keV Sterile Neutrino Dark Matter from Singlet Scalar Decays: Basic Concepts and Subtle Features", *JCAP*, vol. 06, pp. 011, 2015.

[134] Johannes König, Alexander Merle, and Maximilian Totzauer, "keV Sterile Neutrino Dark Matter from Singlet Scalar Decays: The Most General Case", *JCAP*, vol. 11, pp. 038, 2016.

[135] Marco Drewes and Jin U Kang, "Sterile neutrino Dark Matter production from scalar decay in a thermal bath", *JHEP*, vol. 05, pp. 051, 2016.

[136] M. Laine, "Thermal right-handed neutrino production rate in the relativistic regime", *JHEP*, vol. 08, pp. 138, 2013.

[137] I. Ghisoiu and M. Laine, "Right-handed neutrino production rate at T $>$ 160 GeV", *JCAP*, vol. 12, pp. 032, 2014.

[138] Lorenzo Calibbi, Francesco D'Eramo, Sam Junius, Laura Lopez-Honorez, and Alberto Mariotti, "Displaced new physics at colliders and the early universe before its first second", *JHEP*, vol. 05, pp. 234, 2021.

[139] Morad Aaboud et al., "Search for heavy charged long-lived particles in the ATLAS detector in 36.1 fb^{-1} of proton-proton collision data at $\sqrt{s} = 13$ TeV", *Phys. Rev. D*, vol. 99, no. 9, pp. 092007, 2019.

[140] Morad Aaboud et al., "Search for long-lived charginos based on a disappearing-track signature in pp collisions at $\sqrt{s} = 13$ TeV with the ATLAS detector", *JHEP*, vol. 06, pp. 022, 2018.

[141] Albert M Sirunyan et al., "Search for disappearing tracks as a signature of new long-lived particles in proton-proton collisions at $\sqrt{s} = 13$ TeV", *JHEP*, vol. 08, pp. 016, 2018.

[142] Albert M Sirunyan et al., "Search for disappearing tracks in proton-proton collisions at $\sqrt{s} = 13$ TeV", *Phys. Lett. B*, vol. 806, pp. 135502, 2020.

[143] Georges Aad et al., "Search for Displaced Leptons in $\sqrt{s} = 13$ TeV pp Collisions with the ATLAS Detector", *Phys. Rev. Lett.*, vol. 127, no. 5, pp. 051802, 2021.

[144] Vardan Khachatryan et al., "Search for Displaced Supersymmetry in events with an electron and a muon with large impact parameters", *Phys. Rev. Lett.*, vol. 114, no. 6, pp. 061801, 2015.

[145] "Search for displaced leptons in the e-mu channel", 2016.

[146] Georges Aad et al., "Search for long-lived charginos based on a disappearing-track signature using 136 fb^{-1} of pp collisions at $\sqrt{s}$ = 13 TeV with the ATLAS detector", *Eur. Phys. J. C*, vol. 82, no. 7, pp. 606, 2022.

[147] Georges Aad et al., "Search for displaced leptons in $\sqrt{s} = 13$ TeV and 13.6 TeV pp collisions with the ATLAS detector", *Phys. Rev. D*, vol. 112, no. 1, pp. 012016, 2025.

[148] Marco Drewes, Juraj Klarić, and Yuan-Zhen Li, "New particles at the Z-pole:", *Eur. Phys. J. C*, vol. 86, no. 4, pp. 337, 2026.

[149] Marco Drewes, Andrea Giammanco, Jan Hajer, and Michele Lucente, "New long-lived particle searches in heavy-ion collisions at the LHC", *Phys. Rev. D*, vol. 101, no. 5, pp. 055002, 2020.

[150] Marco Drewes, Yannis Georis, Juraj Klarić, and Inar Timiryasov, "Heavy Fermion Interaction Rates at Finite Temperature in Fermi Theory", *in preparation*.

[151] Xiang-Dong Shi and George M. Fuller, "A New dark matter candidate: Nonthermal sterile neutrinos", *Phys. Rev. Lett.*, vol. 82, pp. 2832–2835, 1999.

[152] Xun-Jie Xu and Boting Zhou, "Dark Photons in the Early Universe: From Thermal Production to Cosmological Constraints", 12 2025.

[153] G. F. Giudice, M. Peloso, A. Riotto, and I. Tkachev, "Production of massive fermions at preheating and leptogenesis", *JHEP*, vol. 08, pp. 014, 1999.

[154] JiJi Fan, Kaloian D. Lozanov, and Qianshu Lu, "Spillway Preheating", *JHEP*, vol. 05, pp. 069, 2021.

[155] Xun-Jie Xu, Yong Xu, Qiqin Yin, and Junyu Zhu, "Full-spectrum analysis of gravitational wave production from inflation to reheating", *JHEP*, vol. 10, pp. 141, 2025.

[156] H. Arthur Weldon, "Effective Fermion Masses of Order gT in High Temperature Gauge Theories with Exact Chiral Invariance", *Phys. Rev. D*, vol. 26, pp. 2789, 1982.

[157] Catarina Cosme, Francesco Costa, and Oleg Lebedev, "Freeze-in at stronger coupling", *Phys. Rev. D*, vol. 109, no. 7, pp. 075038, 2024.

[158] Yoshiki Ueno and Kazuhiro Yamamoto, "Constraints on α-attractor inflation and reheating", *Phys. Rev. D*, vol. 93, no. 8, pp. 083524, 2016.

[159] Nicola Barbieri, Thejs Brinckmann, Stefano Gariazzo, Massimiliano Lattanzi, Sergio Pastor, and Ofelia Pisanti, "Current Constraints on Cosmological Scenarios with Very Low Reheating Temperatures", *Phys. Rev. Lett.*, vol. 135, no. 18, pp. 181003, 2025.

[160] M. Kawasaki, Kazunori Kohri, and Naoshi Sugiyama, "Cosmological constraints on late time entropy production", *Phys. Rev. Lett.*, vol. 82, pp. 4168, 1999.

[161] M. Kawasaki, Kazunori Kohri, and Naoshi Sugiyama, "MeV scale reheating temperature and thermalization of neutrino background", *Phys. Rev. D*, vol. 62, pp. 023506, 2000.

[162] Takuya Hasegawa, Nagisa Hiroshima, Kazunori Kohri, Rasmus S. L. Hansen, Thomas Tram, and Steen Hannestad, "MeV-scale reheating temperature and thermalization of oscillating neutrinos by radiative and hadronic decays of massive particles", *JCAP*, vol. 12, pp. 012, 2019.

[163] P. F. de Salas, M. Lattanzi, G. Mangano, G. Miele, S. Pastor, and O. Pisanti, "Bounds on very low reheating scenarios after Planck", *Phys. Rev. D*, vol. 92, no. 12, pp. 123534, 2015.

[164] Gilles Buldgen, Marco Drewes, Jin U. Kang, and Ui Ri Mun, "General markovian equation for scalar fields in a slowly evolving background", 2019.

[165] Yann Cado, Mathieu Gross, Yann Mambrini, and Keith Olive, "Phenomenological constraints on Higgs reheating", *Phys. Rev. D*, vol. 112, no. 11, pp. 115027, 2025.

[166] Renata Kallosh, Andrei Linde, and Diederik Roest, "Superconformal Inflationary α-Attractors", *JHEP*, vol. 11, pp. 198, 2013.

[167] Andrei D. Linde, "Chaotic Inflation", *Phys. Lett. B*, vol. 129, pp. 177–181, 1983.

[168] Thibaut Louis et al., "The Atacama Cosmology Telescope: DR6 power spectra, likelihoods and ΛCDM parameters", *JCAP*, vol. 11, pp. 062, 2025.

[169] E. Camphuis et al., "SPT-3G D1: CMB temperature and polarization power spectra and cosmology from 2019 and 2020 observations of the SPT-3G Main field", 6 2025.

[170] Evan McDonough and Elisa G. M. Ferreira, "The spectrum of n_s constraints from DESI and CMB data", 12 2025.

[171] M. Fairbairn, Laura Lopez Honorez, and M. H. G. Tytgat, "Radion assisted gauge inflation", *Phys. Rev. D*, vol. 67, pp. 101302, 2003.

[172] Nima Arkani-Hamed, Hsin-Chia Cheng, Paolo Creminelli, and Lisa Randall, "Pseudonatural inflation", *JCAP*, vol. 07, pp. 003, 2003.

[173] David E. Kaplan and Neal J. Weiner, "Little inflatons and gauge inflation", *JCAP*, vol. 02, pp. 005, 2004.

[174] Nima Arkani-Hamed, Hsin-Chia Cheng, Paolo Creminelli, and Lisa Randall, "Extra natural inflation", *Phys. Rev. Lett.*, vol. 90, pp. 221302, 2003.

[175] Barun Kumar Pal, Supratik Pal, and B. Basu, "Mutated Hilltop Inflation : A Natural Choice for Early Universe", *JCAP*, vol. 01, pp. 029, 2010.

[176] Barun Kumar Pal, Supratik Pal, and B. Basu, "A semi-analytical approach to perturbations in mutated hilltop inflation", *Int. J. Mod. Phys. D*, vol. 21, pp. 1250017, 2012.

[177] Lotfi Boubekeur and David. H. Lyth, "Hilltop inflation", *JCAP*, vol. 07, pp. 010, 2005.

[178] Kazunori Kohri, Chia-Min Lin, and David H. Lyth, "More hilltop inflation models", *JCAP*, vol. 12, pp. 004, 2007.

[179] Renata Kallosh and Andrei Linde, "Universality Class in Conformal Inflation", *JCAP*, vol. 07, pp. 002, 2013.

[180] Claire Rigouzzo and Sebastian Zell, "No Dark Matter Axion During Minimal Higgs Inflation", 4 2025.

[181] Claire Rigouzzo and Sebastian Zell, "On Non-Minimal Couplings to Gravity and Axion Isocurvature Bounds", 12 2025.